

The University of Nottingham

Nottingham Geospatial Institute

MULTI-FREQUENCY GPS/GALILEO COMBINATIONS FOR QUICK PRECISE POINT POSITIONING IN URBAN ENVIRONMENTS

Francesco Basile

Thesis submitted to the University of Nottingham for the degree of Doctor of Philosophy

March 2019

Abstract

High-end applications, such as surveying, geodesy, and mapping, require positioning accuracies in the order of centimetres or even millimetres. Global Navigation Satellite Systems (GNSS) enables such high accuracy levels by exploiting very precise carrier phase measurements. While, in the past, high accuracy GNSS was dominated by differential techniques, such as Real Time Kinematic (RTK), in recent years the interest in Precise Point Positioning (PPP) has considerably grown. Thanks to its high computational efficiency, no need for any synchronous measurements from nearby reference stations, and homogeneous positioning quality on a global scale, it is widely used for many applications characterized by open sky conditions, e.g. precision agriculture. Unfortunately, the main downside of PPP, i.e. its long (re-)convergence time, strongly limits its use in constrained and transient signal environments associated with urban areas.

The modernisation process of the GNSS will positively affect the PPP solutions thanks to the higher number of satellites in view broadcasting multi-frequency ranging signals. Indeed, previous studies identified the number and geometry of the observed satellites as one of the factors impacting on the PPP (re-) convergence time. It was observed that, when multi-constellation GNSS measurements are employed, the PPP solutions are greatly improved, especially in particularly masking environments. At the same time, many publications showed that triple-frequency observables benefit ambiguity fixing, but not the float solutions.

In this PhD thesis, the PPP float solutions based on multi-frequency GPS and Galileo measurements recorded on-board kinematic platforms in urban areas are investigated, in terms of precision and convergence time. In addition, the specific benefit of the Galileo AltBOC modulated signal E5 on PPP is also analysed. This research has been conducted in five stages.

Firstly, GPS+Galileo PPP solutions were compared against GPS only, and Galileo only PPP solutions. The current state of the Galileo constellation and its PPP products, as well as of the GPS next generation constellation, is still not mature for a clear evaluation of multi-frequency multi-GNSS PPP. Hence it was decided to employ simulated data.

The second part of this research is aimed to identify the GPS and Galileo two-frequency ionosphere-free combinations that guarantee the best accuracy and convergence time in PPP. Both for GPS and Galileo, this is the combination between L1/E1 and L5/E5a.

Then, the GPS, Galileo, and GPS+Galileo PPP solutions were compared in open sky conditions. In a multipath-free environment, the positioning solution based on Galileo measurements, on average, converges to an accuracy of better than 10 cm in 2.5 minutes horizontally and 6.5 minutes vertically. As a comparison, it takes 4 and 10.5 minutes to have an average error, respectively, in the horizontal and vertical GPS PPP solution smaller than 10 cm. This has been justified by the lower noise in the Galileo pseudoranges. On the other hand, in a multipath-rich site, where the quality of the GPS and Galileo pseudoranges is comparable, GPS offers better PPP performance. For example, the horizontal RMS error in the GPS PPP solution converges in 20 minutes, while the average convergence time for the horizontal Galileo solution is as large as 33.5 minutes. In all cases, the GPS+Galileo solutions are more accurate and take less time to converge below 10 cm of error than the single-constellation configurations. Indeed, in a multipath-rich site, the RMS horizontal error in the GPS+Galileo PPP solution takes only 16.5 minutes to go below 10 cm and reaches a final accuracy of about 9.6 mm. In contrast, the horizontal accuracy in the GPS solution is about 1.3 cm.

The fourth part analyses the performance of GPS+Galileo PPP in urban environments. Although, there are areas where satellite availability is good enough to compute a GNSS positioning solution, the slow PPP (re-) convergence may not allow high accuracies. In the scenario that was simulated, once the receiver loses track of most of the satellites, the horizontal GPS+Galileo PPP solution never re-converges below 50 cm for 95% of the time. Nonetheless, the results showed that GPS+Galileo PPP easily enables sub-meter level horizontal accuracy for most of the time.

Finally, to fulfil the needs of higher accuracy applications, more refined positioning algorithms, aimed to reduce the PPP (re-)convergence time, are proposed. These are based on triple-frequency ionosphere-free combinations. Unlike the most successful methods that can be found in literature, they do not rely on any external ionospheric information. Therefore, these algorithms, not

exploiting the spatial correlation in the ionospheric delay, but only the temporal correlation, for a given level of ionosphere activity, guarantee homogeneous performance with increasing distance of the receiver from the network of reference stations that was used to compute the PPP corrections. In urban areas, while the horizontal GPS+Galileo PPP solution based on the traditional ionosphere-free combination is not able to re-converge below 20 cm, in the first method, a re-convergence time of a few tens of seconds can be obtained by employing smoothed-ionosphere corrected, low-noise pseudorange combinations. The second approach uses triple-carrier ionosphere-free combinations that minimize the noise in the ambiguity observable to shorten the first convergence of the float Galileo PPP horizontal solution from 20.43 minutes, adopting the two-frequency ionosphere-free combinations, to 8.58 minutes.

To the strangers who become family…

Acknowledgements

I will start my acknowledgments by thanking the University of Nottingham and the Rockwell Collins UK Limited (now rebranded Collins Aerospace) for sponsoring this PhD project and for the financial support during these past few years.

I sincerely thank my supervisors, Prof. Terry Moore, Dr. Chris Hill, and Dr. Gary McGraw, for giving me the opportunity to work in this exciting research project, and for their patient guidance, and valuable and constructive suggestions during the development of this research work. I am also grateful to Mr. Andrew Johnson for scheduling the monthly supervision meetings.

Dr. Paul Groves and Dr. Mounir Adjirad from the UCL need to be warmly recognized for their contribution to the development of the GPS/Galileo Simulink tool. For the same reason, I thank Dr. Kevin Sheridan from Terrastar GNSS Limited for sharing the real-time PPP products for Galileo. It is all my fault if I never used these products for validating my simulation models.

I want to thank all the PhD students and post-docs at the NGI. Thank you Jareer for your help with the POINT software. Thank you Ammar for patiently going through any idea that came into my mind. Thank you Lin, Ioulia, and Brian for the nice moments we had together. One day we will escape from that Egyptian room. Thank you Lukasz for letting me try the smelliest and most delicious French cheese. I also want to mention Simone, Pekka, Nicolas, Adrian, Bertrand, Lei, Alex, and Fei for all the time we have spent together.

I can’t find words to thank my dearest friends Matteo, Allegra, Andrea, Alessandro, Gianfranco, Diana, little Elio, Roxy, Chris, Federico, Kamila, Alberto, and Francesca. You have been my family in these three years and I am glad I met you.

I have to deeply thank my parents and my sister Gloria. I can’t even count the hours spent on WhatsApp trying to reduce the 2249 km between us. Thank you for coming to Nottingham by train, but, even more, thank you for flying to Nottingham when I was homesick.

A gigantic thank you goes to Roberta. It is mostly for your patience if I find myself sitting at my desk, writing this last and important paragraph of my thesis. Thank you for making our small apartment in Lenton Manor our home. Thank

you for supporting me in any decision I took, even if it meant (and it means) leaving our family and friends to move around Europe. I love you.

Table of Contents

List of Figures vi

List of Tables xvi

Acronyms and Abbreviations xxii

Chapter 1 Introduction 1

1.1 Aims and Objectives 4

1.2 Contribution to Knowledge 5

1.3 Thesis Overview 5

1.4 Publications 7

Chapter 2 Literature review 8

2.1 Overview of the Galileo system 8

2.2 Multi-Constellation GNSS 14

2.3 Precise Point Positioning 19

2.4 Chapter summary 27

Chapter 3 Precise Point Positioning 29

3.1 Observation equation 29

3.2 Errors in GNSS measurements and corrections in PPP 31

3.2.1 Satellite orbits and clocks 31

3.1.1 Relativistic effects 35

3.1.2 Ionospheric delay 38

3.1.3 Tropospheric delay 41

3.1.4 Site displacement effects 43

3.1.4.1 Solid Earth Tides 44

3.1.4.2 Ocean Tides 44

3.1.4.3 Pole Tides 45

3.1.4.4 Earth Orientation Parameters 45

3.1.5 Antenna effects 46
3.1.5.1 Phase centre offset and variation 46
3.1.5.2 Phase wind-up effect 47
3.1.6 Signal biases 49
3.1.6.1 Pseudorange biases 49
3.1.6.2 Phase biases 50
3.2 Integer ambiguity resolution 50
3.2.1 Integer bootstrapping 50
3.2.2 LAMBDA 51
3.2.3 Triple Carrier Ambiguity Resolution (TCAR) 52
3.3 Chapter summary 55
Chapter 4 POINT software 57
4.1 Software structure and capability 58
4.1.1 Orbits and clocks 60
4.1.2 Relativistic effects 60
4.1.3 Ionosphere delay 60
4.1.4 Tropospheric delay 61
4.1.5 Site displacements 61
4.1.6 Antenna corrections 61
4.1.7 Signal biases 62
4.2 Software developments in this thesis 62
4.3 Chapter summary 63
Chapter 5 Initial comparison between GPS and GPS+Galileo PPP 64
5.1 GPS PPP using CODE IGS and CODE MGEX products 66
5.2 GPS and GPS+Galileo PPP in 2016 68
5.3 GPS, Galileo, and GPS+Galileo PPP in 2018 74
5.4 Chapter summary 82

Chapter 6 Multi-frequency GPS/Galileo simulator 83
6.1 Reasons for using simulated data.....83
6.2 Description of the triple-frequency GPS/Galileo Simulink.....85
6.2.1 SensorModel block 87
6.2.2 AGSS block 88
6.2.3 GeometryProcess block 89
6.2.4 ErrorModel block.....90
6.2.4.1 Tropo block.....92
6.2.4.2 Iono block.....94
6.2.4.3 Multipath block.....96
6.2.4.4 AntBias block 99
6.2.4.5 ThermNoise block 99
6.2.4.6 Receiver IF Bias block 101
6.2.5 GpsMsgBuilder block 101
6.3 Simulation of the Real-Time precise orbits and clocks 104
6.4 Randomness test.....117
6.5 Validation using real GPS measurements.....118
6.6 Chapter summary.....124
Chapter 7 Single and multi-constellation PPP with simulated data.....127
7.1 Preliminary study on the best two-frequency IF combinations 128
7.2 Open sky conditions.....135
7.3 Urban area: University College of London.....141
7.4 Chapter summary.....152
Chapter 8 Quick (re-)convergence in PPP.....155
8.1 Quick re-convergence by reducing the noise in the ionosphere-free pseudorange combinations.....156
8.1.1 Low noise pseudorange combinations with smoothed ionosphere correction 156

8.1.1.1 Low noise pseudorange combinations 157
8.1.1.2 Smoothed ionosphere correction 163
8.1.1.3 Ionosphere prediction 168
8.1.1.4 Weighting method 174
8.1.1.5 Results on quick re-convergence in open sky conditions 177
Sensitivity of the method to different multipath correlation time constants 180
8.1.1.6 Results on quick re-convergence in urban environments 189
8.2 Quick convergence by amplifying the narrow-lane wavelength 191
8.2.1 Triple-carrier ionosphere free combinations that minimise the noise in the narrow lane ambiguity 192
8.2.1.1 Results on quick convergence in open sky conditions 197
Sensitivity of the method to different multipath correlation time constants 200
8.3 Triple Carrier Ambiguity Resolution (TCAR) with smoothed ionosphere correction 207
8.4 Chapter summary 222
Chapter 9 Conclusions 225
9.1 Galileo capability in POINT 226
9.2 Effect of the current state Galileo constellation and MGEX products on PPP 226
9.3 Simulation of the precise orbits and clocks 228
9.4 Best GPS and Galileo two-frequency combinations for PPP 229
9.5 Comparison between GPS, Galileo, and GPS+Galileo PPP 229
9.6 Satellite availability and geometry conditions in urban areas 230
9.7 GPS+Galileo PPP in a kinematic urban scenario 231
9.8 Quick (re-)convergence PPP enabled by multi-frequency IF combinations 232

9.9 Prediction of the ionosphere estimate in urban environments 233

9.10 Use of the q-α_3-n plot for studying triple-frequency GNSS measurements combinations 234

9.11 Conclusions summary 234

9.12 Recommendations for future work 235

References 236

List of Figures

Figure 2.1 Galileo frequency bands, signals and components (Teunissen and Montenbruck, 2017).....9
Figure 3.1 Sagnac effect.....38
Figure 3.2 Typical day and night profile of the electron density in the ionosphere (Istituto Nazionale di Geofisica e Vulcanologia (INGV), 2018). .40
Figure 3.3 PCO (blue) and PCV (red) of a receiving choke-ring antenna. The solid red line indicates the elevation- and azimuth-dependent PCV with respect to a reference wave-front (dotted red line) (Teunissen and Montenbruck, 2017). 47
Figure 3.4 Satellite and receiver body coordinates used for the computation of the phase wind-up effect (Teunissen and Montenbruck, 2017).....49
Figure 3.5 Correlated (a) and decorrelated (b) search spaces. 2D example....52
Figure 3.6 Extra-wide lane and wide lane combinations (Werner and Winkel, 2003). 53
Figure 4.1 POINT software general structure.....60
Figure 5.1 IGS stations used to evaluate the quality of MGEX products and the GPS+GALILEO PPP performance.....65
Figure 5.2 Comparison between the RMS of the GPS and GPS+Galileo PPP 3D errors, for the 9 considered IGS stations between 3rd and 12th June 2018. Units of centimetres. 79
Figure 5.3 Comparison between the RMS of the GPS and GPS+Galileo PPP 3D convergence times, for the 9 considered IGS stations between 3rd and 12th June 2018. Units of minutes.....79
Figure 5.4 PDOP, HDOP, and VDOP time series. Galileo only (top), GPS only (middle), and GPS+Galileo (bottom) PPP processing of the data recorded by station SEYG between the 7th June 2018 at 22:51:30 and the 8th June 2018 at 12:24:00. 81
Figure 5.5 Positioning errors in the north, east and up components. Galileo only (top), GPS only (middle), and GPS+Galileo (bottom) PPP processing of the data recorded by station SEYG between the 7th June 2018 at 22:51:30 and the 8th June 2018 at 12:24:00. 81
Figure 6.1 Triple-frequency GPS/Galileo Simulink main block diagram. 86

Figure 6.2 SensorModel block. 88
Figure 6.3 AGSS block. 89
Figure 6.4 GeometryProcess block. 90
Figure 6.5 ErrorModel block. 91
Figure 6.6 Autocorrelation function of the MP1 combination. Top plot is simulated data, bottom plot is real data. 97
Figure 6.7 Magnitude of the multipath delays as a function of the elevation angle. The high multipath group (blue) includes the Galileo E1 and E6 and GPS L1 and L2 pseudoranges. The medium multipath group (orange) includes the Galileo E5a, E5b and GPS L5 pseudoranges. The low multipath group (yellow) includes Galileo E5 pseudoranges. The multipath on the carrier phase measurements is also shown in purple. 98
Figure 6.8 Receiver noise for different GPS and Galileo signals as function of the CN0. 101
Figure 6.9 GpsMsgBuilder block. 102
Figure 6.10 Assumed receiver antenna gain pattern as a function of the satellie's elevation angle. 103
Figure 6.11 Common logarithm of the probability of cycle slip as function of the carrier to noise ratio. 104
Figure 6.12 Difference between the IGS real-time and ESA final orbits for GPS PRN 14 on the 2nd October 2016. The upper plot shows the products' difference in the radial component of the satellite's position, the middle plot shows the difference in the cross-track component, while the lower one shows the difference in the along-track component. 106
Figure 6.13 Difference between the IGS real-time and ESA final clocks for GPS PRN 14 on the 2nd October 2016. The top plot shows the undifference case, while the bottom plot displays the single difference with respect to PRN 1 108
Figure 6.14 Spectrum of the error in the radial (top), cross-track (middle), and along-track (bottom) orbit components. GPS PRN 5. On the x axis, the frequencies as in units of times-per-day. 109
Figure 6.15 Spectrum of the error in the radial (top), cross-track (middle), and along-track (bottom) orbit components. GPS PRN 14. On the x axis, the frequencies as in units of times-per-day. 109

Figure 6.16 Spectrum of the single difference between satellite clock error with respect to GPS PRN 1. Top plot is for GPS PRN 5, while the bottom plot is for the GPS PRN 14. On the x axis, the frequencies as in units of times-per-day. 110
Figure 6.17 IGC orbit's error in the radial (top), cross-track (middle), and along-track (bottom) components for GPS PRN 14 on the 2nd October 2016. The blue dots represent the real data, while the red curve is the result of the fitting process to the second order Fourier expansion. 111
Figure 6.18 Histogram of the bias and amplitudes of the sinusoids that best fits the radial error in the IGC orbits. The plot in red is the generalized extreme value distribution that approximates the histogram of the empirical values. 112
Figure 6.19 Histogram of the bias and amplitudes of the sinusoids that best fits the cross-track error in the IGC orbits. The plot in red is the generalized extreme value distribution that approximates the histogram of the empirical values. 112
Figure 6.20 Histogram of the bias and amplitudes of the sinusoids that best fits the along-track error in the IGC orbits. The plot in red is the generalized extreme value distribution that approximates the histogram of the empirical values. 113
Figure 6.21 Histogram of the bias and amplitudes of the sinusoids that best fits the error in the IGC clocks. The plot in red is the generalized extreme value distribution that approximates the histogram of the empirical values. 113
Figure 6.22 Q-Q plot of the bias in the radial component against the generalized extreme value distribution.....114
Figure 6.23 Spectrum of the error in the radial (top), cross-track (middle), and along-track (bottom) orbit components. GLONASS PRN 23. On the x axis, the frequencies as in units of times-per-orbit.....116
Figure 6.24 Q-Q plot to prove that the "rand" function of Matlab generates uniformly distributed numbers.....117
Figure 6.25 Q-Q plot to prove that the "randn" function of Matlab generates uniformly distributed numbers.....118
Figure 6.26 IGS stations used to validate the multi-frequency GPS/Galileo simulator. 119
Figure 7.1 Comparison between the horizontal (left) and vertical (right) errors obtained by processing the GPS L1-L2 IF (blue) and L1-L5 IF (red) combinations. Station SEY2. 130

Figure 7.2 Comparison between the horizontal (left) and vertical (right) errors obtained by processing the Galileo E1-E5a IF (blue), E1-E5b IF (red), E1-E5 IF (yellow), E1-E6 IF (purple) combinations. Station SEY2. 131
Figure 7.3 Comparison between the horizontal error in the GPS (blue), Galileo(red), and GPS+Galileo (yellow) PPP solution. The left plot shows the RMS over 50 simulations, while in the right plot is the 95th percentile. Station SEY2. Benign environment. 137
Figure 7.4 Comparison between the HDOP in the GPS (blue), Galileo(red), and GPS+Galileo (yellow) case. 138
Figure 7.5 Comparison between the horizontal error in the GPS (blue), Galileo(red), and GPS+Galileo (yellow) PPP solution. The left plot shows the RMS over 50 simulations, while in the right plot is the 95th percentile. Station SEY2. Multipath-rich site. 140
Figure 7.6 Points in which the building boundaries were available. The background map was achieved from OpenStreet map. 142
Figure 7.7 Location of the urban sites that were considered in the satellites availability analysis. The background map was achieved from OpenStreet map. 143
Figure 7.8 Sky plot of the building obstruction masks to satellite visibility for each of the five sites. Both the azimuth angles and the elevation angles, which figure in the radial direction, are in units of degrees. 145
Figure 7.9 Junction between Gower Street and University Street. StreetView from Google maps. 146
Figure 7.10 Junction between University Street and Huntley Street. StreetView from Google maps. 146
Figure 7.11 The measured trajectory (red) of the pedestrian kinematic test. The background map was achieved from OpenStreet map. 148
Figure 7.12 HDOP (blue plot with the y axes on the left) and total number of visible GPS and Galileo satellites (red plot with y axes on the right) for the kinematic part of the pedestrian test. 150
Figure 7.13 GPS (top) and Galileo (bottom) satellites availabiolity for the kinematic part of the pedestrian test. 150
Figure 7.14 RMS (blue) and 95th percentile (red) of the horizontal error component for the kinematic test using GPS and Galileo data. 151

Figure 8.1 Colour-map of the geometry-preserving surface in the space q-α_3-n for the GPS L1-L2-L5 pseudorange combinations. 161
Figure 8.2 Colour-map of the geometry-preserving surface in the space q-α3-n for the Galileo E1-E5a-E5b pseudorange combinations. 161
Figure 8.3 Colour-map of the geometry-preserving surface in the space q-α3-n for the Galileo E1-E5a-E6 pseudorange combinations. 162
Figure 8.4 Colour-map of the geometry-preserving surface in the space q-α3-n for the Galileo E1-E5b-E6 pseudorange combinations. 162
Figure 8.5 Colour-map of the geometry-preserving surface in the space q-α3-n for the Galileo E1-E5-E6 pseudorange combinations. 163
Figure 8.6 Results for Hatch filters with different smoothing windows based on simulated data. The plot shows the errors in the raw pseudorange (black diamonds), the errors in the pseudorange smoothed by a single-frequency Hatch filter with N equal to 60 seconds (green squares) and 300 seconds (blue circles), and the errors in in the pseudorange smoothed by a divergence-free Hatch filter with N equal to 300 seconds (red crosses). Image from Teunissen and Montenbruck (2017). 166
Figure 8.7 Ionosphere delay computed from C1-P2 combination (raw blue dots, smoothed orange line), and C1-C5 combination (raw yellow dots, smoothed purple line). 167
Figure 8.8 RMS of the errors obtained when predicting the ionosphere using the constant bias model (blue), the linear fitting model with a time window large 60 seconds (red), 120 seconds (yellow), 240 seconds (purple), and 300 seconds (green). Elevation angles above 30°. 170
Figure 8.9 RMS of the errors obtained when predicting the ionosphere using the constant bias model (blue), the linear fitting model with a time window large 60 seconds (red), 120 seconds (yellow), 240 seconds (purple), and 300 seconds (green). Elevation angles below 30°. 170
Figure 8.10 RMS of the errors obtained when predicting the ionosphere using the constant bias model (blue), the linear fitting model with a time window large 120 seconds (red). Driving test around Birmingham. 172
Figure 8.11 Left plot (blue circle) is the percentage of continuous data arcs that are longer that the times on the x axis. Right plot (red star) is the RMS of the actual prediction time due to not having available the minimum number of

observations required to run the linear fitting model. Driving test around Birmingham on the 22nd June 2017. 173
Figure 8.12 RMS of the errors obtained when predicting the ionosphere using the constant bias model (blue), the linear fitting model with a time window large 120 seconds (red). Driving test in the city of Nottingham on the 13th June 2017. 173
Figure 8.13 Left plot (blue circle) is the percentage of continuous data arcs that are longer that the times on the x axis. Right plot (red star) is the RMS of the actual prediction time due to not having available the minimum number of observations required to run the linear fitting model. Driving test in the city of Nottingham on the 13th June 2017. 174
Figure 8.14 Error in the ionospheric delay observable. Blue dots shows the time-series of the error in the ionosphere computed from the raw pseudoranges, the red line is the error in the smoothed ionosphere, while the yellow lines are the 95% confidence level (2σ) achieved by the proposed weighting method. Simulated data with a multipath time constant of 2 seconds. 177
Figure 8.15 Comparison between the horizontal error achieved using the GPS L1-L5 IF combination (blue) and the one obtained by using the low-noise pseudorange combination corrected by the smoothed ionosphere (red). The multipath correlation time is set to 2 seconds. Only the last one and a half hour is plotted. 179
Figure 8.16 Comparison between the horizontal error achieved using the Galileo E1-E5 IF combination (blue) and the one obtained by using the E5 pseudorange corrected by the smoothed ionosphere (red). The multipath correlation time is set to 2 seconds. Only the last one and a half hour is plotted. 179
Figure 8.17 Comparison between the horizontal error achieved using the GPS+Galileo IF combinations (blue) and the one obtained by using the low-noise pseudoranges corrected by the smoothed ionosphere (red). The multipath correlation time is set to 2 seconds. Only the last one and a half hour is plotted. 180
Figure 8.18 Sensitivity of the convergece time (RMS) to different multipath correlation time for GPS (blue), Galileo (red), and GPS+Galileo (yellow) cases.

Comparison between the IF pseudoranges (circle) and the smoothed ionosphere corrected low-noise pseudoranges (star).....181
Figure 8.19 Sensitivity of the convergece time (95th percentile) to different multipath correlation time constants for GPS (blue), Galileo (red), and GPS+Galileo (yellow) cases. Comparison between the IF pseudoranges (circle) and the smoothed ionosphere corrected low-noise pseudoranges (star).....182
Figure 8.20 Comparison between the horizontal error achieved using the GPS L1-L5 IF combination (blue) and the one obtained by using the low-noise pseudorange combination corrected by the smoothed ionosphere (red). The multipath correlation time is randomly generated. Only the last one and a half hour is plotted. 184
Figure 8.21 Comparison between the horizontal error achieved using the Galileo E1-E5 IF combination (blue) and the one obtained by using the E5 pseudorange corrected by the smoothed ionosphere (red). The multipath correlation time is randomly generated. Only the last one and a half hour is plotted. 184
Figure 8.22 Comparison between the horizontal error achieved using the GPS+Galileo IF combinations (blue) and the one obtained by using the low-noise pseudoranges corrected by the smoothed ionosphere (red). The multipath correlation time is randomly generated. Only the last one and a half hour is plotted. 185
Figure 8.23 Error in the ionospheric delay observable. Blue dots shows the time-series of the error in the ionosphere computed from the raw pseudoranges, while the red line is the error in the smoothed ionosphere. The 95% confidence level (2σ) achieved by the proposed weighting method (yellow line) and by the modified version (purple line) are also plotted . Simulated data with a multipath time constant of 60 seconds. 186
Figure 8.24 Comparison between the horizontal re-convergence for the GPS L1-L5 IF case (blue) and for the smoothed ionosphere corrected low-noise pseudorange (red) with the modified weighting methd. The multipath correlation time is randomly generated.....187
Figure 8.25 Comparison between the horizontal re-convergence for the Galileo E1-E5 IF case (blue) and for the E5 pseudorange corrected by the smoothed

ionosphere (red) with the modified weighting methd. The multipath correlation time is randomly generated. 188
Figure 8.26 Comparison between the horizontal re-convergence for the GPS+Galileo IF combinations (blue) and for the low-noise pseudoranges corrected by the smoothed ionosphere (red) with the modified weighting methd. The multipath correlation time is randomly generated 188
Figure 8.27 Comparison between the horizontal error achieved using the traditional GPS+Galileo IF pseudorange combinations (blue) and the one obtained by using the low-noise pseudoranges corrected by the smoothed ionosphere (red). Kinematic test. 190
Figure 8.28 Noise in the NL ambiguity observable as a function of the amplified NL wavelength. GPS L1-L2-L5 IF combinations. 194
Figure 8.29 Noise in the NL ambiguity observable (blue plot with y axis on the left) and amplification factor of the corresponding triple-carrier IF combination (red plot with y axis on the right) as a function of the amplified NL wavelength. GPS L1-L2-L5 IF combinations. 196
Figure 8.30 Comparison between the horizontal error achieved using the traditional GPS L1-L5 IF combination (blue) and the one obtained by using also the triple-carrier IF combination that minimize the noise in the NL ambiguity observable (red). The multipath correlation time is equal to 5 seconds. 198
Figure 8.31 Comparison between the horizontal error achieved using the Galileo E1-E5 IF combination (blue) and the one obtained by using also the triple-carrier IF combination that minimize the noise in the NL ambiguity observable (red). The multipath correlation time is equal to 5 seconds. 199
Figure 8.32 Comparison between the horizontal error achieved using the GPS and Galileo IF combinations (blue) and the one obtained by using also the triple-carrier IF combinations that minimise the noise in the NL ambiguity observable (red). The multipath correlation time is equal to 5 seconds. 199
Figure 8.33 Sensitivity of the horizontal convergence time (RMS) to different multipath correlation time for GPS (blue), Galileo (red), and GPS+Galileo (yellow) cases. Comparison between the two-frequency IF combinations (circle) and the triple-carrier IF combinations (star). 201
Figure 8.34 Sensitivity of the horizontal convergence (95^{th} percentile) time to different multipath correlation time for GPS (blue), Galileo (red), and

GPS+Galileo (yellow) cases. Comparison between the traditional two-frequency IF combinations (circle) and the new triple-carrier IF combinations (star). 202
Figure 8.35 Comparison between the horizontal error achieved using the GPS L1-L5 IF combination (blue) and the one obtained by using also the triple-carrier IF combination that minimises the noise in the NL ambiguity observable (red). The multipath correlation time is randomly generated. 203
Figure 8.36 Comparison between the horizontal error achieved using the Galileo E1-E5 IF combination (blue) and the one obtained by using also the triple-carrier IF combination that minimises the noise in the NL ambiguity observable (red). The multipath correlation time is randomly generated. 203
Figure 8.37 Comparison between the horizontal error achieved using the GPS and Galileo two-frequency IF combinations (blue) and the one obtained by using also the triple-carrier IF combinations that minimise the noise in the NL ambiguity observable (red). The multipath correlation time is randomly generated. 204
Figure 8.38 Comparison between the horizontal error achieved using the GPS L1-L5 IF combination (blue) and the one obtained by using also the triple-carrier IF combination that minimises the noise in the NL ambiguity observable (red) when the WL ambiguity is fixed with the new method. 206
Figure 8.39 Comparison between the horizontal error achieved using the Galileo E1-E5 IF combination (blue) and the one obtained by using also the triple-carrier IF combination that minimises the noise in the NL ambiguity observable (red) when the WL ambiguity is fixed with the new method. 206
Figure 8.40 Horizontal error achieved using the GPS and Galileo two-frequency IF combinations (blue) and the one obtained by using also the triple-carrier IF combinations that minimise the noise in the NL ambiguity observable (red) when the WL ambiguity is fixed with the new method. 207
Figure 8.41 WL ambiguity correct-fix rate for GPS L1-L2-L5 (blue) and Galileo E1-E5-E6 (red) combinations for a benign environment (left) and multipath-rich site (right). 211
Figure 8.42 Sensitivity of the WL ambiguity fix time to the multipath correlation time constant. 211

Figure 8.43 NL ambiguity correctness rate for GPS L1-L2-L5 (blue) and Galileo E1-E5-E6 (red) combinations for a benign environment (left) and multipath-rich site (right). The NL ambiguity has been computed using the AFIF combination. 212
Figure 8.44 Correct-fix rate of the wide lane ambiguity resolution for the new method and the one proposed in Geng and Bock (2013) for GPS L1-L2-L5 combinations. For the new method, low-noise combinations with different ionosphere amplification factors (q) are considered. Severe multipath case. 217
Figure 8.45 Correct-fix rate of the wide lane ambiguity resolution for the new method and the one proposed in Geng and Bock (2013) for Galileo E1-E5-E6 combinations. For the new method, low-noise combinations with different ionosphere amplification factors (q) are considered. Severe multipath case. 218
Figure 8.46 Noise on the NL ambiguity observable achieved with the new method (blue) as a function of the NL wavelength amplified by the factor β_3. For comparison, the noise level obtained with the TCAR method proposed in Geng and Bock (2013) is also shown (red). GPS L1-L2-L5 signals are considered. 220
Figure 8.47 Correct-fix rate of the narrow lane ambiguity resolution for the new method and the method proposed in Geng and Bock (2013) for GPS L1-L2-L5 (left subplot) and Galileo E1-E5-E6 (right subplot) combinations. For the new method, triple-carrier IF combinations with different amplified narrow lane wavelengths are considered. Benign environment..... 222

List of Tables

Table 3.1 PPP a priori correction models (Teunissen and Montenbruck, 2017). 31

Table 3.2 GPS precise orbits and clocks products from IGS (IGS, 2018a). ...33

Table 3.3 Analysis centers contributing to IGS MGEX.....35

Table 3.4 The IGS GIMs (IGS, 2018a). 41

Table 3.5 GPS and Galileo extra-wide lane and wide lane combinations: wavelengths and noise amplifications. 54

Table 3.6 GPS and Galileo AFIF combinations: wavelength and noise amplification. 54

Table 3.7 GPS and Galileo narrow lane wavelengths. 55

Table 5.1 Comparison between the RMS of the positioning errors achieved using COM and COD products, for the 9 considered IGS stations between 10th and 19th February 2016. Units of centimetres. In bracket is the relative difference. 66

Table 5.2 Comparison between the RMS of the convergence times achieved using COM and COD products, for the 9 considered IGS stations between 10th and 19th February 2016. Units of minutes. In bracket is the relative difference. 66

Table 5.3 Comparison between the RMS of the positioning errors achieved using COM and COD products, for the 9 considered IGS stations between 3rd and 12th June 2018. Units of centimetres. In bracket is the relative difference. 67

Table 5.4 Comparison between the RMS of the convergence times achieved using COM and COD products, for the 9 considered IGS stations between 3rd and 12th June 2018. Units of minutes. In bracket is the relative difference. 68

Table 5.5 Model included in the PPP data processing. 69

Table 5.6 Galileo satellites availability and geometry for the 9 IGS stations. From left to right: average number of Galileo satellites in view, longest time period in which there are more than 5 available Galileo satellites, average PDOP for GPS and GPS+Galileo cases over 10 days in 2016. 71

Table 5.7 Comparison between the RMS of the GPS(G) and GPS+Galileo (GE) PPP errors, for the 9 considered IGS stations between 10th and 19th February 2016. Units of centimeters. In bracket is the relative difference. 72
Table 5.8 Comparison between the RMS of the GPS (G) and GPS+Galileo (GE) PPP convergence times, for the 9 considered IGS stations between 10th and 19th February 2016. Units of minutes. In bracket is the relative difference.....73
Table 5.9 Model included in the PPP data processing. 75
Table 5.10 Galileo satellites availability and geometry for the 9 IGS stations. From left to right: average number of Galileo satellites in view, longest time period in which there are more than 5 available Galileo satellites, average PDOP for GPS and GPS+Galileo cases over 10 days in 2016. 76
Table 5.11 Comparison between the RMS of the GPS(G) and GPS+Galileo (GE) PPP errors, for the 9 considered IGS stations between 3rd and 12th June 2018. Units of centimetres. In bracket is the relative difference. 77
Table 5.12 Comparison between the RMS of the GPS (G) and GPS+Galileo (GE) PPP convergence times, for the 9 considered IGS stations between 3rd and 12th June 2018. Units of minutes. In bracket is the relative difference.....78
Table 6.1 Average values of the five meteorological parameters used by the EGNOS model. The latitude (φ) is in units of degrees, the pressure (P) and water vapour (e) are in mbar, the temperature (T) is expressed in K, and its lapse rate (β) is in mK/m, while the water vapour lapse rate (η) is a dimensionless quantity. 93
Table 6.2 Seasonal variation values of the five meteorological parameters used by the EGNOS model. The latitude (φ) is in unites of degrees, the pressure (P) and water vapour (e) are in mbar, the temperature (T) is expressed in K, and its lapse rate (β) is in mK/m, while the water vapour lapse rate (η) is a dimensionless quantity. 93
Table 6.3 Coefficients used in the exponential law of the multipath magnitude as a function of the elevation angle. C_0 and C_1 are in units of meters, while C_2 is in unit of degrees. 98
Table 6.4 Coefficients adopted to model the standard deviation of the pseudorange noise for GPS and Galileo. C_0 and C_1 are in units of meters, while C_2 and C_3 are in units of dB-Hz 100
Table 6.5 Received minimum power levels on the ground in units of dBW.103

Table 6.6 Root Mean Square (RMS) of the difference between the IGC and ESA orbits and clocks in a four weeks period spanning from the GPS week 1917 to 1920 (from 2nd to 29th October 2016). The difference in the orbits are reported in the radial, along-track, and cross track components. Units of cm. 105
Table 6.7 RMS of the bias a_0, and amplitudes a_1 and a_2 used to fit the errors' data to the seond order Fourier expansion. Values in units of centimeters. ..111
Table 6.8 RMS and 95th percentile of the correlation coefficients between the clocks' error and the orbits' errors in the radial, cross-track and along-track components. 115
Table 6.9 Coordinates of the IGS stations used to validate the multi-frequency GPS/Galileo simulator. 119
Table 6.10 Model included in the PPP data processing of real data. 121
Table 6.11 Model included in the PPP data processing of simulated data....122
Table 6.12 Median of the positioning errors for simulated and real data. Values in units of centimetres. 124
Table 6.13 Median of convergence times for simulated and real data. Values in units of minutes. 124
Table 7.1 Expected standard deviation of the error in GPS and Galileo pseudoranges that was assumed when designing the Kalman filter. Units of meters. 129
Table 7.2 Standard deviations of the initial error in the state vector and of the process noise used to tune the Kalman filter. 129
Table 7.3 Comparison between the horizontal (H) and vertical (Up) errors achieved using the L1-L2 IF and L1-L5 IF combinations. 95th and RMS over the four simulated stations. Benign environment. Values in units of cm. In bracket is the relative difference. 131
Table 7.4 Comparison between the horizontal (H) and vertical (Up) convergence times achieved using the L1-L2 IF and L1-L5 IF combinations. 95th and RMS over the four simulated stations. Benign environment. Values in units of minutes. In bracket is the relative difference. 131
Table 7.5 Comparison between the horizontal (H) and vertical (Up) errors achieved using the E1-E5a IF, E1-E5b IF, E1-E5 IF, and E1-E6 IF combinations. 95th and RMS over the four simulated stations. Benign environment. Values in units of cm. In bracket is the relative difference. 132

Table 7.6 Comparison between the horizontal (H) and vertical (Up) convergence times achieved using the E1-E5a IF, E1-E5b IF, E1-E5 IF, and E1-E6 IF combinations. 95th and RMS over the four simulated stations. Benign environment. Values in units of minutes. In bracket is the relative difference. 132
Table 7.7 Expected standard deviation of the error in GPS and Galileo pseudoranges that was assumed when designing the Kalman filter. Units of meters. 132
Table 7.8 Comparison between the horizontal (H) and vertical (Up) errors achieved using the L1-L2 IF and L1-L5 IF combinations. 95th and RMS over the four simulated stations. Values in units of cm. In bracket is the relative difference. 134
Table 7.9 Comparison between the horizontal (H) and vertical (Up) convergence times achieved using the L1-L2 IF and L1-L5 IF combinations. 95th and RMS over the four simulated stations. Values in units of minutes. In bracket is the relative difference. 134
Table 7.10 Comparison between the horizontal (H) and vertical (Up) errors achieved using the E1-E5a IF, E1-E5b IF, E1-E5 IF, and E1-E6 IF combinations. 95th and RMS over the four simulated stations. Values in units of cm. In bracket is the relative difference. 135
Table 7.11 Comparison between the horizontal (H) and vertical (Up) convergence times achieved using the E1-E5a IF, E1-E5b IF, E1-E5 IF, and E1-E6 IF combinations. 95th and RMS over the four simulated stations. Values in units of minutes. In bracket is the relative difference. 135
Table 7.12 Comparison between the horizontal (H) and vertical (Up) errors in the GPS, Galileo, and GPS+Galileo PPP solutions. 95th and RMS over the four simulated stations. Benign environment. Values in units of centimetres. In bracket is the relative difference. 139
Table 7.13 Comparison between the horizontal (H) and vertical (Up) convergence times in the GPS, Galileo, and GPS+Galileo PPP solutions. 95th and RMS over the four simulated stations. Benign environment. Values in units of minutes. In bracket is the relative difference. 139
Table 7.14 Comparison between the horizontal (H) and vertical (Up) errors in the GPS, Galileo, and GPS+Galileo PPP solutions. 95th and RMS over the four

simulated stations. Multipath-rich site. Values in units of centimetres. In bracket is the relative difference. 140
Table 7.15 Comparison between the horizontal (H) and vertical (Up) convergence times in the GPS, Galileo, and GPS+Galileo PPP solutions. 95th and RMS over the four simulated stations. Multipath-rich site. Values in units of minutes. In bracket is the relative difference. 141
Table 7.16 Percentage of epochs in 24 hours for which dual-constellation GNSS meets the minimum requirements in terms of visibility and geometry. N is the number of satellites. 147
Table 7.17 Standard deviations of the initial error in the state vector and of the process noise used to tune the Kalman filter. 149
Table 8.1 Assumed ratios between the standard deviation of the errors in the GPS and Galileo pseudoranges with respect to the one on L1/E1. 160
Table 8.2 Standard deviations of the initial error in the state vector and of the process noise used to tune the Kalman filter. 178
Table 8.3 Expected standard deviation of the error in GPS and Galileo pseudoranges that was assumed when designing the Kalman filter. Units of meters. 178
Table 8.4 Comparison between the horizontal convergence times obtained from using only the two-frequency IF combinations and also the triple-carrier IF combination that minimiz the error in the NL ambiguity observable. RMS and 95^{th} percentile over 50 simulations. Station SEY2. The multipath correlation time is set to 5 seconds. Values in units of minutes. In bracket is the relative difference. 200
Table 8.5 Comparison between the horizontal convergence times obtained from using only the two-frequency IF combinations and also the triple-carrier IF combination that minimiz the error in the NL ambiguity observable when the WL ambiguity is fixed with the new method presented in Section 8.3. RMS and 95^{th} percentile over 50 simulations. The multipath correlation time is randomly generated. Values in units of minutes. In bracket is the relative difference. . 207
Table 8.6 Expected standard deviation of the error in GPS and Galileo pseudoranges for benign environments. Values in unites of meters. 213

Table 8.7 GPS and Galileo low-noise pseudorange combinations: coefficients, ionosphere amplification factor, and noise in unit of meters. Benign environment. 213
Table 8.8 Noise in the WL ambiguity observable in unites of cycle for different pseudorange and carrier phase combinations. Begign environment.....214
Table 8.9 Expected standard deviation of the error in GPS and Galileo pseudoranges for severe multipath environments. Values in unites of meters. 215
Table 8.10 GPS and Galileo low-noise pseudorange combinations: coefficients, ionosphere amplification factor, and noise in unit of meters. Severe multipath environments.....215
Table 8.11 Noise in the WL ambiguity observable in unites of cycle for different pseudorange and carrier phase combinations. Severe multipath environment. 217

Acronyms and Abbreviations

AC	Analysis Centre
AFIF	Ambiguity Fixed Ionosphere-Free
AltBOC	Alternate Binary Offset Carrier
ANTEX	Antenna Exchange
AR	Ambiguity Resolution
ARP	Antenna Reference Point
BOC	Binary Offset Carrier
BPSK	Binary Phase Shift Keying
CDDIS	Crustal Dynamics Data Information System
CDMA	Code Division Multiple Access
CIR	Cascade Integer Resolution
CLS	Collecte Localisation Satellites
CN0	Carrier-to-Noise Ratio
CNES	Centre National d'Etudes Spatiales
CODE	Centre for Orbit Determination in Europe
CoM	Centre of Mass
CORS	Continuously Operating Reference Stations
CRAIM	Carrier Receiver Autonomous Integrity Monitoring
DCB	Differential Code Bias
DD	Double Difference
DOP	Dilution of Precision
EC	European Commission
ECEF	Earth Centred Earth Fixed
ECI	Earth Centred Inertial
ECOM	Empirical CODE Orbit Model
EKF	Extended Kalman Filter
EOP	Earth Orientation Parameters
EPSRC	Engineering and Physical Science Research Council
ESA	European Space Agency
ESTEC	European Space Research and Technology Centre
EU	European Union
EWL	Extra Wide Lane

FCB	Fractional Cycle Bias
FOC	Full Operational Capability
GDOP	Geometry Dilution of Precision
GEV	Generalized Extreme Value
GFZ	GeoForschungsZentrum
GGTO	GPS-Galileo Time Offset
GIM	Global Ionosphere Map
GIOVE	Galileo In-Orbit Validation Element
GMF	Global Mapping Function
GNSS	Global Navigation Satellite System
GPS	Global Positioning System
GPT	Global Pressure and Temperature
GRAPHIC	Group And Phase Ionosphere Correction
GRGS	Groupe de Recherche de Geodesie Spatiale
GSA	European GNSS Agency
GSTB	Galileo System Test Bed
HAS	High Accuracy Service
HDOP	Horizontal Dilution of Precision
IERS	International Earth Rotation and Reference System Service
IF	Ionosphere-Free
IGS	International GNSS Service
iHDOP	Integrity Horizontal Dilution of Precision
INS	Inertial Navigation System
iNsight	Innovative Navigation Using New GNSS Signals with Hybridised Technologies
IONEX	Ionosphere Exchange
IOV	In-Orbit Validation
IRC	Integer Recovery Clock
ITRF	International Terrestrial Reference Frame
ITU	International Telecommunications Union
JAXA	Japanese Aerospace Exploration Agency
LAMBDA	Least Squares Ambiguity Decorrelation Adjustment
LOS	Line of Sight

MGEX	Multi-GNSS Experiment
NL	Narrow Lane
NLOS	Non-Line of Sight
NMF	Neill Mapping Function
NTRIP	Network Transport of RTCM via Internet Protocol
OS	Open Service
PCO	Phase Centre Offset
PCV	Phase Centre Variation
PDOP	Position Dilution of Precision
PNT	Positioning, Navigation, and Timing
PPP	Precise Point Positioning
PRN	Pseudo Random Number
PRS	Public Regulated Service
Q-Q	Quantile-Quantile
RAIM	Receiver Autonomous Integrity Monitoring
RINEX	Receiver Independent Exchange
RMS	Root Mean Square
RTCM	Radio Technical Commission for Maritime Services
RTK	Real-Time Kinematic
RTS	Real-Time Service
SADF	Satellite Appearance Distribution Function
SAR	Search and Rescue
SD	Single Difference
SINEX	Solution Independent Exchange
SISRE	Signal In Space Ranging Error
SLR	Satellite Laser Ranging
SP3	Standard Product 3
SPACE	Seamless Positioning in All Conditions and Environments
SPP	Single Point Positioning
SRP	Solar Radiation Pressure
TCAR	Triple Carrier Ambiguity Resolution
TEC	Total Electron Content
TECU	TEC Unit

TUM	Technische Universitat Munchen
UCL	University College of London
UD	Un-Differenced
UNB	University of New Brunswick
US	United States
UWB	Ultra-Wide Band
VDOP	Vertical Dilution of Precision
VGC	Virtual Galileo Constellation
VMF	Vienna Mapping Function
VTEC	Vertical TEC
WL	Wide Lane
WUM	Wuhan University
ZTD	Zenith Tropospheric Delay

Chapter 1

Introduction

Since the launch of the Global Positioning System (GPS), Global Navigation Satellite Systems (GNSS) have dominated the Positioning, Navigation, and Timing (PNT) scenario. Position estimates with accuracy of about 10 m can be easily obtained by using single-frequency pseudorange measurements (Teunissen and Montenbruck, 2017). Due to the spatial and temporal correlations of the biases affecting the GNSS measurements, e.g. the error in satellite ephemeris or atmospheric delays, higher positioning accuracies, of the order of several decimetres or a few meters, can be achieved by emplying corrections from reference stations (Teunissen and Montenbruck, 2017). This is the foremost fundamental of differential GNSS. Nevertheless, users who are interested in centimetre-level positioning must exploit the very precise carrier phase measurements. Indeed, assuming that all the delays have been correctly mitigated, the carrier phase measurements reach a precision of a few millimetes. Unfortunately, while the temporal variation in the signal phase can be observed with extreme precision, the number of whole carrier cycles along the satellite-to-receiver path remains ambiguous. Also, in case the continuous tracking of a satellite is interrupted, this carrier phase ambiguity changes its value. This phenomenon is known as cycle slip. High positioning accuracies can be obtained only after the phase ambiguities have been solved. However, estimating both position and ambiguities with high precision takes a long observation time (known as convergence time), which is due to the slow change in the receiver-to-satellite geometry. Fortunately, unlike un-differenced ambiguities, the double-differenced ones are integers. This can be exploited in ambiguity resolution (Teunissen, 1995). Once the integer ambiguities are fixed, the carrier phase measurements become very precise pseudoranges, and can be used to estimate extremely accurate solutions, known as (ambiguity) fixed solutions. For these reasons, differential GNSS positioning techniques, such as Real Time Kinematic (RTK), use observations from Continuously Operating Reference Stations (CORS) both to mitigate the delays in the GNSS measurements and to double-differenciate the ambiguities, making them

integers. Usually, ambiguity fixed solutions, in real-time, can be achieved in a few seconds if the distance between the user and the reference receiver is shorter than a few tens of kilometers (Dai, 2000; Dai et al., 2007). However, the integer ambiguity resolution success-rate is related to the quality of the corrections provided by the receiver, that becomes poorer for larger baselines. Although inter-station distances can be extended to a few hundreds of kilometres using refined atmospheric corrections from a network of CORS (Grejner-Brzezinska et al., 2009), as in Network RTK (NRTK), they can cover only a regional area due to the high costs of the CORS. Hence, NRTK can hardly be adopted in a global scale (Rizos, 2007).

In recent years Precise Point Positioning (PPP) (Zumberge et al., 1997) has become an attractive solution for high accuracy positioning in remote areas which, for logistics or economic reasons, cannot have access to the corrections computed by nearby reference stations. It can be considered as an improvd version of the classic pseudorange based positioning (Teunissen and Montenbruck, 2017), in which broadast navigation data are replaced with precise orbit and clock products from a global network solution. PPP is currently a standard for many applications characterised by open sky conditions such as precise positioning in open environments (Geng et al., 2010a), atmospheric studies (Douša, 2009; Zhang et al., 2012), earthquake and tsunami monitoring (Shi et al., 2010), and precision agriculture (Mondal and Tewari, 2007). The long (re-)convergence time of PPP, in the order of several tens of minutes, represents the main drawback of this technique. It explains why PPP is rarely used in constrained and transient signal environments associated with urban areas, where the limited satellite visibility and frequent cycle slips or data gaps due to building obstractions force the PPP filter to restart very often.

The use of multi-constellation GNSS can marginally resolve this problem. It is forecast that, when the Galileo and the BeiDou constellations will reach their full operational capability, the more than 120 GNSS satellites orbiting around the Earth will largely improve the avalibility conditions particularly in urban environments (Pan et al., 2016). Also, having more satellites available can sensibly reduce the convergence time of the PPP solution (Afifi and El-Rabbany, 2015; Garcia et al., 2010; Juan et al., 2012; Miguez et al., 2016; Shen and Gao, 2006). Unfortunately, in very severe urban canyons the availability of

multi-constellation GNSS satellites is still far from satisfying the requirements for most of the navigation applications (Ji et al., 2010). For this reason, the reduction of the (re-)convergence time is of primarily importance to extend the use of PPP also to ground navigation in cities.

Today, very efficient tecqhniques aimed to bridge between data gaps or recover from cycle-slips exist. These techniques adopt un-combined observables and very precise ionospheric corrections to estimate the residual ionospheric error. Quick PPP re-convergence can be achieved by exploiting the temporal and spatial correlation of the ionospheric delay to tightly constrain the estimation of the new ambiguity values (Geng et al., 2010a; Li, 2012; Zhang et al., 2013). However, the performances of these methods depend on the constraints used for the ionosphere prediction and estimation, on a careful handling of the Differential Code Biases (DCBs), and on the quality of the ionospheric corrections, which degrades with the increasing distance of the user from the network. Indeed, these configurations perform the best only if the user is located in proximity of the reference receivers used to estimate the ionosphere corrections. It means that the main property that differtiates PPP from RTK, i.e. high accuracy globally, is lost. Moreover, the great reduction in the PPP (re-) convergence time given by the un-combined measurements configuration comes with a downside: the computational penalty associated with the filter formulated with dual-frequency measurements and ionosphere states becomes more pronounced with increasing numbers of satellites associated with the use of multi-GNSS, which is desirable for PPP in degraded signal environment. For these reasons, the use of ionosphere-free combinations might still be the preferable option in a large number of applications.

The modernisation process in GNSS is not only bringing more satellites but also new signals and frequencies. Next generation GPS satellites will broadcast signals over three frequency bands (L1, L2 and L5), while Galileo has signals over four different frequencies (E1, E5a, E5b and E6). Employing multi-frequency GNSS measurements is another effective way to reduce the (re-) convergence time in PPP. Although, only small improvements, in terms of accuracy and convergence time, were observed with respect to PPP float solutions based on two-frequency ionosphere-free combinations (Deo and El-Mowafy, 2016; Elsobeiey, 2014), multi-frequency GNSS greatly benefit the

ambiguity resolution success-rate (Geng and Bock, 2013; Henkel and Gunther, 2008).

1.1 Aims and Objectives

Following the brief literature review presented in the previous section, a few gaps have been identified in the state of the art. These mainly regard the use of PPP in urban areas and the effect of multi-frequency multi-constellation GNSS measurements on the float PPP solutions. For these reasons, this thesis will investigate the impact of multi-frequency Galileo signals, on their own or in combination with multi-frequency GPS observables, on the kinematic PPP float solutions in urban areas and in open sky conditions. The University of Nottingham POINT software will be used to process observation data from multi-constellation multi-frequency GNSS station (static case) as well as from receivers on-board kinematic platforms. In addition, the specific benefits of using the Galileo E5 signal will also be analysed.

To pursue this aim, the following objectives have been defined:

- Contribute to the POINT software by completing the implementation of the Galileo capability.
- Investigate on the impact of the current state Galileo system, in combination with GPS, on the PPP solution, in comparison with the single constellation case, in terms of accuracy and convergence time.
- Develop a GPS/Galileo simulator in Simulink for multi-frequency GNSS observations and precise PPP products.
- Compare different GPS and Galileo ionosphere-free combinations and investigate those providing the most accurate PPP solution and the quickest convergence time.
- Compare the GPS, Galileo, and GPS+Galileo PPP solution in terms of final accuracy and convergence time.
- Analyse the satellite availability and geometry conditions offered by the GPS+Galileo system in urban environments.
- Analyse the PPP solutions based on GPS+Galileo measurements in urban environments.
- Investigate alternative multi-frequency ionosphere-free combinations that speed up the PPP (re-)convergence time.

1.2 Contribution to Knowledge

This study, which has been sponsored through a studentship agreement between the University of Nottingham and the Collins Aerospace (former Rockwell Collins UK Limited), contributes to our knowledge by addressing the following important issues:

- Presentation of a new approach for simulating the PPP products that takes into account the temporal characteristic of the products' error, rather than assuming it Gaussian.
- Assessment of the performance of Galileo only PPP as an alternative to GPS only or GPS+Galileo PPP.
- Assessment of the GPS and Galileo two-frequency ionosphere-free combinations that offer the smallest error and quickest convergence time in the PPP solutions.
- Assessment of the performance of GPS+Galileo PPP in urban areas.
- Development of a new concept of ionosphere-free combination based on the smoothed ionosphere combination for quick PPP re-convergence.
- Development of a new weighting method that takes into account the increasing precision of the ionosphere corrected pseudorange.
- Assessment of the impact of new triple-carrier ionosphere-free combinations aimed to minimize the noise in the narrow-lane ambiguity observable on the PPP convergence time.
- Development of a new triple carrier ambiguity resolution algorithm based on the smoothed ionosphere combination.

1.3 Thesis Overview

This thesis is structured in nine chapters which are outlined as follows.

Chapter 2 covers the literature review. Firstly, an overview of the Galileo system is presented and the main differences with respect to the GPS system, in terms of constellation, signals structure, and measurements quality, are highlighted. Next, the papers analysing the benefit of multi-constellation GNSS are covered. Finally, PPP is reviewed. In particular, all the efforts towards assessing the performance of GPS+Galileo PPP and all the methods for quick (re-)convergence PPP are discussed.

Chapter 3 introduces all the correction models that must be applied to the GNSS pseudorange and carrier phase measurements in order to achieve centimetre-level of accuracy in PPP. Integer ambiguity resolution is also discussed.

Chapter 4 presents the University of Nottingham in-house GNSS/INS data processing software, POINT. The publications, whose outcome were based on the POINT capability, are quickly reviewed.

Chapter 5 presents and discusses the initial results for GPS and GPS+Galileo PPP based on real data recorded by multi-GNSS stations within the IGS network. The main limitations of the current state of the GPS and Galileo constellations, as well as, the PPP products are here highlighted.

Chapter 6 presents the GPS/Galileo Simulink tool developed in this thesis. The structure of the simulator is carefully described, and the models used to simulate the delays affecting the GNSS measurements are discussed. The strategy to simulate the precise orbits and clocks products, based on the analysis of the difference between the GPS products provided by the IGS Real-Time Service (RTS) and the Final products computed by ESA, is presented. Finally, as an attempt to validate the simulator, a comparison between PPP solutions computed from real and simulated measurements is performed.

Chapter 7 analyses the PPP solutions achieved by processing two-frequency ionosphere-free combinations of pseudorange and carrier phase measurements simulated through the GPS/Galileo Simulink tool, in different scenarios. A preliminary study on different GPS and Galileo combinations is performed with the aim to identify the ionosphere-free combination that guarantees the best accuracy and convergence time. These combinations will then be adopted to compare the positioning performance of single and multi-constellation PPP in open sky environment. Finally, satellite availability, geometry conditions, and positioning performance achievable in an urban area with GPS+Galileo will be discussed.

Chapter 8 proposes innovative solutions to reduce the (re-)convergence time in PPP, and therefore, to solve the main limitation for PPP in urban areas. New multi-frequency GPS and Galileo combinations intended to either reduce the noise in the ionosphere-free pseudorange or to enlarge the narrow lane wavelength will be studied and their impact on the PPP (re-)convergence time will be discussed. Finally, a new triple carrier ambiguity resolution algorithm

based on the smoothed ionosphere correction is proposed and compared with already existing methods.

Chapter 9 summarizes the main points and highlights the contributions of this thesis.

1.4 Publications

1. Basile, F., Moore, T. & Hill, C. (2017). Analysis on the Potential Performance of GPS and Galileo Precise Point Positioning using simulated Real-Time products. International Navigation Conference (INC), Brighton, UK.
2. Basile, F., Moore, T., Hill, C., McGraw, G. & Johnson, A. (2018). Multi-Frequency Precise Point Positioning using GPS and Galileo Data with Smoothed Ionospheric Corrections. IEEE/ION PLANS, Monterey, CA, USA, 1388-1398. Peer reviewed.
3. Basile, F., Moore, T., Hill, C., McGraw, G. & Johnson, A. (2018). Two are better than one: Multi-Frequency Precise Point Positioning Using GPS and Galileo. GPS World. **29:** 27-37.
4. Basile, F., Moore, T., Hill, C. & McGraw, G. (2018). Performance Analysis of Triple Carrier Ambiguity Resolution in Precise Point Positioning with Smoothed Ionosphere Corrections. 31st International Technical Meeting of the Satellite Division of the Institute of Navigation (ION GNSS+ 2018), Miami, FL, USA, 3868-3880. (Best presentation award). Peer reviewed.
5. Basile, F., Moore, T. & Hill, C. (2019). "Analysis on the Potential Performance of GPS and Galileo Precise Point Positioning using Simulated Real-Time Products." Journal of Navigation **72**(1): 19-33. Peer reviewed.
6. Basile, F., Moore, T., Hill, C. & McGraw, G. “GPS and Galileo Triple-Carrier Ionosphere-Free Combinations for Quick Convergence in Partially Float Precise Point Positioning Solutions.” To be submitted.

Chapter 2

Literature review

2.1 Overview of the Galileo system

It was acknowledged in the early nineties that GNSS would had already revolutionized many activities using positioning and navigation, and had created new markets and services. Even though the annual world market volume for GNSS receivers was already estimated to be close to 3 billion Euro (Commission of the European Communities, 1994), the applications for GNSS were still limited to aviation, shipping, geodesy and surveying. Smartphones, that now dominate the global installed base of GNSS devices today (European GNSS Agency, 2017a), were not even on the radar of the phone manufacturers, while navigation systems in land vehicles were not common. With more than 120 million cars used, in Europe alone, at that time, the potential market was already huge. Increasing the European Union (EU) industrial competitiveness in such lucrative market was one of the reasons that brought the European Commission (EC), in collaboration with the European Space Agency (ESA), to develop and deploy the European GNSS, Galileo. Commission of the European Communities (1998) highlighted how dangerous it was for the user community, especially in civil aviation, to rely only on one navigation system controlled by a third country, such as GPS. The EU was not only concerned about the weak position of European industry with respect to the United States (US), but also about the possible future fees for the services offered by GPS, and the serious security problems related to the lack of control over the safety-of-life navigation systems.

Developing Galileo has not been easy. The program management had to face the big challenge of meeting the views of the 28 Member States that form the EU, and cooperating with many independent intergovernmental bodies. All this made the decision process extremely intricate. In parallel, a delicate international mediation between EU and US was carried out on the agreement on the spectrum allocation, carrier phase frequency selection, and signal design for Galileo, in order to promote its interoperability with GPS. In June 2000, the International Telecommunications Union (ITU), during the World Radio

Communications Conference held in Istanbul, allocated three frequency bands to Galileo signals.

The E1 frequency band (centred at 1575.42 MHz) provides three navigation signal components. E1-A is only accessible to authorized users, while the other two components, the data channel E1-B and the pilot channel E1-C, are open access. Similarly, the E6 frequency band (centred at 1278.75 MHz) provides one encrypted component, E6-A, and a pair of data and pilot components, E6-B/C, that are intended for commercial access signals. The E5 frequency band (centred at 1191.795 MHz) comprises two pilot-data pairs in the sidebands at 1176.45 MHz (E5a) and at 1207.14 MHz (E5b). The two sidebands can be tracked individually, or as a composite signal. Thanks to its very large bandwidth, the composite signal E5 provides pseudoranges with very low noise and excellent multipath rejection.

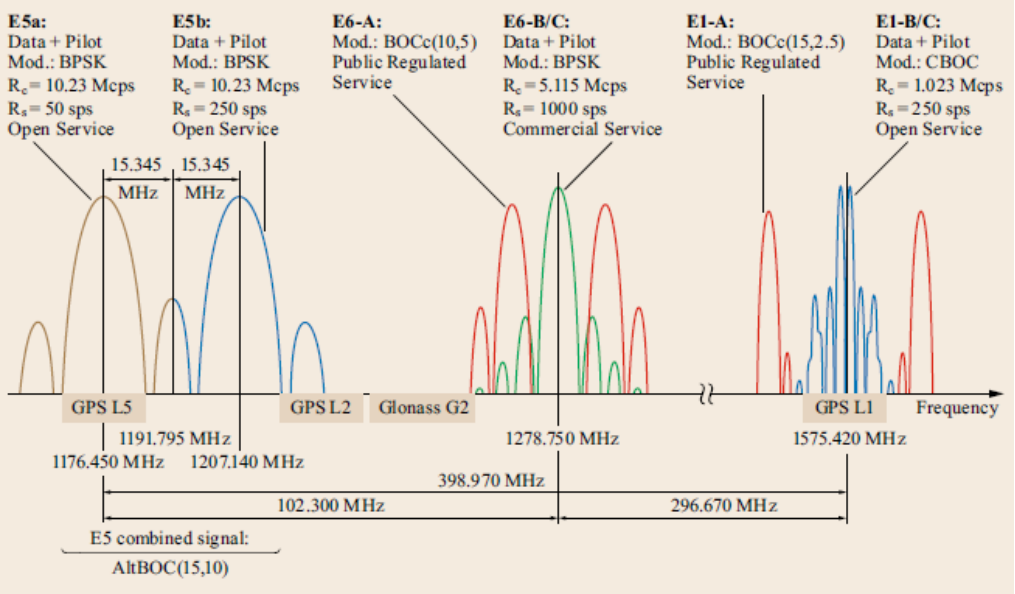


Figure 2.1 *Galileo frequency bands, signals and components* (Teunissen and Montenbruck, 2017).

After several years of development and qualification of critical technologies, in 2002 ESA launched the Galileo System Test Bed 1 (GSTB-V1) program aimed at developing an experimental platform to validate the algorithms for the generation of Galileo navigation and integrity data (Romay Merino et al., 2004). In 2005, the first Galileo In-Orbit Validation Element (GIOVE-A) was launched and on the 12th January 2006 it transmitted for the first time a Galileo signal

towards the Earth. A few years later, GIOVE-B was launched. The objective of these two satellites were to (Falcone et al., 2006):

- Test, and secure, the use of the frequencies allocated by the ITU for the Galileo system.
- Verify the on-board atomic clocks and signal generators.
- Verify the resistance to interference and multipath of the novel Galileo signals.
- Characterize the radiation environment of the orbit planned for the Galileo constellation.

In the summer 2012 the two satellites were decommissioned.

In the following In-Orbit Validation (IOV) stage, a reduced constellation of four satellites, in combination with Galileo's ground network, was used to validate the system. On 12th March 2013 the very first position fix was computed at the Navigation Laboratory at ESA's European Space Research and Technology Centre (ESTEC), in the Netherlands. The results from the IOV campaign, conducted throughout 2013, were used as a reference for the expected performance of the completed constellation.

The Full Operational Capability (FOC) constellation comprise 24 satellites plus 6 spares, distributed over 3 orbital planes with a semi-major axis of 29600 km and an inclination of 56°. The first two FOC satellites were launched on the 22nd August 2014. Unexpectedly, the Soyuz rocket's upper stage left the two satellites into a highly elliptical orbit and with the wrong inclination with respect to the equator. These two satellites had their orbits partially corrected in November 2014 and in March 2015 (ESA, 2015). They are currently under testing for navigation purposes (European GNSS Agency, 2016a, 2016b).

The full Galileo constellation is forecast to be ready by 2020, while early Galileo services started in December 2016. Once the full capability will be reached, Galileo proposes to offer four different services:

- The Open Service (OS) will be available free of charge. It will support single and dual-frequency ranging and positioning, as well as UTC linked time dissemination (European Union, 2016a). The single-frequency OS is provided by each of the dedicated signals: E1-B/C, E5a

and E5b, while the dual-frequency OS is provided by the E1-E5a or E1-E5b signal combinations.

- The High Accuracy Service (HAS) completes the OS by providing an additional navigation signal, and PPP products in real-time, in the E6-B/C frequency band, without the need for an additional communication channel.
- The Public Regulated Service (PRS) is dedicated to government-authorized users, for sensitive applications that require a high level of service continuity. The PRS is similar to the OS and HAS, but it ensures better continuity of service when access to other services is degraded and higher probability of continuous availability of the signal in case of interference. Indeed, it was designed to be more resistant against jamming and spoofing. The signals are encrypted so that the PRS will be available only to those receivers loaded with a valid decryption key. The PRS will be provided by the E1-A and E6-A bands.
- The Search and Rescue (SAR) service was designed as a support for the Cospas-Sarsat program. This is an international search and rescue distress alert detection system capable of locating emergency beacons anywhere in the world. The SAR service comprises an automatic forward repeater, as part of the payload of the Galileo satellites, and a unique return link alert, embed into the navigation message of the E1 OS data component, which informs the sender that their message has been received.

Galileo signals have some unique properties that do not exist in the legacy GPS signals. Nurmi et al., (2015) identified three main differences pertaining to the spreading codes and sub-carriers:

- The first difference between the GPS and Galileo signals is in the spreading code creation for some of the frequency bands. While in GPS L1, as well as in Galileo E5a and in E5b, the Gold codes are generated with dedicated linear feedback shift register structures, in Galileo E1 the codes are specified and implemented as memory codes stored into a local memory to be available to channels when needed. This approach guarantees improved tracking performance and interference mitigation

at the cost of increasing the implementation complexity, the signal processing resource utilization, and the power consumption of the receiver because of the memory needed.

- Another major update in Galileo signals compared to the legacy GPS signals is the use of the Binary Offset Carrier (BOC) modulation, which replaces the Binary Phase Shift Keying (BPSK) modulation on the E1 signals.
- Finally, Galileo signals introduce new types of composite signals. Here, pilot components, not containing any navigation data, are broadcast orthogonally with the traditional data signal. The advantage of this new configuration comes from the dispersion of the two main properties of GNSS signal: navigation data and timing information. The pilot channel can be integrated over longer periods, without crossing a data transition. As a consequence, the carrier-to-noise ratio of the received signals is greatly increased. The pilot signals are used in the modernized GPS signals as well.

These new features contained in the Galileo signals drove many researchers to study and compare the noise and multipath in Galileo pseudoranges against those computed from GPS signals.

Angrisano et al. (2013) assessed the quality of the Galileo E1 pseudorange in comparison with GPS L1 ones. The Galileo IOV satellites 11, 12, and 19 were tracked by the Septentrio PolarRxS receiver, connected to the Javad RingAnt-G3T antenna, for one week. The absolute value of the pseudorange errors was plotted against the carrier-to-noise ratio (CN0). It clearly emerged that Galileo pseudoranges had smaller errors than GPS pseudoranges. The average error was 0.57 m for GPS and 0.38 m for Galileo, the Root Mean Square (RMS) was 2.52 m for GPS and 2.41 m for Galileo, and the maximum value was 12.65 m for GPS and 8.20 m for Galileo. Also the standard deviation of the Galileo pseudoranges was lower than the GPS case. The authors concluded that the improved structure of Galileo signals allows GNSS receivers to extract less noisy pseudorange measurements for the same input CN0.

Gioia et al. (2014) came to similar conclusions. The authors also observed an unexpected degradation of the Galileo E5a measurements respect to E1. Indeed

the mean error passed from 0.48 m on E1 to 0.83 m on E5a for the weakest signal conditions. The cause of this slight degradation was addressed to the presence of residual ionosphere errors which are 1.8 times larger on E5a than on E1.

Cai et al. (2014) analysed the received signals' strength and the error of pseudoranges recorded on the 28th March 2013 by the Trimble NetR9 receiver at the REUN station, in France, and the Septentrio PolaRx4TR at BRUX station, in Belgium. The GPS signals were restricted to the 3 Block IIF satellites while the Galileo signals were from the 4 IOV satellites. This study showed how Galileo pseudoranges are subject to less noise and multipath errors than GPS, in particular at high elevation angles (above 40°). Also, it was shown that Galileo E5, thanks to its bandwidth of 51 MHz using the Alternate BOC (AltBOC) modulation, exhibits the smallest code multipath.

Richardson et al. (2016) used multi-constellation data extracted for a 24 hours period from three reference stations within the Veripos control network (Aberdeen, Seoul, and India). The Galileo signals provided a great improvement in terms of code measurements noise compared to the other signals of GPS and BeiDou, exhibiting the smallest RMS error values as the CN0 increased.

Simsky et al. (2008) summarized the results of about 1.5 years of observations of the GIOVE-A satellite and classified the Galileo signals into 3 groups, based on their multipath suppression properties: high performance (E5, E1-A, E6-A), medium performance (E5a, E5b), and E1-B/C and E6-B/C signals, which had the lowest performance among Galileo signals, but they were still better than GPS L1 C/A. This classification, can be accepted as a general rule, although in some tests E6-B/C, E5a and E5b showed the same performance as E1-B/C, and E6-A in other cases could be included into the medium performance group. The relationship between the signals for individual sites depends upon spectra of the multipath delays. For sites where the long-range multipath was clearly dominant, the wide band signals performed the best. On the other hand, when the short-range multipath was dominant, the advantage of more advanced codes was less pronounced. Smaller values for the multipath were observed during a car-based test. On this occasion the inter-signal differences were less pronounced.

On the other hand, Circiu et al. (2017) demonstrated that even though the pseudorange noise plus multipath in GPS L5 signals is slightly more prominent than in Galileo E5a signals, the theoretical noise (without multipath) computed from observed CN0 in GPS L5 is about two times smaller than Galileo E5a thanks to its higher CN0. GPS L1 has higher noise than Galileo E1, despite the higher CN0. This was attributed to the use of the BOC (1, 1) signal in E1.

GPS and Galileo were also compared from the constellation point of view in Wang et al. (2006), where the global coverage, in terms of Satellite Appearance Distribution Function (SADF), was evaluated as a function of the latitude. SADF can be seen as a measure of the extent with which each cell composing the orbit contributes to the number of visible satellites at a given station. The number of satellites visible from a station on the Earth can be computed by summing the SADF for all the satellites. With an elevation mask of 15°, the maximum number of satellites was available at the equator, while the minimum was at 60° of latitude. At least 4 GPS satellites and 6 Galileo satellites were visible anytime from any location on the globe. With the two systems combined, at least 11 satellites could be tracked anywhere a multi-constellation GNSS receiver is placed. The Dilution of Precision (DOP) parameters were also analysed starting from the SADF. At the Equator and the Poles the Horizontal DOP (HDOP) reached its minimum, whereas the maximum of the HDOP function was located at about 55° latitude. The Vertical DOP (VDOP) increased from the Equator to the Poles. Overall Galileo had better DOP than GPS. Further improvements could be achieved by using the two systems combined. The authors concluded that, from the constellation point of view, Galileo is superior to GPS and that a combined GPS+Galileo system offers, potentially, extraordinary positioning performance.

2.2 Multi-Constellation GNSS

Despite some technical or organisational problems hitting the 4 aspiring GNSS systems, Gibbons (2009) declared the advent of the Golden Age of GNSS and listed within the reasons that pushed him to make this statement the future development of new and modernized systems. Indeed, while the US and Russia launched the first GPS Block IIF satellite, with L5 signal capability, and the first GLONASS-K satellite, which was able to broadcast the additional civilian Code

Division Multiple Access (CDMA) signals, respectively; in Europe Galileo was starting its IOV phase, and China was expanding its constellation, BeiDou, from a regional to a global system. It is forecast that, once Galileo and BeiDou will reach the full capability, more than 120 satellites will be available to those users equipped with a multi-constellation receiver.

Rizos et al. (2005) categorized the benefits of the expected extra satellites and their signals in terms of continuity, accuracy, availability and reliability. Being independent systems, it is very unlikely that GPS, GLONASS, Galileo, and BeiDou experience failures simultaneously. Therefore multi-constellation GNSS has better continuity than the single constellation. With more satellites and signals available, the position accuracy is less susceptible to the influence of the satellite geometry, as the Geometry DOP (GDOP) everywhere will be lower and largely constant. Also, a given level of accuracy will be achieved sooner. Having more satellites and signals means that the availability will be greatly improved even in areas where satellite signals can be obscured, such as in urban canyons. Extra measurements enhance the data redundancy, which helps identifying the outliers, and makes the system more reliable. For high accuracy, carrier phase based, positioning techniques, extra signals are not only useful to mitigate the delay due to the ionosphere, but also to significantly reduce the time required to achieve an ambiguity fixed solution. On top of this, Ochieng et al. (2001) proved that a combined GPS+Galileo navigation system can improve the Receiver Autonomous Integrity Monitoring (RAIM). In particular, it was demonstrated that the RAIM availability, i.e. the percentage of samples at which the minimum size of position shift that could be detected was within the alarm limit, is significantly improved using a combined GPS+Galileo constellation.

Significant research efforts have been made towards using and evaluating the GPS+Galileo multi-constellation system using different simulation tools.

Feng (2005) evaluated the potential performance of the GPS+Galileo by means of the Virtual Galileo Constellation (VGC) approach. The concept is to combine GPS measurements data sets from two epochs, separated by a few hours, to compute the user state. The full Galileo constellation was assumed to be the same as the current GPS constellation in terms of number of satellites in orbit, measurement types and accuracy. The author analysed the positioning

performance in terms of positioning accuracy, Position DOP (PDOP) and HDOP. By considering 2 hours separation, the GPS+VGC offered an improvement in the positioning accuracy between 28% and 37%. Similar improvement levels are in the average PDOP (24%), and HDOP (33%). The paper also analysed the RAIM performance by means of the integrity HDOP (iHDOP). This is defined as the worst case HDOP at a particular epoch obtained by excluding one satellite from the visible set. An enhancement of about 70% was found in its maximum value.

The VGC approach was also used in Feng and Ochieng (2006) to study the potential performance for GPS+Galileo mass-market users in urban areas and high accuracy positioning. The paper shows how in urban areas the horizontal accuracy level of 20 m can be achieved for nearly 98% of the time using the GPS+VGC system, while for only 27% of the time using the GPS constellation alone, assuming an elevation mask angle of 45°.

O'Keefe (2001) compared the HDOP of GPS, Galileo, and the combined system using a simulation software. More than 1700 points spread worldwide and elevation masks up to 40° were analysed. The paper showed how the contribution of Galileo, in addition to GPS, was significant especially in extreme masking environments, while with elevation masks below 20° no improvements were recorded. Indeed, even GPS or Galileo alone were able to provide HDOP less than 2 for nearly 100% of the simulated points. An urban canyon simulation was also conducted in the city of Calgary, using an elevation mask corresponding to a user located in the middle and at the side of a street running both North/South and East/West. The street is assumed to be 20 m wide and surrounded by 15 m tall buildings on either side. The authors highlighted how navigation in urban canyons is almost impossible using only one system without additional sensors or dynamic modelling, while with access to both GPS and Galileo, more than 5 satellites were in view for most of the time. Therefore single epoch positioning was possible.

Ji et al. (2010) made a more comprehensive study of the potential navigation performance offered by GPS+GLONASS+Galileo in a simulated urban canyon, such as Hong Kong. Availability, coverage and continuity were evaluated. To model the urban environment, a realistic 3D urban building information was used. Availability and coverage were assessed in location points of three

different categories: major roads (wider than 20 m), minor roads (narrower than 20 m), and intersections. Using only the GPS system, HDOP less than 10 was available for 1% of the time both in major and minor roads. Slight improvements were offered by the combined use of GPS and Galileo: the percentage of epochs with HDOP no higher than 10, on a major road, became as large as 17%. Unfortunately on a minor road, satellite availability was still as small as 3%, even if the GLONASS system was included. In terms of coverage, the paper demonstrated how multi-constellation was far from satisfying the general requirement of 90% coverage for applications in urban environments. Continuity was evaluated by considering the distance covered without navigation solution during a simulated driving test. With the two-constellation GPS+Galileo system the user had to drive for maximum 1 km before a new position could be computed. The triple-constellation case offered much better continuity, with the maximum distance covered without navigation solution improved to 450 m. In summary, the authors concluded that even though multi-GNSS had the potential to provide better positioning performance, it was far from satisfying most of navigation applications in an urban canyon such as Hong Kong.

Similar conclusions are in Viandier et al. (2009), where signal availability and positioning accuracy of GPS and GPS+Galileo were compared in simulated urban environments corresponding to the cities of Toulouse and Rouen. The authors concluded that even though the combined GPS+Galileo system offered higher satellite availability and less frequent signal discontinuities than the single constellation case, in urban canyons only by exploiting both the line of sight (LOS) and non-line of sight (NLOS) signals was it possible to optimise the chances of computing an accurate position.

Although the small number of Galileo satellites available can be a limiting factor, a few papers have analysed GPS+Galileo positioning using real data.

For example, Cai et al. (2014) evaluated the performance of the four Galileo IOV satellites in respect of single point positioning (SPP) accuracy for GPS and Galileo single constellation and combined modes. To assess the Galileo only positioning performance against the GPS system, data from only four GPS satellites with PDOP similar to the one achieved with the four IOV satellites were used. The average RMS values of the Galileo positioning error in the north,

east and up directions are slightly higher than those of GPS. This was attributed to the lower accuracy of the Galileo broadcast orbits and clocks. In the combined mode, the positioning accuracy was improved by approximately 10% in the vertical component over the GPS solution (considering all the satellites), while no significant improvement was observed in the horizontal plane. The authors concluded that in order to have some improvements also in the horizontal components more Galileo satellites were needed.

Similarly, Angrisano et al. (2013) evaluated the positioning accuracy of the combined GPS+Galileo solution in comparison with the GPS only solution. The RMS of the GPS+Galileo positioning errors in the horizontal and vertical components are reduced by approximately 20 cm with respect to the GPS alone configuration.

Gioia et al. (2014) found that the mean horizontal error using the Galileo constellation is reduced from 6 m to 4 m respect to the GPS case with similar HDOP. Adding measurements from Galileo to those from the full GPS constellation seemed to provide only a slight improvement for both horizontal and vertical components compared to the GPS only case. The mean horizontal error is reduced by only 10 cm, while the mean vertical error is reduced by only 2 cm. More significant improvements are in the maximum horizontal error recorded, which passes from 14 m, in the GPS only case, to 11 m, in the GPS+Galileo configuration.

Pan et al. (2016) compared the positioning performance of multi-GNSS systems with the GPS only case both in static and kinematic scenarios and using different elevation masks. Four different configurations were analysed: GPS only, GPS+GLONASS, GPS+GLONASS+BeiDou, and GPS+GLONASS+BeiDou+ Galileo. Only limited benefit was offered by multi-constellation in open sky conditions, while significantly larger improvements were visible in extremely masked environments. In particular the 3D error improved from about 16 m using GPS only to less than 4 m using three or four constellations. Also, the availability of a position solution was greatly increased. With a mask angle of 40°, the percentage of epoch on which the position could be computed was only 37% with GPS and 52% for the GPS+GLONASS case, while it remains 100% for the triple and quad-constellation cases. This paper confirmed, once again, the benefit of multi-GNSS, in particular in urban canyons, where it greatly

outperforms the single constellation in terms of the availability and positioning solutions.

2.3 Precise Point Positioning

PPP (Zumberge et al., 1997) is a carrier phase based positioning technique that enables centimetre-level (static processing) to decimetre-level (kinematic processing) accuracy, with no need for local reference stations as required with RTK techniques. PPP can be considered as an improved version of the classic pseudorange based positioning (Teunissen and Montenbruck, 2017), in which broadcast navigation data are replaced with precise orbits and clock estimates from a global or regional network solution. GNSS algorithms engineers are generally well aware of the corrections that must be applied to pseudorange and carrier phase measurement to eliminate large delays due to special and general relativity, the Sagnac effect, and the atmospheric propagation delays. However in PPP, it is important to account for some other effects that are not usually considered in pseudorange or precise differential phase processing models. A rigorous description of the correction models can be found in Héroux and Kouba (2001) and in Section 3.2. The use of carrier phase measurements, in addition to code pseudoranges, implies that the initial carrier phase ambiguities have to be estimated, causing long convergence times. Typically, 15 to 60 minutes are required to have the final accuracy. The long convergence time represents the main drawback of PPP, and explains why it is rarely used in constrained and transient signal environments associated with urban areas, but mainly for applications characterized by open sky conditions such as precise positioning in open environments (Geng et al., 2010a), atmosphere studies (Douša, 2009; Zhang et al., 2012), earthquake and tsunami monitoring (Shi et al., 2010), and precision agriculture (Mondal and Tewari, 2007).

The International GNSS Service (IGS) has provided to the scientific community combined orbit and clock products for GPS since 1994 and for GLONASS since 2000. Different type of products exist, differing mainly by their varying quality and latency. The Final products are generated as a weighted mean of the solutions provided by 9 different Analysis Centres (ACs). Details of the individual AC's processing strategy can be found in ftp://igs.org/pub/center/analysis/. Most AC final solutions have an agreement at

less than 5 mm (3D) to each other (Villiger and Dach, 2017). The IGS Final products have the highest accuracy and internal consistency of all IGS products, but, because of the special care to ensure the highest level of consistency with the associated reference frame, Earth rotation parameters, and receiver and satellite clocks, the latency is between 12 and 18 days. Griffiths and Ray (2009) found that the standard deviations for Satellite Laser Ranging (SLR) residuals for the two GPS satellites equipped with SLR retro-reflectors, the satellites PRN 05 and 06, were 19 mm and 25 mm respectively.

The various ACs contributing to the IGS provide other type of products, less accurate, but with a shorter latency. Those users interested in real-time applications, such as hazard detection and warning, weather forecasting, precision farming and many others, can either use the predicted part of the Ultra-Rapid products, with significant degradation of the performance, or can use the more precise orbits and clocks provided by the IGS RTS, which have been available since April 2013 (Jean and Dach, 2014). Currently the available real-time IGS products include only corrections to GPS satellites broadcast orbits and clocks; corrections to GLONASS are offered as an experimental product. The precise corrections are encoded into the Radio Technical Commission for Maritime Services (RTCM) State Space Representation messages and transmitted using the Network Transport of RTCM via Internet Protocol (NTRIP). Hadas and Bosy (2015) reviewed the quality of the IGS real-time products in terms of availability, latency and accuracy. In the period analysed, for 10 GPS satellites no interruption in data delivery occurred, and for another 10 satellites less than 1% of data were missing. Latency is the difference between the epoch when the corrections were computed and the epoch when they can be applied. The best and the worst-case scenario were considered, namely when the corrections were updated and just before it. The minimum latency time is about 30 seconds, while the maximum is 92 seconds for orbits and 42 seconds for clocks. However, it is worth emphasizing that the corrections are provided with rates and therefore are valid over some period. To evaluate the quality of the real-time products, they were compared with the final products provided by ESA. On average, the radial component is the most accurate, being the difference only 1.5 cm. The error in the cross-track component is 2.5 cm, while it is 3.9 cm for the along-track component. The real-time clock corrections

have poorer accuracy with errors as large as 8.4 cm. Small degradations were registered during eclipse periods.

In recognition of the evolving GNSS landscape, in 2012 IGS set up the Multi-GNSS Experiment (MGEX) to explore and promote the use of new navigation signals and constellations. Details of the program can be found in Montenbruck et al. (2014), (2013); Rizos et al. (2013). The aim of MGEX is to build up a new network of multi-constellation capable stations, to characterise user equipment and space segment, to develop new concepts and data processing tools, and, finally, to generate post-processing products for Galileo, QZSS, and BeiDou. Currently, six ACs are providing multi-GNSS products for MGEX on a routine basis:

- Centre National d'Etudes Spatiales (CNES), Collecte Localisation Satellites (CLS), Groupe de Recherche de Geodesie Spatiale (GRGS)
- Centre for Orbit Determination in Europe (CODE)
- GeoForschungsZentrum Potsdam (GFZ)
- Technische Universitat Munchen (TUM)
- Wuhan University (WUM)
- Japanese Aerospace Exploration Agency (JAXA)

The quality of the Galileo IOV satellites products provided by CNES, CODE, GFZ, and TUM is studied in Steigenberger et al. (2015). It also includes a short description of the processing strategy adopted by each AC for the computation of the precise orbits and clocks. Satellite ephemerides are analysed in terms of daily discontinuities, direct orbit comparisons (from different ACs) and SLR residuals. The Allan deviation (Allan, 1966) was used to assess the clock stability. The authors concluded that CODE orbit and clock products were the best. They have better internal consistency, smaller SLR residuals, and better clock stability than any other ACs' products. Similar conclusions can be found in Guo et al. (2016). These two research also confirmed the presence of a bow-tie pattern in the SLR residuals and its dependence on the elevation angle of the Sun above the orbital plane, as already described in Montenbruck et al. (2014); and the existence of a bias of about 5 cm, that was also reported in Prange et al. (2013); Uhlemann et al. (2013). Svehla et al. (2016) addressed the bias in the

SLR residual to the orbit shift opposite to the Sun direction due to the thermal re-radiation of the satellite body.

The relationship between the radial component of the ephemeris error and the position of the Sun indicates a subtle mismodelling of the Solar Radiation Pressure (SRP). To overcome this issue, a new orbit model, the Empirical CODE Orbit Model-2 (ECOM-2) was proposed in Arnold et al. (2015), while Montenbruck et al. (2015) presented a new analytical cuboid-box model for the SRP acceleration. Results showed that these new models bring an enhanced clock quality and reduce the systematics in SLR validation of the GNSS orbits. These models have been adopted, respectively by CODE and Wuhan University in their processing since 2015. In November 2016 TUM joined Wuhan University by switching to the a priori cuboid-box model (Villiger and Dach, 2016). Yet, the spread of the SLR residuals is still quite large for low Sun elevation angles (Sośnica et al., 2017).

Although the IGS RTS officially provides products only for GPS and GLONASS, one of its contributing AC, CNES, has recently started broadcasting real-time Galileo and BeiDou corrections to the broadcast orbits and clocks via NTRIP. However, the quality of these products is from 3 to 7 times worse than the corresponding GPS products (Kazmierski et al., 2018).

Within the factors that impact on the convergence time of PPP are the number and geometry of the observed satellites and the quality of the measurements (Abou-Galala et al., 2017). For this reason, the use of the good quality Galileo measurements (see Section 2.1) combined with the GPS ones, and the consequent improvement in terms of satellite availability and geometry, are expected to greatly benefit the convergence time of PPP.

Afifi and El-Rabbany (2015), for example, used GPS+Galileo data from 6 stations within the IGS network, and the MGEX products, to examine several PPP models. The dual-frequency GPS+Galileo observations were combined in the un-differenced and between-satellite-single-difference modes. Results show that the un-differenced configuration reduces the time the solution takes to converge below 10 cm by 25%. Up to 50% improvements were recorded when the single difference configurations were adopted. It is not clear, however, what the specific impact of Galileo in this configuration is, as the two-constellation case was the only one analysed. Also, the authors mention that the phase centre

offset and variations were applied, but accurate Galileo satellites' antenna corrections were made available only after the European GNSS Agency (GSA) published the metadata on 16 December 2016 (Villiger and Dach, 2016), while the receiver antenna corrections are still not available.

The same products were used in Li et al. (2015) to compare the performance of single and multi-constellation PPP using different elevation cut-off angles. It was shown that there was a huge benefit of four-constellation PPP in case of extremely masked environments. In particular with a 40° elevation mask, the time required to achieve an accuracy level of better than 10 cm is reduced from more than 2 hours to less than 30 minutes. The specific PPP performance of Galileo was also evaluated. The authors concluded that the small number of Galileo satellite visible from a single station is a limiting factor when evaluating Galileo only PPP, however they still contribute to the combined GPS+Galileo PPP solution to some extent. On the other hand, Kazmierski et al. (2017) observed slightly poorer performance when processing GPS+Galileo or GPS+BeiDou data in kinematic PPP mode. The authors attributed this problem to the poor quality of the precise products used in this analysis. Similarly Wang et al. (2018) observed extremely low repeatability of the kinematic PPP performance, and attributed the large differences in the accuracy and convergence time to the quality of the multi-constellation real-time products provided by CNES and to the poor stability of the data stream during some periods.

The low number of available satellites and the poor quality of the products limit a proper evaluation of the Galileo system in a PPP context. For this reason, many researchers preferred to use simulation tools in their analysis. Shen and Gao (2006) used a Matlab toolbox developed by GPSoft to simulate observations from GPS and Galileo systems. The errors in the simulated measurements include troposphere, ionosphere, receiver noise, receiver clock errors, and system time offset, while the error in the precise products was assumed to be negligible. The authors evaluated accuracy and convergence time for four simulated open sites; 75% improvements were recorded in both horizontal and vertical accuracy when using the completed Galileo system together with GPS, while the convergence time was reduced by more than half. Similar conclusions were drawn by Garcia et al. (2010), the kinematic PPP

convergence time below 10 cm was improved from about 40 minutes to about 25 minutes and the final accuracy was improved from about 8 cm to 5 cm. Unfortunately, the authors do not explain how the precise orbits and clocks have been simulated. In Juan et al. (2012) and Miguez et al. (2016) real GPS and GLONASS data were mixed with simulated Galileo data. Random errors of different magnitudes where applied to the orbit and clock corrections. These two papers confirmed that better accuracy and convergence time could be obtained with multi-constellation PPP with respect to the GPS only solution.

Another way to improve the convergence time in PPP is by applying the ambiguity resolution techniques. The two mostly used ambiguity resolution methods are integer bootstrapping (Teunissen, 1998) and the Least Squares Ambiguity Decorrelation Adjustment (LAMBDA) method (Teunissen, 1995). Wang and Gao (2006) used simulated GPS data to show that the convergence period can be reduced from more than 16 minutes to roughly 2 minutes in kinematic PPP. On the other hand, Mervart et al. (2008) found that, using real data, 15 to 30 minutes were usually required before ambiguities could be reliably fixed to integers. When we speak of ambiguity resolution in PPP, we have to remember that the un-differenced carrier phase ambiguities are not integers, as they are corrupted by hardware biases. These biases need to be corrected for in order to retrieve the integer nature of the ambiguities. The corrections can be categorised into two groups: the Fractional Cycle Biases (FCBs) and the Integer Recovery Clocks (IRCs). The FCBs are the fractional-cycle part of the hardware biases and they can be estimated in a network solution using the methods developed in Bertiger et al. (2010); Ge et al. (2008) or Geng et al. (2009). The IRCs are used in PPP to directly generate integer ambiguity estimates, and therefore they are different from the precise clocks provided by the IGS. They can be generated in the network solution following Laurichesse et al. (2009) or Collins (2008). Geng et al. (2010b) demonstrated that these two families of corrections are equivalent from the theoretical point of view and therefore, if well implemented, should bring to the same results.

As previously stated, one key factor that impacts on the convergence time of PPP is the large pseudorange error. Traditionally in PPP, the ionosphere-free combination is used to mitigate the effect of the ionosphere, however it is well known that this combination amplifies the noise in the measurements up to three

times. As an alternative, PPP algorithms adopting un-combined observables have been proposed. Here the ionospheric delay can be mitigated by applying external corrections and/or estimated in the Kalman Filter. Teunissen et al. (2010) showed that instantaneous ambiguity fixed solution can be obtained if the ionosphere correction coming from a very dense regional network are included in the data processing. In Geng et al. (2010a), almost instantaneous re-convergence was obtained using un-combined measurements and estimating the ionosphere delays. The ionospheric delay predicted from the previous estimates was used to constrain the estimation of the new ambiguity in the case of cycle slips. Similarly, Li et al. (2013) used corrections from the Global Ionosphere Map (GIM) to tightly constrain the estimation of the ionosphere delays. The time to have a float PPP solution with accuracy better than 10 cm was improved from 31 to 19 minutes, while the time to have an ambiguity fix solution was reduced from 24 to 15 minutes. Even better results were obtained in terms of re-convergence: the new configuration enables instantaneous cycle slip repair. These great performance improvements are unfortunately limited by the quality of the ionosphere corrections used, which degrades with the increasing distance of the user from the network, and by the spatial and temporal constraints used for the ionosphere estimation.

Indeed, Banville et al. (2014) compared the float and fixed positioning solutions computed with and without the tight constraint offered by accurate ionospheric maps. For this purpose, data from 24 stations in Canada were tested during particularly quiet ionospheric conditions (average Kp index of 2.25). Despite having an accuracy of 15 cm for satellites at high elevations and of 25 cm for satellites at low elevations, employing the GIM provided by the IGS, does not significantly reduce the horizontal convergence time, below 10 cm of error, for the float ambiguity solutions, while it reduces the convergence time of the fixed solutions from about 27 minutes to about 24 minutes (95^{th} percentile). On the other hand, when using a Regional Ionospheric Map, computed by a network in the east coast of Canada, even instantaneous ambiguity fixed solutions could be achieved.

The modernisation process in GNSS is not only bringing more satellites but also new signals and frequencies. Next generation GPS satellites will broadcast signals over three frequency bands (L1, L2 and L5), while Galileo has signals

over five different frequencies (E1, E5a, E5b, E5, and E6). Triple-frequency observations have been considered to obtain the best performance from float PPP. Elsobeiey (2014) compared the PPP performance of 9 different triple-frequency GPS combinations with the traditional L1-L2 ionosphere-free combination. The best performance was achieved by a combination that was not completely ionosphere-free and with a significant noise amplification of 3.85, while the L1-L2 ionosphere-free combination, which completely mitigates the effect of the ionosphere and has a noise amplification factor of 2.97, was the second best. In a similar way, Deo and El-Mowafy (2016) compared the float PPP performance of the L1-L2, the triple-frequency ionosphere-free combination with minimum noise amplification (only 2.55), the un-combined observations, and a mixed code-phase triple-frequency combination. Results showed only minimum improvements from the use of three frequencies against the L1-L2 combination. Indeed, the average convergence time was only reduced from 29.4 minutes to 26.3 minutes with triple-frequency ionosphere-free combination, to 26.8 with the mixed code-phase combination and to 27 minutes using the un-combined configuration. For this reason, most of the studies of making use of the additional frequency signals are focusing on improving the time to first ambiguity fix. An example of these research efforts is the Triple Carrier Ambiguity Resolution (TCAR) method, an instantaneous ambiguity resolution method which was originally proposed for relative positioning over short baseline (Forsell et al., 1997; Jung et al., 2000; Vollath et al., 1999; Werner and Winkel, 2003). The float ambiguities are estimated through geometry-free combinations and then fixed with integer rounding. Cocard et al. (2008) made a rigorous analysis to find the most effective set of combinations to be used in TCAR. The perspective of instantaneous ambiguity fixed solutions pushed many researchers to study new triple-frequency ionosphere-free combinations with the aim of exporting the concept of TCAR to PPP. The combinations presented in Geng and Bock (2013) allowed to have a fixed solution within a few minutes. Unfortunately, this method only performs well in multipath-free environments. Better results can be achieved considering geometry preserving combinations and improved ambiguity resolution methods, such as integer bootstrapping or the LAMBDA method. For instance, Henkel and Gunther (2008) found an optimal triple-frequency ionosphere-free code-carrier

combination for Galileo signals that provides ambiguity fixed solution, via integer bootstrapping, in about 5 seconds. However, in this study, the effect of multipath on pseudorange measurements was not considered.

Laurichesse and Banville (2018) showed that instantaneous ambiguity fixed solutions is possible in PPP even by employing only the GIM if quad-frequency Galileo measurements (E1-E5a-E5b-E6) are used in combination with dual-frequency GPS measurements (L1-L2).

2.4 Chapter summary

To conclude, because of the limited number of satellites in view, so far Galileo has been considered only as an augmentation system to GPS aimed to improve satellite availability in urban canyons, reduce the DOP fluctuation, and enhance the positioning performance offered by GPS. No report has been found using Galileo PPP as an independent solution to GPS PPP or GPS+Galileo PPP. Moreover, the immature quality of the Galileo precise orbits and clocks was addressed by some authors as the reason for the degradation of the GPS+Galileo PPP solution with respect to the GPS only solution.

Given the technical limitations brought by the current Galileo constellation status, namely poor satellite availability and precise products' quality, at the moment, it is advisable to evaluate Galileo only and GPS+Galileo PPP through simulated data. Even though an extensive number of research efforts have been dedicated to create a realistic simulation tool, a rigorous approach to simulate the error in the products is still missing.

Simulated data can be very useful to study the performance of the Galileo E5 AltBOC signal in PPP. With its low pseudorange noise and excellent multipath suppression property, E5 can be an important asset for PPP. Since the precise products are based on the E1-E5a ionosphere-free combination, E5 has not been largely considered in dual-frequency PPP.

The long convergence time is the main reason why PPP has not been used in urban areas, where frequent cycle slips/data gap are likely to happen. Reduction of PPP (re-)convergence time is essential for precise navigation of land vehicle in cities. Most successful techniques, today, involve the use of un-combined observable, external ionosphere corrections, estimation of the residual ionosphere error, and ambiguity resolution. However, these configurations only

perform at their best if the user is located in proximity of the continuous operative reference network of receivers used to estimate the ionosphere corrections. It means that the best performance of PPP, i.e. high accuracy globally, is lost. Moreover, the great reduction in the PPP (re-)convergence time given by the un-combined measurements configuration comes with a downside: the computational penalty associated with the filter formulated with dual-frequency measurements and ionosphere states becomes more pronounced with increasing numbers of satellites associated with the use of multi-GNSS, which is desirable for PPP in degraded signal environment. For these reasons, the use of ionosphere-free combinations might still be the preferable option in a large number of applications.

Finally, triple-frequency PPP revealed to be effective only to improve ambiguity resolution. Probably, further evaluation of triple-frequency PPP with float ambiguity is necessary to study the potential benefit provided by the third frequency over the convergence time.

Chapter 3

Precise Point Positioning

The key to achieving high accuracy in Precise Point Positioning (PPP) is to mitigate the potential sources of error affecting the pseudorange and carrier phase measurements.

This chapter describes the correction models commonly used in PPP.

3.1 Observation equation

The GNSS pseudorange $P_{r,i}^{s}(t)$ and carrier phase $L_{r,i}^{s}(t)$ on frequency f_i transmitted by the satellite *s* and recorded at time *t* by the receiver *r* can be written as (Teunissen and Montenbruck, 2017)

$$\begin{aligned} P_{r,i}^{s}(t) = {} & g_r^s(t) + c\left(dt_r(t) - dt^s(t) + \delta t^{rel}(t)\right) \\ & + I_{r,i}^{s}(t) + T_r^s(t) \\ & + c\left(d_{r,i} - d_i^s\right) + \xi_{r,i}^{s}(t) + e_{r,i}^{s}(t) \end{aligned} \tag{3.1}$$

$$\begin{aligned} L_{r,i}^{s}(t) = {} & g_r^s(t) + c\left(dt_r(t) - dt^s(t) + \delta t^{rel}(t)\right) \\ & - I_{r,i}^{s}(t) + T_r^s(t) \\ & + c\left(\delta_{r,i} - \delta_i^s\right) + \zeta_{r,i}^{s}(t) \\ & - \lambda_i\left(\omega_r^s(t) + N_{r,i}^{s}\right) + \varepsilon_{r,i}^{s}(t) \end{aligned} \tag{3.2}$$

where g_r^s is the geometric range between the centre of mass of the transmitting satellite *s* and the reference point of the receiving antenna *r*, *c* is the speed of the light, dt_r and dt^s are the receiver and satellite clock offsets. The relativistic clock correction and the relativistic signal delay due to space-time curvature have been included in δt^{rel}. The delay due to the troposphere and ionosphere are T_r^s and $I_{r,i}^{s}$ respectively. In equation (3.1) the receiver and satellite pseudorange hardware biases are represented by $d_{r,i}$ and d_i^s, while the phase centre offset for the transmitting and receiving antennas are considered in $\xi_{r,i}^{s}$. In equation (3.2), the carrier phase hardware biases are $\delta_{r,i}$ and δ_i^s. Similarly to the pseudorange observables, the carrier phase measurements are affected by

the phase centre offset and variation. To emphasize that this term is different for the two measurements, the phase centre offset for the carrier phase is denoted as $\zeta_{r,i}^{s}$. In equation (3.2), two additional terms appear: the phase wind-up (ω_{r}^{s}) and the integer ambiguity ($N_{r,i}^{s}$). Finally, $e_{r,i}^{s}$ and $\varepsilon_{r,i}^{s}$ include the residual or un-modelled errors, such as multipath, for pseudorange and carrier phase.

Note that, in the two equations, the indices for arrival and transmission time have been ignored. However, it must be highlighted that the difference between these two times is crucial to achieve the right geometric range. One other important effect that needs to be taken into account when modelling the geometric range is the rotation of the Earth Centred Earth Fixed (ECEF) reference frame during the signal propagation time. This is known as the Sagnac correction.

The next sections give more detail about each source of error in the GNSS measurements and explains how these error terms are handled or mitigated. An overview of the magnitude of the individual error components and their residual bias, after the correction models have been applied, is provided in **Table 3.1**. These values are approximate and should be taken only as a reference. In reality, both the magnitudes and the uncertainty may vary from case to case.

Table 3.1 *PPP a priori correction models* (Teunissen and Montenbruck, 2017).

Model component		Magnitude	Uncertainty
Satellite	Position		Depends on the type of products used
	Clock offset	< 1 ms	Depends on the type of products used
	Relativistic effects	10 – 20 m	
	Antenna phase centre offset	0.5 – 3 m	10 cm
	Phase wind-up	10 cm	Depends on various factors
	Differential code biases	< 15 ns	0.1 – 1 ns
	Fractional phase biases	< 0.5 cycles	0.01 cycles
Atmosphere	Troposphere (dry)	2.3 m	5 mm
	Troposphere (wet)	< 0.3 m	
	Ionosphere (1^{st} order)	< 100 m	0 – 1 m
	Ionosphere (higher order)	0 – 2 cm	1 – 2 mm
Site displacement	Solid Earth tides	< 0.4 m	1 mm
	Ocean tides	1 – 10 cm	1 – 2 mm
	Pole tides	25 mm	
Receiver	Phase centre offset	5 – 15 cm	
	Phase centre variations	< 3 cm	1 – 2 mm

3.2 Errors in GNSS measurements and corrections in PPP

3.2.1 Satellite orbits and clocks

In order to compute the pseudorange between the receiver and the transmitting satellite, knowledge of the satellite's position and the clock offset are required. In the standard pseudorange-based positioning, the ephemerides broadcast in

the navigation message are used. The predicted offset between the satellite clock and the system time can be also derived from the navigation message. The combined accuracy of these two terms is named Signal-In-Space Ranging Error (SISRE). The SISREs for the GPS and Galileo systems have largely improved in the last few years dropping well below 1 m (Chatre and Verhoef, 2018; Montenbruck et al., 2018). However, this value is still too large for high accuracy positioning techniques such as PPP. As an alternative, precise orbit and clock models are made available by different sources. Beside the commercial services, the IGS provides free of charge GPS products both for post-processing and real-time applications (through the IGS RTS).

The post-processing products can be divided into ultra-rapid (observed-half), rapid and final products based on the increasing accuracy and decreasing time latency. The final products have the best quality and internal consistency of all IGS products. They are made available every Friday with a delay up to 18 days. These products are the basis for the realization of the International Terrestrial Reference Frame (ITRF) made by the IGS, and are intended for those applications demanding high consistency and quality. The rapid products have a quality nearly comparable with that of the final products, but they are made available every day, 17 hours after the end of the previous observation period. For most applications, users of the IGS products will not notice any significant difference in the results obtained with the final and rapid products. The ultra-rapid products are mainly intended for near real-time applications. They are released four times per day, at 00:00, 06:00, 12:00 and 18:00 UTC, to reduce the prediction time to 6 hours. Unlike the other IGS products, the ultra-rapid orbits file contains 48 hours of tabulated orbital ephemerides. The first 24 hours are based on the most recent GPS observation data from the IGS hourly tracking network. The last 24 hours are predictions extrapolated from the observed data in the first half. A summary of the accuracy and latency of the different type of GPS products can be found in **Table 3.2**.

The precise orbits and clocks are generally tabulated in the Standard Product 3 (SP3) format file (Spofford and Remondi, 2018). This file contains a 24-hours record of the GNSS satellites' position components and clock offset, usually sampled every 15 minutes. In PPP, these satellite products need to be interpolated to coincide with the sample interval of the measurements. While

the interpolation of the orbit can lead to only very small errors, the same cannot be said for the clocks. The errors resulting from the interpolation of the clock data depends on the sampling rate and the Allan deviation of the clock itself (Zumberge and Gendt, 2001). For this reason, the precise clock products can be found also in a dedicated Receiver Independent Exchange (RINEX) clock file (Gurtner and Estey, 2018; Ray and Gurtner, 2018) with much higher sampling rate up to 5 seconds.

In 2001 the IGS established a Real-Time working group with the aim of designing and implementing real-time infrastructure and processes for the delivery of real-time data to analysis centres, and the dissemination of real-time products to users (Meindl et al., 2011). These real-time products consist of GNSS satellites' orbit and clock corrections to the broadcast ephemeris and have been available since April 2013 (Jean and Dach, 2014). The product streams available at the RTS are combination solutions generated by processing individual solutions from the ACs contributing to the RTS. Two different combinations are currently available for GPS:

- IGS01/IGC01 is a single epoch combination. This configuration has the advantage that the full accuracy is available as soon as the product generation starts. The products are offered with the orbit solution referred to the antenna phase centre under the designation IGS01 or to the centre of mass of the satellite under the designation IGC01.

Table 3.2 *GPS precise orbits and clocks products from IGS* (IGS, 2018a).

Type		Accuracy	Latency
Ultra-rapid (predicted half)	Orbits	~ 5 cm	Real-time
	Clocks	~ 3 ns RMS ~ 1.5 ns STD	
Ultra-rapid (observed half)	Orbits	~ 3 cm	3 – 9 hours
	Clocks	~ 150 ps RMS ~ 50 ps STD	
Rapid	Orbits	~ 2.5 cm	17 – 41 hours
	Clocks	~ 75 ps RMS ~ 25 ps STD	
Final	Orbits	~ 2.5 cm	12 – 18 days
	Clocks	~ 75 ps RMS ~ 20 ps STD	

- IGS02 is a Kalman filter combination. This solution requires a few minutes to converge to the final accuracy.

The orbit corrections vector $\delta\bar{O}$ is provided in the radial (δO_r), along-track (δO_a) and cross-track (δO_c) components. The corrections are also provided with their velocities ($\delta\dot{\bar{O}}$) to make them valid over a certain period. Such implementation results in reduced bandwidth (Hadas and Bosy, 2015). The algorithm to apply the orbit corrections is the following:

1. Propagate the corrections from the epoch in which they have been generated t_0 to the current epoch *t*

$$\delta\bar{O}(t) = \begin{bmatrix} \delta O_r(t_0) \\ \delta O_a(t_0) \\ \delta O_c(t_0) \end{bmatrix} + \begin{bmatrix} \delta\dot{O}_r \\ \delta\dot{O}_a \\ \delta\dot{O}_c \end{bmatrix} \cdot (t - t_0) \tag{3.3}$$

2. Compute the unit vectors in the radial ($\hat{e}_r$), along-track ($\hat{e}_a$) and cross-track ($\hat{e}_c$) directions

$$\begin{aligned} \hat{e}_a &= \frac{\dot{\bar{r}}}{\left\|\dot{\bar{r}}\right\|} \\ \hat{e}_c &= \frac{\bar{r} \times \dot{\bar{r}}}{\left\|\bar{r} \times \dot{\bar{r}}\right\|} \\ \hat{e}_r &= \hat{e}_a \times \hat{e}_c \end{aligned} \tag{3.4}$$

3. Transform the corrections into the geocentric reference frame

$$\delta\bar{X} = \begin{bmatrix} \hat{e}_r & \hat{e}_a & \hat{e}_c \end{bmatrix} \cdot \delta\bar{O} \tag{3.5}$$

4. Apply the geocentric corrections ($\delta\bar{X}$) to the broadcast orbits ($\bar{X}_b$) in order to obtain the precise orbits ($\bar{X}_p$)

$$\bar{X}_p = \bar{X}_b - \delta\bar{X} \tag{3.6}$$

The clock corrections δC are given as a set of three parameters: the bias (C_0) computed at epoch t_0, the drift (C_1), and the drift rate (C_2). These parameters allow users to compute the error in the broadcast clock at the current epoch *t* as in the following equation:

$$\delta C = C_0 + C_1(t - t_0) + C_2(t - t_0)^2 \tag{3.7}$$

$$dt^s = dt_b^s - \frac{\delta C}{c} \tag{3.8}$$

Galileo products for post-processing applications are made available thanks to the IGS MGEX. Real-time Galileo products can be obtained from commercial providers (e.g. Veripos, GMV). Alternatively, they are distributed, free of charge, by the CNES.

Table 3.3 *Analysis centers contributing to IGS MGEX.*

Institution	ID	Constellation
CNES/CLS	grm	GPS+GLO+GAL
CODE	COD0MGXFIN	GPS+GLO+GAL+BDS+QZS
GFZ	gbm	GPS+GLO+GAL+BDS+QZS
JAXA	JAX0MGXFIN	GPS+GLO+QZS
TUM	tum	GAL+QZS
Wuhan University	wum	GPS+GLO+GAL+BDS+QZS

3.2.2 Relativistic effects

Both general and special theory of relativity impact on GNSS measurements (Kaplan and Hegarty, 2005). The effect of the special relativity needs to be corrected any time the signal source (i.e. the GNSS satellite) or the signal receiver is moving with respect to the chosen isotropic light speed frame. On the other hand, the general relativity has to be taken into account when the signal source and the receiver are located at different gravitational potentials. In order to compensate for the effects of both special and general relativity on satellite clocks, their frequency is adjusted before the launch, so that a user at sea level will observe a frequency of 10.23 MHz. For example, GPS satellites have their clock's proper frequency lowered to 10.229999999543 MHz (Pascual-Sánchez, 2007).

Beside this, other four relativistic effects have to be considered.

The Shapiro delay on satellite signals is caused by the space-time curvature due to the presence of the Earth's gravitational field. The correction can be computed as (Ashby, 2003)

$$\delta t_{stc}^{rel} = \frac{2\mu_{\oplus}}{c^3} \ln\left(\frac{r^s + r_r + g_r^s}{r^s + r_r - g_r^s}\right) \tag{3.9}$$

In equation (3.9), $\mu_{\oplus}$ is the Earth's gravitational constant (approximately equal to 398600 km^3s^{-2}), r^s and r_r are the distances of the satellite and receiver from the centre of the Earth, and g_r^s is the geometric distance between the receiver and the transmitting satellite. The Shapiro delay is about 60 ps for GPS, Glonass, Galileo and BeiDou satellites in medium Earth orbit, while it is of the order of 70 ps for the BeiDou satellites in the inclined geosynchronous orbits (Teunissen and Montenbruck, 2017).

The slight eccentricity of the GNSS satellites' orbits causes another relativistic effect, half of which is caused by the periodic change in the satellite velocity and the other half is due to the periodic change in the satellite gravitational potential. When a satellite is at the perigee (i.e. the closest point of the orbit to the Earth), the velocity reaches its highest value, while the geopotential the lowest. These effects caused by the special and general relativity make the on-board clocks to run more slowly. On the other side, when the satellite is at the apogee (i.e. the furthest point to the Earth), the clocks run quicker. These effects of the orbit eccentricity on the satellite clocks can be corrected using (Ashby, 2003)

$$\delta t_{clk}^{rel} = -\frac{2}{c^2}\sqrt{a\mu_{\oplus}}\, e \sin E \tag{3.10}$$

where *a* is the semi-major axis of the orbit, *e* is the orbit eccentricity, and *E* is the eccentric anomaly of the satellite. Assuming an eccentricity for the GPS orbit of 0.02, the maximum value for δt_{clk}^{rel} is about 45 ns (Teunissen and Montenbruck, 2017).

It is clear from equation (3.10) that in case the satellite orbit is perfectly circular (eccentricity equal to zero) the relativistic effect that has been just described disappears. In reality, even satellites in circular orbits would experience periodic changes in the geopotential due to the fact that the Earth is not perfectly spherical with homogeneous mass distribution. The most prominent effect is due to the Earth oblateness, which is described by the J_2 term of the gravitational field expansion series (Montenbruck and Gill, 2000). This effect can be accounted for using (Ashby, 2003)

$$\delta t_{clk,J_2}^{rel} = -J_2 \frac{3}{2} \frac{R_\oplus^2}{c^2} \sqrt{\frac{\mu_\oplus}{a^3}} \sin^2 i \sin^2 2u \tag{3.11}$$

where the J_2 term equals $1.083 \cdot 10^{-3}$, $R_\oplus$ is the equatorial radius of the Earth, i is the inclination of the orbit, and u is the argument of latitude.

The last relativistic effect, which has to be taken into account only when working in the ECEF coordinate system, is known as Sagnac effect. Due to the rotation of the Earth during the signal transmission time, a clock on the Earth will experience a finite rotation with respect to the Earth Centred Inertial (ECI) reference frame. **Figure 3.1** describes this effect: if, during the transmission time, the user experiences a rotation away from the transmitting satellite, the propagation time will increase. The Sagnac effect can amount for several hundreds of nanoseconds (Ashby, 2003) and can be applied as a correction to the satellite-to-user range as in Teunissen and Montenbruck (2017)

$$\Delta g_r^s = \frac{1}{c} \left(\bar{r}_r(t_A) - \bar{r}^s(t_E) \right) \cdot \left(\bar{\omega}_\oplus \times \bar{r}_r(t_A) \right) \tag{3.12}$$

where $\bar{\omega}_\oplus$ is the Earth rotation vector, $\bar{r}_r$ is the receiver position at time of reception t_A, and $\bar{r}^s$ is the satellite position at time of emission t_E.

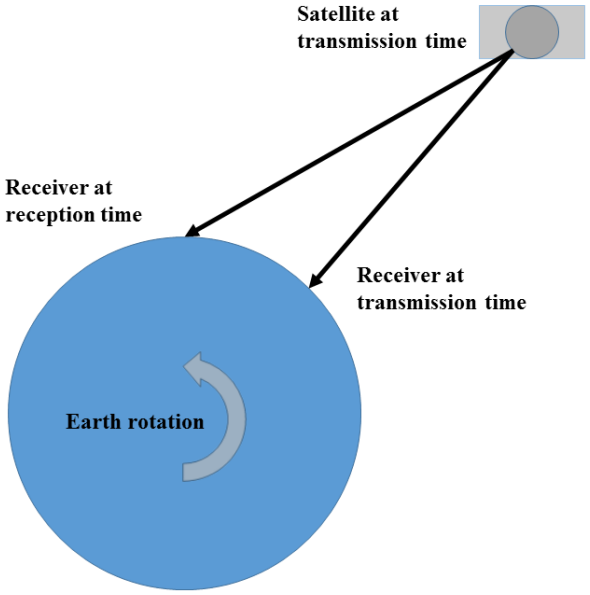


Figure 3.1 *Sagnac effect.*

3.2.3 Ionospheric delay

The ionosphere is the part of the atmosphere between 50 km and 1000 km above the Earth's surface that contains electrically charged particles. The ultraviolet radiations from the Sun ionize the gas molecules and release free electrons and ions. These electrons influence the propagation of electromagnetic waves. The ionosphere is a dispersive medium. It means that its refractive index, defined as the ratio between the speed of light in vacuum and in the medium, depends on the frequency (f_i). Moreover, in a dispersive medium the carrier of the signal and its modulation travel at different velocities (Kaplan and Hegarty, 2005). The refractive index for the phase (n_p) is related to the modulation (or group) refractive index (n_g) by the following

$$n_g = n_p + f_i \frac{dn_p}{df_i} \tag{3.13}$$

The delay of the signal due to the ionosphere depends on the number of electrons along its path. This number can be quantified by the Total Electron Content (TEC), defined as the number of electrons in a tube with a cross section of 1 m^2. The TEC is measured in TEC Units (TECUs) which are defined as 10^{16} electrons/m^2.

$$TEC = \int_{s}^{r} n_e(l)dl \tag{3.14}$$

In Equation (3.14), n_e is the electron density along the signal path, which is not uniformly distributed along the ionosphere. Indeed, the radiation from the Sun affects the various layers of the ionosphere in different ways; the maximum density of charged particles can be found in the so called F2 region (see **Figure 3.2**) between 250 km and 400 km.

The refractive index for the carrier phase n_p can be approximated to the first order as

$$n_p \approx 1 - \frac{40.3 n_e}{f_i^2} \tag{3.15}$$

While the group refractive index can be obtained by replacing (3.15) into (3.13)

$$n_g \approx 1 + \frac{40.3 n_e}{f_i^2} \tag{3.16}$$

The delay in the carrier phase and pseudorange measurements due to the first order ionosphere can be found by integrating the electron density along the signal path

$$I_{r,i}^{s} = \mp \frac{40.3 \cdot TEC}{f_i^2} \tag{3.17}$$

In Equation (3.17) the minus sign holds for the ionospheric delay on the carrier phase, while the plus sign is for the pseudorange. One TECU delays the GPS carrier on L1 by approximately 16.2 cm. Typically, the magnitude of the first order ionosphere is between 1 m to 50 m, but it can be as large as 100 m in period of extreme solar activity.

The second order ionospheric effect depends on the geomagnetic field (Alizadeh et al., 2013) and it is no larger than 2 cm at the zenith (Bassiri and Hajj, 1993).

Methods to mitigate for the ionospheric delay can be divided into models, combinations of measurements and estimation.

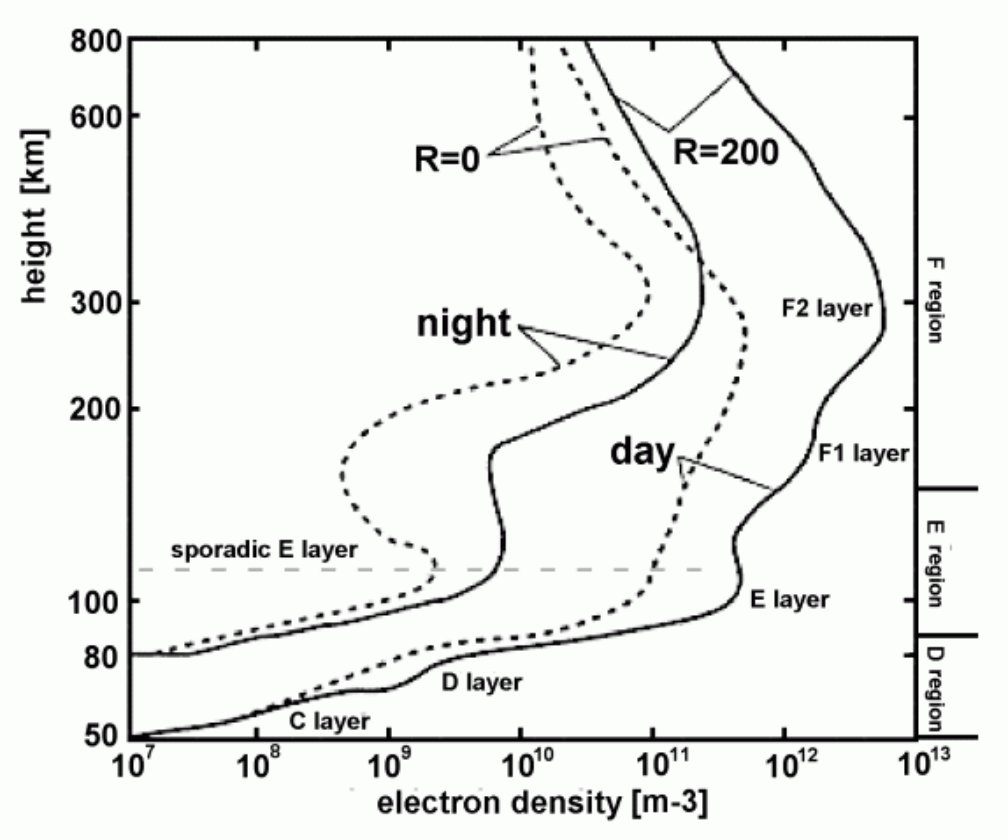


Figure 3.2 *Typical day and night profile of the electron density in the ionosphere* (Istituto Nazionale di Geofisica e Vulcanologia (INGV), 2018).

Single frequency GNSS receivers can rely on different models to get rid of the ionospheric delay. The most widely used is perhaps the Klobuchar model (J. Klobuchar, 1987), which removes on average 50% of the delay at mid-latitudes through a set of coefficients included in the GPS navigation message. Similarly, the navigation message broadcast by Galileo satellite includes the coefficients for the NeQuick ionosphere model (European Union, 2016b). More precise Global Ionosphere Maps (GIMs) can be also used. They are distributed by the IGS and other organizations (CODE for example) in Ionosphere Exchange (IONEX) format (Shaer et al., 1998). As per the IGS precise orbits and clocks, rapid and final GIMs exist, differing on the accuracy and latency (see **Table 3.4**). Real-time GIMs are distributed by some ACs (e.g. CNES or JPL) or commercial services (e.g. GMV). Alternatively, the first order ionospheric delay can be completely eliminated by using the Group And Phase Ionosphere Correction (GRAPHIC) (Yunck, 1993), which is a code and phase ionosphere-

free combination. Positioning accuracy of better than 1.5 m RMS was obtained in Montenbruck (2003) using the GRAPHIC. Finally, attempts to estimate the zenith ionospheric delay plus gradients have been investigated in Chen and Gao (2005). With this strategy, accuracy levels comparable to the one obtained by applying the GIM can be achieved at mid-latitudes.

Table 3.4 *The IGS GIMs* (IGS, 2018a).

Type	Accuracy	Latency
Final GIM	2-8 TECU	~ 11 days
Rapid GIM	2-9 TECU	< 24 hours

Since the ionospheric delay is frequency dependent, multi-frequency receivers can remove large part of the error by combining the measurements in the ionosphere-free (IF) combination.

$$P_{r,IF}^{s} = \frac{f_1^2}{f_1^2 - f_2^2} P_{r,1}^{s} - \frac{f_2^2}{f_1^2 - f_2^2} P_{r,2}^{s} \tag{3.18}$$

$$L_{r,IF}^{s} = \frac{f_1^2}{f_1^2 - f_2^2} L_{r,1}^{s} - \frac{f_2^2}{f_1^2 - f_2^2} L_{r,2}^{s} \tag{3.19}$$

Equations (3.18) and (3.19) are the code and phase IF combinations between measurements on frequency f_1 and f_2. Although the ionosphere delays are removed, this approach has the disadvantage of greatly amplifying the measurements' residual error (including multipath). Despite this drawback, the IF combination is the most widely used way to mitigate for the ionospheric error in two-frequency GNSS measurements. As an alternative, slant ionosphere delays can be included in the state vector and estimated in the Kalman Filter/Least Squares process. Depending on the constraints imposed to the estimation parameters, the configuration has been proved to benefit the convergence time of PPP (Geng et al., 2010a; B. Li et al., 2013; Li, 2012; Zhang et al., 2013) at the cost of largely increasing the size of the state vector and design matrix.

3.2.4 Tropospheric delay

The effect of the neutral atmosphere (i.e. the non-ionized part) is denoted as the tropospheric delay. The troposphere and the stratosphere, which together form

the neutral atmosphere, are non-dispersive media with respect to radio waves up to frequencies of 15 GHz (Hofmann-Wellenhof et al., 2001). It means that the delay affecting GNSS measurements does not depend on the frequency of the signal. The magnitude of the tropospheric delay can vary from 2.4 m for a satellite at the zenith and user at sea-level to 25 m for a satellite at low elevation (Hofmann-Wellenhof et al., 2001). This delay can be divided into a hydrostatic, or dry, part, which only depends on the pressure along the signal path, and a wet part, which depends on the water vapour profile. The wet component accounts for only ~10% of the delay, however it is very difficult to model because of the uncertainty and the dynamics in the distribution of the water vapour in the neutral atmosphere.

A number of models have been developed to characterize the zenith tropospheric delay (ZTD). Mapping functions, different for the dry and wet part, can be used to project the ZTD to the slant delay.

$$T_r^s = ZTD_d m_d(E) + ZTD_w m_w(E) \tag{3.20}$$

In (3.20), the total tropospheric delay T_r^s is written as sum of the dry ZTD (ZTD_d) and wet ZTD (ZTD_w). Each component is multiplied by the corresponding mapping function, m_d and m_w, which are function of the elevation angle E of the satellite.

The Saastamoinen model (Saastamoinen, 1972) is one of the most commonly used methods to model the ZTD as a function of the pressure P_0, the temperature T_0, and the water vapour e_0.

$$ZTD = 0.002277\left[P_0 + \left(\frac{1255}{T_0} + 0.05\right)e_0\right] \tag{3.21}$$

The standard pressure and temperature values at sea level are usually adopted to model the dry ZTD. As an alternative, the global pressure and temperature (GPT) model (Boehm et al., 2007) can be used to evaluate the temperature and the pressure anywhere on the Earth.

To model the wet part, instead, global meteorological information regarding pressure, temperature and water vapour are necessary. One example is the

model developed at the University of New Brunswick (UNB), the UNB3m model (Leandro et al., 2006). This model provides look-up tables to compute pressure, temperature and water vapour partial pressure from latitude and time. Another commonly used model is the EGNOS tropospheric model (Penna et al., 2001). As per the UNB3m model, look-up tables are used to compute the meteorological information.

Mapping functions describe how the slant tropospheric delay varies with the elevation angle E of the satellite. The Neill mapping function (NMF) is based on the following formula

$$m(E) = \frac{1 + \left(\frac{a}{1 + \frac{b}{1+c}} \right)}{\sin(E) + \left(\frac{a}{\sin(E) + \frac{b}{\sin(E)+c}} \right)} \tag{3.22}$$

The coefficients a, b, and c, different for the dry and wet component, have been derived from a fit through radiosonde data from the northern hemisphere and are site and time dependent. The Vienna Mapping Function (VMF) (Johannes Boehm et al., 2006) is also based on (3.22). The coefficients, however, have been derived from a numerical weather model. These same coefficients have been used as a basis in the development of the Global Mapping Function (GMF) (J Boehm et al., 2006).

For high accuracy positioning techniques, it may not be enough to only model the wet and dry tropospheric delay using empirical models since the residual error is of the order of a few centimetres. For this reason, it is common practise in PPP to include the residual wet ZTD (after the models have been applied) in the state vector. Moreover, Bar-Sever et al. (1998) demonstrated that estimating also the horizontal gradients could improve the accuracy and precision for PPP if a sufficient number of satellites are visible at low elevation.

3.2.5 Site displacement effects

PPP provides positioning solutions in a global terrestrial reference frame such as the ITRF. The realization of such a frame is complicated by the fact that the

Earth and its crust in not perfectly solid, but it is subject to periodic deformations caused by different forces that need to be accounted in PPP applications.

3.2.5.1 Solid Earth Tides

The gravitational attractions of the Sun and the Moon cause a slight deformation of the Earth and the consequent vertical and horizontal displacements. These displacements can be modelled using a spherical harmonic expansion. Accounting for only the second order terms is often enough to achieve an accuracy of better than 5 mm.

$$\Delta\bar{r} = \sum_{j=\odot,\mathbb{C}} \frac{\mu_j}{\mu_\oplus} \frac{\|\bar{r}\|^4}{\|\bar{r}_j\|^3} \left\{ \left[3l_2 \left(\hat{e}_j \cdot \hat{e} \right) \right] \hat{e}_j + \left[3\left(\frac{h_2}{2} - l_2 \right) \left(\hat{e}_j \cdot \hat{e} \right)^2 - \frac{h_2}{2} \right] \hat{e} \right\} + \left[-0.025 \sin\varphi \cos\varphi \sin(\theta_g + \lambda) \right] \hat{e} \quad (3.23)$$

In Equation (3.23), the displacement $\Delta\bar{r}$ experienced by a receiver located at $\bar{r}$ is written as a function of the Earth, the Sun and the Moon gravitational constants ($\mu_\oplus$, $\mu_\odot$, and $\mu_\mathbb{C}$), the geocentric unit vectors in direction of the Sun, the Moon, and the receiver ($\hat{e}_\odot$, $\hat{e}_\mathbb{C}$, and $\hat{e}$), the latitude φ and the longitude λ of the receiver site, the Greenwich mean sidereal time θ_g, and the second degree Love and Shida numbers (l_2 and h_2).

Overall, the solid Earth tides introduce vertical displacements of about 30 cm and horizontal displacements of about 5 cm (Teunissen and Montenbruck, 2017).

3.2.5.2 Ocean Tides

The deformation of the seafloor and coastal land due to the uneven distribution of the water during ocean tides causes displacements of the order of centimetres mainly on the vertical direction. The coordinate shift Δc due to ocean tides loading can be written as a harmonic series (Petit and Luzum, 2010) for each of the three components.

$$\Delta c = \sum_{j=1}^{11} A_{cj} \cos\left(\chi_j(t) - \Phi_{cj} \right) \quad (3.24)$$

The individual elements composing the series (3.24) correspond to one of the 11 semidiurnal, diurnal, and long-period tide waves. The time dependent angles χ_j can be computed using the subroutine ARG2.f provided by the International Earth Rotation and Reference System Service (IERS) (Petit and Luzum, 2010), while the site dependent amplitudes A_{cj} and phases Φ_{cj} are provided by the ocean loading service website (http://holt.oso.chalmers.se/loading/index.html). According to Kouba and Héroux (2001) the ocean tides loading always have to be taken into account in PPP unless the receiver is more than 1000 km far away from the coast.

3.2.5.3 Pole Tides

Beside the luni-solar effects described before, small periodic deformations of the Earth are also caused by the polar motion, i.e. the change of the Earth's spin axis relative to its crust. Following Petit and Luzum (2010), the displacements in the north, east and up components at a site with longitude λ and colatitude θ are

$$\begin{aligned} \Delta r_E &= 9\cos\theta\left[m_1\sin\lambda - m_2\cos\lambda\right] \\ \Delta r_N &= 9\cos 2\theta\left[m_1\cos\lambda + m_2\sin\lambda\right] \\ \Delta r_U &= -33\sin 2\theta\left[m_1\cos\lambda + m_2\sin\lambda\right] \end{aligned} \tag{3.25}$$

In (3.25), m_1 and m_2 are the pole coordinates variations from the mean pole. Since the polar motion can reach up to 0.8 arc sec, the maximum displacements due to the pole tides are about 2.5 cm in the vertical direction and 7 mm horizontally.

3.2.5.4 Earth Orientation Parameters

The orientation of the Earth in the space in defined by three kind of motions: the change in the Earth's rotation axis direction with respect to the space, the change in the axis direction with respect to the Earth itself, and finally the velocity change around the Earth's rotation axis. The Earth orientation parameters (EOPs) are used to quantify these three movements. The corrections for these movements can be applied using the information regarding the orientation of the Earth as a function of the time and the EOPs provided by the

IERS (https://www.iers.org/IERS/EN/DataProducts/EarthOrientationData/eop.html).

3.2.6 Antenna effects

3.2.6.1 Phase centre offset and variation

Unlike the broadcast ephemeris, the precise products provided by the IGS describe the position of the centre of mass of the satellites. However, since the GNSS measurements are made between transmitting and receiving antennas' phase centres, the phase centre offset (PCO) with respect to the centre of mass needs to be taken into account. PCO for GNSS satellites can be as large as a few meters in the radial direction pointing towards the Earth (Teunissen and Montenbruck, 2017). Azimuth and elevation dependent phase centre variation (PCV) also have to be considered. **Figure 3.3** well describes the modelling of PCO and PCV for a choke-ring antenna. The mean electrical phase centre differs from the antenna reference point (ARP) by the PCO. This offset is frequency dependant. Only including the mean antenna phase centre in our modelling would lead to a residual error. Therefore, scalar corrections for the frequency, elevation, and azimuth dependent PCV have to be applied.

Corrections for receivers and satellites antenna PCO/PCV are included in the Antenna Exchange (ANTEX) file format (Schmid et al., 2007) and distributed by the IGS, in which the PCO and PCV are tabulated for different GNSS signals, satellites and receivers.

In order to apply the corrections, knowledge of satellites' attitude is required. A good approximation is the yaw-attitude model, which assumes the transmitting antenna pointing towards the Earth and the solar panels always oriented towards the Sun. However, this model fails to provide accurate attitude information during eclipse season (Kouba, 2008).

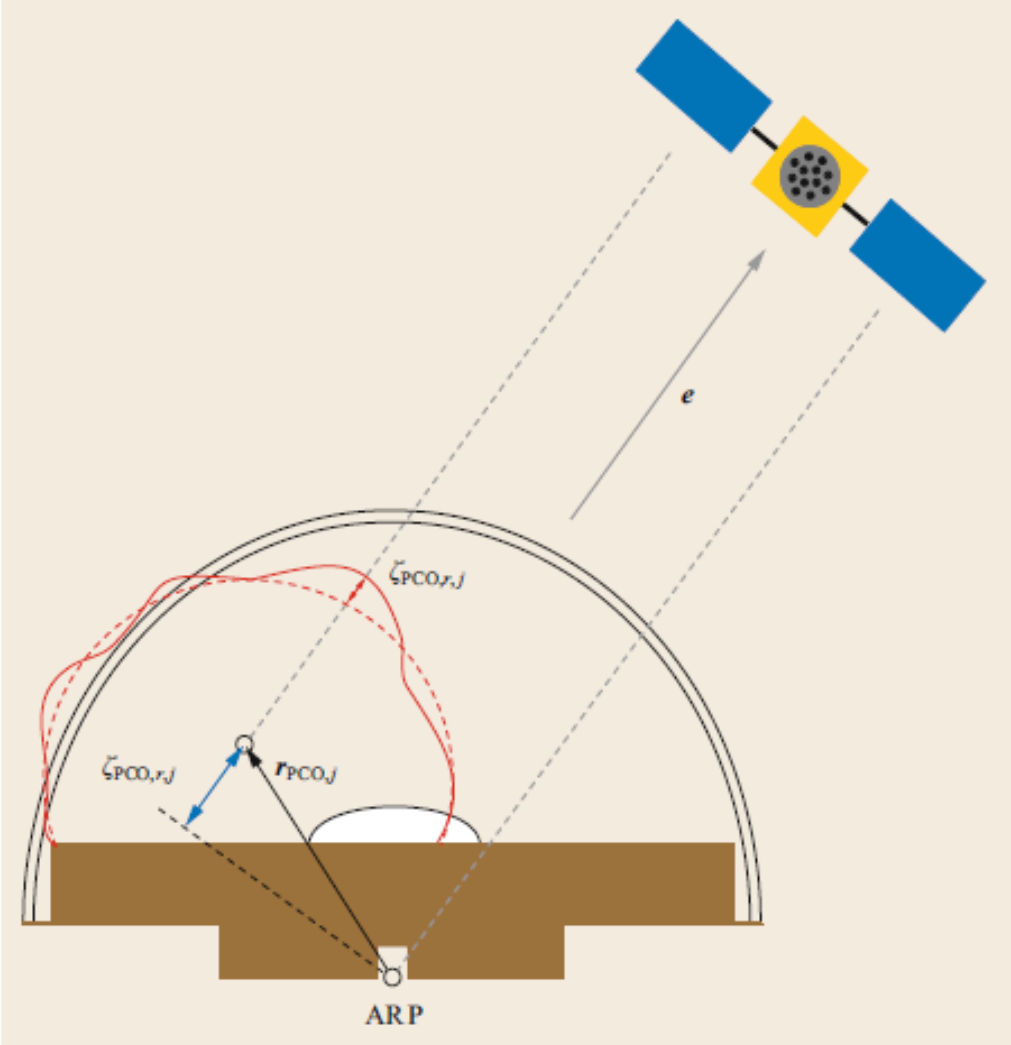


Figure 3.3 *PCO (blue) and PCV (red) of a receiving choke-ring antenna. The solid red line indicates the elevation- and azimuth-dependent PCV with respect to a reference wave-front (dotted red line)* (Teunissen and Montenbruck, 2017).

3.2.6.2 Phase wind-up effect

GNSS satellites transmit right-hand circularly polarized electromagnetic waves. As a consequence, the measured carrier phase changes not only because of the distance between the transmitting and receiving antennas, but also because of the orientation of either two antennas with respect to the line of sight (LOS). This effect is known as phase wind-up (Wu et al., 1993). Satellite antennas experience slow rotations in order to reorient the solar panels in direction of the Sun. Furthermore, during eclipse season, satellites are subjected to rapid rotations, the so-called noon or midnight turns. These turns cause rotations by up to one complete revolution, and consequently a change in the phase measurements by one full cycle, in less than half an hour.

The phase wind-up effect can be taken into account following the algorithm presented in Wu et al. (1993). Assuming k to be the LOS unit vector, the effective dipole vectors $\bar{D}$ and $\bar{D}'$, for the receiving and transmitting antenna respectively, can be computed from the receiver and satellite body coordinate unit vectors $\begin{bmatrix}\hat{x} & \hat{y} & \hat{z}\end{bmatrix}$ and $\begin{bmatrix}\hat{x}' & \hat{y}' & \hat{z}'\end{bmatrix}$ (see **Figure 3.4**).

$$\begin{aligned}\bar{D} &= \hat{x} - \hat{k}\left(\hat{k}\cdot\hat{x}\right) + \hat{k}\times\hat{y} \\ \bar{D}' &= \hat{x}' - \hat{k}\left(\hat{k}\cdot\hat{x}'\right) + \hat{k}\times\hat{y}'\end{aligned} \tag{3.26}$$

The phase wind-up in unit of cycles can be found from the following formula

$$\omega_r^s = sign(\gamma)\arccos\left(\frac{\bar{D}'\cdot\bar{D}}{\left\|\bar{D}'\right\|\left\|\bar{D}\right\|}\right) \tag{3.27}$$

with γ defined as

$$\gamma = \hat{k}\cdot\left(\bar{D}'\times\bar{D}\right) \tag{3.28}$$

The phase wind-up effect for the receiver antenna is the same for all the measured carrier phases and, therefore, it can be safely included in the receiver clock offset estimate.

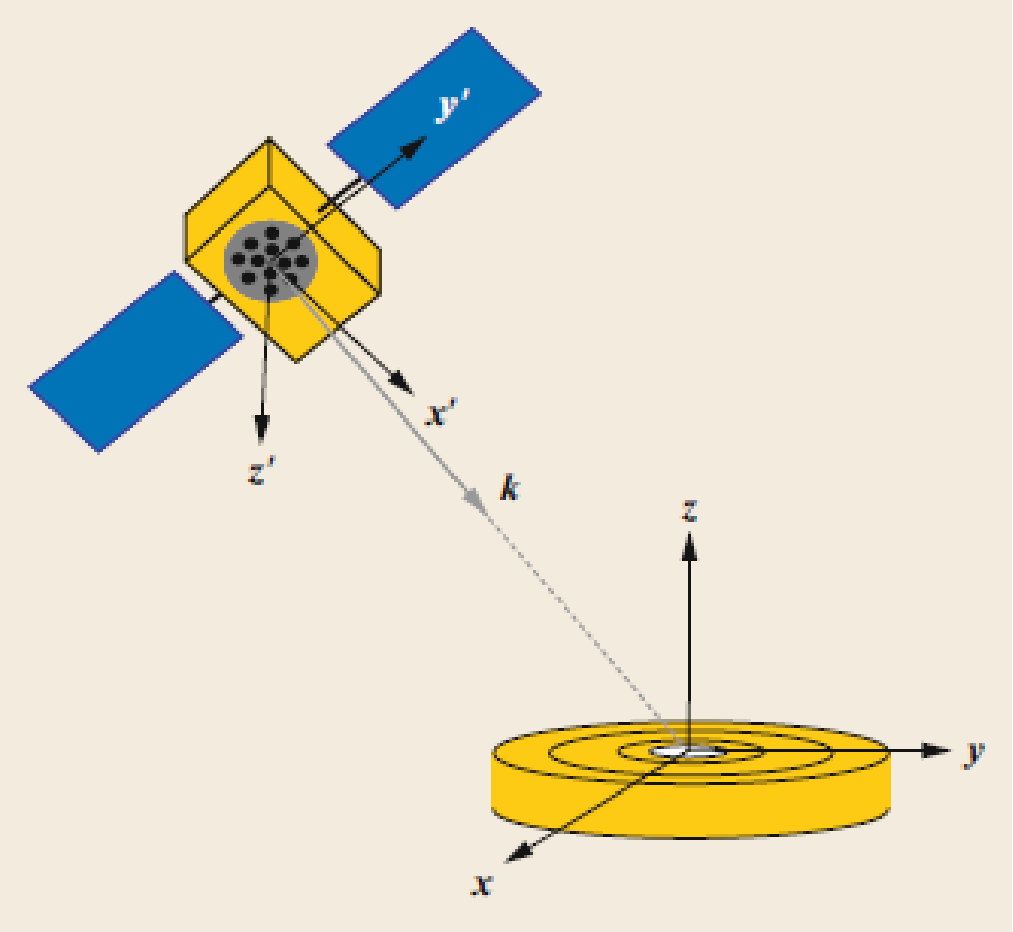


Figure 3.4 *Satellite and receiver body coordinates used for the computation of the phase wind-up effect* (Teunissen and Montenbruck, 2017).

3.2.7 Signal biases

3.2.7.1 Pseudorange biases

In Equation (3.1), the receiver ($d_{r,i}$) and satellite (d_i^s) pseudorange biases have been included to account for instrumental delays caused by imperfect synchronization of the different signals. It is worth saying that only the DCB between two signals are observable, while the absolute biases are unobservable and lumped into the satellite clock corrections. In case of GPS, for instance, the IF combination between the P(Y) signal on L1 and L2 is used in the computation of the precise clocks. If a user processes single frequency observations or a different combination of observations, the corresponding DCB with respect to P1-P2 IF must be applied. Several ACs contributing to the IGS include pseudorange bias corrections within their products.

3.2.7.2 Phase biases

The carrier phases are also affected by receiver and satellite instrumental delays ($\delta_{r,i}$ and δ_i^s in Equation (3.2)). These biases are particularly important in PPP as their fractional part does not allow integer ambiguity resolution. Satellite correction values can be computed from a global or regional reference network (Bertiger et al., 2010; Collins, 2008; M Ge et al., 2008; Geng et al., 2009b; Denis Laurichesse et al., 2009) and distributed to the users who also deal with the receiver part.

3.3 Integer ambiguity resolution

After the phase biases have been corrected for, the integer nature of the carrier phase ambiguities is retrieved and integer ambiguity resolution (AR) can be performed. The purpose of AR is to exploit the integer constraints on the ambiguity to get a better estimation. It consists of the following steps:

1. In the first step, the integer nature of the ambiguities is discarded and a standard Kalman filter/Least Squares solution, the so-called float solution, is obtained.
2. In the second step the integer AR is performed. Here, the integer constraints are taken into account to fix the ambiguities to their integer values.
3. In the final step, the fixed ambiguities are used to correct the float solution and to obtain the fixed solution.

In the next sections three of the most commonly used AR techniques are briefly introduced.

3.3.1 Integer bootstrapping

Integer bias bootstrapping (Teunissen and Montenbruck, 2017), or sequential bias rounding, sequentially fix the ambiguities to their closest integer by taking the correlation between the float ambiguities into account. The rounding procedure is based on the assumption that if a float ambiguity estimate is close to an integer and has a high precision, this integer is likely to be the correct one (Dong and Bock, 1989). The fixing decision is based on the probability

$$P_0 = 1 - \sum_{i=1}^{\infty} \left(efrc\left(\frac{i - \left|\hat{N} - N\right|}{\sqrt{2}\sigma} \right) - efrc\left(\frac{i + \left|\hat{N} - N\right|}{\sqrt{2}\sigma} \right) \right) \tag{3.29}$$

where *efrc*(*x*) is the complementary error function

$$efrc(x) = \frac{2}{\sqrt{\pi}} \int_{x}^{\infty} e^{-t^2} dt \tag{3.30}$$

and $\hat{N}$ is the float ambiguity estimate, σ is its standard deviation conditioned by the previous ambiguity fixing, and N is its closest integer. For a given confidence level α, the fixed ambiguity can be accepted only if

$$P_0 \geq 1-\alpha \tag{3.31}$$

Initially, only a few ambiguities can be successfully fixed using this criterion, however, as the AR progresses, more and more ambiguities can be fixed.

3.3.2 LAMBDA

The LAMBDA method gives the highest probability of correct ambiguity fixing (Joosten and Tiberius, 2002). This approach is based on the integer Least Squares in which we try to minimize the cost function

$$S = \left(\hat{N} - N\right)^T Q_{\hat{N}}^{-1} \left(\hat{N} - N\right) = \min \tag{3.32}$$

in which $Q_{\hat{N}}$ is the covariance matrix of the float ambiguity vector $\hat{N}$ of length m.

Because of the integer constraint on the ambiguity, the right candidates that solve Equation (3.32) can only be found through a search in the m-dimensional search space. In order to simplify this process, a sub-space that satisfies Equation (3.33) can be employed (Teunissen, 1995).

$$S = \left(\hat{N} - N\right)^T Q_{\hat{N}}^{-1} \left(\hat{N} - N\right) \leq \chi^2 \tag{3.33}$$

The threshold χ^2 has to be chosen in order to ensure that the integer solution lies in the sub-space. Details on how to pick the right value for χ^2 are in De Jonge and Tiberius (1996). The size and the shape of the search space is governed by both χ^2 and $Q_{\hat{N}}$. Because of the high correlation between the float ambiguity estimates, the search space can be strongly elongated, making

the search highly complicated. **Figure 3.5** (a) visualizes this problem. In order to make the search more efficient, Teunissen (1995) proposed a volume-preserving integer transformation matrix Z that reshapes the elliptical search space into a spherical one (see **Figure 3.5** (b)).

$$\begin{aligned} N' &= ZN \\ \hat{N}' &= Z\hat{N} \\ Q_{\hat{N}'} &= ZQ_{\hat{N}}Z^T \end{aligned} \tag{3.34}$$

The ambiguity search can be efficiently performed in this new search space and the solution is then transformed back to the original one.

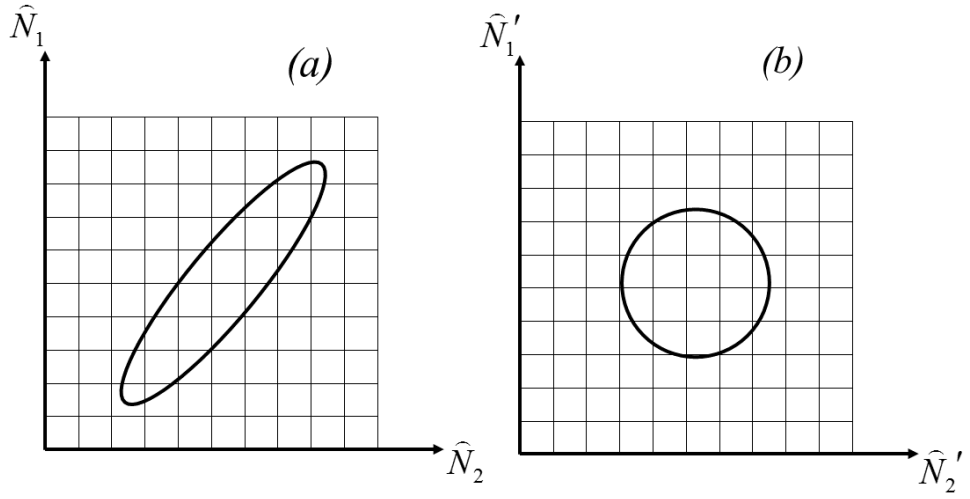


Figure 3.5 *Correlated (a) and decorrelated (b) search spaces. 2D example.*

3.3.3 Triple Carrier Ambiguity Resolution (TCAR)

Even though the LAMBDA guarantees the best ambiguity fixing success-rate, identifying the decorrelation transformation matrix Z and searching within the search space introduces a significant computational burden. In recent years, the development of the next generation GNSS satellites and the advent of multi-frequency GNSS have led to the computationally less intensive Triple Carrier Ambiguity Resolution (TCAR) or Cascade Integer Resolution (CIR) methods (Forsell et al., 1997; Jung et al., 2000; Vollath et al., 1999; Werner and Winkel, 2003). In TCAR/CIR, the so-called extra-wide lane (EWL) ambiguity (also known as super-wide lane), i.e. the ambiguity in phase combinations between two closely spaced frequencies, wide lane (WL) ambiguity, i.e. the ambiguity in phase combinations between two widely spaced frequencies, and the base

frequency or narrow-lane (NL) ambiguity are sequentially fixed using the gap-bridging concept. It means that ambiguities in carrier phase measurements of decreasing wavelength can be instantaneously fixed using base pseudorange estimates of increasing accuracy.

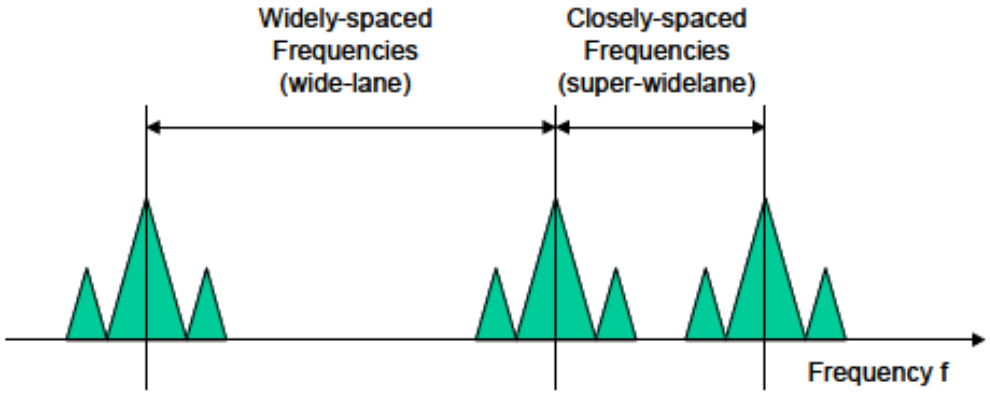


Figure 3.6 *Extra-wide lane and wide lane combinations* (Werner and Winkel, 2003).

Due to the large ionospheric delay, this method was originally designed for relative positioning over short baseline, however Geng and Bock (2013) proposed an implementation of TCAR for PPP. The following description of the TCAR method refers to GPS frequencies, but it can be easily applied to any other GNSS system broadcasting signals on more than two frequencies.

In the first step, the EWL ambiguity $N^s_{r,em}$ is fixed using the Melbourne-Wubbena combination $L^s_{r,em}$ (Melbourne, 1985; Wubbena, 1985) between L2 and L5.

$$\begin{aligned} L^s_{r,em} &= \frac{f_2 P^s_{r,2} + f_5 P^s_{r,5}}{f_2 + f_5} - \frac{f_2 L^s_{r,2} - f_5 L^s_{r,5}}{f_2 - f_5} \\ &= \lambda_{ew}\left(N^s_{r,em} + d^s_{r,em}\right) \end{aligned} \tag{3.35}$$

In Equation (3.35), $d^s_{r,em}$ represents the receiver and satellite instrumental delays within the combination. They can be mitigated using the FCB corrections estimated within a network solution. The EWL wavelength λ_{ew} is so large (about 5.86 m) that makes the instantaneous AR success rate over 99.9%.

Table 3.5 *GPS and Galileo extra-wide lane and wide lane combinations: wavelengths and noise amplifications.*

Combinations		Wavelength	Noise amplification
EWL	L2 – L5	5.86 m	33.24
	E5a – E5b	9.77 m	54.92
	E5a – E6	4.19 m	24.56
	E5b – E6	2.93 m	16.98
	E5 – E6	3.45 m	20.10
WL	L1 – L2	0.86 m	5.74
	L1 – L5	0.75 m	4.93
	E1 – E5b	0.81 m	5.39
	E1 – E6	1.01 m	6.84
	E1 – E5	0.78 m	5.15

Once the EWL ambiguity is fixed, the WL ambiguity can be solved in the second step. The IF combinations between the pseudoranges on frequencies L1 and L2 ($P^s_{r,IF}$) and between the WL and the unambiguous EWL carrier phase combinations ($L^s_{r,x}$) are used for this purpose.

$$\begin{aligned} P^s_{r,IF} &= \frac{f_1^2}{f_1^2 - f_2^2} P^s_{r,1} - \frac{f_2^2}{f_1^2 - f_2^2} P^s_{r,2} \\ L^s_{r,x} &= \frac{f_1}{f_1 - f_5} L^s_{r,w} - \frac{f_5}{f_1 - f_5}\left(L^s_{r,ew} + \lambda_{ew}\bar{N}^s_{r,ew}\right) \\ &= g^s_r - \lambda_w \frac{f_1}{f_1 - f_5}\left(N^s_{r,w} + d^s_{r,x}\right) + \varepsilon^s_{r,x} \end{aligned} \tag{3.36}$$

In Equation (3.36), $d^s_{r,x}$ denotes the hardware biases in $L^s_{r,x}$ that have to be corrected to obtain an integer ambiguity. According to Ge et al. (2008), the accuracy of the estimated WL FCBs is as small as 0.05 cycles.

Table 3.6 *GPS and Galileo AFIF combinations: wavelength and noise amplification.*

Frequencies	Amplified wavelength	Noise amplification
L1 – L2 – L5	3.40 m	109.97
E1 – E5a – E5b	3.21 m	172.29
E1 – E5a – E6	3.99 m	67.03
E1 – E5b – E6	4.32 m	97.43
E1 – E5 – E6	4.15 m	79.41

Even though the noisy $P^s_{r,IF}$ is used as base pseudorange and the noise on $L^s_{r,x}$ is roughly 110 times larger than the carrier phase error, the WL wavelength is amplified to 3.40 m. This is large enough to reliably fix the WL ambiguity to its nearest integer value in a few epochs.

In a few tens of seconds the WL ambiguity can be reliably fixed to its integer value $\bar{N}^s_{r,w}$ (Geng and Bock, 2013) and $L^s_{r,x}$ becomes unambiguous. This ambiguity fixed IF combination is also known as AFIF. $L^s_{r,x}$ can be used as base pseudorange to fix the NL ambiguity $N^s_{r,n}$ in the IF combination $L^s_{r,IF}$ between carrier phase measurements on L1 and L2. NL FCBs are required to remove the hardware biases $d^s_{r,n}$.

$$\begin{aligned} L^s_{r,IF} &= \frac{f_1^2}{f_1^2 - f_2^2} L^s_{r,1} - \frac{f_2^2}{f_1^2 - f_2^2} L^s_{r,2} + \frac{f_2^2}{f_1^2 - f_2^2} \lambda_2 \bar{N}^s_{r,w} \\ &= g^s_r - \lambda_n \left(N^s_{r,n} + d^s_{r,n} \right) + \varepsilon^s_{r,IF} \end{aligned} \tag{3.37}$$

Although $\varepsilon^s_{r,x}$ is at a few decimetres level (see **Table 3.6**), the AFIF combination represents a better option than $P^s_{r,IF}$ as base pseudorange to fix $N^s_{r,n}$. Unfortunately the NL wavelength is so small (10.7 cm) that it still requires more than one minute to achieve an AR success rate over 99.9% (Geng and Bock, 2013).

Table 3.7 *GPS and Galileo narrow lane wavelengths.*

Combinations	Wavelength
L1 – L2	10.7 cm
L1 – L5	10.89 cm
E1 – E5b	10.77 cm
E1 – E6	10.5 cm
E1 – E5	10.83 cm

3.4 Chapter summary

PPP provides decimetre to centimetre level accurate positioning solutions by processing un-differenced pseudorange and carrier phase measurements. In order to achieve such a high accuracy, it is necessary to mitigate for a wide

range of errors. This chapter describes the main error sources and provides an introduction to the most commonly used correction models. Finally, AR methods, such as integer bootstrapping, LAMBDA and TCAR, were briefly discussed.

Chapter 4

POINT software

In this research project, extensive use of the POINT software is made to process GPS and Galileo multi-frequency data in PPP mode.

The POINT software is a GNSS/INS data processing software that was originally developed in the framework of the Seamless Positioning in All Conditions and Environments (SPACE) project. This was a collaborative research project sponsored by the Engineering and Physical Science Research Council (EPSRC) between academic institutions, such as the University College of London (UCL), the Imperial College of London, the University of Leeds, and the University of Nottingham, and supported by eight industrial companies and government agencies. The aim of the project was to undertake the basic research needed to build a prototype GNSS-based positioning system that can deliver cm-level accuracy positioning everywhere and at all times (Feng and Ochieng, 2006). After the SPACE project, the software has been further developed at the Institute of Engineering Surveying and Space Geodesy (IESSG) of the University of Nottingham. Later on, POINT was adopted as basis software for the Innovative Navigation using new GNSS Signals with Hybridised Technologies (iNsight) project. This project was aimed to investigate the scientific and technical barriers of using the new GNSS signals.

Since 2008, when the iNsight project started and the POINT software was developed, many research papers, whose outcomes were based on the POINT capability, have been published. The main contributions regard integrity monitoring and tropospheric models in PPP.

In Feng et al. (2008) and Ochieng et al. (2008), a new carrier phase-based integrity monitoring algorithm, named CRAIM, for differential GNSS over short baseline was implemented in POINT. Jokinen et al. (2012) used the POINT software to monitor the integrity in PPP through ambiguity fix algorithm based on CNES products and the CRAIM developed at the Imperial College. Jokinen et al. (2013) presented the results for GPS+GLONASS float and (GPS only) fixed PPP and tested the CRAIM algorithms to exclude GPS satellites in case of failures detection.

Jokinen et al. (2013b) compared the PPP solutions obtained using the tropospheric correction based on numerical weather model from the University of Nottingham against the ones achieved with the UNB3m tropospheric model. Similarly Yang et al. (2013) evaluated the effects of the numerical weather models on the accuracy and convergence time of PPP. While, Mohammed et al. (2017) discussed different way to mitigate for the tropospheric delay in PPP. In particular, the conventional method, in which the dry tropospheric delay is modelled and the wet component is estimated in the Kalman filter, is compared with an alternative strategy, where both the dry and wet components are estimated.

The POINT software has been validated against one of the most widely used scientific GNSS processing software package available, the Bernese GNSS software developed at the Astronomical Institute of the University of Bern. Indeed, Mohammed et al. (2016) assessed the accuracy and repeatability of PPP daily solutions when processing data from GPS, GLONASS and GPS+GLONASS in comparison with Double Difference GPS daily solution computed with the Bernese GNSS software. The RMS of the differences between the weekly solution coordinate estimates from GPS PPP and Double Difference was 3.6 mm in the horizontal plane and 5.5 mm in the vertical direction.

Finally, Mohammed et al. (2018) compared the float PPP solutions obtained processing GPS, GLONASS, and GPS+GLONASS data in static mode in combination with different precise products from three ACs, namely Natural Resources Canada, ESA, and GFZ.

4.1 Software structure and capability

The POINT software is an implementation of the Extended Kalman filter (EKF) in C++ to process multi-frequency and multi-constellation GNSS data in double-difference (DD), between satellite single-difference (SD), and un-differenced (UD) modes, as well as integrated with Inertial Navigation Systems (INS). It also offers the possibility to process measurements from Ultra-Wide Band (UWB) sensors. Since this research project focuses on PPP, in this paragraph only the relevant part of the POINT source code will be described.

The software can be operated through a control file that contains the list of settings to be used during the PPP processing. These can be divided into four main groups:

1. With the *Sensors options*, users can choose the type of sensors (in this research only GNSS was considered), the GNSS constellations and the multi-frequency linear combinations. POINT has the capability to process GPS, GLONASS, Galileo, and BeiDou data, which can be linearly combined using measurements on up to three different frequencies. The type of ephemeris to be used and some common error mitigation models, e.g. relativistic effects or troposphere models, can be selected here.
2. The name and path of the observation and ephemeris files, as well as the file containing the antenna corrections, the pseudorange and phase biases, and GIM have to be included within the *Input filename options*.
3. In *PPP options*, users can select the corrections that are mainly relevant to PPP, such as solid Earth, ocean and pole tides loading, phase wind-up, and whether to perform ambiguity resolution with the LAMBDA method or having as output a float solution.
4. Options regarding the type of Kalman filter (forward only, or forward and backward to perform a smoothing process), the assumed state process noise, and the threshold to be used in the residual check are within the *Kalman filter options*.

Once the control file is completed, the POINT software can be run through the command line. A simplified description of the source code can be found in **Figure 4.1**.

In the main part of the C++ code, the control file is read, and all the options are stored in predefined classes. Depending on the settings in input, the code selects the type of sensors to be used. In case of PPP, un-differenced GNSS measurements are processed. The next step is to store the observations from the RINEX 2.11 file, the ephemeris from the SP3 and RINEX clock files or from the RINEX navigation file, the antenna correction from the ANTEX file, and other corrections in a constellation-specific measurement class. The multi-frequency measurements will, then, be linearly combined using the coefficients specified in the control file and stored in an observation array. Finally, this array

will be used as input in the Kalman Filter: first the predicted state is computed based on the latest estimate and the assumed state transition matrix; then the observed minus computed measurement vector, which is known as innovation, is formed and the design matrix is populated; finally the EKF can compute the estimated state, which is written in an output file.

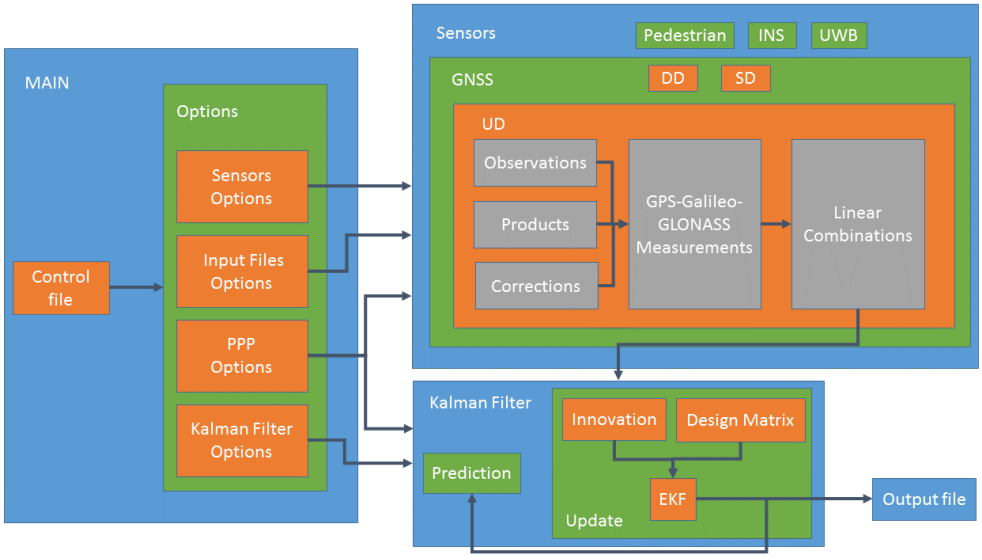


Figure 4.1 *POINT software general structure.*

POINT offers a wide range of state-of-the-art correction models to mitigate for the errors affecting GNSS pseudorange and carrier phase measurements.

4.1.1 Orbits and clocks

In PPP, the precise satellites' orbits and clocks information have to be used. These are commonly stored in files in SP3 and RINEX clock formats. POINT accepts as input these files, as well as the broadcast ephemeris included in RINEX navigation files.

4.1.2 Relativistic effects

In POINT, the largest relativistic effects, such as the effect of orbit eccentricity or Earth oblateness on satellites' clocks, are automatically applied. If users want to take into account minor effects, e.g. the Shapiro delay, they need to include the relative setting in the control file. All the relativistic effects are implemented as described in Ashby (2003).

4.1.3 Ionosphere delay

Traditionally in PPP, the first order ionosphere delay is removed by means of the IF linear combination. In POINT it is possible to perform such combinations

by specifying the appropriate coefficients that multiply the triple-frequency GNSS measurements in the control file. As an alternative, the ionosphere can be estimated in the Kalman filter. Ionosphere models based on the Klobuchar model or GIMs are also implemented. Furthermore, second and third order ionospheric delays can be included in the data processing for improved accuracies.

4.1.4 Tropospheric delay

POINT offers different ways to model the wet and dry component of the tropospheric delay and different mapping function to transform the slant delay into zenith delay. Users can choose between the Saastamoinen (Saastamoinen, 1972), GPT (Boehm et al., 2007), UNB3m (Leandro et al., 2006), and EGNOS (Penna et al., 2001) models, and between GMF (J Boehm et al., 2006), Neill (Niell, 1996), EGNOS (Penna et al., 2001), and a few other mapping functions. Although POINT allows any combination between tropospheric models and mapping functions, it is worth emphasising that some mapping functions are matched to a specific model, e.g. GMF and GPT models, and therefore they should be only used together.

The residual error has to be estimated. POINT offers the possibility to estimate only the wet zenith tropospheric residual error, both the wet and dry components, as well as the horizontal gradients as proposed in Zhang and Gao (2006).

4.1.5 Site displacements

Users have to specify in the control file whether they want to include the effects of solid Earth tides and ocean tides in their PPP processing. In POINT, the site displacements' corrections are implemented following Petit and Luzum (2010).

4.1.6 Antenna corrections

The precise orbits are computed with respect to the centre of mass (CoM) of the GNSS satellites, while the broadcast ephemeris contains information about the position of the transmitting antenna phase centre. For this reason, the PCO and PCV corrections must be considered only if the precise products are used. These antenna corrections are included in ANTEX files (Schmid et al., 2007).

The phase wind-up effect only affects the phase measurements. In POINT, this is corrected following Wu et al. (1993).

To take the antenna corrections into account, users have to include the appropriate settings in the control file.

4.1.7 Signal biases

Signal biases have to be considered only if necessary. DCBs have to be corrected for only if a user processes combinations of pseudoranges that are not consistent with the precise clocks. FCBs have to be taken into account only if ambiguity resolution is performed.

These biases are provided in specific file formats by the ACs contributing to the IGS, e.g. CODE. The name of the files have to be indicated in the control file of POINT.

4.2 Software developments in this thesis

In order to test the innovative algorithms proposed in this thesis, the POINT software has been greatly updated by the author. The major developments to the source code are summarized here:

- Implementation of the full Galileo capability. This includes the definition of the Galileo frequencies, the implementation of a class to manage the observations from the Galileo satellites, the addition of Galileo measurements in the observations vector of the Kalman filter and Least Squares estimators, and the development of the capability to read the multi-GNSS measurements from RINEX observations 2.11 file format, and corrections from SP3 (versions c and d), RINEX clocks 2.0, and ANTEX files format.
- Development of a pseudorange smoothing filter, commonly known as Hatch filter, to reduce the noise on the multi-frequency ionosphere observable.
- Implementation of the TCAR described in Section 3.3.3 to rapidly fix the EWL, WL, and NL ambiguities.
- Implementation of a method to improve the convergence time in PPP by fixing only the EWL and WL ambiguities while keeping the NL as a float value.
- Implementation of a MATLAB script to speed up and automate the processing of a large number of data. Based on predefined settings, this script writes the control file, downloads the observation data and the

precise products, runs POINT, reads the output file, computes the errors, stores the plots in a selected folder, and saves the achieved accuracy level and convergence time in an Excel file.

4.3 Chapter summary

The POINT software is the GNSS data processing tool available at the University of Nottingham. It has been widely used, tested, and validated in a large number of research projects. The papers that exploited the POINT software in their analysis are briefly reviewed.

This chapter describes the general structure of the source code and illustrates the main capability of the POINT software.

All the PPP results presented in this thesis, in particular those in Chapters 5, 7, and 8, are achieved using the POINT software following the author's improvements and modifications. The major development made during this research are also introduced in this chapter.

Chapter 5

Initial comparison between GPS and GPS+Galileo PPP

In Chapter 2, a series of papers that analysed the PPP results achieved by processing data from GPS and Galileo were reviewed and discussed. These efforts highlighted how the number of Galileo satellites and the quality of the precise products provided by MGEX influenced the GPS+Galileo PPP performance.

This chapter is aimed to assess what benefit the current Galileo constellation can offer to the PPP solution, as well as how the impact of Galileo evolved during this research. To do so, observations recorded for two periods of 10 consecutive days, at the beginning (10^{th} to 19^{th} February 2016) and towards the end (3^{rd} to 12^{th} June 2018) of the PhD study period, by 9 multi-constellation stations within the IGS global network are processed in static PPP mode. CODE MGEX products, which provide the best quality within all the ACs contributing to MGEX (F. Guo et al., 2016; Steigenberger et al., 2015), are used for this purpose. The metrics used to define the positioning performance are the errors in the north, east, and vertical component of the position local coordinates at the end of the processing and the time these errors take to converge below 10 cm. The errors are computed with respect to the double-differenced (DD) solutions computed by the IGS, and included in the Solution Independent Exchange (SINEX) files.

Furthermore, the GPS solutions computed using the CODE's products for IGS and MGEX are compared to assess the quality of MGEX data processing.

Figure 5.1 shows the stations used for this analysis. These are BOGT in Colombia, DJIG in Djibouti, KERG in the Kerguelen Islands, KIT3 in Uzbekistan, LMMF in Martinique, MIZU in Japan, NEWL in the UK, SEYG in the Republic of Seychelles, and SUTM in the Republic of South Africa. They have been selected within the IGS multi-GNSS stations according to the following criteria:

- They provided both GPS and Galileo observations.
- They had not to be included in CODE's data processing for the generation of its products for MGEX. This to avoid any correlation between observation and products error.

- They needed to be globally distributed in order to have a global outlook of the Galileo satellites visibility and geometry conditions.
- Their position had to be included in the IGS SINEX files to have a reference for the computation of the errors and convergence times.

The RINEX observation files can be downloaded from the Crustal Dynamics Data Information System (CDDIS) archive, which contains 24 hours of data, with 30 seconds sampling rate, from the global network of permanent stations supporting the IGS.



Figure 5.1 *IGS stations used to evaluate the quality of MGEX products and the GPS+GALILEO PPP performance.*

Float PPP solutions were achieved by processing these RINEX files in POINT. The GPT tropospheric model, together with the associated GMF, was used to mitigate the effect of the wet and dry tropospheric delay. The residual wet ZTD was estimated in the Kalman filter. Relativistic effects, including the Shapiro delay, phase wind-up effect and site displacement effects were also considered in the data processing. Satellite and receiver antenna PCO and PCV, stored in the ANTEX file, could be applied only when available. In particular, accurate Galileo satellites' antenna PCO/PCV were made available only after the GSA disclosed their metadata in December 2016 (Dilssner et al., 2017), while

receiving antennas corrections are still not available for Galileo, as well as for GPS L5, signals. The PPP solution obtained from the POINT software were, then, compared to the DD solutions, included in the SINEX file, which are taken as reference truth. These files can also be found in the CDDIS repository.

5.1 GPS PPP using CODE IGS and CODE MGEX products

Even though the background models and the processing standards for the CODE's MGEX solutions are adopted from CODE's rapid scheme for the IGS, some modelling deficiencies for the new GNSS systems can affect the quality of the solution (Prange et al., 2016). The PPP solutions greatly depend on the precise products that are used in the data processing. In this section, the float GPS PPP solutions achieved using the precise orbits and clocks computed by CODE for MGEX (COM) and IGS (COD) are compared. This analysis is to assess the effect of multi-GNSS on CODE's processing.

The IF combinations between GPS code pseudorange and carrier phase measurements on L1 and L2 frequencies are used.

Table 5.1 and **Table 5.2** show the RMS of the errors and convergence times over all the processed data in 2016 achieved by using the COM and COD products. Large outliers may give a distorted outline of the overall statistics, in particular the mean, which could be moved away from the actual value. For this reason, outliers have been removed from the dataset before computing the RMS using the 3-sigma rule.

Table 5.1 *Comparison between the RMS of the positioning errors achieved using COM and COD products, for the 9 considered IGS stations between 10th and 19th February 2016. Units of centimetres. In bracket is the relative difference.*

Products	East	North	Up	3D
COD	0.39	0.53	1.52	1.71
COM	1.04 (+166.7%)	0.63 (+18.7%)	1.71 (+12.5%)	2.12 (+24.0%)

Table 5.2 *Comparison between the RMS of the convergence times achieved using COM and COD products, for the 9 considered IGS stations between 10th and 19th February 2016. Units of minutes. In bracket is the relative difference.*

Products	East	North	Up	3D
COD	22.53	6.05	30.82	40.50
COM	56.31 (+149.9%)	25.07 (+314.4%)	49.64 (+61.1%)	79.12 (+95.4%)

We can see how the positioning errors obtained with COD products are slightly smaller than those achieved using the COM products. The largest difference is in the east component, where the COM error is 2.7 times larger than the COD's one, while the north and vertical errors increased by roughly 19% and 12%, respectively. Even bigger differences can be observed in the convergence times. Indeed, for COM products, the average time that float solution takes to converge at centimetre-level is up to 4.14 times larger (north component) than for COD.

J. Guo et al. (2016) already acknowledged the lower quality of MGEX GPS products compared to those submitted to the IGS. Besides the possible mismodelling in the multi-constellation processing, there is one other factor that impact on the poorer performance of the COM products: the interpolation of the precise clocks. Since the COM products are disseminated with a 5 minutes sampling rate, they need to be interpolated to match the observation rate of 30 seconds. It is well known that the interpolation of the precise clocks introduce further errors that affect the PPP solution (Montenbruck et al., 2005; Zumberge and Gendt, 2001).

For this reason, since 13th July 2017 (GPS week 1962) CODE started providing a 30 seconds clock solution to MGEX (Villiger and Dach, 2017). These high-rate clock products were used in the second part of the analysis to study how the models used in the CODE's multi-constellation processing improved with time and what are the effects of this improved solution in GPS float PPP. **Table 5.3** and

Table 5.4 show the RMS of the errors and convergence times over all the processed data in 2018 achieved by using the COM and COD products, after the outliers have been removed. Differently from the results previously shown, in 2018 the PPP performance achieved using the COM products are much closer to those with COD products.

Table 5.3 *Comparison between the RMS of the positioning errors achieved using COM and COD products, for the 9 considered IGS stations between 3rd and 12th June 2018. Units of centimetres. In bracket is the relative difference.*

Products	East	North	Up	3D
COD	0.54	0.57	1.69	1.81
COM	0.61 (+13.0%)	0.66 (+15.8%)	1.81 (+7.1%)	2.03 (+12.2%)

Table 5.4 *Comparison between the RMS of the convergence times achieved using COM and COD products, for the 9 considered IGS stations between 3rd and 12th June 2018. Units of minutes. In bracket is the relative difference.*

Products	East	North	Up	3D
COD	36.56	15.83	54.52	61.55
COM	35.96 (-1.6%)	15.11 (-4.5%)	54.89 (-0.1%)	63.17 (+2.6%)

The effect of having high-rate clocks in COM products can be seen in a dramatic reduction of the convergence time, now at the same level of the COD's one. Slight differences are still visible in the RMS of the errors at the end of the 24 hour long data processing, but much smaller than those visible in **Table 5.1**. Indeed, the difference between the COD and COM errors in **Table 5.3** is no larger than 16% for the north component, while the same component had an error with COM products more than 4 times larger than the one with COD.

These results show that since MGEX started, the quality of the GPS orbits and clocks have constantly improved, getting closer to the precise products for the official IGS.

5.2 GPS and GPS+Galileo PPP in 2016

In this section, the GPS and GPS+Galileo static PPP solutions from the multi-constellation data, recorded by the 9 stations in **Figure 5.1** between the 10th and 19th February 2016 and stored in RINEX observation files with a sampling rate of one measurement every 30 seconds, are compared.

Table 5.5 summarizes the models included in the float PPP processing. The IF combinations between GPS measurements on L1 and L2 frequencies and between Galileo observables on E1 and E5a are used to remove the first order ionosphere delay. This data processing includes all the mitigation models commonly used in PPP, as described in Chapter 3. The CODE's products for MGEX, COM, are adopted. The multi-constellation precise clocks are based on the same system time (Steigenberger et al., 2015), therefore it is unnecessary to estimate the GPS-Galileo Time Offset (GGTO). However, as it was also pointed in Afifi and El-Rabbany (2014), it is advisable to include possible existing inter-system biases, that may affect the GNSS measurements, as a further unknown in the state vector.

Table 5.5 *Model included in the PPP data processing.*

Error source		Model	Note
Satellite	Position	COM precise orbits	Included in SP3 files and sampled every 15 minutes. Interpolation needed
	Clock offset	COM precise clocks	Included in RINEX CLK files and sampled every 5 minutes. Interpolation needed.
	Relativistic effects	Ashby (2003)	The largest delays due to orbit eccentricity and Sagnac effect, as well as the smaller Shapiro delay and the J_2 effect, are considered.
	Antenna phase centre offset	ANTEX file igs08_1882.atx	Galileo satellites' antenna PCO are those proposed in Rizos et al. (2013). No PCV are applied.
	Phase wind-up	Wu et al., (1993)	
Atmosphere	Troposphere	GPT and GMF	Wet ZTD estimated in the EKF.
	Ionosphere	IF combination	L1-L2 for GPS and E1-E5a for Galileo
Site displacement	Solid Earth tides	Petit and Luzum (2010)	
	Ocean tides	Petit and Luzum (2010)	Site dependent amplitudes and phase are provided by the ocean loading service.
	Pole tides	Petit and Luzum (2010)	
Receiver	Antenna phase centre offset	ANTEX file igs08_1882.atx	Not applied for GPS+Galileo.
	Inter-system bias		Lumped in the estimation of the GGTO.

For the troposphere, the GPT model and the GMF were used to mitigate for the dry tropospheric delay, while the wet ZTD is estimated in the Kalman filter.

The antenna corrections, included in the ANTEX file, require particular care. The *igs08_1882.atx* file, which is the ANTEX file used here, includes the Galileo satellites' antenna PCO proposed by Rizos et al. (2013) for MGEX which are up to a few decimetres different from those published later by the European GNSS Agency (2017b). The receivers' antenna PCO for Galileo signals are not included in the ANTEX file. For this reason, these corrections could not be applied in the GPS+Galileo PPP processing. As a consequence, further errors of a few centimetres were expected in the GPS+Galileo PPP solution.

In open sky conditions, the expected benefit from having a second constellation is mainly in the convergence time, but the accuracy was also expected to be improved to some extent. Unfortunately, there are some factors that can impact on the GPS+Galileo positioning such as the number of Galileo satellites and the quality of the products provided by the ACs contributing to MGEX.

In February 2016, only 7 Galileo satellites, out of 12 orbiting around the Earth, were usable for positioning purposes. It is possible to see from **Table 5.6** that average number of Galileo satellites visible by each of the considered stations is always smaller than 3. In some instances, even 5 satellites, which is the minimum number to compute a PPP solution, are visible simultaneously by a single receiver, but for no more than 14 minutes. Considering that the typical convergence time is between 20 and 60 minutes, it is impossible to have a Galileo PPP solution at cm-level of accuracy in these conditions.

Given that in open areas the GPS constellation already provides excellent visibility and geometry conditions, it was already expected to have very little improvements in the PDOP from introducing Galileo for positioning. Indeed, maximum 7.5% of reduction in the average PDOP was observed for station SEYG.

Table 5.7 compares the RMS of the errors in the north, east, up components, as well as the RMS of the 3D error, achieved with GPS only to those obtained using GPS+Galileo, for each of the considered stations. Generally, the multi-constellation solution offers poorer performance than the single-constellation case. Indeed, the 3D error for GPS+Galileo can be up to almost 6 times larger than the GPS one for station LMMF, which is the third station with the highest number of visible Galileo satellites on average (after SEYG and DJIG). For this

station, while the horizontal errors for GPS and GPS+Galileo are very close to each other, the vertical error differs by 7 cm. This difference can be explained by the fact that the GPS L1 PCO for the TRM57971.00 antenna (which is the one installed in LMMF) is 6.8 cm in the vertical direction.

Table 5.6 *Galileo satellites availability and geometry for the 9 IGS stations. From left to right: average number of Galileo satellites in view, longest time period in which there are more than 5 available Galileo satellites, average PDOP for GPS and GPS+Galileo cases over 10 days in 2016.*

Station	Average number of available Galileo satellites	Minutes with at least 5 Galileo satellites in view	Average PDOP – GPS	Average PDOP – GPS+Galileo
BOGT	1.57	14	2.03	1.95
DJIG	2.23	0	1.88	1.75
KERG	2.11	0	1.87	1.74
KIT3	1.91	3	2.01	1.91
LMMF	2.18	0	1.93	1.80
MIZU	2.00	0	1.89	1.78
NEWL	2.05	14.5	1.89	1.77
SEYG	2.27	0	1.86	1.72
SUTM	2.01	0	1.94	1.82

KERG is the only one station where the GPS+Galileo solution has smaller errors than the GPS only solution, even though its antenna, the ASH701945E_M type SNOW, has a PCO for GPS L1 of about 9 cm vertically. The differences in the east, north and up errors are 5 mm, 2 mm, and 1 mm, respectively. Hence, it is difficult to understand how much of the error is related to not having applied the receiver's antenna PCO and how much is related to other factors, such as the quality of the precise products and the small number of visible satellites for Galileo.

The biggest benefit of two-constellation in PPP is in the convergence time, which is supposed to be reduced by more than a half once Galileo will reach its fully operational capability (Shen and Gao, 2006). In this research, the convergence time is defined as the time required to have an error of less than 10 cm.

Table 5.7 *Comparison between the RMS of the GPS(G) and GPS+Galileo (GE) PPP errors, for the 9 considered IGS stations between 10th and 19th February 2016. Units of centimeters. In bracket is the relative difference.*

Station	Constellation	East	North	Up	3D
BOGT	G	0.72	0.53	2.07	2.26
	GE	0.70 (-2.8%)	0.64 (+20.8%)	2.79 (+34.8%)	2.95 (+30.5%)
DJIG	G	1.08	0.34	2.22	2.49
	GE	1.09 (+0.1%)	0.25 (-26.5%)	3.13 (+41.0%)	3.32 (+33.3%)
KERG	G	1.51	0.78	2.42	2.96
	GE	1.02 (-32.4%)	0.58 (-25.6%)	2.33 (-3.7%)	2.61 (-11.8%)
KIT3	G	0.80	0.23	0.81	1.16
	GE	0.48 (-40%)	0.91 (+295.7%)	2.99 (+269.1%)	3.16 (+172.4%)
LMMF	G	0.43	0.47	1.26	1.41
	GE	0.73 (+69.8%)	0.52 (+10.6%)	8.20 (+550.8%)	8.23 (+483.7%)
MIZU	G	0.27	0.55	1.46	1.58
	GE	0.95 (+251.9%)	0.46 (-16.4%)	2.43 (66.4%)	2.65 (+67.7%)
NEWL	G	1.09	0.72	0.80	1.53
	GE	1.02 (-6.4%)	0.61 (-15.3%)	7.91 (+888.7%)	8.00 (+422.9%)
SEYG	G	1.63	0.52	2.10	2.71
	GE	1.73 (+6.1%)	0.39 (-25%)	2.88 (+37.1%)	3.38 (+24.7%)
SUTM	G	1.64	1.03	2.01	2.79
	GE	1.36 (-17.1%)	1.92 (+86.4%)	2.22 (+10.4%)	3.24 (+16.1%)

Table 5.8 is a comparison between the convergence times for the east, north, and up components, as well as for the 3D position, in GPS and GPS+Galileo PPP. In many cases, the convergence time offered by the multi-constellation PPP processing for the horizontal components is slightly shorter than the one achieved with GPS PPP. For example, in SEYG the convergence time was reduced by 12.5 minutes in the east component and by 1 minute in the north component. The vertical convergence time, instead, is always, or almost, worse for GPS+Galileo. The only exceptions are for DJIG and KERG, which see an improvement in the vertical convergence time of roughly 24 and 3 minutes, respectively. Not having applied the receiver antennas' corrections in the

GPS+Galileo data processing can be one of the reasons why its vertical convergence is often slower than the GPS only vertical convergence.

Table 5.8 *Comparison between the RMS of the GPS (G) and GPS+Galileo (GE) PPP convergence times, for the 9 considered IGS stations between 10th and 19th February 2016. Units of minutes. In bracket is the relative difference.*

Station	Constellation	East	North	Up	3D
BOGT	G	120.38	25.41	54.44	136.09
	GE	115.54 (-4.0%)	23.86 (-6.1%)	74.73 (-37.3)	135.02 (-0.8%)
DJIG	G	51.23	22.51	57.35	71.49
	GE	45.47 (-11.2%)	19.92 (-11.5%)	33.28 (-41.9%)	52.44 (-26.6%)
KERG	G	84.99	20.36	56.40	101.89
	GE	76.46 (-10.0%)	20.39 (-0.1%)	52.12 (-7.6%)	85.19 (-16.4%)
KIT3	G	41.29	23.37	55.03	72.33
	GE	56.95 (+37.9%)	26.34 (+12.7%)	55.39 (+0.1%)	77.02 (+6.5%)
LMMF	G	148.12	38.93	109.73	166.45
	GE	149.04 (+0.6%)	29.77 (-23.5%)	642.39 (+485.4%)	748.81 (+349.9%)
MIZU	G	53.05	26.91	45.63	71.23
	GE	47.93 (-9.7%)	28.63 (+6.4%)	57.06 (+25.0%)	70.79 (-0.6%)
NEWL	G	54.17	40.90	53.09	72.35
	GE	49.42 (-8.8%)	31.10 (-24.0%)	63.83 (+20.2%)	104.13 (+43.9%)
SEYG	G	64.12	24.54	54.60	69.56
	GE	51.61 (-19.5%)	23.51 (4.2%)	67.14 (+23.0%)	75.29 (+8.3%)
SUTM	G	58.21	18.76	50.78	146.85
	GE	76.08 (+30.7%)	18.60 (-0.9%)	91.67 (+80.5%)	111.46 (-24.1%)

To summarize, for most of the stations considered in this analysis, a degradation of the PPP performance, both in terms of final accuracy and convergence time, was observed when using GPS+Galileo in PPP. Kazmierski et al. (2017) and Wang et al. (2018) addressed this problem to the small number of Galileo satellites in view and to the lower quality of the precise orbits and clocks. However, the uncertainties in the receivers' and satellites' antenna PCO for Galileo signals also have to be included within the causes of the reduction in the PPP performances.

5.3 GPS, Galileo, and GPS+Galileo PPP in 2018

In this section, the multi-constellation data, recorded by the 9 stations in **Figure 5.1** between the 3rd and 12th June 2018, are processed in static PPP mode and the results are compared to evaluate how the Galileo constellation and products status evolved during this research project.

Table 5.9 summarizes the models included in the PPP processing. The main differences with respect to the processing of the 2016 data set are in some of the products adopted. In particular, the COM precise clocks, stored in the RINEX CLK file, are sampled every 30 seconds starting at midnight of each day. It means that when processing the multi-GNSS measurements from the stations within the IGS network, which are disseminated with the same data, the interpolation of the precise clocks is no longer necessary, thus removing the interpolation error. Finally, accurate Galileo satellites' antenna PCO/PCVs corrections are included in the ANTEX files since GPS week 1972 for the IOV satellites and since GPS week 1986 for the FOC satellites.

On the 17th November 2016, for the first time 4 Galileo satellites (GSAT0207, GSAT0212, GSAT0213, and GSAT0214) were simultaneously launched with the Ariane 5 ES rocket. Since then, the number of Galileo satellites in orbits have greatly increased. In June 2017, 14 Galileo satellites, out of 22 orbiting around the Earth, were usable for positioning purposes. The result of a higher number of Galileo satellites orbiting around the Earth is visible in **Table 5.10**. The average number of Galileo satellites visible by a single station is in most cases close to 4 and, as a consequence, the time in which at least 5 Galileo satellites are simultaneously in view is considerably longer than in 2016. In SEYG, for example, 5 or more Galileo satellites are visible for almost 14 hours, making it possible to have a converged Galileo PPP solution.

The geometry conditions are also improved. The biggest reduction in the average PDOP with respect to using GPS only is in BOGT, where the PDOP was improved by roughly 21%.

In **Table 5.11** are the RMS of the errors for each of the 9 considered stations. KERG is still the only station where processing Galileo data together with GPS measurements improve the positioning solution. In all the other cases, possible mismodelling, in particular in the receiver's antenna PCOs and in the precise

Table 5.9 *Model included in the PPP data processing.*

Error source		Model	Note
Satellite	Position	COM precise orbits	Included in SP3 files and sampled every 15 minutes. Interpolation needed
	Clock offset	COM precise clocks	Included in RINEX CLK files and sampled every 30 seconds. Interpolation not needed.
	Relativistic effects	Ashby (2003)	The largest delays due to orbit eccentricity and Sagnac effect, as well as the smaller Shapiro delay and the J_2 effect, are considered.
	Antenna phase centre offset	ANTEX file igs14_2000.atx	Galileo satellites' antenna PCO and PCVs are those included in European GNSS Agency (2017b). No PCV are applied.
	Phase wind-up	Wu et al. (1993)	
Atmosphere	Troposphere	GPT and GMF	Wet ZTD estimated in the EKF.
	Ionosphere	IF combination	L1-L2 for GPS and E1-E5a for Galileo
Site displacement	Solid Earth tides	Petit and Luzum (2010)	
	Ocean tides	Petit and Luzum (2010)	Site dependent amplitudes and phase are provided by the ocean loading service.
	Pole tides	Petit and Luzum (2010)	
Receiver	Antenna phase centre offset	ANTEX file igs14_2000.atx	Not applied for GPS+Galileo.
	Inter-system bias		Lumped in the estimation of the GPS-Galileo Time Offset.

orbits and clocks, prevent from having more accurate solutions from GPS+Galileo.

The same mismodelling also affect the convergence times, which are summarized in **Table 5.12**. In only 5 cases out of 9 (DJIG, KERG, KIT3, MIZU, SUTM), the RMS of the 3D convergence time for GPS+Galileo PPP is shorter than GPS PPP. The best improvement is for SUTM, where the convergence time is reduced from about 95 minutes to approximately 20 minutes. Within those 5 stations, the vertical convergence is the one that is mostly affected by having two constellations, while in most cases the horizontal convergence is comparable to the one achieved with GPS only. In contrast, the east and north convergence time for NEWL pass from 154 and 71 minutes for GPS only to 29 and 10 minutes for GPS+Galileo, while the vertical convergence goes from 66 to 195 minutes. In case of KERG, despite the horizontal convergence times for GPS+Galileo are at the same level as for GPS only, and the vertical convergence is about 7 minutes slower, the 3D convergence for GPS+Galileo is still quicker that the one for GPS.

Table 5.10 *Galileo satellites availability and geometry for the 9 IGS stations. From left to right: average number of Galileo satellites in view, longest time period in which there are more than 5 available Galileo satellites, average PDOP for GPS and GPS+Galileo cases over 10 days in 2016.*

Station	Average number of available Galileo satellites	Minutes with at least 5 Galileo satellites in view	Average PDOP – GPS	Average PDOP – GPS+Galileo
BOGT	3.98	412.5	2.12	1.68
DJIG	4.14	471.5	1.80	1.49
KERG	3.78	276	1.86	1.53
KIT3	3.42	160	2.16	1.80
LMMF	4.05	474.5	1.86	1.53
MIZU	1.84	0	1.93	1.80
NEWL	3.82	269	1.95	1.58
SEYG	4.23	812	1.82	1.51
SUTM	3.75	322	1.92	1.59

The data recorded by station SEYG between the 7th and the 8th June 2018, corresponding to the 14 hours period when 5 or more Galileo satellites were visible (see **Table 5.10**), have been used to assess the PPP results from Galileo

only, in comparison with GPS only, and GPS+Galileo. The top plot in **Figure 5.4** shows the time series of the DOPs for this particular dataset. Despite being in open sky conditions, the VDOP is quite large, reaching a maximum value of 6.63. On the other hand, the HDOP is almost always less than two. This large VDOP can be seen as a consequence of the low number of Galileo satellites in orbit. For comparison, the middle and bottom plots in **Figure 5.4** show the DOPs for GPS and GPS+Galileo, respectively. In the case of GPS, the VDOP, with a maximum value of 2.56, is on average 1.82 times smaller than the one obtained

Table 5.11 *Comparison between the RMS of the GPS(G) and GPS+Galileo (GE) PPP errors, for the 9 considered IGS stations between 3rd and 12th June 2018. Units of centimetres. In bracket is the relative difference.*

Station	Constellation	East	North	Up	3D
BOGT	G	0.40	0.24	2.15	2.20
	GE	0.36 (-10%)	0.20 (-16.7%)	2.27 (+5.6%)	2.31 (+5.0%)
DJIG	G	0.90	0.57	2.21	2.46
	GE	0.87 (-3.3%)	0.78 (+36.8%)	3.70 (+67.4%)	3.88 (+57.7%)
KERG	G	0.66	0.54	3.05	3.17
	GE	0.61 (-7.6%)	0.34 (-37.0%)	1.74 (-43.0%)	1.87 (-41.0%)
KIT3	G	0.30	1.08	0.91	1.44
	GE	1.28 (+326.7%)	0.38 (-64.8%)	3.00 (+229.7%)	3.29 (+128.5%)
LMMF	G	0.67	0.32	0.88	1.16
	GE	0.99 (+47.8%)	0.30 (-6.2%)	7.19 (+717.0%)	7.27 (+526.7%)
MIZU	G	0.41	0.47	1.64	1.75
	GE	1.33 (+224.4%)	0.62 (+31.9%)	2.76 (+68.3%)	3.12 (+78.3%)
NEWL	G	1.03	0.86	1.78	2.22
	GE	0.71 (-31.1%)	0.47 (-45.3%)	7.58 (+325.8%)	7.63 (+243.7%)
SEYG	G	0.78	0.76	2.02	2.29
	GE	0.63 (-19.2%)	0.92 (+21.1%)	3.74 (+85.1%)	3.91 (+70.7%)
SUTM	G	0.62	0.78	1.21	1.57
	GE	1.25 (+101.6%)	1.86 (+138.5%)	3.14 (+159.5%)	3.85 (+145.2%)

Table 5.12 *Comparison between the RMS of the GPS (G) and GPS+Galileo (GE) PPP convergence times, for the 9 considered IGS stations between 3rd and 12th June 2018. Units of minutes. In bracket is the relative difference*

Station	Constellation	East	North	Up	3D
BOGT	G	80.34	6.80	107.56	116.39
	GE	77.17 (-3.9%)	7.06 (+3.8%)	108.60 (+1.0%)	118.41 (+1.7%)
DJIG	G	101.20	27.69	195.19	208.26
	GE	37.63 (-62.8%)	18.26 (-34.1%)	115.40 (-40.9%)	126.70 (-39.2%)
KERG	G	32.75	20.41	35.19	68.21
	GE	31.83 (-2.8%)	21.13 (+3.5%)	42.74 (+21.4%)	49.56 (-27.3%)
KIT3	G	93.42	35.45	99.43	113.80
	GE	91.58 (-2.0%)	26.88 (-24.2%)	73.09 (-26.5%)	101.87 (-10.5%)
LMMF	G	27.89	18.85	25.52	40.81
	GE	93.40 (+234.9%)	12.65 (-32.9%)	73.80 (+189.2%)	128.07 (+213.8%)
MIZU	G	19.77	5.27	68.98	77.14
	GE	18.34 (-7.2%)	9.66 (+83.3%)	31.61 (-54.2%)	38.65 (-49.9%)
NEWL	G	154.10	70.79	66.12	173.53
	GE	28.59 (-81.4%)	9.68 (-86.3%)	194.81 (+194.6%)	244.48 (-40.9%)
SEYG	G	44.75	7.13	32.70	100.52
	GE	24.34 (-45.6%)	8.02 (+12.5%)	123.57 (+277.9%)	127.81 (+27.1%)
SUTM	G	18.93	11.53	20.33	94.75
	GE	17.64 (-6.8%)	11.02 (-4.4%)	15.31 (-24.7%)	20.53 (-78.3%)

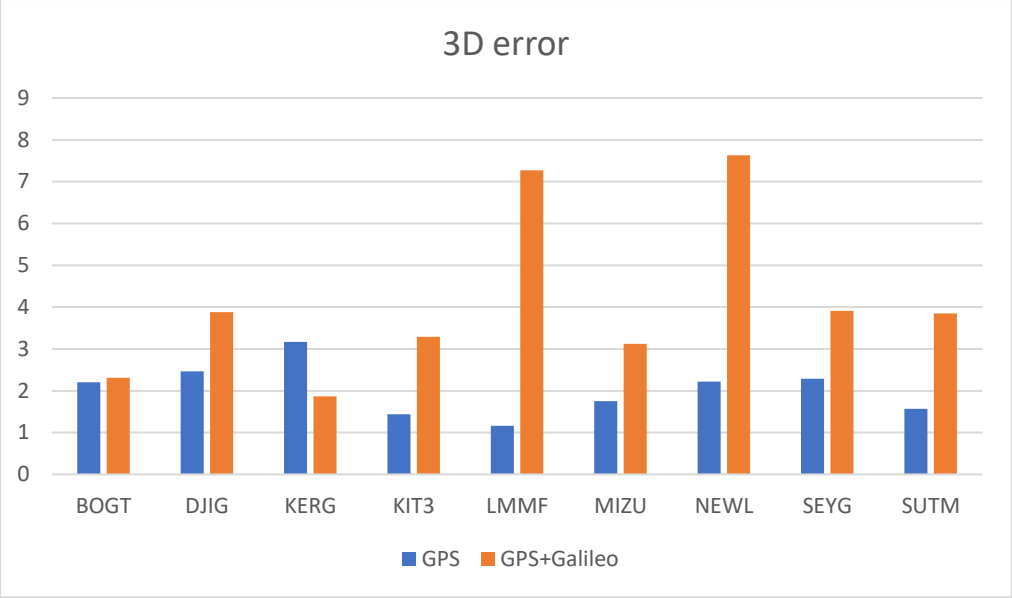


Figure 5.2 *Comparison between the RMS of the GPS and GPS+Galileo PPP 3D errors, for the 9 considered IGS stations between 3rd and 12th June 2018. Units of centimetres.*

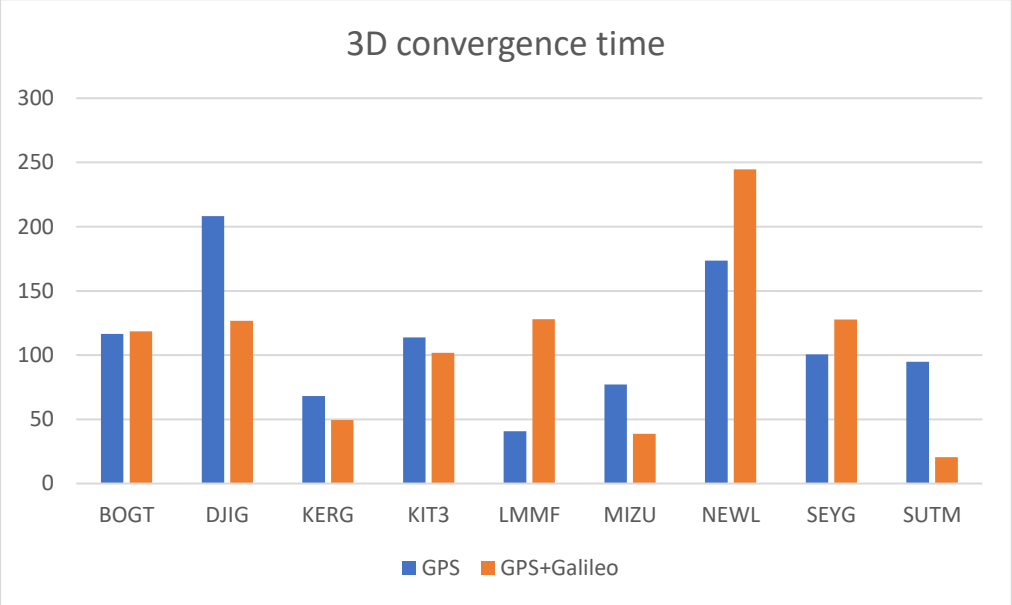


Figure 5.3 *Comparison between the RMS of the GPS and GPS+Galileo PPP 3D convergence times, for the 9 considered IGS stations between 3rd and 12th June 2018. Units of minutes.*

by considering only the Galileo satellites. Given the open sky conditions and the relatively poor geometry offered by the Galileo satellites, considering both constellations doesn't offer a big improvement with respect to the GPS single constellation case. Indeed, the average VDOP is reduced from 1.62 to 1.31, while the average HDOP reduces from 0.88 to 0.68. The errors in the PPP solutions for the three cases (Galileo, GPS, and GPS+Galileo) are shown in **Figure 5.5**. The positioning errors are always smaller than 10 cm, even for

Galileo only. In this case, the PPP solution reaches a precision of 3.12 cm in the north, 2.00 cm in the east, and 4.54 cm in the up components at the end of the processing of the 812 minutes long data set. The convergence time for the north, east, and vertical errors to go below 10 cm are 13.5, 151, and 70 minutes, respectively. Despite Galileo satellites broadcast signals of higher quality (Angrisano et al., 2013; Cai et al., 2014; Richardson et al., 2016; Simsky et al., 2008), the better geometry conditions and quality of PPP products for GPS lead to improved positioning performance, both in terms of precision and convergence time. As a matter of fact, the north, east, and up errors are as small as 0.15 cm, 1.10 cm, and 1.45 cm, while the convergence times are 1.5, 22, and 8 minutes. With the receiver being in open sky conditions, one would not expect to have great advantages from using two constellations, in terms of positioning accuracy. However, a reduction in the time the PPP solution takes to reach a precision of better than 10 cm would be expected to be apparent. Unfortunately, longer convergence times were observed. The north convergence for GPS+Galileo was 8 minutes, while it takes 22.5 and 10 minutes to have a centimetre-level error in the east and vertical direction. Apart from the poorer quality of the Galileo products, not applying the receiver antenna corrections also have a negative impact on the PPP solution.

It is clear from these results, that the Galileo system and its PPP products are still not mature for a clear evaluation of the potential impact of Galileo signals in single and multi-constellation PPP. Despite having 14 Galileo satellites usable for positioning, the results presented in this section still do not match the expected outcome from GPS+Galileo PPP as was forecast by previous studies based on simulated data.

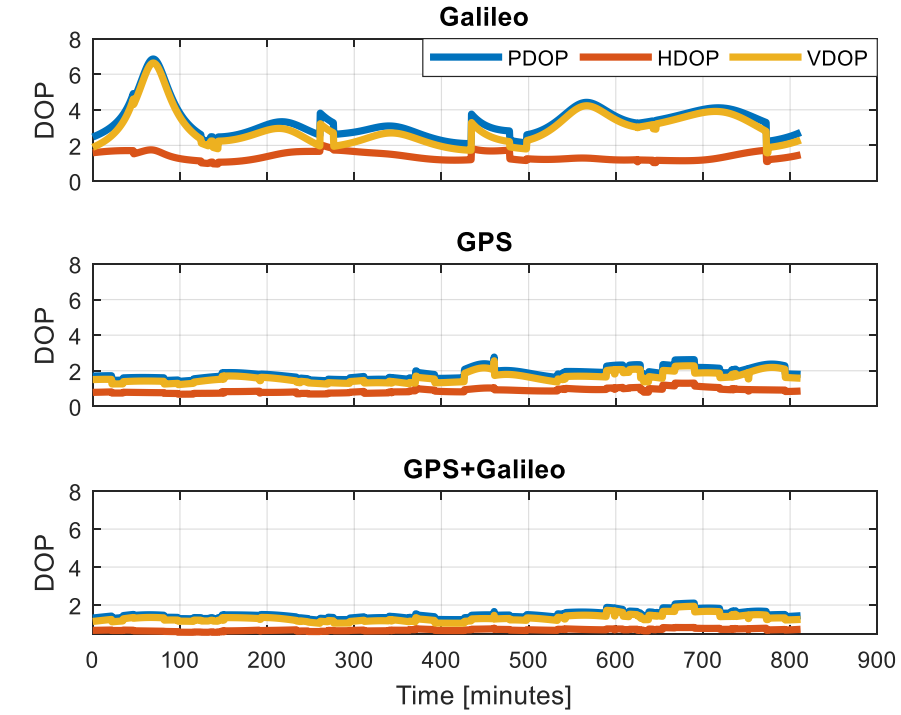


Figure 5.4 *PDOP, HDOP, and VDOP time series. Galileo only (top), GPS only (middle), and GPS+Galileo (bottom) PPP processing of the data recorded by station SEYG between the 7th June 2018 at 22:51:30 and the 8th June 2018 at 12:24:00.*

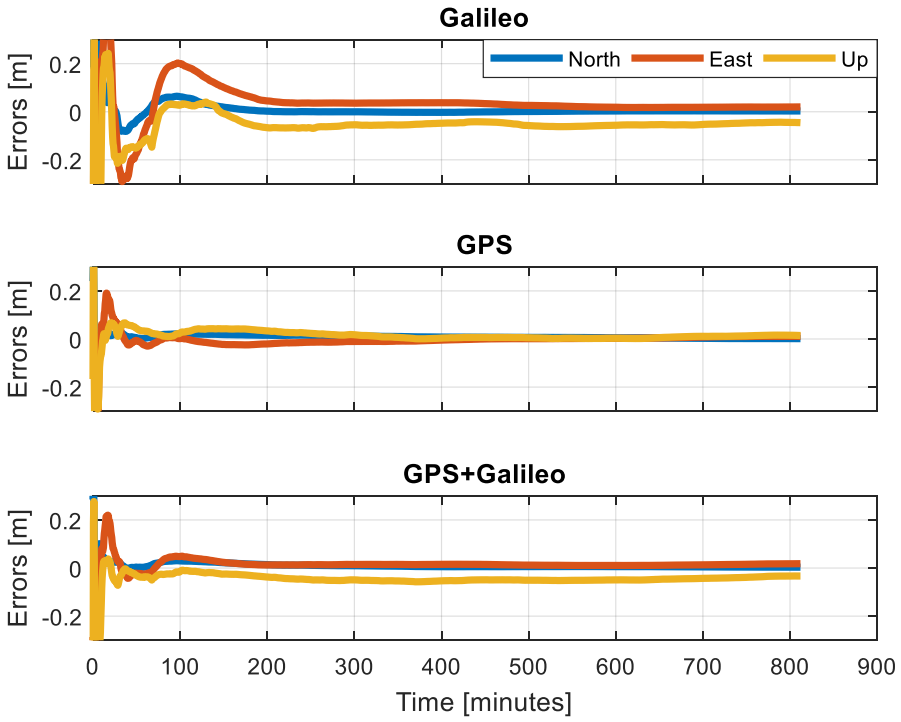


Figure 5.5 *Positioning errors in the north, east and up components. Galileo only (top), GPS only (middle), and GPS+Galileo (bottom) PPP processing of the data recorded by station SEYG between the 7th June 2018 at 22:51:30 and the 8th June 2018 at 12:24:00.*

5.4 Chapter summary

In the last couple of years, the number of Galileo satellites orbiting around the Earth has consistently increased, enabling Galileo based, as well as GPS+Galileo, positioning. At the same time, the ACs contributing to MGEX are providing precise Galileo products to the PPP community. In this chapter, the PPP solutions computed using CODE's products for MGEX and IGS are compared to assess the quality of CODE's multi-constellation processing with respect to the traditional GPS only processing. The results from 2016 showed noticeable differences in the positioning performance using COM and COD products, in particular in the convergence time. The gap between the convergence times with COM and COD products has been reduced when CODE changed the data-rate of the COM clocks to 30 seconds. Small differences between the two products are still visible in the positioning errors. It can be interpreted as a sign of some mismodelling in the multi-constellation data processing that affect the quality of the GPS products.

The GPS only PPP solutions using COM products were also compared to the GPS+Galileo solutions. Even though one would expect better performance in the two-constellation case, the low number of Galileo satellites in view, the poorer quality of the precise orbits and clocks, and the lack of accurate antenna corrections for Galileo, makes the GPS+Galileo PPP solution worse than the GPS only solution.

A Galileo only float PPP solution was also computed using the data recorded by SEYG between the 7th and 8th June 2018, when 5 Galileo satellites were visible at the same time for about 14 hours. Centimetre-level positioning is available by processing the Galileo measurements. However, despite Galileo broadcast better signals than GPS, the final accuracy and convergence time of the GPS PPP solution is much better than the Galileo one. This was attributed to the small number of visible satellites and the poor quality of the Galileo products available.

It can be concluded that the GPS only processing has still to be considered the favourite data processing standard in PPP, at least until more satellites and more accurate products will be available for Galileo.

Chapter 6

Multi-frequency GPS/Galileo simulator

Part of this chapter has been published in Basile et al. (2019) and Basile et al. (2017).

In this research the performance of GPS, Galileo, and GPS+Galileo PPP are analysed through a multi-frequency GPS/Galileo Simulink tool. This simulator provides GNSS measurements from the GPS system and the future completed Galileo constellation, as well as precise products whose quality is comparable to the real-time products distributed by the IGS RTS.

6.1 Reasons for using simulated data

The reasons why, in this research, simulated data were adopted are mainly related to the small number of satellites in orbit, broadcasting multi-frequency GPS and Galileo signals, and to the availability and quality of precise products for the next generation GNSS signals. In this section, details of these motivations will be provided.

- At the date of writing (November 2018), 18 Galileo satellites are usable for positioning purposes (European GNSS Agency, 2018), however, at the beginning of the research study period in 2016, only 7 of them were available. The low availability of Galileo satellites is one of the main limiting factors for this research. In Chapter 5, the satellite visibility from a number of stations within the IGS network was evaluated. The results showed how no more than 5 satellites were simultaneously visible by a single receiver. And this number of visible satellites occurred for stations BOGT and NEWL for less than 15 minutes. Given the long convergence time in PPP, it was, therefore, not only impossible to study the Galileo PPP performance, but also the benefit of Galileo in multi-constellation positioning were very marginal. In an urban environment, this problem would be further amplified by the high elevation mask provided by the buildings. In a similar manner, the number of GPS Block IIF satellites, broadcasting modernized GNSS signals over the three frequencies L1, L2, and L5, is a limiting factor for this research. On the 5th February 2016, the twelfth GPS Block IIF satellite, PRN 32, was launched from Cape Canaveral and it became

operational on the 9th March 2016 (Navigation Center, 2016). While the launch of the first GPS block IIIA satellite is scheduled for December 2018.

- One of the aims of this research is to analyse the performance of multi-frequency PPP. To do so, new triple-frequency IF combinations are proposed to be processed. When using IF combinations that are not consistent with the precise clocks, which are based on L1-L2 IF for GPS and E1-E5a IF for Galileo, the DCBs corrections need to be considered in the data processing. Currently, two ACs are providing the DCBs for multi-constellation GNSS signals: the Chinese Academy of Science (CAS) in Wuhan and the Deutsche Forschungsanstalt für Luftund Raumfahrt (DLR) in Germany. Unfortunately, the DCBs for every signal were made available only after the second quarter of 2017.
- In PPP, the FCB corrections are necessary to restore the integer nature of the carrier phase ambiguities. Even though these corrections are not necessary to compute a float solution, the FCBs are still required to improve the convergence time following the approach presented in this thesis. Unfortunately, multi-constellation FCBs corrections are still not available to the public.
- Unlike the broadcast ephemeris, the precise orbits published by IGS describe the position of the centre of mass of the satellites. For this reason, in PPP antenna PCO/PCV corrections included in ANTEX files have to be applied. Accurate Galileo satellites' antenna corrections were only made available after the GSA published the satellite metadata on the 16th December 2016 (Villiger and Dach, 2016), and were included in the ANTEX files since GPS week 1972 for the IOV satellites and since GPS week 1986 for the FOC satellites. Currently, no satellites' nor receivers' antenna corrections are available for GPS L5 signals, as well as receivers' antenna corrections for Galileo signals.
- Given the proposed applications for this research project (ground navigation in urban areas), real-time orbits and clocks should be employed. The IGS RTS only provides real-time corrections to the broadcast ephemeris for GPS and, in an experimental stage, GLONASS.

Galileo real-time products are computed by one of the contributing AC to MGEX, CNES. However, the quality of these products is from 3 to 7 times worse than the corresponding GPS products (Kazmierski et al., 2018).

Given these technical limitations brought by the current status of the next-generation GNSS constellations, it is advisable to evaluate the future fully operational performance of Galileo and GPS+Galileo PPP, in comparison with GPS PPP, through simulated data.

Many commercial GNSS simulators exist. Although, the University of Nottingham has available a Spirent GS8000, in this study, a Simulink model was adopted to simulate the GNSS measurements. The reason behind this choice was to be free from the capability of a specific receiver, and to be able to simulate pseudorange and carrier phase measurements on any frequency.

6.2 Description of the triple-frequency GPS/Galileo Simulink

The original version of the GPS/Galileo Simulink model was developed by the engineers at the Rockwell Collins US (now rebranded Collins Aerospace) for their internal feasibility studies. Initially, the model simulated only GPS measurements on L1 and L2 frequencies. Later, the Simulink tool was partially updated by including the constellation of Galileo satellites broadcasting signals on the same L1 and L2 frequencies as the GPS satellites. In order to correctly simulate GPS and Galileo multi-frequency measurements, the GPS/Galileo Simulink model has been greatly updated by the author. The major developments to the simulator are summarized here:

- Definition of the correct frequencies for Galileo.
- Implementation of the capability to output pseudorange and carrier phase measurements, as well as signals' strength on three frequencies.
- Implementation of a suitable model to simulate the noise in the measurements based on Richardson et al., (2016).
- Implementation of a suitable model to simulate the multipath affecting the measurements based on Simsky et al. (2008) and Khanafseh et al. (2018).
- Integration of the building boundaries to consider the signals obstruction due to the presence of buildings in urban areas.

- Implementation of a model to simulate the error in the PPP products.
- Implementation of a Matlab function to create RINEX observation 2.11 files from the simulated measurements.
- Implementation of a Matlab function to create SP3c and RINEX clock 2.0 files from the simulated orbit and clock products.

This section provides a detailed description of the Simulink model to simulate the GNSS measurements.

The main block diagram of the triple-frequency GPS/Galileo Simulink is shown in **Figure 6.1**. The input file is a Matlab structure containing the time-series of the reference trajectory for user motion. This is expressed in terms of latitude, longitude, and height at each epoch. In case the desired output rate does not match the input data-rate, an interpolation between points is performed to obtain the user's position at the required epoch. For each of the reference points, building boundaries, i.e. the minimum elevation angle below which satellite visibility is obstructed by the presence of buildings, are required. This reference truth is processed in the *SensorModels* block and the *SensorData* are output. The output can be completely customized based on the user needs.

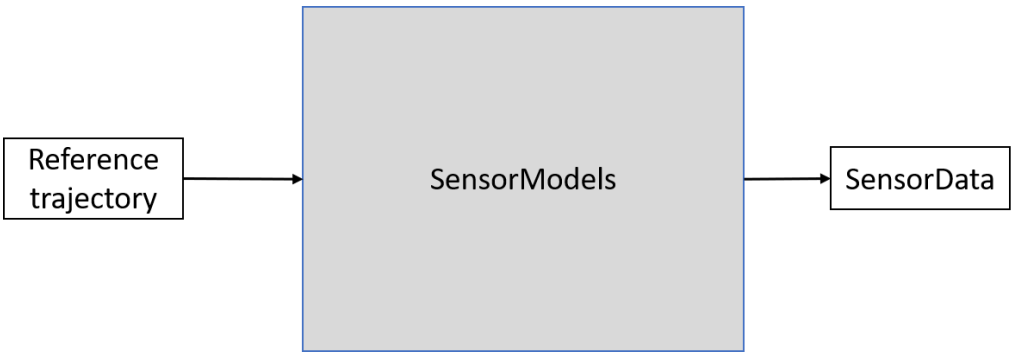


Figure 6.1 *Triple-frequency GPS/Galileo Simulink main block diagram.*

Within the full list of available output, the following figure:

- **Time stamp information** – GPS week; seconds of the week (SOW); number of leap seconds.
- **GNSS measurements** – Pseudoranges; carrier phases; CN0; availability flag, which tells you whether a measurements set is actually usable for positioning or not.

- **Transmitting satellites information** – Position and velocity of the GNSS satellites at transmission time; clock offset and drift at transmission time; satellites elevation over the horizon; PRN number.
- **Ionosphere delay information** – Coefficients for the Klobuchar model used to simulate the first order ionospheric delay affecting the GNSS measurements; time-series of simulated ionospheric delay affecting the GNSS measurements on L1 for each of the satellites in view.
- **Other outputs** – Time-series of the receiver clock offset; carrier phase ambiguities; noiseless pseudorange measurements; time-series of the multipath affecting the pseudorange and carrier phase measurements on L1.

Most of these outputs are stored in n-by-m Matlab matrices, with n being the number of channels in the receiver and m the number of epochs. In order to promote the interaction between the Simulink model and GNSS data processing software, the multi-constellation multi-frequency GNSS measurements, satellites' position, and clock offset can be also saved in RINEX 2.11, SP3c, and RINEX clock 2.0 files, respectively.

Other information, not included in the previous list, can be made available in output by quickly modifying the Simulink model.

The full set of parameters used to define the models in this simulator can be managed through the *PM_init.m* Matlab function. With this function, users can also choose the set of Galileo triple-frequency signals to be simulated.

6.2.1 SensorModel block

Figure 6.2 describes the content of the *SensorModel* block. The blue elliptic block represents the input in the *SensorModel* block, while the orange one is the output. The *TimeData* block defines and outputs the time for each epoch of the simulation in form of GPS time (GPS week and SOW). The two main subsystems of the *SensorModel* block are the Air GNSS Sensor Subsystems (AGSS) for GPS and Galileo (*AGSS GPS* and *AGSS Gal* blocks), which are responsible for the simulation of the GNSS measurements.

The number of simulated satellites tracked at each epoch is limited by the number of channels defined for each *AGSS* block, 11 as default option. For this reason, in open sky conditions up to 22 satellites would be available, 11 GPS

satellites and 11 Galileo satellites. Following the information included in the Yuma almanac, the GPS constellation is assumed to have up to 32 satellites distributed on 6 orbital planes (for example, the Yuma almanac of GPS week 1920 included 31 satellites, since the GPS satellite PRN04 was excluded). The *GpsEphem* block reads the selected Yuma almanac and stores the GPS satellites ephemeris in a matrix. The same is done for the Galileo ephemeris in the *GalEphem_idealconst* block. However, in this case, the ephemeris are read from a file containing the information regarding an ideal Galileo constellation of 27 operational satellites allocated on 3 orbital planes. The *CommonRcvrDelay* block outputs a first order Gauss-Markov process, which is then used as a residual error in the tropospheric delay. Finally, the eight Klobuchar parameters used to simulate the ionospheric delay are loaded in the *KlobucharCoefficient* block.

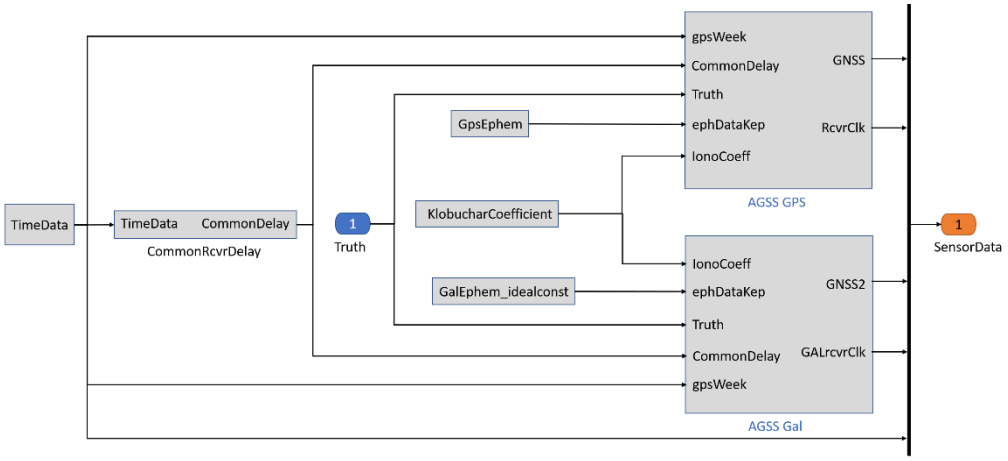


Figure 6.2 *SensorModel block.*

6.2.2 AGSS block

Figure 6.3 shows the structure of the *AGSS* block. The most important subsystems are the *RcvrClkModel*, the *GeometryProcess*, the *ErrorModel*, and the *GpsMsgBuilder* blocks. The *RcvrClkModel* block outputs the receiver clock offset in units of meters. It is simulated as a first order Gauss-Markov process. The *GeometryProcess* block is responsible for selecting the satellites in view and for computing the geometric satellite-to-user distance from the user's reference position and the satellite's ephemeris. The receiver and satellite clock offsets are also added, making the geometric range a pseudorange. The relativistic effects are included in the computation of satellites' clock offsets. The error-less pseudorange is then passed into the *ErrorModel* block, which

models and adds the appropriate delays to form the pseudorange and carrier phase measurements. Finally, the *GpsMsgBuilder* block packs all the GNSS observables and ephemeris information in one bus containing: the GPS Time, PRN number of the visible satellites, pseudoranges, carrier phase, and CN0 on the three frequencies, validity flag for the GNSS measurements, cycle slips indicator, satellites' position and velocity, satellites' clock offset and drift, and the Klobuchar parameters to compute the first order ionospheric delay. The *GpsMsgBuilder* block also determines the carrier phase ambiguities, handles the cycle slips, and simulates the CN0.

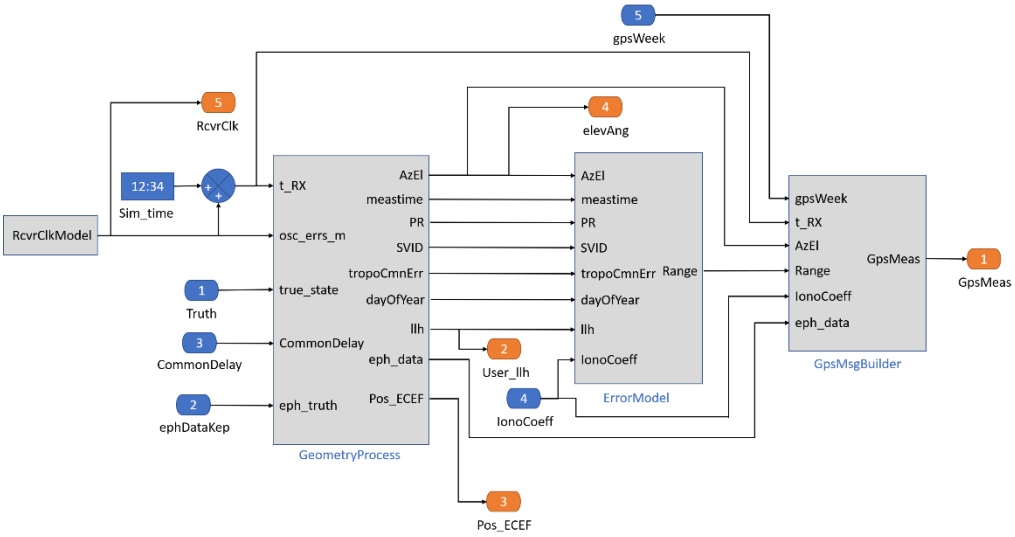


Figure 6.3 *AGSS block.*

6.2.3 GeometryProcess block

The *GeometryProcess* block is in **Figure 6.4**. Firstly, the true position of the receiver, in the ECEF reference frame is computed in *CalRcvrTruePosition*. The receiver position is used, together with the satellites' ephemeris and the receiver clock offset, to obtain the error-less pseudorange in the *CalcTrueRange* block. The satellites' position in ECEF, which is also output by the *CalcTrueRange* block, as well as the the receiver coordinates are used to compute the satellites' elevation and azimuth angles in *CalcAzEl*. Lastly, the computed pseudoranges, the azimuth and elevation angles, the ephemeris data, and the common residual tropospheric error are assigned by the *ChannelSelect* block to a specific channel, based on the satellite visibility.

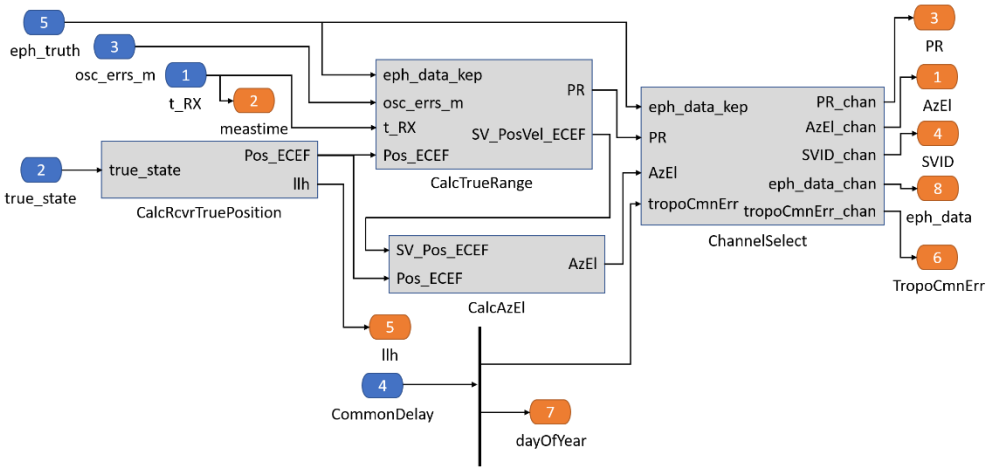


Figure 6.4 *GeometryProcess block.*

6.2.4 ErrorModel block

The *ErrorModel* block simulates the most common delays affecting the GNSS measurements and adds them to the noiseless pseudoranges. Its structure is described in **Figure 6.5**. The noiseless pseudorange passes iteratively through the *Tropo*, *Iono*, *Multipath*, *AntBias*, *ThermNoise*, and *Receiver IF Bias* blocks that add the specific delay to the GNSS measurements. The *Range* bus that is in output contains the simulated pseudorange and carrier phase measurements on the three predefined frequencies.

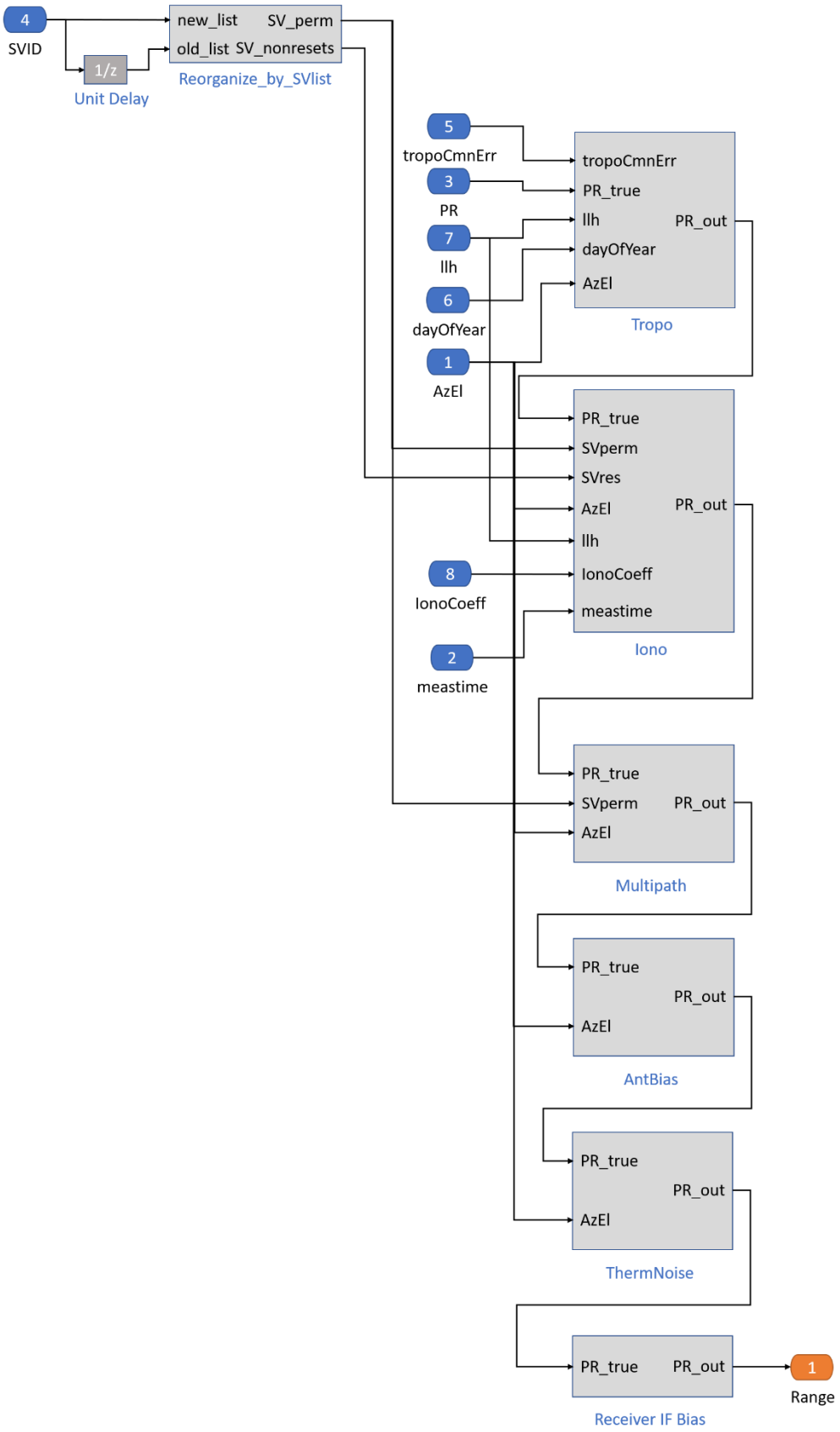


Figure 6.5 *ErrorModel block.*

6.2.4.1 Tropo block

The model adopted in the original version of the GPS/Galileo Simulink tool to simulate the effect of the troposphere on GNSS measurements is the EGNOS model. Penna et al. (2001) demonstrated that the EGNOS seasonal tropospheric model agreed with the accurate zenith tropospheric estimates from carrier phase data processing at a few centimetres. Therefore this model was assumed to be accurate enough to characterise the delay due to the troposphere, and has not been modified by the author.

The EGNOS model is based on look-up tables for average and seasonal variation values for meteorological parameters, such as pressure, temperature and water vapour pressure at mean sea level, and temperature and water vapour lapse rates from latitude and time.

The dry and wet ZTDs are computed using

$$\begin{aligned} ZTD_d &= ZTD_{d,0}\left(1-\frac{\beta H}{T}\right)^{\frac{g}{R_d\beta}} \\ ZTD_w &= ZTD_{w,0}\left(1-\frac{\beta H}{T}\right)^{\frac{(\eta+1)g}{R_d\beta}-1} \end{aligned} \tag{6.1}$$

where g is equal to 9.80665 m/s^2, H is the height of the receiver above the mean sea level in units of meters, T is the temperature at the mean sea level in units of Kelvin, β is the temperature lapse rate in units of K/m, R_d equals 287.054 J/kg/K, η is the water vapour lapse rate, while $ZTD_{d,0}$ and $ZTD_{w,0}$ are the dry and wet delay at mean sea level in units of meters. These delays can be computed from

$$\begin{aligned} ZTD_{d,0} &= \frac{10^{-6}k_1R_dP}{g_m} \\ ZTD_{w,0} &= \frac{10^{-6}k_2R_d}{g_m(\eta+1)-\beta R_d}\cdot\frac{e}{T} \end{aligned} \tag{6.2}$$

In Equation (6.2), k_1 and k_2 are respectively equal to 77.604 K/mbar and 382000 K^2/mbar, P is the pressure at mean sea level in units of millibar, g_m equals 9.784 m/s^2, and e is the water vapour pressure at mean sea level in units of millibar.

A residual error factor (ε_{cmn}), common to all GNSS measurements, is applied to the ZTD in order to have an uncertainty in the tropospheric model.

The total ZTD, composed by dry and wet ZTD and by the residual error, is then multiplied by a mapping function (m), which depends on the elevation angle of the satellite E, to form the slant tropospheric delay T_r^s.

$$T_r^s = (ZTD_d + ZTD_w + \varepsilon_{cmn}) \cdot m(E) \tag{6.3}$$

$$\begin{aligned} m(E) &= \frac{1.001}{\sqrt{\sin^2(E) + 0.002001}} \cdot \gamma \\ \gamma &= 1 - 0.015 \max(0, 4 - E)^2 \end{aligned} \tag{6.4}$$

Equation (6.4) is an implementation of the mapping function presented in Black and Eisner (1984), in which the term γ is applied to adjust for elevation angles below 4°.

The look-up tables for the average values and seasonal variations of the five meteorological parameters are given in **Table 6.1** and in **Table 6.2**, respectively.

Table 6.1 *Average values of the five meteorological parameters used by the EGNOS model. The latitude (φ) is in units of degrees, the pressure (P) and water vapour (e) are in mbar, the temperature (T) is expressed in K, and its lapse rate (β) is in mK/m, while the water vapour lapse rate (η) is a dimensionless quantity.*

φ	***P***	***T***	***e***	***β***	***η***
≤ 15	1013.25	299.65	26.31	6.30	2.77
30	1017.25	294.15	21.79	6.05	3.15
45	1015.75	283.15	11.66	5.58	2.57
60	1011.75	272.15	6.78	5.39	1.81
≥ 75	1013.00	263.65	4.11	4.53	1.55

Table 6.2 *Seasonal variation values of the five meteorological parameters used by the EGNOS model. The latitude (φ) is in unites of degrees, the pressure (P) and water vapour (e) are in mbar, the temperature (T) is expressed in K, and its lapse rate (β) is in mK/m, while the water vapour lapse rate (η) is a dimensionless quantity.*

φ	***P***	***T***	***e***	***β***	***η***
≤ 15	0.00	0.00	0.00	0.00	0.00
30	-3.75	7.00	8.85	0.25	0.33
45	-2.25	11.00	7.24	0.32	0.46
60	-1.75	15.00	5.36	0.81	0.74

≥ 75	-0.50	14.50	3.39	0.62	0.30

Using these values, each meteorological parameter (X) can be computed starting from the day of the year (DOY) and the receiver's latitude (φ).

$$X(\varphi, DOY) = X_0(\varphi) - \Delta X(\varphi) \cdot \cos\left(\frac{2\pi(DOY - DOY_{\min})}{365.25}\right) \qquad (6.5)$$

where $X_0(\varphi)$ and $\Delta X(\varphi)$ are the average value and seasonal variation of the meteorological parameter X at the specific latitude φ obtained by interpolating the values in **Table 6.1** and in **Table 6.2**. DOY_{min} equals 28 for northern latitudes and 211 for southern latitudes.

6.2.4.2 Iono block

The delay due to the ionosphere was simulated in the original version of the *Iono* block using one of the most well-known models: the Klobuchar model (J. A. Klobuchar, 1987). It approximates the diurnal variation of the ionospheric delay with a cosine function varying in amplitude and in period with the user latitude. Although the Klobuchar model is accurate only at meter-level, its implementation simplicity represents the main reason why it has been adopted also in the new version of the simulator, as well as in commercial simulators such as Spirent.

The ionospheric delay is computed as it follows:

Chapter 1 Calculate the Earth-centred angle from the elevation angle E.

$$\psi = \frac{0.0137}{E + 0.11} - 0.022 \qquad (6.6)$$

Chapter 2 Compute latitude of the ionosphere pierce point (IPP) from the user's latitude φ, the Earth-centred angle ψ, and the azimuth angle A.

$$\Phi_{IPP} = \varphi + \psi \cos A \qquad (6.7)$$

if $\Phi_{IPP} > 0.416 \Rightarrow \Phi_{IPP} = 0.416$, or if $\Phi_{IPP} < -0.416 \Rightarrow \Phi_{IPP} = -0.416$

.

Chapter 3 Compute the longitude of the IPP from the user's longitude λ, the Earth-centred angle ψ, the azimuth angle A, and IPP latitude Φ_{IPP}.

$$\lambda_{IPP} = \lambda + \frac{\psi \sin A}{\cos \Phi_{IPP}} \tag{6.8}$$

Chapter 4 Find the geomagnetic latitude from the IPP latitude Φ_{IPP} and longitude λ_{IPP}.

$$\Phi_m = \Phi_{IPP} + 0.064 \cos\left(\lambda_{IPP} - 1.617\right) \tag{6.9}$$

Chapter 5 Find the local time from the IPP longitude λ_{IPP} and the GPS time t_{GPS}.

$$t = 43200 \cdot \lambda_{IPP} + t_{GPS} \tag{6.10}$$

if $t > 86400 \Rightarrow t = t - 86400$, else if $t < 0 \Rightarrow t = t + 86400$.

Chapter 6 Compute the slant factor from the elevation angle E.

$$F = 1 + 16\left(0.53 - E\right)^3 \tag{6.11}$$

Chapter 7 Compute the ionospheric time delay.

$$\begin{aligned} I_{r,1}^s &= F\left[5 \cdot 10^{-9} + \sum_{n=0}^{3} \alpha_n \Phi_m^n \left(1 - \frac{x^2}{2} + \frac{x^4}{4}\right)\right] \\ x &= \frac{2\pi\left(t - 50400\right)}{\sum_{n=0}^{3} \beta_n \Phi_m^n} \end{aligned} \tag{6.12}$$

The eight coefficients (α_n and β_n) in (6.12) are included in the GPS navigation message.

The ionosphere delay models, such as the Klobuchar model, are usually aimed at characterizing only the first order ionospheric delay. Higher order terms however exist and account for millimetres-to-centimetres level delays. Indeed,

according to Petrie et al. (2011), the second and third order ionospheric delays rarely exceed 45 mm and 35 mm, respectively, in exceptionally active ionosphere conditions. Hence, for standard ionosphere conditions, the higher order ionospheric delays can be considered negligible with respect to order biases affecting the GNSS measurements, such as the residual error in the precise clocks (see Section 6.3). Despite so, a residual error modelled as a random walk has been added to the ionospheric delay affecting the simulated pseudorange and carrier phase measurements.

6.2.4.3 Multipath block

Multipath is the simultaneous reception of multiple signals due to the reflection of the direct signal caused by the ground or other reflective surfaces in proximity of the antenna. These reflections distort the received signal and cause errors in the code and phase measurements. The characteristics of the multipath error are strictly related to the environment in which the receiver operates.

In this triple-frequency GPS/Galileo Simulink, the multipath is modelled as a first-order Gauss-Markov process (Khanafseh et al., 2018; McGraw et al., 2000; O'Keefe et al., 2006).

$$e^{s}_{r,mp}\left(t_k\right) = w\left(t_k\right) + e^{s}_{r,mp}\left(t_{k-1}\right)\cdot e^{-\frac{\Delta t}{\tau}} \tag{6.13}$$

In Equation (6.13), $e^{s}_{r,mp}\left(t_k\right)$ is the multipath error being generated at epoch t_k, $w(t_k)$ is the driving noise term simulated using a normally distributed random number generator, Δt is the observation data-rate, while τ is the correlation time constant.

To prove that the multipath error can be actually modelled as a Gauss-Markov process, the multipath in the L1 pseudorange, recorded by a Leica GS10 receiver located between two buildings in the Jubilee campus of the University of Nottingham on the 25/07/2017, was compared with the multipath simulated through Equation (6.13). The correlation time constant used to simulate the multipath was 365 seconds. **Figure 6.6** shows the autocorrelation functions for the simulated and real multipath for different time lags from 0 to 90 minutes. The two functions look similar, in particular for small lags, when the multipath is largely autocorrelated.

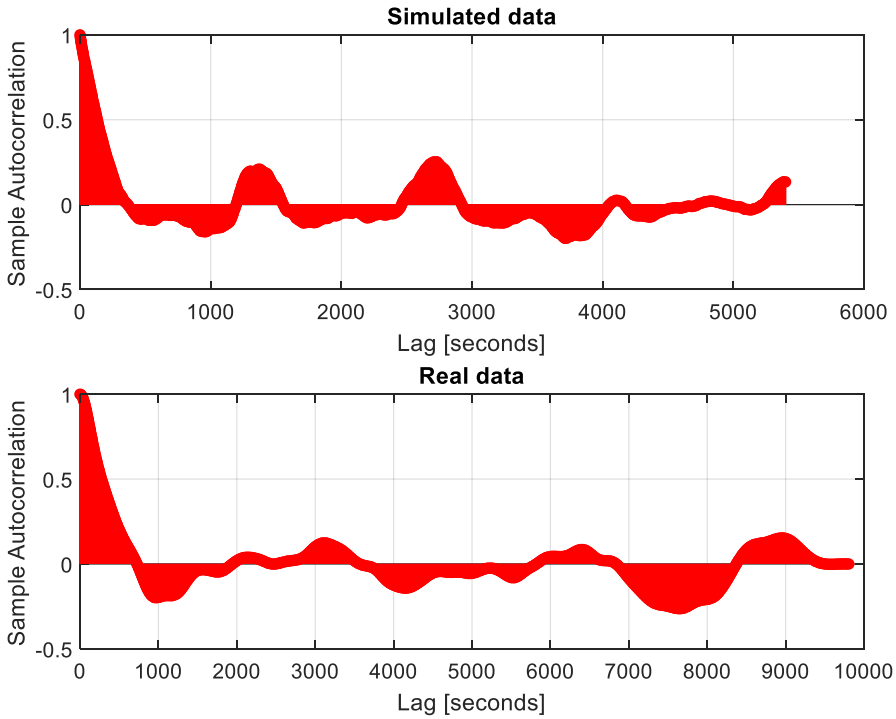


Figure 6.6 *Autocorrelation function of the MP1 combination. Top plot is simulated data, bottom plot is real data.*

Simsky et al. (2008) analysed 1.5 years of observations from GIOVE-A satellite and compared the multipath suppression properties of Galileo and GPS signals. The pseudoranges on GPS L1 and Galileo E1-B/C signals were found to be the most affected by multipath, with the multipath on GPS L1 being slightly larger than the one on Galileo E1-B/C, while the Galileo AltBOC modulated signal E5 and the data-less signals E1-A and E6-A were the least affected. Based on these results, three pseudorange multipath groups were defined: high multipath group, which includes all the signals that are more sensitive to the effect of multipath (Galileo E1-B/C and E6-B/C, GPS L1 and L2); medium multipath group (GPS L5, Galileo E5a, and E5b); low multipath group (Galileo E5, E1-A, and E6-A). The standard deviation of the driving noise term in the multipath error is assumed to be a function of the elevation angle of the satellite.

$$\sigma_w = c_0 + c_1 \cdot e^{\frac{E}{c_2}} \tag{6.14}$$

The three coefficients in Equation (6.14) have been selected to match the results in Simsky et al. (2008). They are reported in **Table 6.3** for the three pseudorange multipath groups, as well as for the carrier phase multipath. The exponential

law of the multipath magnitude as a function of the elevation angle is also shown in **Figure 6.7**. The error for those signals that are more sensitive to the multipath can be as large as 1.2 meters at very low elevation and it decreases to less than 0.50 m at high elevation. For the medium multipath group, the standard deviation of the error is never larger than 1 m, but it can be even smaller than 0.4 m at very high elevation. The standard deviation of the multipath error for E5, E1-A, and E6-A is between 0.22 m, for satellites at very low elevation angles above the horizon, and 0.10 m, for satellites at the zenith. For the carrier phase measurements, the multipath is assumed to be always at millimetres level, with its maximum value being 7.3 mm at low elevations.

Table 6.3 *Coefficients used in the exponential law of the multipath magnitude as a function of the elevation angle. C_0 and C_1 are in units of meters, while C_2 is in unit of degrees.*

	High	**Medium**	**Low**	**Carrier phase**
C_0	0.47	0.37	0.10	0.0015
C_1	0.78	0.70	0.13	0.0060
C_2	20.91	17.84	18.46	35

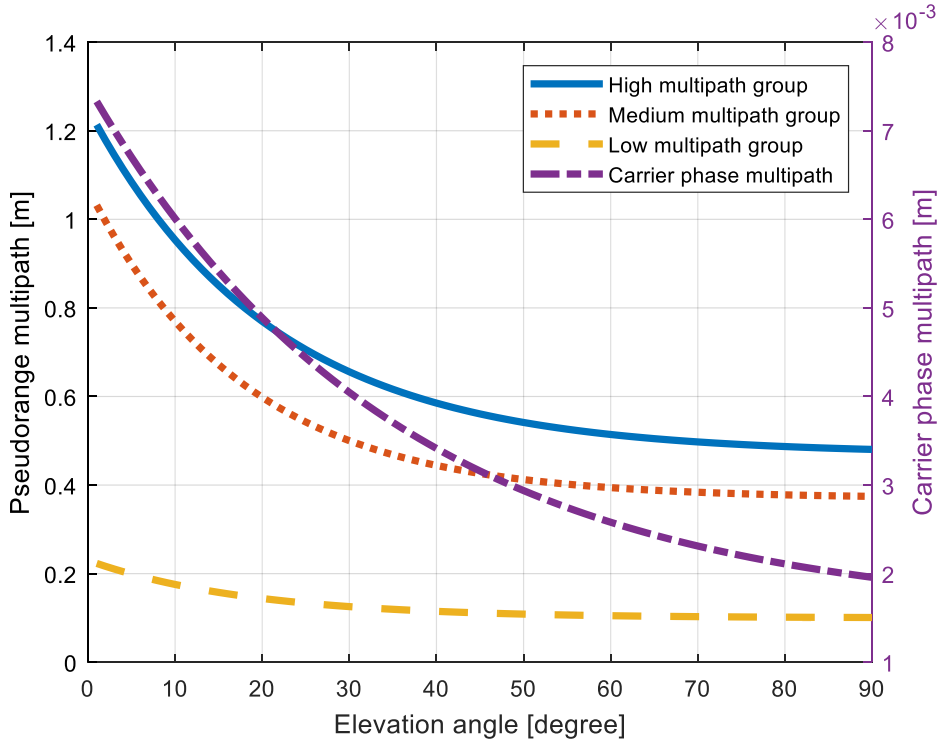


Figure 6.7 *Magnitude of the multipath delays as a function of the elevation angle. The high multipath group (blue) includes the Galileo E1 and E6 and GPS L1 and L2 pseudoranges. The medium multipath group (orange) includes the Galileo E5a, E5b and GPS L5 pseudoranges. The low multipath group (yellow) includes Galileo E5 pseudoranges. The multipath on the carrier phase measurements is also shown in purple.*

The correlation time constant τ is another important factor to characterize the behaviour of the Gauss-Markov process used to model the multipath error. Typical values of τ for a kinematic receiver in urban environments are in the range between 5 and 65 seconds, while for a static receiver are between 40 and 150 seconds (Khanafseh et al., 2018).

6.2.4.4 AntBias block

The triple-frequency GPS/Galileo Simulink also simulates the receiver antenna phase centres in the *AntBias* block. These are modelled using a spherical harmonic expansion function of the elevation angle *E* and the azimuth angle *A* of the transmitting satellite (Wubbena et al., 1997).

$$\xi_r^s = \sum_{n=0}^{n_{MAX}} \sum_{m=0}^{n} \left(A_{nm} \cos mA + B_{nm} \sin mA \right) P_{nm}(\sin E) \tag{6.15}$$

In Equation (6.15) P_{nm} are the normalized Legendre associated functions, while the coefficients A_{nm} and B_{nm} are randomly computed.

In PPP, the antenna PCOs and PCVs can be accurately modelled using the corrections included in ANTEX files. For this reason, in this research, the antenna phase centres are not simulated and they are assumed to be already corrected for.

6.2.4.5 ThermNoise block

The noise in the pseudorange and carrier phase measurements is simulated in the *ThermNoise* block. This block models the GNSS pseudorange noise e_r^s as white noise with a standard deviation σ_e that depends on the incoming signal strength *CN*0 (Kaplan and Hegarty, 2005).

$$\begin{aligned} e_r^s &= N\left(0, \sigma_e^2\left(CN0_r^s\right)\right) \\ \sigma_e &= c_0 + c_1 \cdot e^{-\frac{CN0_r^s - c_2}{c_3}} \end{aligned} \tag{6.16}$$

This model is based on the results presented in Richardson et al. (2016), which analysed the Hatch filter residuals of multi-constellation pseudoranges recorded by four stations within the Veripos global network.

The coefficients used to model the standard deviation of the GPS and Galileo pseudoranges are summarized in **Table 6.4**, while **Figure 6.8** shows the exponential law of σ_e as a function of the *CN*0.

Table 6.4 *Coefficients adopted to model the standard deviation of the pseudorange noise for GPS and Galileo. C_0 and C_1 are in units of meters, while C_2 and C_3 are in units of dB-Hz*

Signal	C_0	C_1	C_2	C_3
L1	0.05	1.05	28	8
L2	0.05	1.35	28	8
L5	0.02	0.65	28	8
E1	0.02	0.55	28	9
E5a	0.02	0.25	28	9
E5b	0.02	0.40	28	9
E6	0.02	0.65	28	9
E5	0.00	0.15	28	9

It is clear from **Figure 6.8** that the legacy GPS pseudoranges, on L1 and L2, have a much larger noise than the Galileo signals, while the modernized signal on GPS L5 provides pseudoranges with noise comparable to the Galileo ones. Surprisingly despite being the same signal, the noise on E5a is still smaller than the one on GPS L5 for the same *CN*0. This difference is further amplified by the fact that GPS L5 has a lower minimum power level on the ground than E5a (European Union, 2015; Global Positioning Systems Wing (GPSW) - Systems Engineering & Integration, 2010). As expected, Galileo E5 is the signal with the smallest pseudorange error, thanks to its very large bandwidth of 51 MHz. The carrier phase measurements are assumed to have a precision of 1 mm.

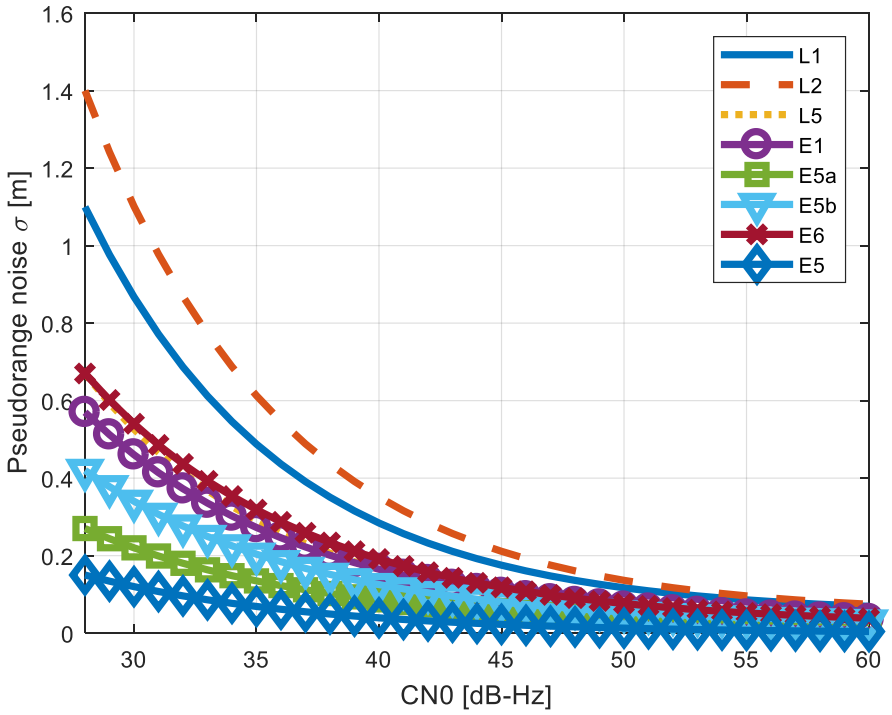


Figure 6.8 *Receiver noise for different GPS and Galileo signals as function of the CN0.*

6.2.4.6 Receiver IF Bias block

The *Receiver IF Bias* block applies a common error to the pseudorange and carrier phase measurements on the same frequency band. This error is modelled as a first order Gauss-Markov process, similarly to Equation (6.13). The standard deviation of the driving noise term, here, is damped using an exponential function of the time.

$$\sigma_w(t_k) = \sigma_w(t_0) \cdot e^{-\frac{t_k}{c_0}} \tag{6.17}$$

In this way, the simulated inter-frequency biases have a higher short-term stability. The assumed values for $\sigma_w(t_0)$ and c_0 are 0.005 m and 86400 seconds, respectively.

6.2.5 GpsMsgBuilder block

The *GpsMsgBuilder* block, described in **Figure 6.9**, performs four main tasks. Firstly, it computes the transmitting satellites' position, velocity, clock offset and drift at the transmission epoch based on the ephemeris in the *CalcSatPosition* block. At the same time, the *CN*0 measurements are simulated in the *CNoSimulator* block based on (Kaplan and Hegarty, 2005)

$$CN0 = P_r + G_a - N_0 \tag{6.18}$$

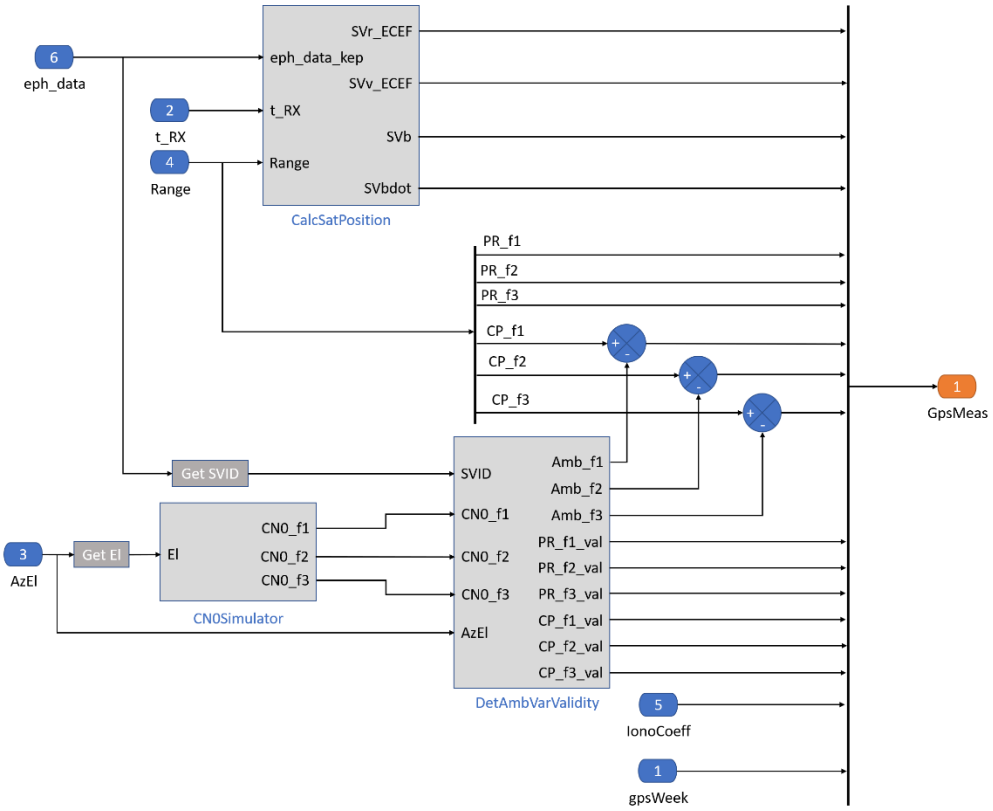


Figure 6.9 *GpsMsgBuilder block.*

in which P_r is the power of the GNSS signal at the receiver position, G_a is the receiving antenna gain, and N_0 is the thermal noise power component.

In this research, the received GPS and Galileo signals power is assumed to be the minimum power levels on the ground reported in **Table 6.5** and defined in Global Positioning Systems Wing (GPSW) - Systems Engineering & Integration (2010), Global Positioning Systems Directorate - Systems Engineering & Integration (2014), and European Union (2015). The assumed receiver antenna gain pattern as function of the elevation angle is showed in **Figure 6.10**, while the noise is assumed to be equal to -201 dB. The *CN*0 observations are also assumed to be affected by a white noise with a standard deviation of 1 dB.

The simulated *CN*0 values are input in the *DetAmbVarValidity* block. Firstly, this block provides a value for the carrier phase ambiguities, which are later added to the carrier phase measurements. Secondly, it determines whether the observations from one satellite can be actually used for positioning purposes,

based on the imposed elevation mask angles. If a satellite is below the minimum elevation, the validity flag for that satellite is set to 0, otherwise it is set to 1.

Table 6.5 *Received minimum power levels on the ground in units of dBW.*

Signal	Minimum power at the ground
L1	-158.5
L2	-164.5
L5	-158
E1	-157
E5a	-155
E5b	-155
E5	-155
E6	-157

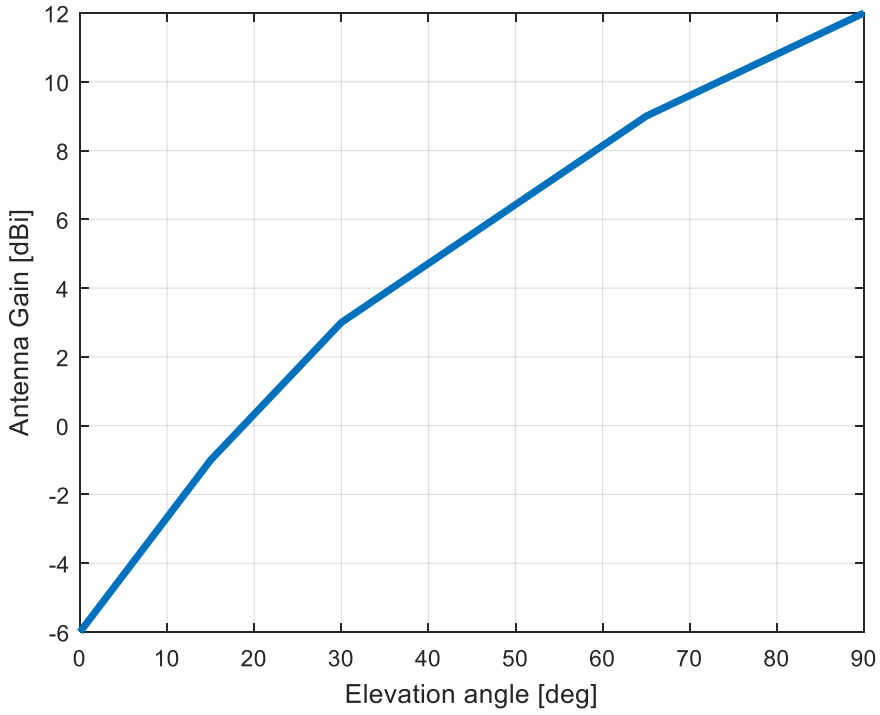


Figure 6.10 *Assumed receiver antenna gain pattern as a function of the satellie's elevation angle.*

These validity flags are then used to determine whether a cycle slip due to data gap is necessary. Cycle slips may be also enabled if the *CN*0 is too low. A table was defined to assign the probability of cycle slip occurring at a given *CN*0 of the signal. As shown in **Figure 6.11**, there is a linear relationship between the *CN*0 in dB and the common logarithm, i.e. the logarithm to the base 10, of the probability (Rockwell Collins, 1997).

If a cycle slip occurs, the simulated receiver has 87% of probability of detecting such cycle slip. If it happens a cycle slip detection flag is set to 1.

The outputs of the *CalcSatPosition*, *CNoSimulator*, and *DetAmbVarValidity* blocks, as well as the timing information, e.g. GPS week and SOW, the Klobuchar parameters, and a few other indicators, are packed into the *GpsMeas* bus, which is finally output from the *GpsMsgBuilder* block.

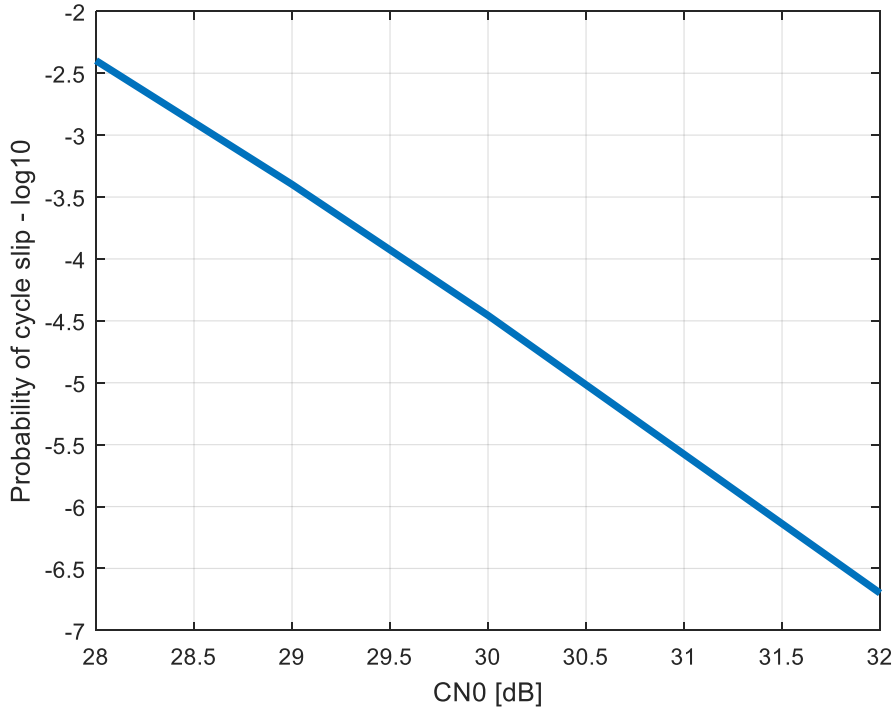


Figure 6.11 *Common logarithm of the probability of cycle slip as function of the carrier to noise ratio.*

6.3 Simulation of the Real-Time precise orbits and clocks

In PPP, precise products must be used in order to achieve high precision. This simulation tool is also able to simulate the precise orbits and clocks with a quality comparable to the Real-Time products distributed by the IGS RTS. These products are provided in SP3c and RINEX clock 2.0 files.

Unlike previous publications based on simulated data (Juan et al., 2012; Miguez et al., 2016; Shen and Gao, 2006), a rigorous study on the difference between the GPS IGS real-time products and the final products provided by ESA, which is taken as reference truth, was performed to define a proper model for the error in the precise orbits and clocks. To do so, four weeks of data (GPS weeks 1917 to 1920) have been analysed.

From this point on, the author will refer to the difference between the real-time and final products as error in the real-time orbits and clocks.

The CDDIS repository archives products generated from a real-time data stream in support of the IGS RTS. The precise orbits files are published in SP3c format at 30 seconds intervals, while the precise clocks files are in RINEX clock 2.0 format at 30 seconds intervals. These products, named IGC, are derived from the IGC01 solution, which is a single epoch, GPS only solution with satellites orbits computed with respect to their CoM. The ESA final products (ESA) can be also found in the CDDIS archive. The ESA orbits are published with a data rate of 15 minutes. In order to match the 30 seconds sampling rate of the IGC products, the ESA orbits have been interpolated. The difference between the IGC and ESA orbits have been transformed from the ECEF reference system into the radial, along-track, and cross-track reference system.

Table 6.6 summarizes the RMS of the products' difference. The orbital differences are of the order of few centimetres level, with the radial direction being the best agreement and the along-track component agreeing the least. The RMS difference between the IGC and ESA clocks is as large as 19.40 cm, which is almost twice as large as the value presented in Hadas and Bosy (2015).

Table 6.6 *Root Mean Square (RMS) of the difference between the IGC and ESA orbits and clocks in a four weeks period spanning from the GPS week 1917 to 1920 (from 2nd to 29th October 2016). The difference in the orbits are reported in the radial, along-track, and cross track components. Units of cm.*

	Radial	**Along-track**	**Cross-track**	**Clocks**
RMS	1.60	3.41	1.91	19.40

Feeding the values in **Table 6.6** into the well-known formula for the signal in space ranging error (SISRE) as a function of the errors in the radial (*dR*), along-track (*dA*), cross-track (*dC*), and clock (*dClk*) components (Oliver Montenbruck et al., 2015)

$$SISRE = \sqrt{\left(0.98 \cdot dR - dClk\right)^2 + \frac{1}{49}\left(dA^2 + dC^2\right)} \qquad (6.19)$$

one would obtain a SISRE of 17.84 cm. This error is too large to be neglected in the PPP analysis, unlike it was done in Shen and Gao (2006).

Figure 6.12 shows the daily time-series of the difference in the three orbital components, radial (top), cross-track (middle), and along-track (bottom), for GPS PRN 14 on the 2nd October 2016. These plots clearly show a periodic behaviour on each of the three components.

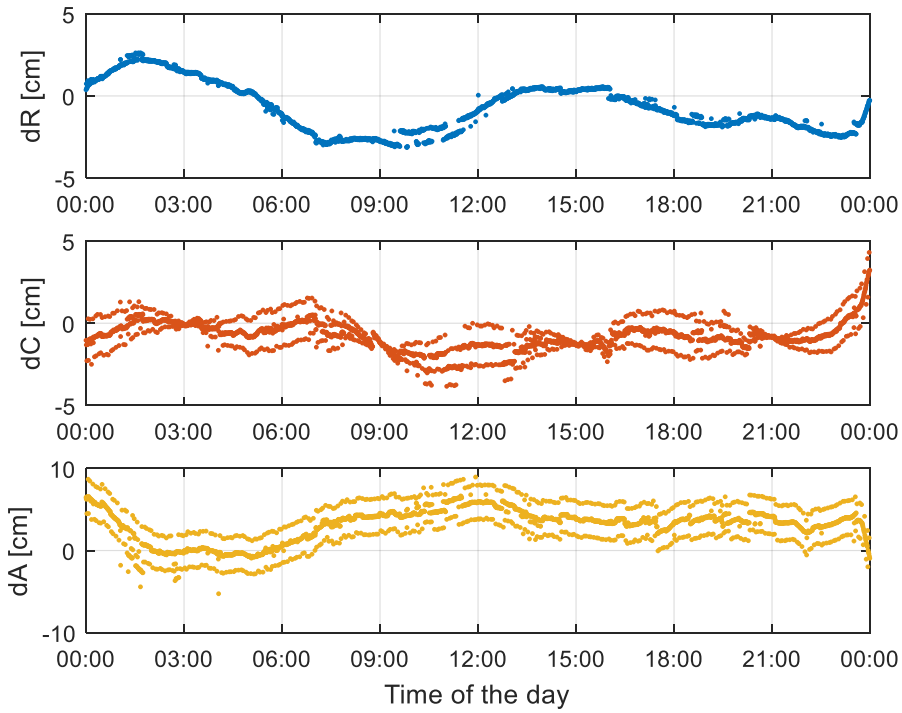


Figure 6.12 *Difference between the IGS real-time and ESA final orbits for GPS PRN 14 on the 2nd October 2016. The upper plot shows the products' difference in the radial component of the satellite's position, the middle plot shows the difference in the cross-track component, while the lower one shows the difference in the along-track component.*

Two peculiar side patterns are also visible in the time-series of the cross-track and along-track errors in **Figure 6.12**. The first one looks like a bow-tie pattern build around the main sinusoidal behaviour of the cross-track error, while the second one shows two constant offsets bounding the along-track error. A reason for these two systematics could not be found by the author; one possible explanation is the presence of discontinuities between adjacent real-time solutions. On the other hand, these patterns are affecting only the along-track and cross-track components, which have a smaller impact on the SISRE with respect to the radial component or the clocks. For this reason, they have been filtered out before analysing the products error.

The top plot (blue) in **Figure 6.13** shows the difference between the IGC and ESA clocks for PRN 14 on the 2nd October 2016. A drift is visible in the daily time-series, which is related to the way the two network solutions are computed.

When estimating the clocks, a reference needs to be defined. The ESA final products are computed by processing seven days of data; the clock of a station at a particular epoch is taken as reference clock for that solution. On the other hand, the IGC products are single epoch solutions. Therefore, while the reference clock for the ESA products is zero for the reference epoch and then it drifts with the time, for the IGC products it is assumed to be always zero. When differentiating the two types of precise clocks, the drift of the ESA reference clock is visible.

To overcome this problem, a single difference between the satellites' clocks was performed, in such a way that the same satellite's clock is always used as reference. The bottom plot in **Figure 6.13** displays IGC clock's error for GPS PRN 14 single-differenced with respect to PRN 1 on the 2nd October 2016. As per the orbital differences, a sinusoidal pattern is visible.

For this reason, instead of applying random errors to the simulated precise products as in Juan et al. (2012); Miguez et al. (2016), a fitting method based on the Fourier series is adopted in this research to characterize the errors in the GPS and Galileo real-time products.

$$\Delta_{RT} = a_0 + \sum_n a_n \sin\left(n\omega t + \Phi_n\right) \tag{6.20}$$

Equation (6.20) describes the assumed behaviour of the general error in one component of the real-time products Δ_{RT} as a function of the time *t*. It can be described as a sum of n sinewaves of amplitude a_n, frequency $n\omega$, and phase Φ_n, biased by a_0.

In order to study what frequencies have to be used in the model, the spectrum of the products' error have been analysed. **Figure 6.14** and **Figure 6.15** present the spectrum of the errors in the precise orbits' components for GPS PRN 5 and PRN 14, respectively. In these two plots, a peak is visible at a frequency of twice-per-day in all the orbit's components, while a peak at a frequency of once-per-day is mainly visible in the along-track direction. Smaller peaks are also visible at frequencies from three- to six-times-per-day.

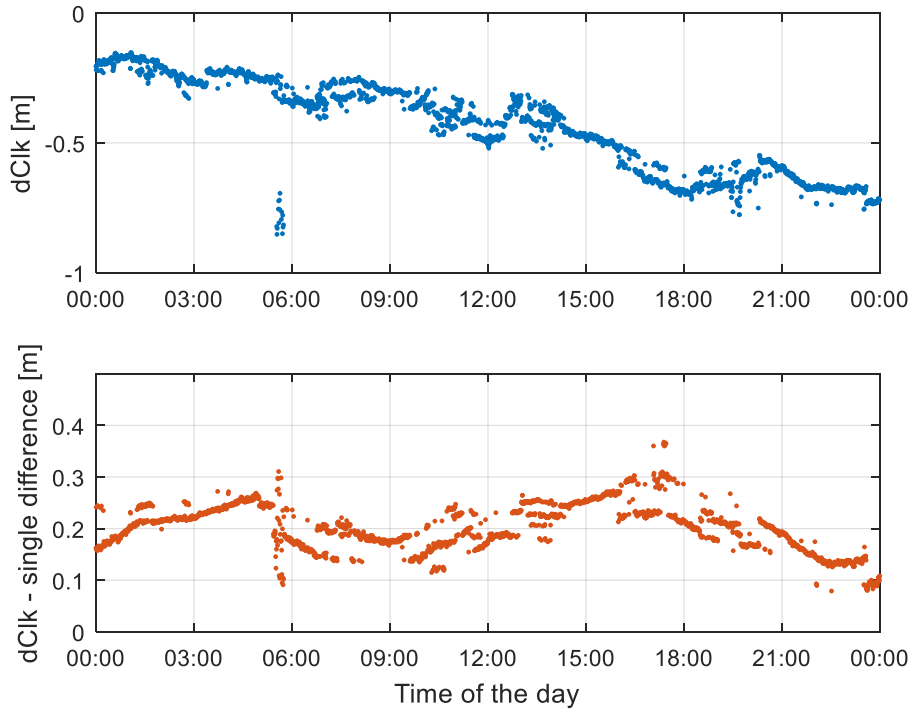


Figure 6.13 *Difference between the IGS real-time and ESA final clocks for GPS PRN 14 on the 2nd October 2016. The top plot shows the undifference case, while the bottom plot displays the single difference with respect to PRN 1.*

Similar conclusions can be drawn by looking at the spectrum of the single difference with respect to GPS PRN 1 clock's error in **Figure 6.16**. A large peak is visible at a frequency of twice-per-day, while smaller peaks are at frequencies of once-per-day and from three- to five-times-per-day.

Hence, in the simulation of the real-time precise products for GPS, the smaller peaks are neglected and only the two major components are considered, namely the sinusoid with frequency of twice-per-day (or equivalently with a period of 11 hours and 58 minutes) and the sinusoid with frequency of once-per-day (or equivalently with a period of 23 hours and 56 minutes).

$$\Delta_{RT} = a_0 + a_1 \sin\left(\omega t + \Phi_1\right) + a_2 \sin\left(2\omega t + \Phi_2\right) \tag{6.21}$$

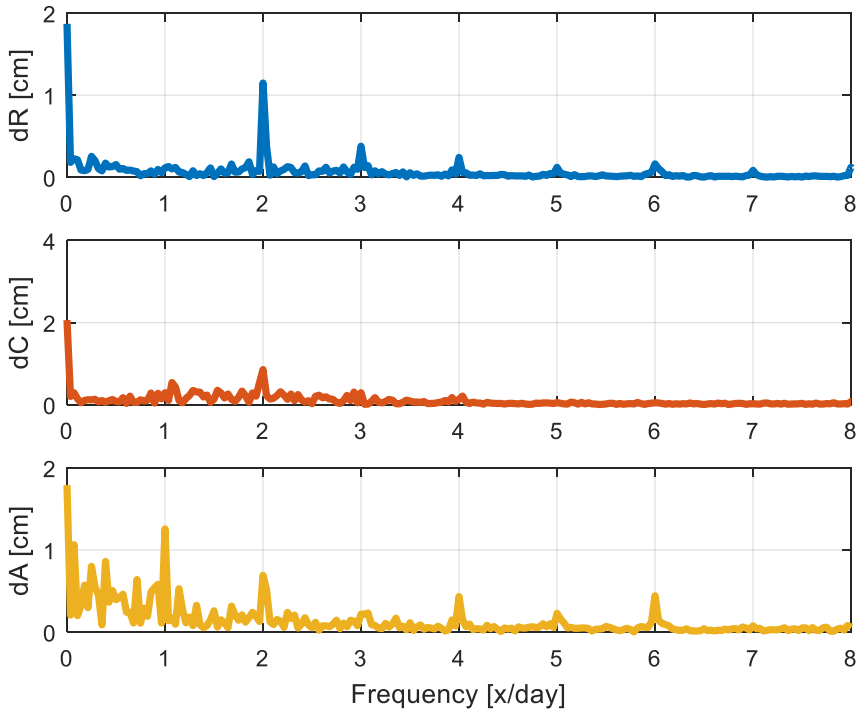


Figure 6.14 *Spectrum of the error in the radial (top), cross-track (middle), and along-track (bottom) orbit components. GPS PRN 5. On the x axis, the frequencies as in units of times-per-day.*

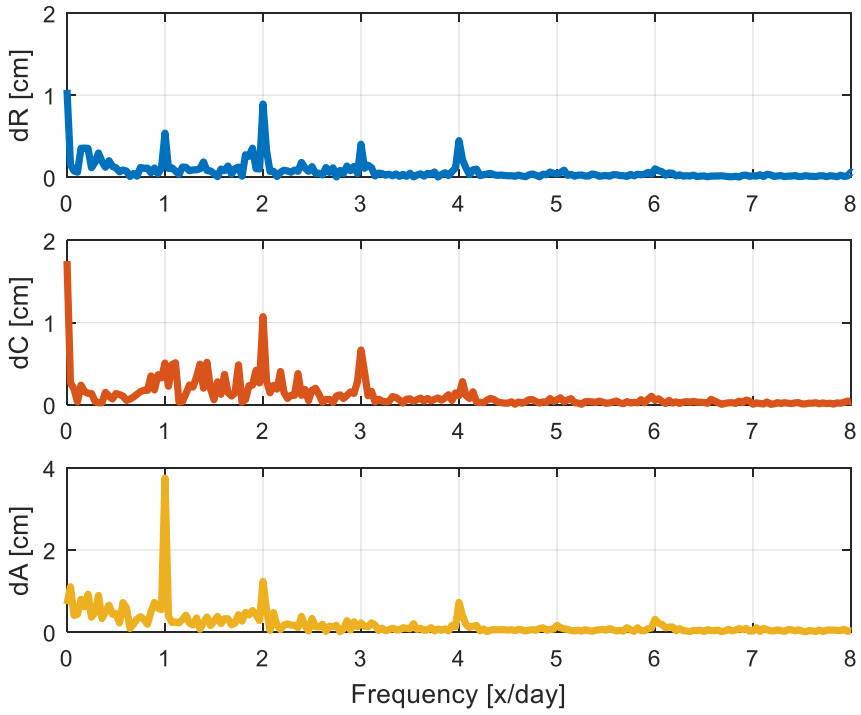


Figure 6.15 *Spectrum of the error in the radial (top), cross-track (middle), and along-track (bottom) orbit components. GPS PRN 14. On the x axis, the frequencies as in units of times-per-day.*

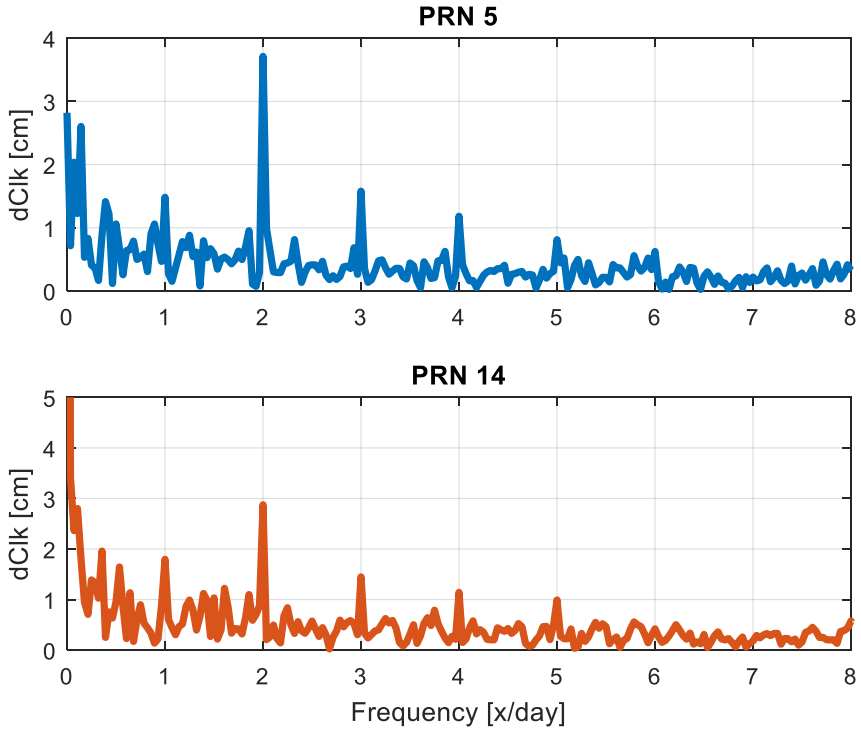


Figure 6.16 *Spectrum of the single difference between satellite clock error with respect to GPS PRN 1. Top plot is for GPS PRN 5, while the bottom plot is for the GPS PRN 14. On the x axis, the frequencies as in units of times-per-day.*

To determine the bias a_0, the amplitudes a_1 and a_2, and the phases Φ_1 and Φ_2, the difference between the IGC and ESA GPS products' is fitted to a second order Fourier expansion with a main angular frequency ω equal to $72.92 \cdot 10^{-6}$ rad/sec (once-per-day). This fitting was performed using the Matlab function *fit.m*. Before doing that, a moving average filter is applied to the time-series of the products' error to remove the noise and the side patterns in the along-track and cross-track components. In this way, only the main behaviour would be characterized.

Figure 6.17 compares the error in the precise orbits' with the fitting curve. It is showed how well the second order Fourier expansion approximates the main pattern of the products' error. **Table 6.7** summarizes the RMS of the bias a_0, and amplitudes a_1 and a_2 used to fit the products' error to the second order Fourier expansion. As expected, for all the errors' components, on average the twice-per-day sinusoids have larger amplitudes than the once-per-day sinusoids. The only exception is in the along-track direction where a_1 is larger than a_2.

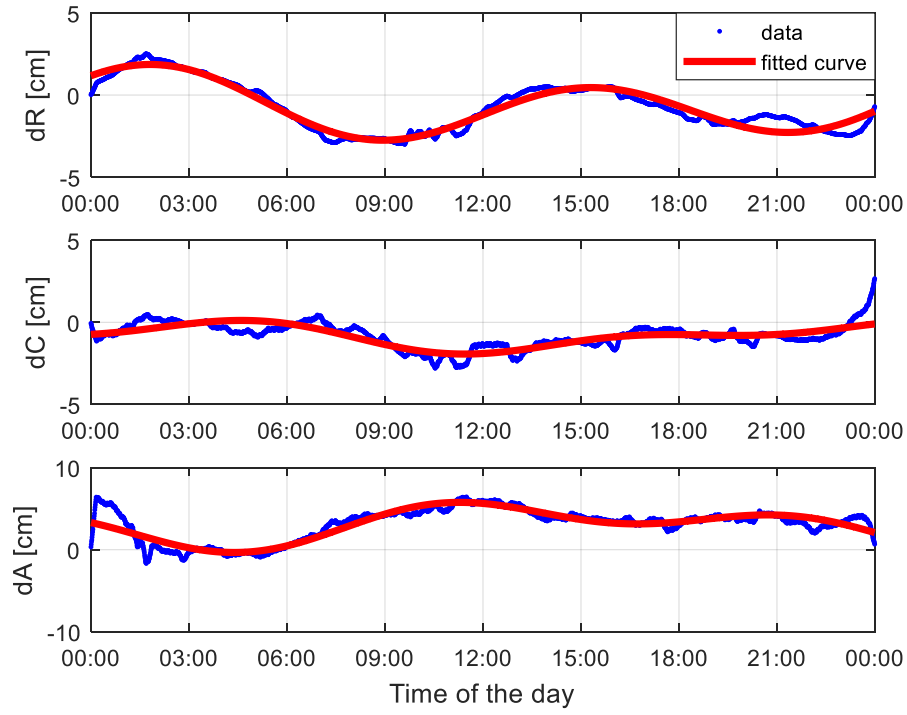


Figure 6.17 *IGC orbit's error in the radial (top), cross-track (middle), and along-track (bottom) components for GPS PRN 14 on the 2nd October 2016. The blue dots represent the real data, while the red curve is the result of the fitting process to the second order Fourier expansion.*

Table 6.7 *RMS of the bias a_0, and amplitudes a_1 and a_2 used to fit the errors' data to the seond order Fourier expansion. Values in units of centimeters.*

	Radial	**Cross-track**	**Along-track**	**Clock**
a_0	1.28	1.77	3.54	17.16
a_1	0.86	1.24	4.32	3.33
a_2	1.45	3.56	3.78	8.92

In **Figure 6.18**, **Figure 6.19**, **Figure 6.20**, and **Figure 6.21** are the histograms of a_0, a_1, and a_2 for the radial, cross-track, along-track, and clock errors. The Matlab *FBD – Find Best Distribution* tool (Aminov, 2012) suggests that within the best distributions that approximate the biases and amplitudes data is the generalized extreme value (GEV) distribution (Markrose and Alentorn, 2011). The theoretical probability density functions (pdf) of the fitted GEV distributions are also plotted in **Figure 6.18**, **Figure 6.19**, **Figure 6.20**, and **Figure 6.21**, together with the histograms of the empirical data. On the x-axis, are the values of the biases or amplitudes, while the y-axis is the number of times a specific value (or interval between two values) occurs. The comparison between the theoretical and empirical distribution shows a good fitting.

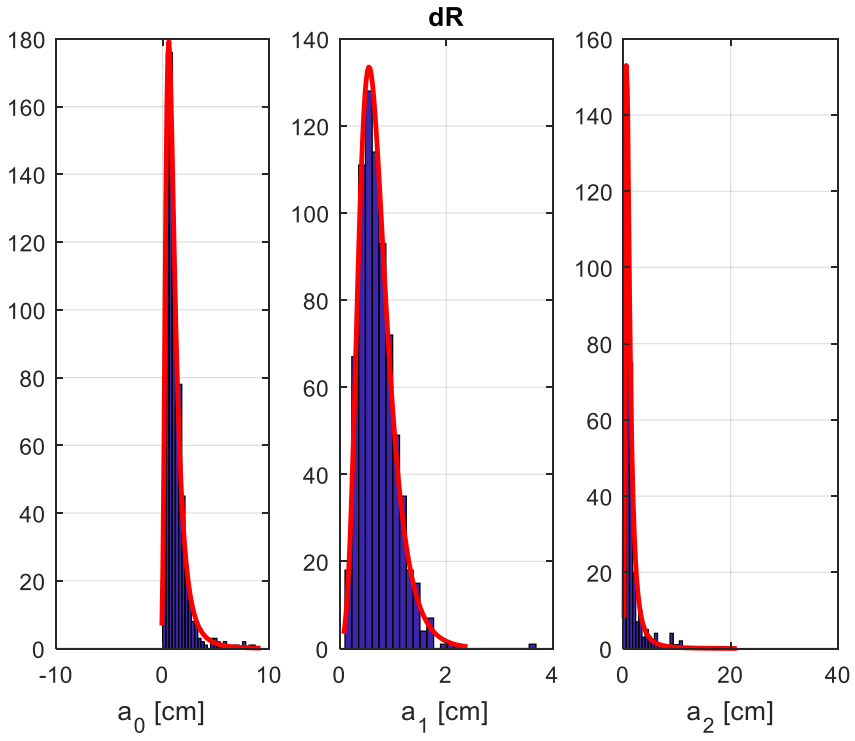


Figure 6.18 *Histogram of the bias and amplitudes of the sinusoids that best fits the radial error in the IGC orbits. The plot in red is the generalized extreme value distribution that approximates the histogram of the empirical values.*

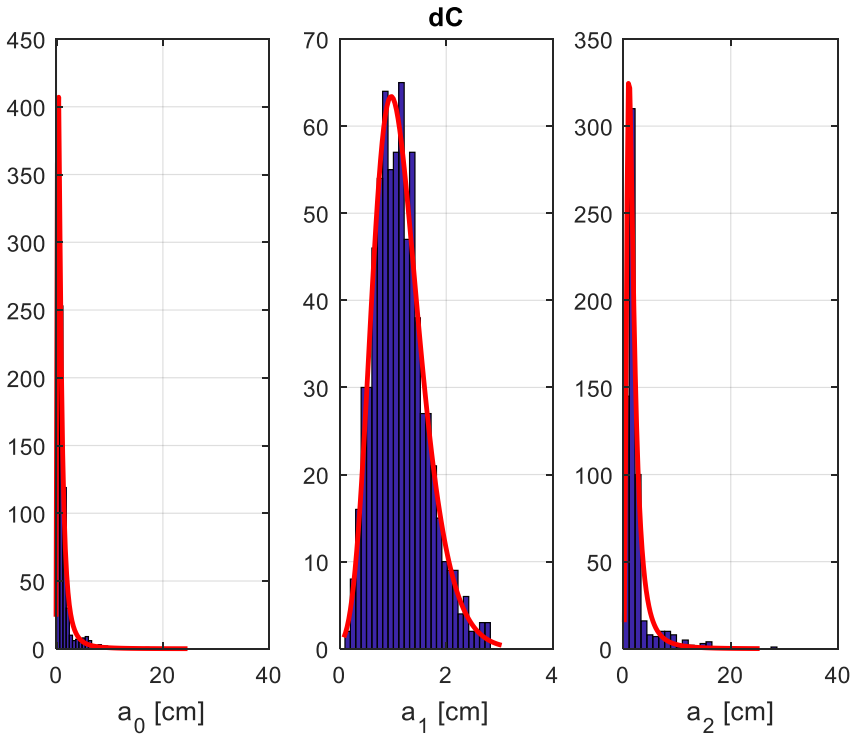


Figure 6.19 *Histogram of the bias and amplitudes of the sinusoids that best fits the cross-track error in the IGC orbits. The plot in red is the generalized extreme value distribution that approximates the histogram of the empirical values.*

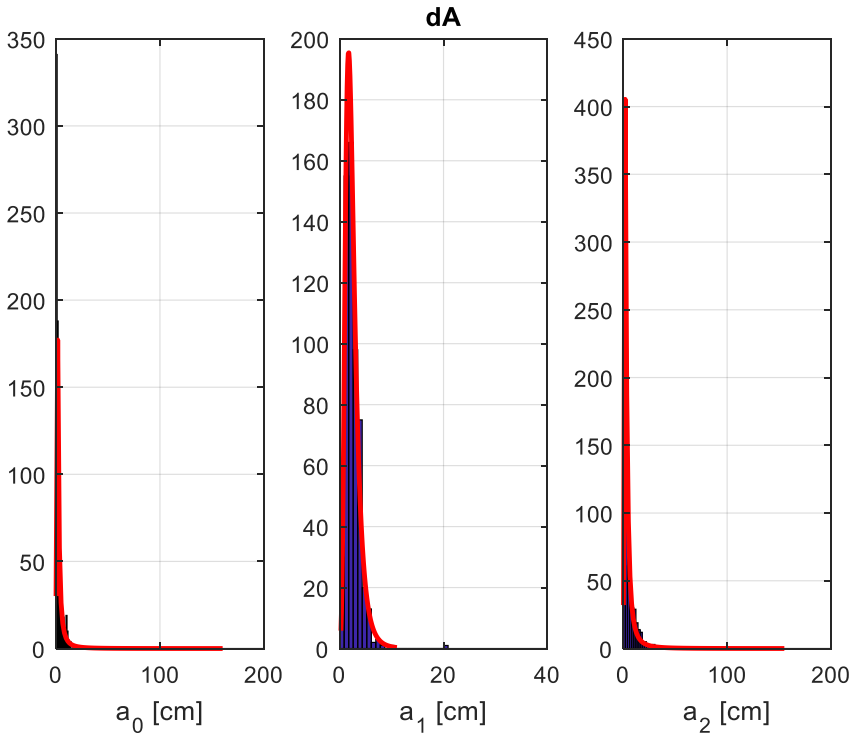


Figure 6.20 *Histogram of the bias and amplitudes of the sinusoids that best fits the along-track error in the IGC orbits. The plot in red is the generalized extreme value distribution that approximates the histogram of the empirical values.*

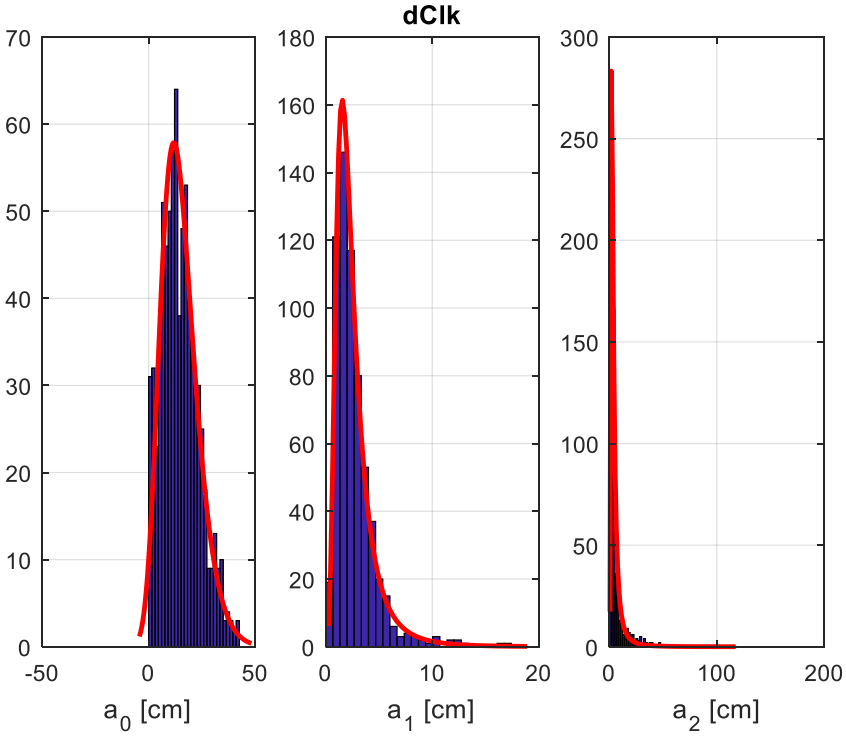


Figure 6.21 *Histogram of the bias and amplitudes of the sinusoids that best fits the error in the IGC clocks. The plot in red is the generalized extreme value distribution that approximates the histogram of the empirical values.*

In order to further validate the hypothesis that the data were GEV distributed, the quantile-quantile (Q-Q) plots were analysed and the Kolmogorov-Smirnov test was also performed (Erto, 2008). The Q-Q plots showed a very good agreement of the empirical biases and amplitudes with the GEV distribution, apart from a slightly discrepancy in the tail. For example, **Figure 6.22** shows the Q-Q plot for the bias a_0 in the radial error. The agreement with the GEV distribution is very solid for most of the data, apart from the last value on the extreme right of the plot that greatly diverges from the fitting distribution. Similar conclusions could be derived from the Q-Q plots for all the other data.

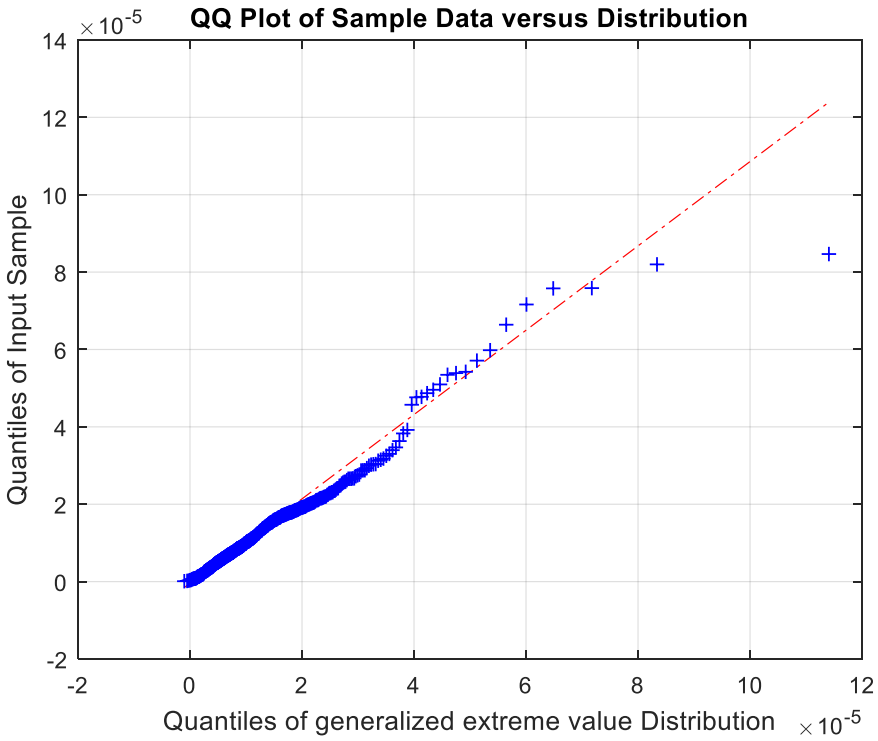


Figure 6.22 *Q-Q plot of the bias in the radial component against the generalized extreme value distribution.*

Despite this discrepancy in the tail, the Kolmogorov-Smirnov test confirmed the zero hypothesis that the empirical biases and amplitudes are GEV distributed. Therefore, for the purpose of modelling the error in the IGC products, the biases a_0 and the amplitudes a_1 and a_2 are simulated using the GEV distribution.

The phases Φ_1 and Φ_2 are another important factor since they determine the correlations between error components for a given satellite. They have been chosen to match the correlation between the errors in the orbit's components and the error in the clock. It is possible to see from **Table 6.8** that the error in the radial direction is the most correlated with the clock's error, while the cross-

track and along-track errors are the least correlated with the error in the precise clocks, with the first one being slightly more correlated than the second one.

Table 6.8 *RMS and 95th percentile of the correlation coefficients between the clocks' error and the orbits' errors in the radial, cross-track and along-track components.*

	Radial	**Cross-track**	**Along-track**
RMS	0.38	0.28	0.28
95th percentile	0.68	0.47	0.49

The proposed model has been used to rigorously simulate the real-time precise products for GPS, as well as for Galileo. In order to extend the findings that have been presented throughout this paragraph to the Galileo products, it is important to understand what the periods of the sinusoids used to fit the products' error to the second order Fourier expansion represent.

As previously stated the error in the IGC products can be approximated by the sum of two sinusoids with periods equal to 23 hours and 56 minutes, and to 11 hours and 58 minutes. While the second period is unequivocally the orbital period of the GPS constellation, understanding the nature of the 23 hours and 56 minutes period requires further attention. Indeed, this period can either define the Earth rotation period or the repeatability period of the GPS constellation, i.e. the time between two subsequent passes of a GPS satellite over the same location on the globe. If a receiver on the Earth sees a given GPS satellites at the zenith every 23 hours and 56 minutes, for Galileo the geometry repeats itself exactly the same after 10 days. Therefore, it is crucial to figure out whether the second component in the precise products errors is defined by the Earth rotation or by the constellation repeatability.

Since real-time Galileo products were not available when the simulator was firstly designed, a cross-analysis using GLONASS products was performed with the aim of studying the periods in the products' error. Unfortunately, only GPS data were decoded and stored in the CDDIS repository. However, in the computation of the real-time products, most ACs contributing to the IGS RTS estimate the precise clocks by fixing the orbits with the predicted half of the ultra-rapid products (IGS, 2018b). For this reason, the spectrum of the difference between the GLONASS ultra-rapid (predicted half) products, IGV, and the ESA final products in a four-weeks period ranging between GPS weeks

1917 and 1920 was studied. To validate the assumed hypothesis that the error in the real-time products can be approximated by two sinusoids with periods of 23 hours and 56 minutes, and of 11 hours and 58 minutes, the spectrum of the error in the IGV products should have a peak at the orbital frequency and a second peak at either the geometry repeatability or Earth rotation frequencies. The GLONASS constellation repeats itself exactly the same every eight days, while the geometry is repeated with different satellites every day. **Figure 6.23** shows the spectrum of the errors in the IGV orbits' components for GLONASS PRN 23. Unlike **Figure 6.14**, **Figure 6.15**, and **Figure 6.16**, in **Figure 6.23** the frequencies on the x axis are in units of times-per-GLONASS-orbit, which has a period of 11 hours and 15 minutes. As per the GPS case, the spectrum for GLONASS shows a peak at a frequency of once-per-orbit in all the orbit's components. Another peak is visible, particularly for the along-track component, at a frequency of roughly 0.47 times-per-orbit. This frequency corresponds to a period of 23 hours and 56 minutes. This study confirms what was found in the analysis of the GPS orbits and clocks, and it clarifies that the error in the real-time products can be modelled as sum of two sinusoids with periods equal to the Earth rotation period and to the constellation orbital period.

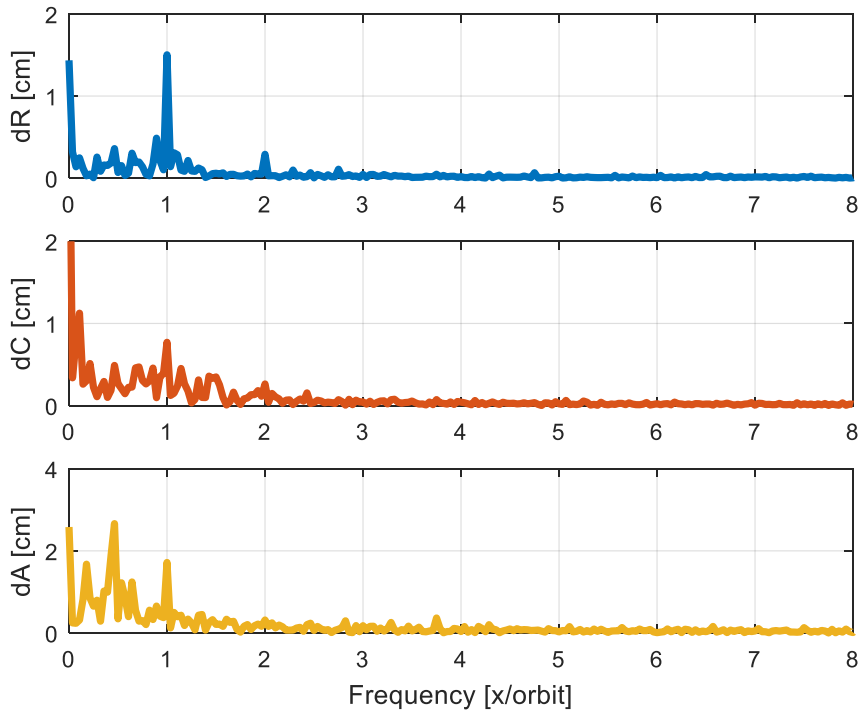


Figure 6.23 *Spectrum of the error in the radial (top), cross-track (middle), and along-track (bottom) orbit components. GLONASS PRN 23. On the x axis, the frequencies as in units of times-per-orbit.*

6.4 Randomness test

The simulation strategy that has been presented relies on the random number generators of Matlab. In this section, the results of a few tests to prove that the Matlab functions “randn”, which outputs normally distributed numbers, and “rand”, which outputs uniformly distributed numbers are close to be actually random. To do so, the Q-Q plot and the Kolmogorov-Smirnov test (Erto, 2008) are considered. These tests were already used in the previous Paragraph to check whether the biases and amplitudes of the errors in the precise orbits and clocks followed a GEV distribution. Two vectors of one million elements each were generated using the “rand” and “randn” functions. In both cases, the Kolmogorov-Smirnov test accepted the zero hypothesis that the randomly generated numbers followed the theoretical distributions.

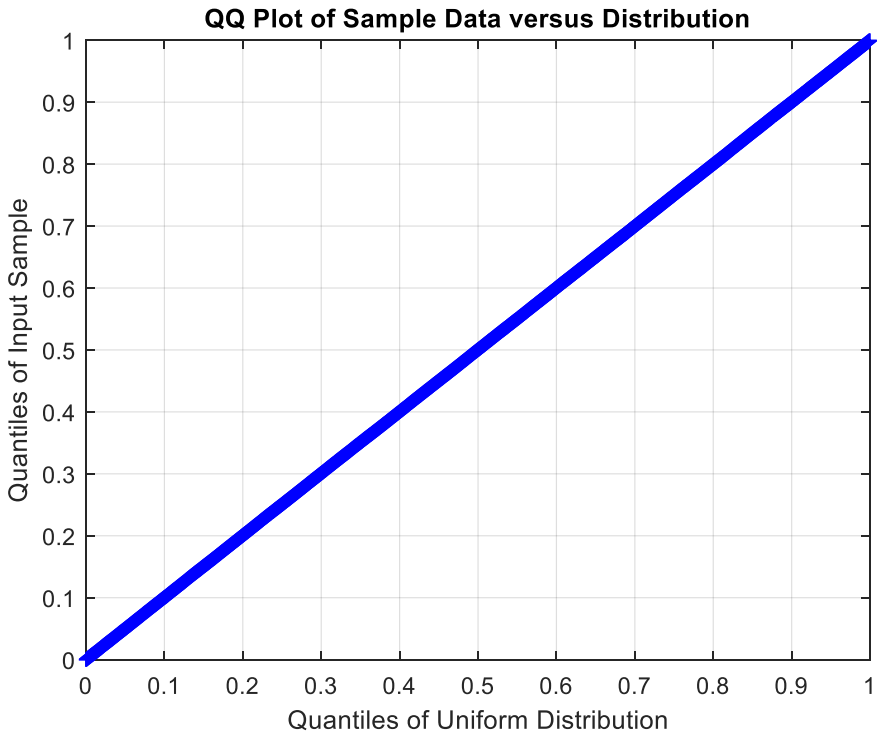


Figure 6.24 *Q-Q plot to prove that the “rand” function of Matlab generates uniformly distributed numbers.*

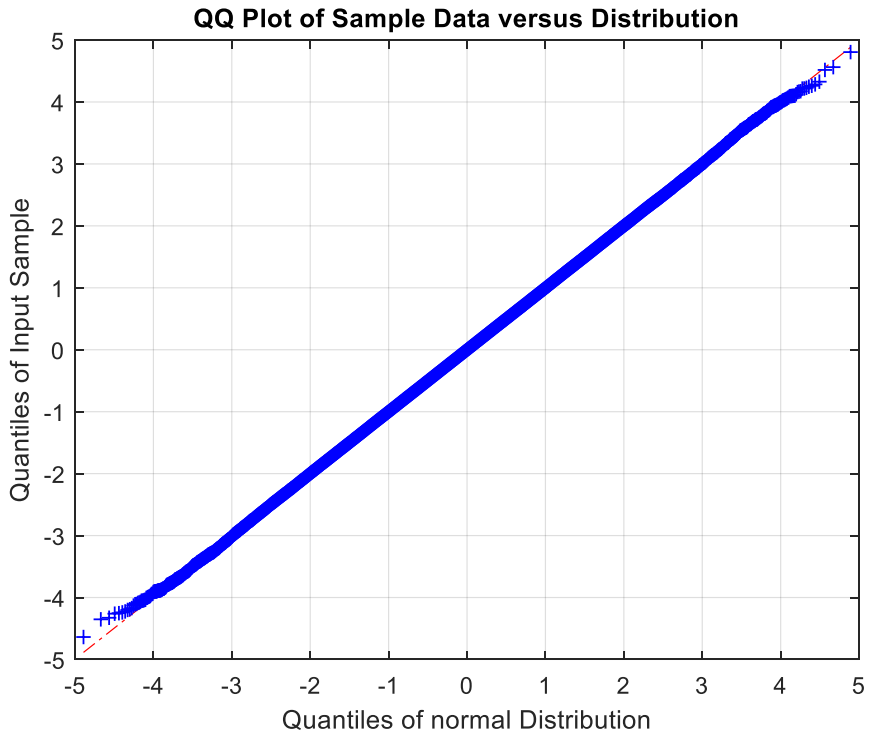


Figure 6.25 *Q-Q plot to prove that the "randn" function of Matlab generates uniformly distributed numbers.*

As a visual support, the Q-Q plots for the two vectors are shown in **Figure 6.24**, for the uniformly distributed vector, and in **Figure 6.25**, for the normally distributed vector. In both cases, the blue crosses are very well distributed along the red line, meaning that the agreement with the theoretical distribution is extremely solid.

6.5 Validation using real GPS measurements

This simulator was validated against real GPS data recorded between GPS weeks 1917 and 1920. Ten stations within the IGS global network and showed in **Figure 6.26** were considered. These are AIRA in Japan, AMC2 in the USA, BOGT in Colombia, CUSV in Thailand, FFMJ in Germany, HLFX in Canada, KERG in the Kerguelen Islands, M0SE in Italy, PERT in Australia, and SEY2 in the Republic of Seychelles. Similarly to the network in Section 5, these stations have been selected within the IGS multi-GNSS stations according to the following criteria:

- They had not to be included in data processing for the generation of the GPS products provided by the IGS Real-Time Service. This to avoid any correlation between observation and products error.

- They needed to be globally distributed in order to have a global outlook of the GPS satellites visibility and geometry conditions.
- Their position had to be included in the IGS SINEX files to have a reference for the computation of the errors and convergence times.



Figure 6.26 *IGS stations used to validate the multi-frequency GPS/Galileo simulator.*

Table 6.9 *Coordinates of the IGS stations used to validate the multi-frequency GPS/Galileo simulator.*

Station	Latitude [deg]	Longitude [deg]	Height [m]
AIRA	31.8240611	130.5995917	314.64
AMC2	38.8031250	-104.5245944	1912.4898
BOGT	4.6400731	-74.0809396	2576.7782
CUSV	13.7359139	100.5339083	76.06
FFMJ	50.0905778	8.6649639	178.2
HLFX	44.6835500	-63.6112778	3.10
KERG	-49.3514669	70.2555239	73.009
M0SE	41.8931139	12.4932583	120.6
PERT	-31.8019000	115.8852000	12.9
SEY2	-4.6736512	55.4794536	538.8156

Float PPP solutions were achieved by processing the IF combination between observations on L1 and L2 frequencies in POINT. The IGC products were used to compute the position of the transmitting satellites and to account for their

clock offsets. The GPT tropospheric model, together with the associated GMF, was used to mitigate the effect of the wet and dry tropospheric delay. The residual wet ZTD was estimated in the Kalman filter. Relativistic effects, including the Shapiro delay, phase wind-up effect and site displacement effects were also considered in the data processing. Satellite and receiver antenna PCO and PCV, stored in the ANTEX file, were applied. The PPP solutions obtained from the POINT software were, then, compared to the double-differenced (DD) solutions, included in the SINEX file, which are taken as reference truth.

Existing data gap in the IGC clocks had a negative impact on the daily solutions. To avoid such data gaps, each daily RINEX observation file was split in two shorter files lasting for 6 hours. The first one from midnight to 6am, the second one from midday to 6pm. Therefore, a total of 560 data points were analysed.

At the same time, the same stations were simulated with the GPS/Galileo Simulink. The simulation scenario assumed a static receiver placed in an open environment with excellent satellites visibility. IGS (2017) lists the conventions that all IGS stations must follow and it clearly states that "the antenna must be setup to minimize code and phase reflections (multipath), by mounting it away from close reflecting surfaces or by applying some passive protection directly below the antenna". As a consequence, in this validation, the effect of multipath on simulated pseudorange and carrier phase measurements was neglected. The simulator was run 55 times per station, to provide a sufficient number of data points to characterize the general behaviour of the processing algorithm. Therefore a total of 550 simulated data were considered.

Table 6.10 and **Table 6.11** summarize the models included in the float PPP processing based on real and simulated data, respectively. Beside the choice of the precise products, the main difference between the two PPP processing is that the corrections for the antenna phase centres and for the site displacements are not considered when POINT processes the simulated measurements, since they are not affected by these errors.

The metrics used to validate the simulator are the 3D positioning error, as well as the error in the north, east, and up components, at the end of the six hours data processing, and the time these errors take to converge below 10 cm. **Table 6.12** and **Table 6.13** show the median of the errors and convergence times

obtained by processing the simulated and real GNSS measurements recorded by each station with POINT.

Table 6.10 *Model included in the PPP data processing of real data.*

Error source		Model	Note
Satellite	Position	IGC precise orbits	Included in SP3 files and sampled every 30 seconds. No interpolation needed
	Clock offset	IGC precise clocks	Included in RINEX CLK files and sampled every 30 seconds. No interpolation needed.
	Relativistic effects	Ashby (2003)	The largest delays due to orbit eccentricity and Sagnac effect, as well as the smaller Shapiro delay and the J_2 effect, are considered.
	Antenna phase centre offset	ANTEX file igs08_1882.atx	No PCV are applied.
	Phase wind-up	Wu et al. (1993)	
Atmosphere	Troposphere	GPT and GMF	Wet ZTD estimated in the EKF.
	Ionosphere	IF combination	L1-L2
Site displacement	Solid Earth tides	Petit and Luzum (2010)	
	Ocean tides	Petit and Luzum (2010)	Site dependent amplitudes and phase are provided by the ocean loading service.
	Pole tides	Petit and Luzum (2010)	
Receiver	Antenna phase centre offset	ANTEX file igs08_1882.atx	

Table 6.11 *Model included in the PPP data processing of simulated data.*

Error source		Model	Note
Satellite	Position	Simulated real-time orbit products.	Included in SP3 files and sampled every 30 seconds. No interpolation needed
	Clock offset	Simulated real-time clock products	Included in RINEX CLK files and sampled every 30 seconds. No interpolation needed.
	Relativistic effects	Ashby (2003)	The largest delays due to orbit eccentricity and Sagnac effect, as well as the smaller Shapiro delay and the J_2 effect, are considered.
	Antenna phase centre offset	Not applied.	The real-time orbits are assumed to be computed with respect to the antenna phase centres.
	Phase wind-up	Not applied.	The phase wind-up effect doesn't affect the simulated carrier phase measurements.
Atmosphere	Troposphere	GPT and GMF	Wet ZTD estimated in the EKF.
	Ionosphere	IF combination	L1-L2
Site displacement	Solid Earth tides	Not applied.	
	Ocean tides	Not applied.	
	Pole tides	Not applied.	
Receiver	Antenna phase centre offset	Not applied.	The simulated observations are free from PCOs.

Even though the IGC products on average have SISRE of roughly 18 cm, they are still able to provide a static PPP solution with errors between several millimetres and a few centimetres. Indeed, it is possible to see from the "Real data" columns in **Table 6.12** that the horizontal components have a precision ranging from 0.69 cm, for the north error in CUSV, to 2.30 cm, for the east error in AMC2. In general, north is the most precise horizontal component. The only

exception is in HLFX, where the north error is slightly larger than the east error. However, the differences are meaningless, being only 0.1 mm. Apart from AMC2, as expected, the vertical component is always less precise than the horizontal ones, with errors as large as 4.33 cm in PERT. The "Simulated data" columns present errors that are comparable to the real ones. The east errors are never larger than 1.6 cm, while the north component always have millimetres level of accuracy. The vertical error is larger than the horizontal one, ranging between 1.98 cm and 3.74 cm. By comparing real and simulated results for a specific station, generally the 3D errors are quite similar. For example, they differ by only 7% for CUSV. On the other side, large discrepancies are visible for FFMJ, where the 3D error for the simulated data is almost twice as large as the one for the real data. Similarly, the times that the simulated solutions take to convergence below 10 cm are quite close to the convergence times for the real solutions. The north convergence requires between 7 and 18 minutes for the real cases, while it takes between 11 and 20 minutes for the simulated scenarios. The east component has a slower convergence than the north. Indeed, actual users have to wait for 16 to 68 minutes to have the east component below 10 cm of precision. In case of simulated measurements, the east convergence is between 17 and 64 minutes. The vertical convergence can, in most cases, be as slow as the east convergence. If for real data, the vertical convergence time ranges between 25 and 84 minutes, it is between 23 and 64 minutes using the GPS/Galileo Simulink model. The comparison between the results for a single station shows that, in most cases, the Simulink model is very close to the reality. Indeed the 3D convergence time with real and simulated data differ by no more than 10% for CUSV, FFMJ, HLFX, KERG, and M0SE. However, **Table 6.13** also highlights significant differences, even by a factor of 2.9, in the 3D convergence for AIRA, BOGT, and PERT.

Although **Table 6.12** and **Table 6.13** show some considerable discrepancies between real and simulated data for a specific stations, it is important to consider that there exist some environmental and hardware components, affecting the real measurements and the PPP performances, that could not be included into the statistical models adopted when building the simulated GNSS measurements. Despite these specific factors, the GPS/Galileo Simulink was demonstrated to be extremely accurate for the purpose of characterizing the

general behaviour of the PPP data processing, thus validating the simulation tool.

Table 6.12 *Median of the positioning errors for simulated and real data. Values in units of centimetres.*

	Real data				Simulated data			
Station	3D	North	East	Up	3D	North	East	Up
AIRA	3.22	0.82	1.14	2.79	3.93	0.61	1.52	3.40
AMC2	4.25	1.85	2.30	2.21	3.17	0.58	1.69	2.24
BOGT	4.49	1.40	1.73	3.36	2.57	0.65	1.12	1.98
CUSV	3.90	0.69	1.54	2.79	3.62	0.36	1.28	3.01
FFMJ	2.13	0.70	0.89	1.28	4.21	0.43	1.47	3.74
HLFX	5.29	1.60	1.59	4.28	4.03	0.61	0.91	3.43
KERG	3.08	0.72	1.25	2.43	3.61	0.62	0.86	3.25
M0SE	2.79	0.68	0.69	1.81	3.16	0.57	0.91	2.76
PERT	5.07	0.75	1.89	4.33	3.49	0.48	1.60	2.76
SEY2	3.70	0.99	1.62	2.44	3.30	0.60	0.93	2.52

Table 6.13 *Median of convergence times for simulated and real data. Values in units of minutes.*

	Real data				Simulated data			
Station	3D	North	East	Up	3D	North	East	Up
AIRA	92	10	68	70	42	13	32	27
AMC2	66	10	27.5	45	82	16	64	64
BOGT	75	7	31	61	35	15	21	28
CUSV	59	8	30	54	53	16	27	47
FFMJ	43	7	16	25	46	13	31	26
HLFX	49	8	33	29	44	16	24	33
KERG	48	12	31	25	43	15	25	23
M0SE	69	12	34	46	62	20	44	44
PERT	116	18	28	84	40	13	32	25
SEY2	64	8	30	40	41	11	17	38

6.6 Chapter summary

Given the limitations in assessing the performance of PPP using triple-frequency GPS and Galileo real-data, in this research a simulation tool was designed in Simulink and Matlab environments. This simulator is able to model GNSS measurements as well as precise PPP products.

The most common delays affecting the code and phase pseudorange were considered using state of the art models. In particular, the effect of the wet and

dry troposphere was simulated using the EGNOS tropospheric model (Penna et al., 2001). This model is based on look-up tables of the meteorological parameters used to compute the wet and dry ZTD. A further common delay was added, in order to account for some uncertainty in the model. The well-known Klobuchar model (J. A. Klobuchar, 1987) was adopted to characterize the ionospheric delay in GPS and Galileo triple-frequency measurements. The multipath was assumed to be a first-order Gauss-Markov process (Khanafseh et al., 2018; McGraw et al., 2000; O'Keefe et al., 2006) with a correlation time constant that depends on the type of simulation. It is larger for static scenarios and shorter for kinematic scenarios. Following Simsky et al. (2008), three groups have been defined to characterize the effect of multipath on pseudorange measurements: a high multipath group, which includes all the signals that are more sensitive to multipath (Galileo E1-B/C and E6-B/C, and GPS L1 and L2); a medium multipath group (Galileo E5a and E5b, and GPS L5); and a low multipath group (Galileo E5, E1-A, and E6-A). The magnitude of the multipath for each group decreases exponentially as the elevation angle of the transmitting satellite increases. A similar model, with much smaller magnitude, was defined for the multipath on the carrier phase measurements. The pseudorange and carrier phase noise was assumed to be a white Gaussian noise with a standard deviation depending on the $CN0$ of the incoming signal. Richardson et al. (2016) was taken as reference for the definition of the standard deviation of the measurements noise. The so simulated triple-frequency GNSS measurements are finally logged in a RINEX 2.11, ready to be processed by GNSS data processing software, such as the POINT software.

Unlike other works based on simulated data, where the error in the precise products is either neglected (Shen and Gao, 2006) or modelled using random numbers generators (Juan et al., 2012; Miguez et al., 2016), in this research a rigorous analysis on the difference between the IGC and ESA products was conducted with the aim of defining an innovative model for the simulation of the real-time precise products. This study demonstrated that the error in the IGC products can be modelled as a sum of two sinusoids. The first one has a period equal to the orbital period of the GNSS constellation (11 hours and 58 minutes for GPS, 14 hours and 4 minutes for Galileo), and the second one has a period

equal to the Earth rotation period (23 hours and 56 minutes). The simulated precise products can be logged in SP3c and RINEX clock 2.0 files.

This system was validated against real GPS observations. A total of 560 data points, spatially and timely distributed, were analysed. Despite some physiological discrepancy due to specific environmental and hardware components, the GPS/Galileo Simulink here proposed was found to be an accurate tool to characterize the general behaviour of PPP.

Chapter 7

Single and multi-constellation PPP with simulated data

Parts of this chapter have been published in Basile et al. (2019), (2018a), (2018b), (2017).

Chapter 6 described the multi-frequency GPS/Galileo Simulink tool used, in this research, to simulate the GNSS observables and the precise products for PPP. The error components affecting the pseudorange and carrier phase measurements, as well as the precise products, can be divided into a deterministic component and a stochastic component. Deterministic elements are, for example, the general behaviour of the ionospheric and tropospheric delays affecting the GNSS measurements or the periods of the two sinusoids used to model the error in the real-time orbits and clocks, while stochastic elements are, for instance, the residual error in the tropospheric delay, the pseudorange noise and the effect of the multipath. The output of a simulation run greatly depends on the realization of the random variables defining the stochastic component of the error models. A typical method to perform stochastic simulations is the Monte Carlo method. This term became popular when it was adopted by Enrico Fermi, Stanislaw Ulam, and John von Neumann during World War II as a code word for secret work on problems related to the atomic bomb. The Monte Carlo method consists on simulating a large number of results of a given phenomenon, that is a function of random variables, by repeating the simulation many times using different realizations of the random variables (Erto, 2008).

In this chapter, the Monte Carlo approach is followed to analyse the PPP solutions achieved by processing two-frequency IF combinations of pseudorange and carrier phase measurements, which have been simulated through the GPS/Galileo Simulink tool, in different scenarios.

A preliminary study on different GPS and Galileo IF combinations is performed with the aim to find the best IF combinations for PPP. In order to have results that only depend on stochastic variables related to the quality of the measurements, the error in the precise orbits and clocks is here neglected. Different levels of multipath will be considered, ranging from no multipath to the multipath characteristics described in Section 6.2.4.

Next, the best GPS and Galileo IF combinations will be used to compare the positioning performance of single and multi-constellation PPP in open sky environments. For this purpose, the errors in the precise products will be modelled as described in Section 6.3.

Finally, satellite availability, geometry conditions, and positioning performance achievable in an urban area with GPS+Galileo will be analysed. For this scenario the neighbourhood of the UCL campus was simulated using realistic building boundaries (Adjrad and Groves, 2016; Wang et al., 2012), i.e. the minimum elevation angle above which GNSS signals can be received due to building obstruction.

7.1 Preliminary study on the best two-frequency IF combinations

Within the factors that impact on the PPP solutions figure the quality of the GNSS measurements and the one of the precise products. In this section, a preliminary study aimed to identify what are the best two-frequency IF combinations to be used in PPP is performed. To eliminate the effect of the PPP products from the solution, the error in the simulated orbits and clocks is here neglected.

A subset made of four stations out of the ten that were used in Section 6.4 for the validation of the simulator is adopted. These are AIRA in Japan, HLFX in Canada, PERT in Australia, and SEY2 in the Republic of Seychelles. These four stations have been chosen to have a global outlook on the user-to-satellite geometry conditions. The simulator was run 50 times per station for 3 hours. The GNSS observation rate was set to 30 seconds.

Initially, as per Section 6.4, the receiving antenna was supposed to be located away from reflecting surfaces, and therefore the effect of multipath was neglected in this preliminary test. The simulated GPS and Galileo measurements are processed in single-constellation PPP mode with the POINT software.

For the computation of the float PPP solutions, it is extremely important to finely tune the Kalman filter. Tuning a Kalman filter means selecting the values that populate the three main matrices involved in the filter: the measurement noise covariance matrix, the process noise covariance matrix, and the initial state errors covariance matrix. Following the results in Richardson et al. (2016),

which showed that the errors in the Galileo pseudoranges were lower than the errors in the GPS pseudoranges, when choosing the values for the elements in the measurements noise covariance matrix, more weight was given to the Galileo pseudoranges than the GPS ones. **Table 7.1** summarizes the assumed standard deviation of the pseudorange errors for GPS and Galileo. The error in L2 is expected to be the largest, while the Galileo E5 pseudorange is predicted to be the most accurate. The standard deviation of the carrier phase error is equally set to 0.5 cm for both GPS and Galileo measurements.

In this configuration of the Kalman filter, the state vector includes the three components of the position, the receiver clock offset, and the residual wet ZTD, after the GPT tropospheric model, together with the associated GMF, was applied to mitigate the effect of the wet and dry tropospheric delay. The standard deviations of the initial error and process noise for the elements included into the state vector are in **Table 7.2**.

Table 7.1 *Expected standard deviation of the error in GPS and Galileo pseudoranges that was assumed when designing the Kalman filter. Units of meters.*

L1	L2	L5	E1	E5a	E5b	E5	E6
0.4	0.7	0.3	0.3	0.2	0.2	0.1	0.3

Table 7.2 *Standard deviations of the initial error in the state vector and of the process noise used to tune the Kalman filter.*

State vector elements	Initial error	Process noise
Position components	2.0 m	0.0 m/√s
Receiver clock offset	1000.0 m	10.0 m/√s
Residual wet ZTD	0.1 m	$3.0 \cdot 10^{-3}$ m/√s
Ambiguities	1000.0 cycles	0.0 cycles/√s

Figure 7.1 compares the errors in the PPP solutions based on the IF combination between GPS measurements on L1 and L2 and on the IF combination between the measurements on L1 and L5 recorded by the simulated station SEY2. The errors have been computed with respect to the reference position input in the simulator. While both solutions reach a similar level of precision after three hours, the convergence for L1-L5 IF is quicker. Indeed, as it is also shown in **Table 7.3** the horizontal and vertical error components obtained with L1-L5 IF and L1-L2 IF only differ by a couple of millimetres for 95% of the time. Larger

differences are observable in **Table 7.4**, where the statistics of the convergence times are compared. The horizontal and vertical solutions computed from the L1-L5 IF take 4.5 and 1.5 minutes less than the L1-L2 IF solutions to converge below 10 cm. This result is not surprising, since the quality of the pseudorange measurements is one of the key factors that impact on the convergence time of the PPP solution (Abou-Galala et al., 2017). Having assumed a much smaller error in the pseudorange on L5 than the one in the L2 pseudorange, it was expected that L1-L5 IF would lead to improved PPP performance.

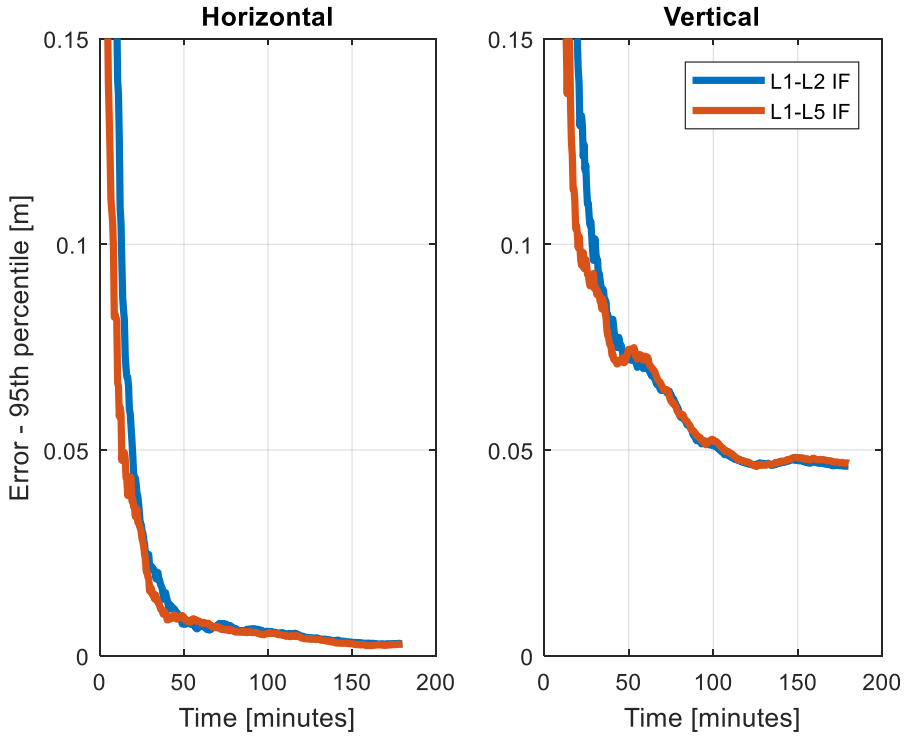


Figure 7.1 *Comparison between the horizontal (left) and vertical (right) errors obtained by processing the GPS L1-L2 IF (blue) and L1-L5 IF (red) combinations. Station SEY2.*

The PPP solutions obtained by processing the Galileo E1-E5a IF, E1-E5b IF, E1-E5 IF, and E1-E6 IF combinations are compared in **Figure 7.2**, **Table 7.5**, and **Table 7.6**. As in the comparison between the GPS solutions, the precision in the four solutions is very close. For 95% of the time, they differ by no more than 0.08 cm horizontally, and by 0.07 cm vertically. More noticeable differences are apparent in the convergence times. The solution computed from the IF combinations between E1 and E6 are the slowest to converge. It takes 10 and 19 minutes for the horizontal and vertical errors to go below 10 cm, 95% of the time. On the other hand, it only takes 5.5 and 14 minutes to have a converged horizontal and vertical solution by either using E1-E5a IF or E1-E5 IF.

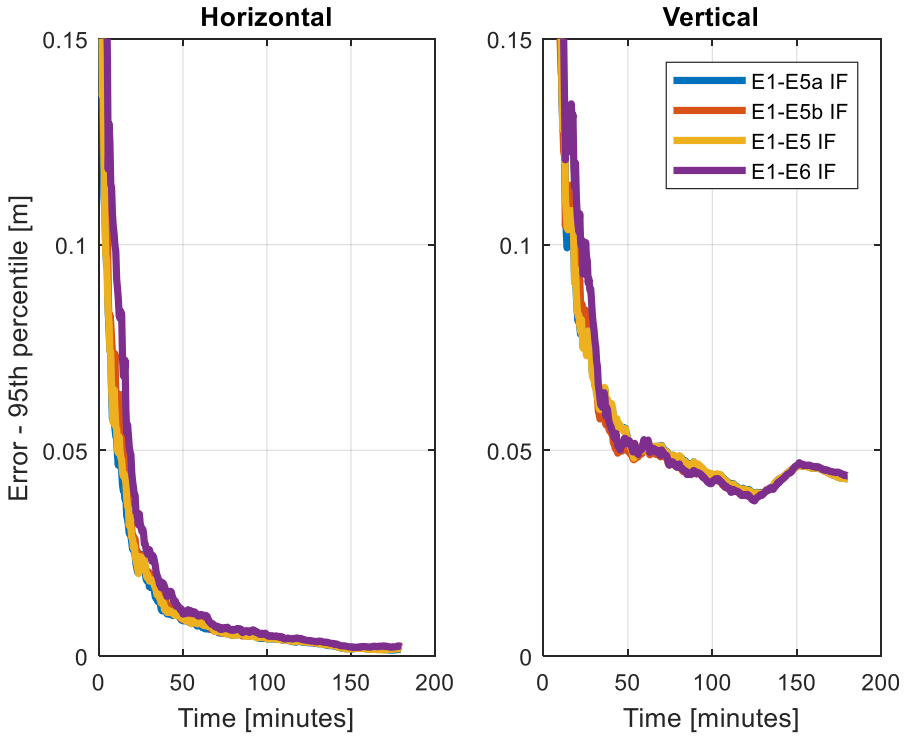


Figure 7.2 *Comparison between the horizontal (left) and vertical (right) errors obtained by processing the Galileo E1-E5a IF (blue), E1-E5b IF (red), E1-E5 IF (yellow), E1-E6 IF (purple) combinations. Station SEY2.*

Table 7.3 *Comparison between the horizontal (H) and vertical (Up) errors achieved using the L1-L2 IF and L1-L5 IF combinations. 95th and RMS over the four simulated stations. Benign environment. Values in units of cm. In bracket is the relative difference.*

	L1-L2 IF		**L1-L5 IF**	
	H	Up	H	Up
95th percentile	0.70	4.53	0.95 (+35.7%)	4.55 (+0.4%)
RMS	0.43	3.53	0.55 (+27.9%)	3.53 (0%)

Table 7.4 *Comparison between the horizontal (H) and vertical (Up) convergence times achieved using the L1-L2 IF and L1-L5 IF combinations. 95th and RMS over the four simulated stations. Benign environment. Values in units of minutes. In bracket is the relative difference.*

	L1-L2 IF		**L1-L5 IF**	
	H	Up	H	Up
95th percentile	12.5	16.5	8.0 (-36.0%)	15.0 (-9.1%)
RMS	8.0	9.0	4.0 (-50.0%)	7.5 (-16.7%)

Table 7.5 *Comparison between the horizontal (H) and vertical (Up) errors achieved using the E1-E5a IF, E1-E5b IF, E1-E5 IF, and E1-E6 IF combinations. 95th and RMS over the four simulated stations. Benign environment. Values in units of cm. In bracket is the relative difference.*

	E1-E5a IF		**E1-E5b IF**		**E1-E5 IF**		**E1-E6 IF**	
	H	Up	H	Up	H	Up	H	Up
95th percentile	0.87	4.11	0.90 (+3.4%)	4.04 (-0.2%)	0.87 (0.0%)	4.12 (+0.2%)	0.95 (+9.2%)	4.02 (-2.2%)
RMS	0.51	3.21	0.52 (+4.0%)	3.22 (+0.3%)	0.51 (0.0%)	3.20 (-0.3%)	0.53 (+3.9%)	3.22 (+0.3%)

Table 7.6 *Comparison between the horizontal (H) and vertical (Up) convergence times achieved using the E1-E5a IF, E1-E5b IF, E1-E5 IF, and E1-E6 IF combinations. 95th and RMS over the four simulated stations. Benign environment. Values in units of minutes. In bracket is the relative difference.*

	E1-E5a IF		**E1-E5b IF**		**E1-E5 IF**		**E1-E6 IF**	
	H	Up	H	Up	H	Up	H	Up
95th percentile	5.5	14.0	6.5 (18.2%)	16.0 (14.3%)	5.5 (0.0%)	14.0 (0.0%)	10.0 (81.8%)	19.0 (37.7%)
RMS	2.0	10.0	2.5 (25.0%)	10.5 (5.0%)	2.5 (+2.5%)	10.5 (+5.0%)	4.5 (125.0%)	12.5 (25.0%)

Table 7.7 *Expected standard deviation of the error in GPS and Galileo pseudoranges that was assumed when designing the Kalman filter. Units of meters.*

L1	**L2**	**L5**	**E1**	**E5a**	**E5b**	**E5**	**E6**
1.0	1.3	0.8	1.0	0.8	0.8	0.4	1.0

From this preliminary comparison, the PPP solutions obtained using the Galileo E1-E5a IF and E1-E5 combinations seem to have nearly the same performance, even though the Galileo E5 signal have much improved ranging properties than E5a, thanks to its much larger bandwidth. The reason for this surprising behaviour can be found in the use of the IF combination with E1. Given that E1 represents the dominant source of error in the IF combinations (see Section 6.2.4), its noise is amplified by a factor of about 2.33 in the IF combination with E5 and by a factor of 2.26 when combined with E5a. At the same time, the smaller errors (than E1) in E5a is amplified by 1.26, while the one in E5 is amplified by 1.34. Therefore, depending on the noise level in the Galileo pseudoranges, there might be instances where the noise in the E1-E5 IF combination is close to the one in the E1-E5a IF, or even larger than that.

A second simulation scenario was created for each of the four stations. Here the receiver was assumed to be placed in a severe multipath environment, and therefore its effect must be considered. As described in Section 6.2.4, multipath was modelled as a Gauss-Markov process with a correlation time constant that was selected to match the characteristics of real data. Khanafseh et al. (2018) analysed the multipath time constant in various scenarios and found a median of 24 seconds for the kinematic tests. This value is adopted in this test to simulate the multipath in the pseudorange and carrier phase measurements.

Given the fact that, in the designed simulation scenarios, the GNSS observables are affected by multipath, larger values (than those in the previous test) were adopted to populate the observations error covariance matrix in the Kalman filter. The assumed weights for the GPS and Galileo pseudorange are listed in **Table 7.7**, while the carrier phase measurements were expected to have an error of 1 cm. On the other hand, the initial error and process noise for the state vector are assumed to be the same as those used in the previous scenario and reported in **Table 7.2**.

The RMS and 95th percentile of the horizontal and vertical error obtained by processing the simulated L1-L2 IF and L1-L5 IF measurements with POINT are in **Table 7.8**, while **Table 7.9** compares the convergence times. Like the previous test, the L1-L5 IF combination provides much better PPP performance than L1-L2 IF, particularly in terms of convergence time. About 3 minutes of improvement was registered in the convergence time below 10 cm (95%). The differences in the horizontal and vertical errors at the end of the data processing is still very small, although L1-L5 IF gives the most precise solution. Note that both the errors and convergence times in **Table 7.8** and **Table 7.9** are larger than the values in **Table 7.3** and **Table 7.4**. This is due to the multipath error affecting the GNSS measurements.

Similarly, the comparisons between the PPP performances achieved by the IF combinations for Galileo are in **Table 7.10** and **Table 7.11**. The differences in the precision is smaller than 3.5 mm, while larger discrepancies are shown in **Table 7.11** for the convergence times. The E1-E5a combination offers the quickest convergence. It only takes 49 and 44.5 minutes to have a horizontal and vertical error (95th percentile) smaller than 10 cm. While the E1-E6 IF is the worst combination; the solution computed with these frequencies linearly

combined is the least precise and the slowest to converge. The reason for this behaviour can be partly explained by the fact that pseudoranges on E6 are noisier than those on E5a. It must be also considered that the E6 frequency is closer to E1 than E5a, and, consequently, the intrinsic noise amplification factor brought by the IF combination in E1-E6 IF is larger than in E1-E5a IF. For the same reason, using E5 doesn't have any benefit to the PPP solution with respect to using E5a. Indeed, assuming negligible the errors in the E5 and E5a pseudoranges with respect to the ones in E1 pseudoranges, the E1-E5 IF combination has its noise amplified by a factor of 2.33, while the noise in E1-E5a IF is only 2.26 times larger than the one on E1. Of course, E5a and E5 also have a contribution to the noise in the IF combinations, however being amplified by only 1.26 and 1.33, respectively, their overall impact is only marginal. As a result, the error in the solution based on E1-E5 IF is up to 0.8 mm larger than the E1-E5a IF one and the convergence time is up to one minute slower.

Table 7.8 *Comparison between the horizontal (H) and vertical (Up) errors achieved using the L1-L2 IF and L1-L5 IF combinations. 95th and RMS over the four simulated stations. Values in units of cm. In bracket is the relative difference.*

	L1-L2 IF		**L1-L5 IF**	
	H	Up	H	Up
95th percentile	2.03	5.39	1.71 (-15.8%)	5.07 (-5.9%)
RMS	1.03	3.82	0.88 (-14.6%)	3.64 (-4.7%)

Table 7.9 *Comparison between the horizontal (H) and vertical (Up) convergence times achieved using the L1-L2 IF and L1-L5 IF combinations. 95th and RMS over the four simulated stations. Values in units of minutes. In bracket is the relative difference.*

	L1-L2 IF		**L1-L5 IF**	
	H	Up	H	Up
95th percentile	34.0	47.5	31.0 (-8.8%)	50.0 (+5.3%)
RMS	21.5	20.5	20.0 (-7.0%)	19.5 (-4.9%)

Table 7.10 *Comparison between the horizontal (H) and vertical (Up) errors achieved using the E1-E5a IF, E1-E5b IF, E1-E5 IF, and E1-E6 IF combinations. 95th and RMS over the four simulated stations. Values in units of cm. In bracket is the relative difference.*

	E1-E5a IF		**E1-E5b IF**		**E1-E5 IF**		**E1-E6 IF**	
	H	Up	H	Up	H	Up	H	Up
95th percentile	1.89	4.81	1.91 (+1.1%)	4.70 (-2.3%)	1.97 (+4.2%)	4.89 (+1.7%)	2.24 (+18.5%)	4.99 (+3.7%)
RMS	0.92	3.41	1.00 (+8.7%)	3.38 (-0.9%)	0.95 (+3.3%)	3.42 (+0.3%)	1.20 (+30.4%)	3.44 (+0.9%)

Table 7.11 *Comparison between the horizontal (H) and vertical (Up) convergence times achieved using the E1-E5a IF, E1-E5b IF, E1-E5 IF, and E1-E6 IF combinations. 95th and RMS over the four simulated stations. Values in units of minutes. In bracket is the relative difference.*

	E1-E5a IF		**E1-E5b IF**		**E1-E5 IF**		**E1-E6 IF**	
	H	Up	H	Up	H	Up	H	Up
95th percentile	49.0	44.5	54.0 (10.2%)	42.5 (-4.5%)	50.5 (+3.1 %)	45.5 (+2.2%)	67.0 (+36.7%)	55.5 (+24.7%)
RMS	32.0	24.0	32.5 (+1.6%)	26.0 (-18.7%)	32.0 (0.0%)	25.0 (+4.2%)	37.5 (+17.2%)	29.0 (+20.8%)

In conclusion, as expected the best GPS IF combination is the one between L1 and L5. Surprisingly, within the Galileo signals, E1-E5a IF offered the best PPP performance even though the pseudoranges on E5 have smaller noise and are less affected by multipath. For these reasons, the following analysis in the next sections will be based on the GPS L1-L5 IF and Galileo E1-E5a IF combinations. Galileo E1-E5 IF combination will be also considered to check whether there are some other instances when it can provide better solutions than E1-E5a IF. The research of possible ways to better exploit the Galileo AltBOC modulated signal in PPP represents one of the main drivers of this PhD project.

7.2 Open sky conditions

In this section, the static PPP solutions achieved using the best GPS and Galileo IF combinations, processed in single and multi-constellation mode, will be compared. For this purpose, a simulation scenario where a static GNSS receiver is assumed to be placed in an open sky area was designed. The locations where the receiver has been simulated are, once again, the four IGS stations as in the previous section: AIRA in Japan, HLFX in Canada, PERT in Australia, and

SEY2 in the Republic of Seychelles. The simulator was run 50 times per station with an observation rate of 30 seconds. Unlike the analysis in Section 7.1, the effect of the error in the precise orbits and clocks, which is simulated as in Section 6.3, is here considered.

In the first simulation case, the receiver was assumed to be placed in a benign environment with no nearby reflective surfaces, hence the effect of multipath is neglected. The simulated measurements are then processed, together with the simulated precise orbits and clocks, in static PPP mode with the POINT software. For this test, the expected errors used to populate the measurements noise covariance matrix in the Kalman filter, are assumed to be the same as those in the first test scenario of Section 7.1 and included in **Table 7.1**, while the values adopted to populate the covariance matrices of the initial errors and process noise are summarized in **Table 7.2**.

As previously stated, the metrics used in this analysis to define the positioning performance are the errors in the horizontal and vertical components of the float solution at the end of the data processing, and the time these errors take to converge below 10 cm. However, since for most ground applications, such as precision farming or positioning of vehicles in urban environments, the horizontal precision is more critical than the vertical one, more emphasis will be given to the horizontal solutions.

Figure 7.3 compares the static PPP horizontal solutions obtained by processing GPS and Galileo IF measurements recorded at SEY2 in single and multi-constellation mode. In the left subplot is the RMS of the errors over the 50 simulations, while the right subplot shows the 95^{th} percentile. The PPP solution computed from GPS L1-L5 IF measurements takes 4 minutes to have a RMS horizontal error below 10 cm and 7.5 minutes to have 95% of all the horizontal errors smaller than 10 cm. After three hours, 95% of the GPS solutions have a horizontal error smaller than 1.40 cm. Quicker convergence can be obtained if adopting either Galileo E1-E5a IF or E1-E5 IF combinations. The RMS of the horizontal error converges in 2.5 minutes, while the 95^{th} percentile is better than 10 cm after 5.5 minutes. At the end of the data processing, the static PPP solution computed with Galileo measurements reaches a precision of better than 1.56 cm for 95% of the time. Even better performance can be observed by adopting the GPS+Galileo multi-constellation system. On average, the

horizontal solution only takes 2 minutes to go below 10 cm, and 95% of the float solutions are converged after 4 minutes. Despite being in open sky conditions, big improvements are also detected in the precision level. The 95th percentile of the horizontal error is as small as 1.17 cm.

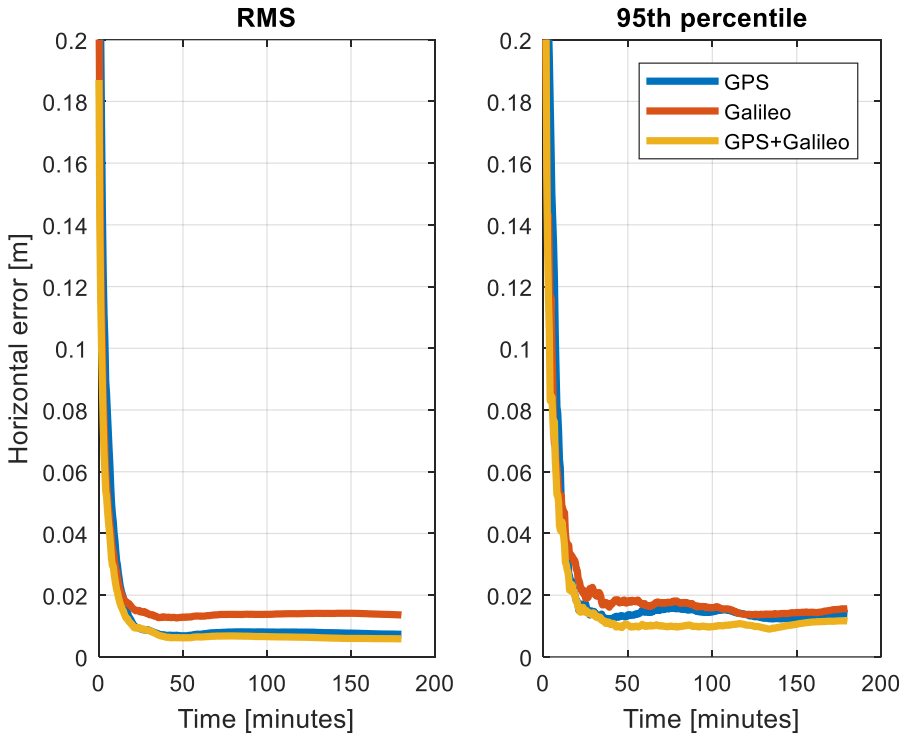


Figure 7.3 *Comparison between the horizontal error in the GPS (blue), Galileo(red), and GPS+Galileo (yellow) PPP solution. The left plot shows the RMS over 50 simulations, while in the right plot is the 95th percentile. Station SEY2. Benign environment.*

The reason why the simulated Galileo system guarantees faster convergence times than GPS, has to be found in the lower noise that was assumed in the code pseudoranges for Galileo (see Section 6.2.4). Indeed, it is was demonstrated in Abou-Galala et al. (2017) that the quality of the pseudorange measurements is one of the key factors that influence the convergence time of the PPP solution. Despite having worse pseudorange measurements, the GPS system still provides a more accurate horizontal solution than Galileo. Looking at **Figure 7.4**, we can observe larger HDOP values for Galileo than GPS, which explain why the GPS horizontal PPP solution is more accurate than the Galileo one.

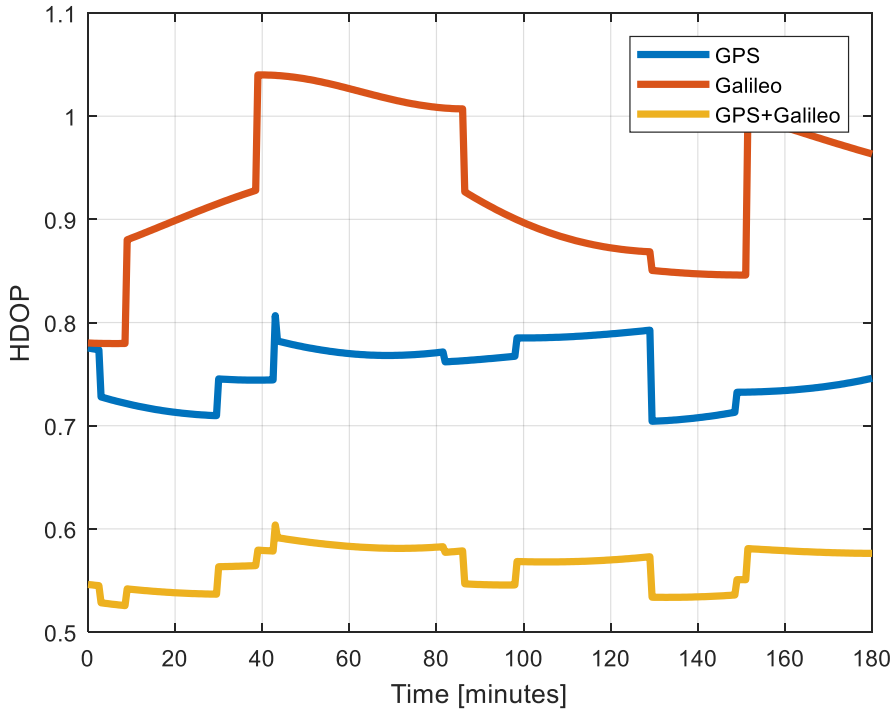


Figure 7.4 *Comparison between the HDOP in the GPS (blue), Galileo(red), and GPS+Galileo (yellow) case.*

Table 7.12 and **Table 7.13** summarizes the horizontal and vertical errors and convergence times for the four simulated stations obtained by processing GPS, Galileo, and GPS+Galileo measurements with POINT. The tables confirm the better performances of the Galileo system over GPS. Indeed, while on average the Galileo solution takes only 2.5 and 6.5 minutes to have a converged horizontal and vertical solution, users have to wait for 4 and 10.5 minutes before achieving a horizontal and vertical GPS solution with a precision of better than 10 cm. Also, for 95% of the times, the vertical error for GPS is 4 mm larger than the Galileo one. By adopting the GPS+Galileo system, further improvements can be observed. Given the open sky conditions, only small improvements were expected in the final precision. Indeed, on average, the horizontal and vertical error can be reduced roughly by 19% and by 4.31%, with respect to the GPS only case. However, the multi-constellation solution has its average convergence time reduced by a factor of two with respect to the one of the GPS only solution, thus validating the results presented in Shen and Gao (2006).

In the second simulation scenario, the errors affecting the GNSS measurements, which are simulated as described in Section 6.2.4, include also the multipath. It was assumed to behave as a Gauss-Markov process. The multipath correlation

time was assumed to be equal to 77 seconds for all the measurements. In Khanafseh et al. (2018), this value was found to be the median correlation time constant for the static multipath detected by a Novatel GNSS1500 antenna placed in proximity of a van with the front oriented in the east-west direction.

Table 7.12 *Comparison between the horizontal (H) and vertical (Up) errors in the GPS, Galileo, and GPS+Galileo PPP solutions. 95th and RMS over the four simulated stations. Benign environment. Values in units of centimetres. In bracket is the relative difference.*

	GPS		**Galileo**		**GPS + Galileo**	
	H	Up	H	Up	H	Up
95th percentile	2.13	5.54	3.02 (+41.8%)	5.14 (-7.2%)	1.70 (-20.2%)	4.83 (-12.8%)
RMS	1.10	3.71	1.47 (+33.6%)	3.48 (-6.2%)	0.89 (-19.1%)	3.55 (-4.3%)

Table 7.13 *Comparison between the horizontal (H) and vertical (Up) convergence times in the GPS, Galileo, and GPS+Galileo PPP solutions. 95th and RMS over the four simulated stations. Benign environment. Values in units of minutes. In bracket is the relative difference.*

	GPS		**Galileo**		**GPS + Galileo**	
	H	Up	H	Up	H	Up
95th percentile	8.0	15.5	7.5 (-6.2%)	15.5 (0.0%)	4.5 (-43.7%)	14.0 (-9.7%)
RMS	4.0	10.5	2.5 (-37.5%)	6.5 (-38.1%)	2.0 (-50.0%)	5.0 (-52.4%)

For this test, the expected errors in the measurements, initial state vector, and process, used to populate the three covariance matrices in the Kalman filter, are assumed to be the same as those in the second test scenario in Section 7.1 and included in **Table 7.7** and in **Table 7.2**. In this case the errors in the GPS and Galileo pseudoranges are quite the same, for this reason similar convergence times can be expected for this test.

Figure 7.5 compares the results for GPS L1-L5 IF, Galileo E1-E5a IF , and GPS+Galileo at the simulated station SEY2, while **Table 7.14** and **Table 7.15** summarizes the RMS and 95th percentile of the errors and convergence times for all the four simulated stations. Surprisingly, shorter convergence times are observed for the GPS solution with respect to the Galileo one. For 95% of the times, the horizontal solution computed from Galileo measurements take as much as 56.5 minutes to converge to centimetres level of accuracy, while the

GPS solution only takes 31 minutes. Beside the quality of the GNSS measurements, the main factor affecting the convergence time in PPP is the change in the user to satellites geometry. Being the Galileo satellites at a higher orbit than the GPS ones, and having a lower velocity, the user to Galileo satellites geometry has a lower change of rate. For this reason, in case the GPS and Galileo pseudoranges have comparable noise levels, the convergence in the GPS solution is faster than the Galileo one. Increasing the number of satellites by considering both constellations can further reduce the horizontal convergence to 16.5 minutes.

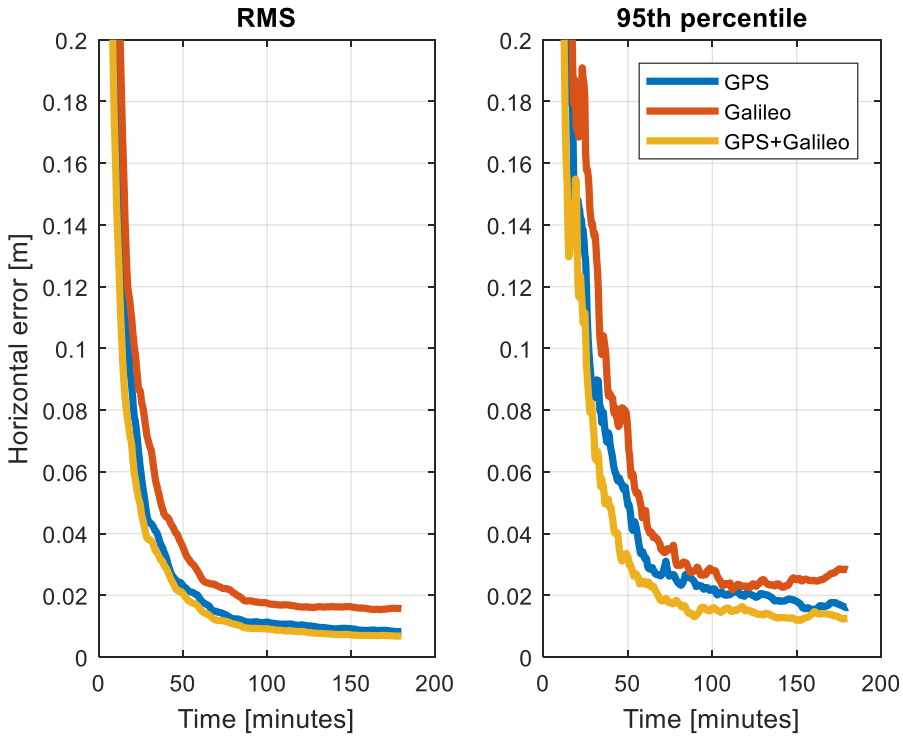


Figure 7.5 *Comparison between the horizontal error in the GPS (blue), Galileo(red), and GPS+Galileo (yellow) PPP solution. The left plot shows the RMS over 50 simulations, while in the right plot is the 95th percentile. Station SEY2. Multipath-rich site.*

Table 7.14 *Comparison between the horizontal (H) and vertical (Up) errors in the GPS, Galileo, and GPS+Galileo PPP solutions. 95th and RMS over the four simulated stations. Multipath-rich site. Values in units of centimetres. In bracket is the relative difference.*

	GPS		**Galileo**		**GPS + Galileo**	
	H	Up	H	Up	H	Up
95th percentile	2.54	5.78	3.75 (+47.6%)	5.36 (-7.3%)	1.86 (-26.8%)	5.00 (-13.5%)
RMS	1.28	3.73	1.82 (+42.2%)	3.41 (-8.6%)	0.96 (-25%)	3.47 (-7.0%)

Table 7.15 *Comparison between the horizontal (H) and vertical (Up) convergence times in the GPS, Galileo, and GPS+Galileo PPP solutions. 95th and RMS over the four simulated stations. Multipath-rich site. Values in units of minutes. In bracket is the relative difference.*

	GPS		**Galileo**		**GPS + Galileo**	
	H	Up	H	Up	H	Up
95th percentile	31.0	42.5	56.5 (+82.3%)	43.5 (+2.4%)	28.0 (-9.7%)	29.0 (-31.8%)
RMS	20.0	21.0	33.5 (+67.5%)	22.0 (+4.8%)	16.5 (-17.5%)	15.5 (-26.2%)

Although it was not specifically shown in the tables and figures, the exact same performance was seen when using the Galileo E1-E5 IF instead of the E1-E5a IF combination.

7.3 Urban area: University College of London

The poor signal visibility and continuity associated to urban environments together with the slow (re-)convergence time of PPP, usually, make it unsuitable for land navigation in cities. However, as demonstrated in the previous section, using dual constellations not only improves the visibility conditions, but also reduces the PPP convergence time. Therefore, it might be possible to extend the applicability of PPP to land navigation in urban areas.

In order to assess the positioning performance of two-constellation GNSS in these constrained environments, accurate 3D city models were necessary to realistically simulate urban areas. Unfortunately, such models were not available at the University of Nottingham. However, Dr. Paul Groves and Dr. Mounir Adjrad, who are acknowledged for this reason, shared the building boundaries for the neighbourhood of the UCL campus. In this way, this urban area could be precisely simulated with the GPS/Galileo Simulink tool. The building boundaries map, for a given location and azimuth angle (with 1° of resolution), the minimum elevation angle above which a satellite is visible due to building obstructions. They were computed based on the Ordnance Survey's 3D city models. These 3D city models can be downloaded from Digimap (https://digimap.edina.ac.uk), an online map and delivery service, operated by EDINA at the University of Edinburgh.

The locations in which the building boundaries were available are represented as blue dots in **Figure 7.6**. On the map, it is possible to recognize the front yard

of Wilkins Building in the UCL campus, a portion of Gower Street, University Street, and a portion of Huntley Street.

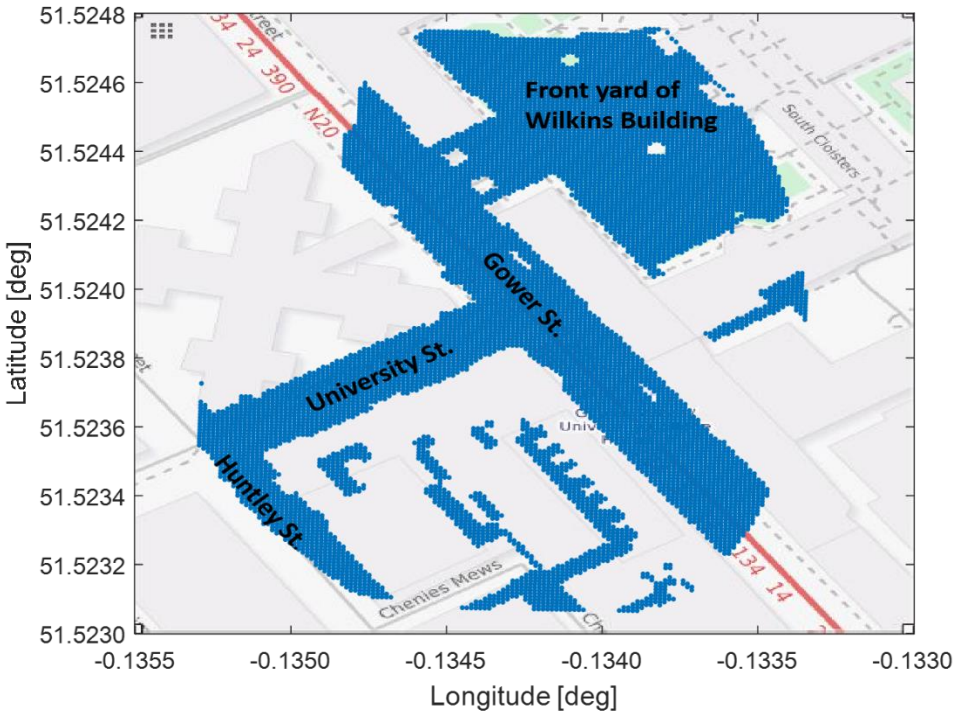


Figure 7.6 *Points in which the building boundaries were available. The background map was achieved from OpenStreet map.*

Satellites availability and geometry conditions were analysed in five sites within this map. **Figure 7.7** illustrates the locations of the five sites, while the sky plot of the building boundaries for each site is in **Figure 7.8**. Sites A, C, and E are three examples of streets that might be travelled when navigating a ground vehicle in European cities. Site A (Gower Street) is a three lane street plus footpaths with relatively short buildings (four-five stories) on each side of the road. It can be seen on the left side of **Figure 7.9**. Site C (University Street) is slightly narrower than Gower Street. It has only one lane, plus parking slots and footpaths on each side (visible in **Figure 7.9** right hand side and in **Figure 7.10** left hand side). As it is illustrated on the right side of **Figure 7.10**, site E (Huntley Street) is as large as University Street, but it is surrounded by taller buildings (six-seven floors), which make this site to be the most challenging in terms of signal obstruction. Indeed, the minimum elevation angle for signal visibility associated to site E can be as large as 79°. For sites B and D, three and four streets, respectively, form a junction.

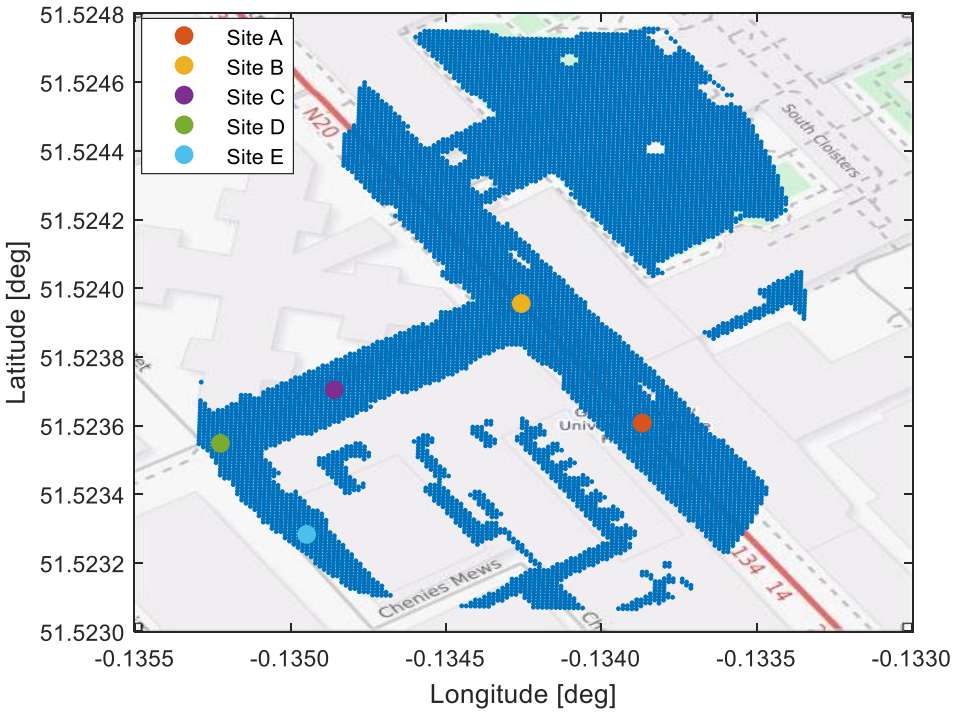


Figure 7.7 *Location of the urban sites that were considered in the satellites availability analysis. The background map was achieved from OpenStreet map.*

When processing data from multi-constellation GNSS, the differences between the system times of the different constellations need to be considered. For this reason, when GPS and Galileo are used for precise positioning, the Kalman filter state vector includes the three components of the position, the receiver clock offset, and the GPS-Galileo Time Offset (GGTO), whether or not a predicted value might be available in a navigation message from one of the constellations. On the other hand, in PPP processing, the multi-constellation precise products are based on the same system time, and therefore, in theory, it is not necessary to estimate the GGTO. However, existing intersystem biases may affect the PPP performance, and so it is advisable to estimate them in the Kalman filter (Afifi and El-Rabbany, 2014). Consequently, the minimum number of satellites required for GPS+Galileo PPP is six. The geometry conditions are also an important factor to assess the GNSS positioning performance. For ground navigation particularly relevant is the HDOP, which provides information about the horizontal accuracy achievable. For many land applications, such as precision agriculture and urban positioning, horizontal accuracy is more critical than vertical accuracy. If the ranging error in the carrier phase, including the SISRE, is 20 cm, in order to have decimetre level horizontal

accuracy, HDOP needs to be no larger than 5. In most cases HDOP values as low as 2 are quite common.

Each of the five urban sites in **Figure 7.7** are simulated through the GPS/Galileo Simulink tool for 24 hours in order to evaluate the daily satellite availability and geometry conditions. **Table 7.16** is an overview of the number of epochs in one day when the minimum visibility and geometry requirements are met. The two junctions seem to be the sites with the best satellite visibility conditions. A multi-GNSS receiver (GPS+Galileo) placed at one of the two road junctions will always, or almost always, see at least six satellites with an HDOP better than 5. In particular, at site B an HDOP better than 5 is available 100% of the epochs, while for 97.99% of the time six satellites offer an HDOP as low as 2. Slightly poorer visibility conditions are found at site D. At least six satellites are available for 98.83% of the time, but epochs with HDOP values better than 2 are only found 71.49% of the day. Navigating a pedestrian walking, or a car driving, along narrow streets such as Grove Street (site A) or University Street (site C) is quite challenging. Despite the building surrounding these two streets aren't that tall, the minimum requirements for satellite availability and geometry (HDOP less than 5) is met for only 76.83% (for site A) and 86.65% (for site C) of the epochs. Even worse conditions can be found in proximity of tall buildings, as in case of site E. The obstruction caused by high buildings allows receivers to track at least six satellites for only 13% of the time, while it is impossible to have HDOP values as small as 2.

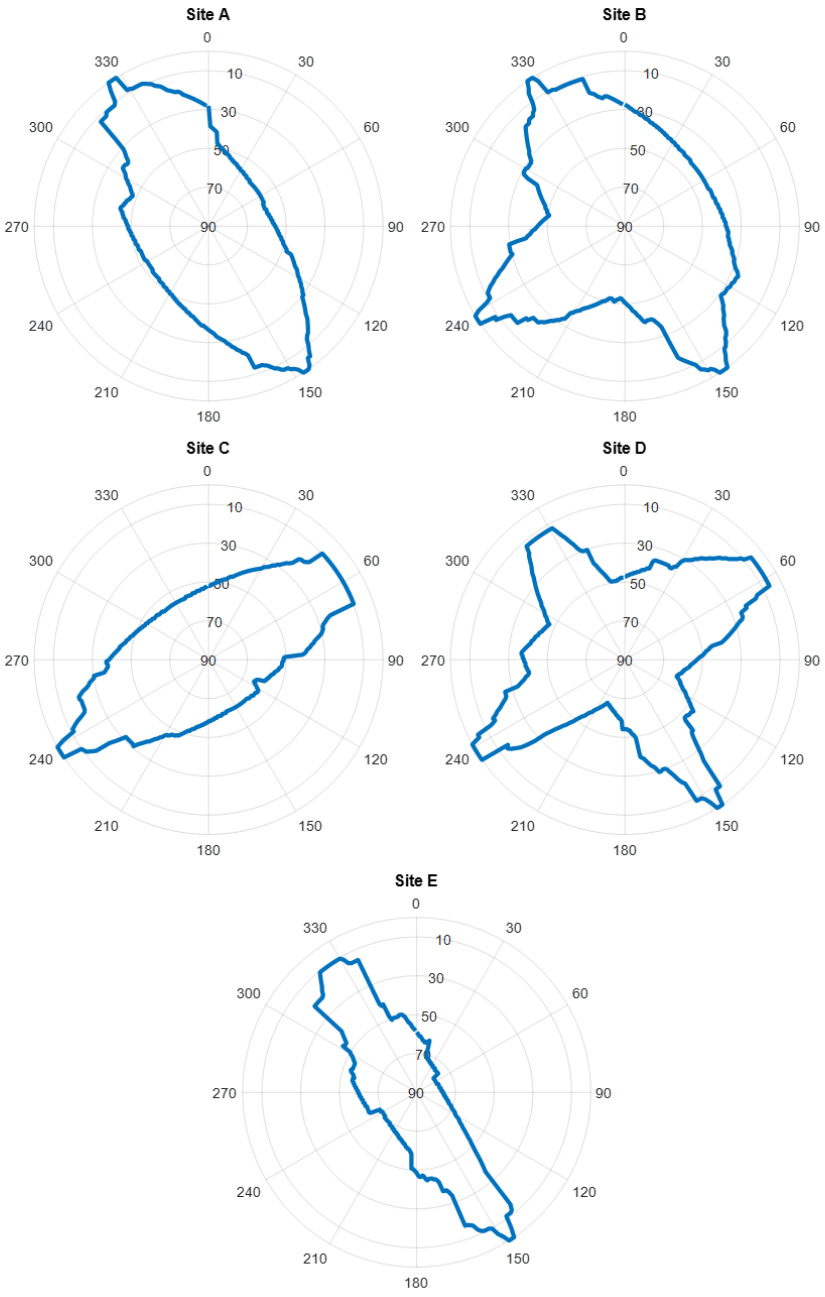


Figure 7.8 *Sky plot of the building obstruction masks to satellite visibility for each of the five sites. Both the azimuth angles and the elevation angles, which figure in the radial direction, are in units of degrees.*



Figure 7.9 *Junction between Gower Street and University Street. StreetView from Google maps.*



Figure 7.10 *Junction between University Street and Huntley Street. StreetView from Google maps.*

From this preliminary study, it seems clear that the presence of tall building compromises the satellite availability and, therefore, the possibility of computing GNSS based positioning solutions in urban environments. On the other hand, it was shown that GNSS may work in certain areas where the streets are wide, or the surrounding buildings are shorter than six floors. In traditional European cities, in proximity of the historical centres, it is common to find narrow roads and relatively short buildings packed together. These streets are usually good candidates for GNSS based positioning. On the other hand, it is not uncommon for drivers and pedestrian to find, even in these areas, slightly taller buildings, like in site E, that completely cover the transmitting GNSS satellites. Similar, or even worse, conditions may occur in the business districts of European cities or in modern American or Asian metropolis, where

skyscrapers are very popular. An example is Canary Wharf in London. In these kinds of areas, it is very difficult to compute the user's position with a GNSS receiver. Things can be improved by considering also GLONASS and BeiDou, and by exploiting the non-line-of-sight signals (Viandier et al., 2009).

In addition, it is well known that a further obstacle for PPP in urban environments is signal discontinuity. Urban infrastructures may block the GNSS signals only for a few epochs before being tracked again. Let's imagine that the GNSS satellites are covered for only one second every ten minutes. Even with excellent geometry conditions and with only 0.003% (one second over ten minutes) of epochs in one day when the number of tracked GNSS satellites is not enough for positioning, it would still be challenging to have a converged PPP solution because of its long convergence time. Indeed, in case the GNSS receiver loses track of the carrier phase, the positioning filter needs to be reinitialized, meaning that further tens of minutes are required before re-convergence.

Table 7.16 *Percentage of epochs in 24 hours for which dual-constellation GNSS meets the minimum requirements in terms of visibility and geometry. N is the number of satellites.*

Site	N ≥ 6	N ≥ 6 and HDOP ≤ 5	N ≥ 6 and HDOP ≤ 2
A	84.17	76.83	44.00
B	100	100	97.99
C	91.22	86.65	18.36
D	98.83	97.24	71.49
E	13.00	4.88	0

To test the re-convergence of PPP in transient signal environments, a pedestrian carrying a GPS+Galileo receiver was simulated to be walking along the path in **Figure 7.11**. The receiver was simulated to be located for the first half hour of the simulation in the front yard of UCL's Wilkins Building (where the simulation begins and ends), before starting to move. This is to allow the initial convergence of the PPP filter. The simulated pedestrian walks along Gower Street and University Street, where the geometry and availability conditions were decent (**Table 7.16**). After reaching Huntley Street, which was truly mediocre in terms of satellites visibility (**Table 7.16**), the pedestrian goes all the way back to the UCL campus. In this simulation the multipath correlation time

was assumed to be equal to 5 seconds, which was found to be the lower bound of the range within the multipath time constant lies for 99% of the time in an urban environment (Khanafseh et al., 2018).

The simulated GPS+Galileo observation file, which has a data rate equal to 1 second, was processed in kinematic PPP mode with the POINT software. The pseudorange measurements weights used to tune the Kalman filter are the same as those reported in **Table 7.7**, the carrier phase measurements were expected to have a precision of 1 cm, while the values adopted to populate the covariance matrices of the initial errors and process noise are summarized in **Table 7.17**. In kinematic positioning processing, since it is impossible to accurately predict the path of receiver, a very large process noise in the prediction of the position components is assumed. Processing the GNSS data in static positioning mode, means that the Kalman filter cannot exploit any previous knowledge of user's dynamics to assist the position's estimation. For this reason, the PPP solution is largely affected by the errors in the GNSS measurements, as well as by the geometry conditions.

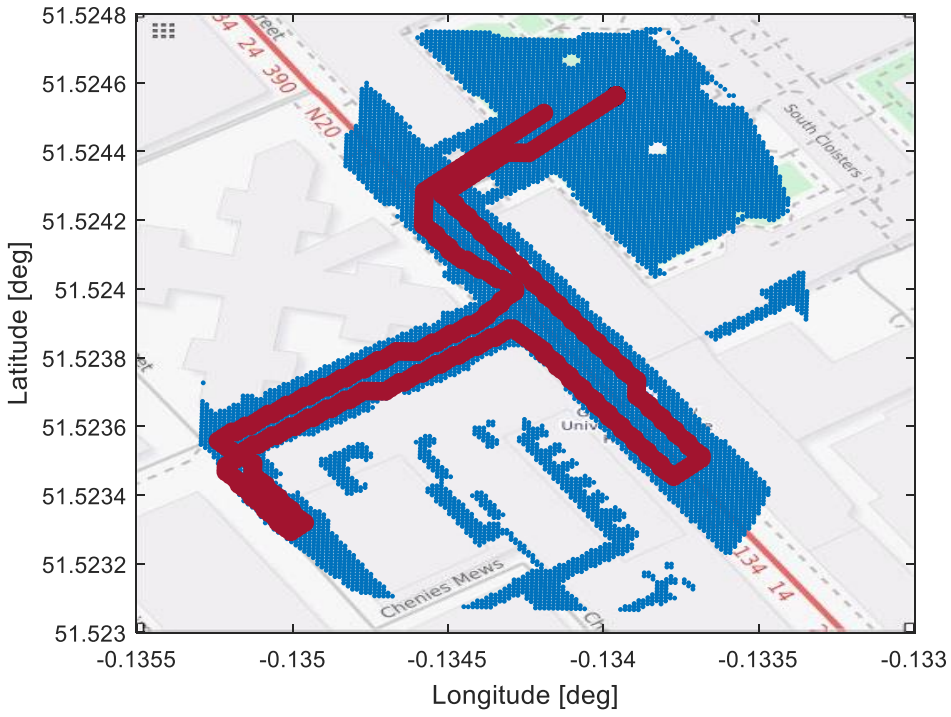


Figure 7.11 *The measured trajectory (red) of the pedestrian kinematic test. The background map was achieved from OpenStreet map.*

Table 7.17 *Standard deviations of the initial error in the state vector and of the process noise used to tune the Kalman filter.*

State vector elements	Initial error	Process noise
Position components	2.0 m	1000.0 m/√s
Receiver clock offset	1000.0 m	10.0 m/√s
Residual wet ZTD	0.1 m	$3.0 \cdot 10^{-3}$ m/√s
Ambiguities	1000.0 cycles	0.0 cycles/√s

Figure 7.12 plots the HDOP and the total number of GNSS satellites available during the pedestrian test. Only the epochs when the receiver is moving are considered. For this reason, the first thirty minutes, when the receiver is simulated to be static in the UCL campus, are not included in the following plots. Many satellites are visible for large part of the simulation. In proximity of the junctions even 14 satellites are available. There are only in two instances when the minimum requirement for computing a GPS+Galileo PPP solution is not guaranteed. As a consequence, the HDOP is often below 5, with the only exception of those epochs when there are just five satellites in view. In these cases, the HDOP rockets to values as large as 34.

The visibility of a given GPS or Galileo satellite is illustrated in **Figure 7.13**. This plot is useful to study the presence and length of satellites tracking discontinuities due to buildings obstruction. For this dataset, data gaps are often visible, with the largest being about 12 minutes and the average less than 2 minutes. As a consequence, every time the receiver acquires a satellite, after it was lost, the carrier phase ambiguity needs to be estimated all over again; and, as previously mentioned, this process usually requires tens of minutes before re-convergence.

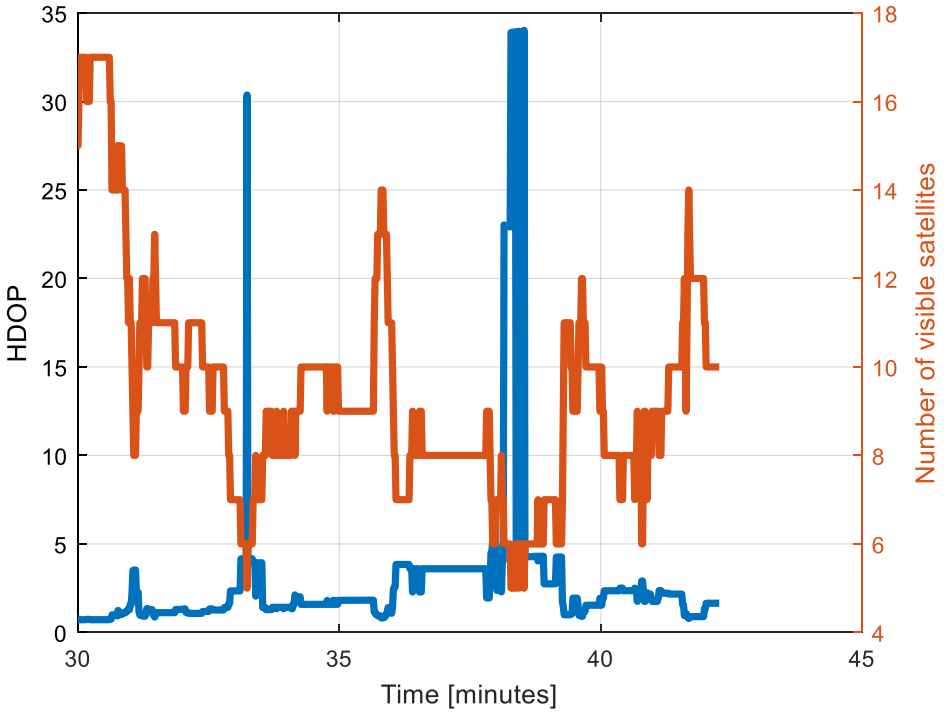


Figure 7.12 *HDOP (blue plot with the y axes on the left) and total number of visible GPS and Galileo satellites (red plot with y axes on the right) for the kinematic part of the pedestrian test.*

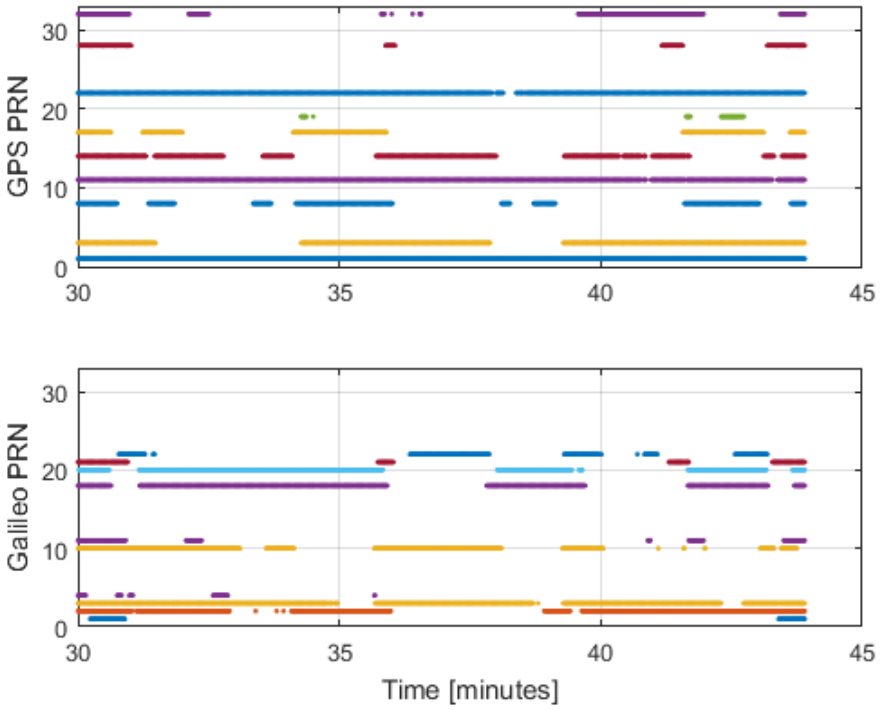


Figure 7.13 *GPS (top) and Galileo (bottom) satellites availabiolity for the kinematic part of the pedestrian test.*

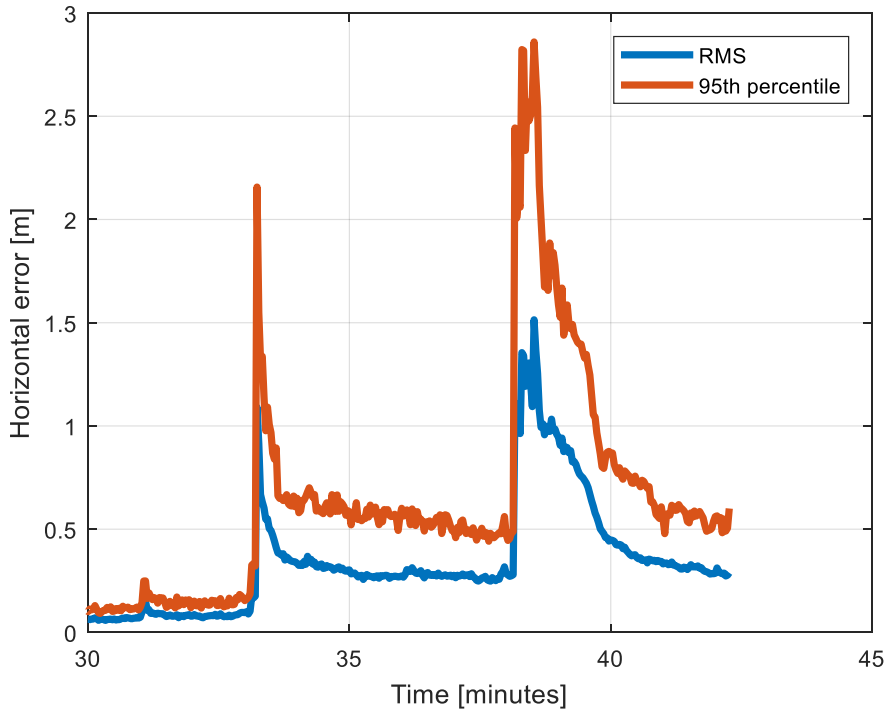


Figure 7.14 *RMS (blue) and 95th percentile (red) of the horizontal error component for the kinematic test using GPS and Galileo data.*

The pseudorange and carrier phase measurements for the GPS L1 and L5, and Galileo E1 and E5 frequencies linearly combined into the IF combination are processed, using POINT, in kinematic PPP mode with float solutions. For each epoch, the RMS and the 95th percentile of the horizontal errors over the 50 simulation runs are computed. These are shown in **Figure 7.14**, where the blue plot represents the RMS and the red plot describes the 95th percentile of the horizontal component of the positioning error. At the very beginning of the kinematic test, when many satellites are in view and the HDOP is very small, sometimes even smaller than 1, the horizontal error is on average well below 10 cm. At minute 33.23, the number of visible satellites drops below 6, and the HDOP becomes as large as 30. From this point on, the first re-convergence pattern is visible in **Figure 7.14**. The horizontal solution, starting from an error of 2.16 m (95% of the time), slowly converges towards higher accuracy levels. Unfortunately, right before reaching an accuracy of better than 50 cm (95% of the time), some satellites go behind the buildings and it is again not possible to compute the GPS+Galileo PPP solution. A second convergence pattern is visible in **Figure 7.14**, approximately from minute 38.27. The horizontal error starts decreasing from a value of 2.86 m, but it never goes below 50 cm (95%).

This short example clearly demonstrates the limitations for GPS+Galileo PPP in urban areas. Even though the geometry and satellites visibility conditions are fairly good for a large part of the test, signal discontinuity due to buildings in cities represents the main threat for PPP. In the first part of the simulation, the horizontal error is only a few centimetres. However, following some data gaps in the GNSS signals, the solution never manages to obtain such level of precision again, despite having a fairly optimistic correlation time constant for simulating the multipath delay. Slow solution re-convergence to the few decimetre/centimetre level still represents the main drawback to the use of PPP for high accuracy applications in cities. Nonetheless, it was demonstrated that GPS+Galileo PPP enables sub-meter level horizontal accuracy for most of the simulations that have been carried out. After signal loss, it only took a few tens of seconds to have an average horizontal accuracy of better than a meter. Hence, some land based applications requiring meter or sub-meter level of accuracy, such as in-car navigation, fleet management, urban traffic control, emergency calls, dynamic route guidance, selective vehicle priority, road pricing, stolen vehicle recovery, or trip travel information (Teunissen and Montenbruck, 2017), can already benefit from GPS+Galileo PPP. Other applications in which better knowledge of the position is necessary, for example collision avoidance, intelligent speed assistance, lane control, or restraint deployment (Teunissen and Montenbruck, 2017), cannot rely on the traditional PPP solution based on GPS and Galileo IF measurements. To fulfil the needs of these type of users, more refined positioning algorithms are required.

7.4 Chapter summary

In this chapter, the GPS+Galileo Simulink tool was used to compare the PPP solutions achieved by processing the simulated GPS and Galileo measurements with the POINT software.

A first comparison was aimed at identifying the two-frequency IF combinations that guarantee the best PPP performance. For this reason, the solutions achieved with the L1-L2 IF and with the L1-L5 IF were analysed. The two PPP solutions were characterized by a similar accuracy level, however a big difference was observed in the convergence time. The time the solution computed from the L1-L5 IF combination takes to go below 10 cm was much shorter. This result was

expected, as it is well known that the quality of the pseudoranges have a big impact on the convergence in PPP. Since the pseudoranges on L5 are simulated to have lower noise and multipath than L2, it could have been easily predicted that the L1-L5 IF was the best combination within the GPS ones. Similarly, the PPP solutions computed from Galileo E1-E5a IF, E1-E5b IF, E1-E5 IF, and E1-E6 IF combinations were compared. The AltBOC modulated signal, E5, is characterized by low noise and excellent rejection properties of both long-range and short-range multipath, thanks to its very large signal bandwidth of at least 51 MHz. For this reason, one would expect the E1-E5 IF to be the best Galileo signal combination. Surprisingly, the PPP solutions obtained using E1-E5a IF have nearly the same performance as the E1-E5 IF ones. The reason for this behaviour was addressed to the IF combination with E1. It is thoroughly recognized that the IF combination amplifies the noise in the GNSS measurements. Assuming negligible the errors in the E5 and E5a pseudoranges with respect to the ones in E1 pseudoranges, the E1-E5 IF combination has its noise amplified by a factor of 2.33, while the noise in E1-E5a IF is only 2.26 times larger than the one on E1. Of course, E5a and E5 also have a contribution to the noise in the IF combinations, however being amplified by only 1.26 and 1.33, respectively, their overall impact is only marginal.

The best GPS and Galileo IF combinations were used for the second comparison between the single and multi-constellation PPP solutions. Static scenarios in open environments were simulated with the GPS/Galileo Simulink tool. In the first case test, the receiving antenna was supposed to be placed away from reflective surfaces that may cause multipath. For this reason, its effect was neglected. The results showed that better PPP solutions, particularly in terms of convergence time, could be obtained when Galileo measurements were adopted instead of the GPS ones. The reason why Galileo, in general, performs so much better than GPS has to be attributed to the lower noise that was assumed in the code pseudoranges. In the second case, multipath was also considered. With this assumption, the simulated GPS and Galileo code pseudoranges have nearly the same noise. For this reason, the difference in the GPS and Galileo PPP performances is mainly driven by the user-to-satellite geometry. As the GPS constellation orbits at a slightly lower altitude than Galileo constellation, the GPS satellites move along their orbit with higher velocity, and the rate of change

of the LOS for GPS is higher than for Galileo. As a consequence, the PPP convergence time for Galileo is slower than the one for GPS.

Given the open sky conditions, it was not expected that there would be large improvements in the accuracy by employing the GPS+Galileo system. The results showed that it is mainly the convergence time that benefits from multi-constellation PPP. On average, over all the simulations, the convergence time for GPS+Galileo PPP can be 50% faster than the GPS solution and 23% faster than the Galileo solution.

Multi-constellation GNSS was also analysed in a simulated urban environment corresponding to the neighbourhood of the UCL campus in London. Accurate building boundaries with an azimuth resolution of only 1° were adopted for this purpose. Satellites availability and geometry conditions were studied in five different sites in this area. Enough satellites for computing a PPP solution, with good geometry conditions, were visible for great part of the day in proximity of streets surrounded by six (or less) storey buildings or next to road junctions. Near narrow streets with buildings taller than six floors, it is impossible to have a GNSS based positioning solution. In this chapter, it was also highlighted that, even with good visibility conditions, data gaps due to building obstruction represent the main limitation for PPP. Because of its long convergence time, in case the GNSS receiver loses track of the carrier phase, the PPP filter needs to be re-initialized, meaning that the horizontal PPP solution never reaches the target accuracy level of a few decimetres or centimetres. Thus, land users requiring high accuracy cannot rely on the traditional PPP based on the IF combinations, but they have to exploit more advanced positioning algorithms aimed to reduce the (re-)convergence time in PPP. On the other hand, the GPS and Galileo PPP solution based on two-frequency IF combinations easily enables land applications seeking for sub-meter level horizontal accuracy.

Chapter 8

Quick (re-)convergence in PPP

Parts of this chapter have been published in Basile et al. (2019), (2018b), (2018c), (2018a), (2017).

Chapter 7 showed that the biggest challenge for GPS+Galileo PPP in urban areas is related to the presence of buildings that may cause gaps in the tracking of satellite. Even in urban environments with generally good visibility conditions, the slow PPP convergence time does not let the solution to re-converge to the target accuracy level of a few decimetres or centimetres, if a building covers the transmitting satellites for a few epochs.

This chapter proposes innovative solutions to reduce the (re-)convergence time in PPP, and therefore, to address the main limitation in urban areas. The PPP convergence time is strictly related to the estimation of the carrier phase ambiguities: a PPP solution is converged only when the float ambiguity estimates have reached a steady constant value. Two of the key factors that impact on the PPP convergence time are the large pseudorange noise (Abou-Galala et al., 2017), and the short NL wavelength.

In the next paragraphs, triple-frequency GPS and Galileo measurements will be analysed to find new combinations intended to either reduce the noise in the IF pseudorange combinations or to enlarge the NL wavelengths. These combinations may be of benefit for the float PPP solutions. Firstly, triple-frequency GPS and Galileo combinations aimed to reduce the noise amplification factor will be considered. It is well known that the IF combination amplifies the residual error in the GNSS measurements up to a factor of 3.51 (for Galileo E1-E6 IF). The third frequency may be exploited to reduce the noise amplification factor in the geometry preserving pseudorange combinations, and, consequently, to improve the time required to reach the target accuracy level in PPP. Next, the concept of smoothed ionosphere correction will be introduced. Here, the ionosphere observable computed from geometry-free pseudorange combinations is smoothed with a Hatch filter (Hatch, 1982) and then it corrects for the ionospheric delay in a triple-frequency low noise pseudorange combination.

In the following section, new triple-carrier IF combinations aimed to amplify the NL wavelength and, at the same time, to enhance the observability of the float NL ambiguity are considered. Once the EWL and WL ambiguities are fixed, these optimal combinations should shorten the first convergence in PPP. Finally, ambiguity resolution is analysed. In particular, a new TCAR algorithm based on the smoothed ionosphere correction is compared with the method proposed in Geng and Bock (2013).

8.1 Quick re-convergence by reducing the noise in the ionosphere-free pseudorange combinations

When two-frequency GNSS measurements are available, the IF combination is the most widely adopted method to remove the effect of the ionosphere on pseudoranges and carrier phases. These combinations remove up to 99.9% of the ionospheric delay with the downside of increasing the noise up to a factor of 3.51 (for Galileo E1-E6 IF) with respect to the un-combined measurements. Abou-Galala et al. (2017) assessed the accuracy and convergence time of PPP and analysed the factors that impact on the time the PPP solution takes to reach a certain level of accuracy. Not surprisingly, the quality of the GNSS measurements was listed within the elements upon which the convergence in PPP depends. The results presented in the previous chapter also confirmed that the PPP solutions converged faster to a given accuracy when the simulated GNSS pseudoranges were affected by a lower level of noise and multipath.

For this reason, it can be concluded that the traditional IF combination is not beneficial for PPP, as pseudorange measurements with larger noise lead to longer convergence times. In this paragraph, new type of IF combinations are proposed which are aimed at reducing the noise amplification and, as a consequence, the re-convergence time in PPP.

8.1.1 Low noise pseudorange combinations with smoothed ionosphere correction

As an alternative to traditional PPP solutions based on the IF combinations, navigation algorithms based on un-combined GNSS measurements in which the ionospheric delays were mitigated through vertical TEC (VTEC) maps and/or included in the state vector (Geng et al., 2010a; Li, 2012; Zhang et al., 2013) were proposed with the aim to reducing the re-convergence time in PPP. There

exist strong temporal and spatial correlations in the slant ionospheric delays affecting the signals transmitted by each satellites. These characteristics were the foremost foundation of the method described in Geng et al. (2010a) for rapid re-convergence. In case of data gaps in the GNSS measurements that cause cycle slips, the new ambiguity value may be quickly estimated by exploiting the slow rate of change of the slant ionospheric delay. The linear model proposed in Dai et al. (2003) was adopted to predict the effect of the ionosphere and bridge the data gaps to improve the estimation of the ionospheric states. Results presented in this publication showed that instantaneous re-convergence to an ambiguity fixed solution is possible even with data gaps as large as 5 minutes (with an ambiguity-fix success rate of 85.8% for the WL and 89.4% for NL ambiguities). Li (2012) further improved these results by applying refined temporal and spatial constraints, based on the information included in the GIMs, when estimating the ionosphere delays. However, as pointed out in Zhang et al. (2013), the performance of these methods greatly depends on the quality of the GIMs, on the temporal and spatial constraints used in the prediction and estimation of the ionosphere, and on a careful handling of the satellites' and receiver's DCBs. Indeed, these configurations perform the best only if the user is located in proximity of the continuous operative reference network of receivers used to estimate the ionosphere corrections. It means that the best property of PPP that differentiate it from RTK, i.e. high accuracy globally, is lost. Moreover, the un-combined measurements configuration increases the computational burden in particular with many multi-GNSS satellites in view, which is desirable for PPP in degraded signal environment.

For these reasons, the use of IF combinations might still be the preferable option in a large number of applications. This section explains the efforts made in this research project to adopt the temporal constraints of the ionosphere, presented in Geng et al. (2010a), Li (2012), and Zhang et al. (2013) for rapid re-convergence, with novel IF pseudorange combinations.

8.1.1.1 Low noise pseudorange combinations

The effect of triple-frequency GPS combinations on float PPP solutions has been studied in Elsobeiey (2014). Ten different combinations have been selected with the only constraint that the geometry term must be preserved. No

other explanation was given to clarify how the triple-frequency combinations were chosen. Surprisingly, the combination that guarantees the quickest convergence time and the smallest positioning error was a combination that does not completely remove the ionospheric delay (the ionosphere was amplified by a factor equal to 0.0419), and has a carrier noise amplification factor equal to 3.86. As a comparison, the carrier noise amplification factor of the two-frequency L1-L2 IF combination is only 3.21. Similarly, Deo and El-Mowafy (2016) compared the PPP performances achieved with dual-frequency and triple-frequency IF combinations that minimize the noise. The results presented in these two publications showed that only minimal improvements in the float PPP solutions could be achieved by exploiting the GNSS measurements on three frequencies.

A linear combination P_r^s between GNSS pseudorange measurements on three frequencies f_1, f_2, and f_3 recorded at time *t* by the receiver *r* and transmitted by the satellite *s* can be written as

$$\begin{aligned} P_r^s(t) &= \alpha_1 P_{r,1}^s(t) + \alpha_2 P_{r,2}^s(t) + \alpha_3 P_{r,3}^s(t) \\ &= (\alpha_1 + \alpha_2 + \alpha_3) \cdot \rho_r^s(t) + \\ &+ \left(\alpha_1 + \alpha_2 \frac{f_1^2}{f_2^2} + \alpha_3 \frac{f_1^2}{f_3^2} \right) \cdot I_{r,1}^s(t) + e_r^s(t) \end{aligned} \tag{8.1}$$

For simplicity, in Equation (8.1) the non-dispersive term ρ_r^s includes the geometric range, the receiver's and satellite's clock offsets, and the tropospheric delay. The ionospheric delay affecting signals on frequency f_1 ($I_{r,1}^s$) is amplified by the term

$$q = \left(\alpha_1 + \alpha_2 \frac{f_1^2}{f_2^2} + \alpha_3 \frac{f_1^2}{f_3^2} \right) \tag{8.2}$$

While the noise in the combination e_r^s has a standard deviation

$$\begin{aligned}\sigma_{e_r^s} &= \sqrt{\alpha_1^2\sigma_{e_{r,1}^s}^2 + \alpha_2^2\sigma_{e_{r,2}^s}^2 + \alpha_3^2\sigma_{e_{r,3}^s}^2} \\ &= \sigma_{e_{r,1}^s}\sqrt{\alpha_1^2 + \alpha_2^2 n_2^2 + \alpha_3^2 n_3^2}\end{aligned} \tag{8.3}$$

$$n = \sqrt{\alpha_1^2 + \alpha_2^2 n_2^2 + \alpha_3^2 n_3^2} \tag{8.4}$$

which is n times larger than the standard deviation of the error in the pseudorange on frequency f_1 ($P_{r,1}^s$).

In order to preserve the non-dispersive term ρ_r^s in the combination, the following condition must be satisfied

$$\alpha_1 + \alpha_2 + \alpha_3 = 1 \tag{8.5}$$

Together, (8.2), (8.4), and (8.5) describe a surface in the space q-α_3-n. This surface depends on the ratios n_i between the standard deviations of the errors in $P_{r,i}^s$ and $P_{r,1}^s$. For example, assuming the ratio between the standard deviation of the errors in the GPS pseudoranges as in **Table 8.1**, one would obtain the surface shown in **Figure 8.1**. This colour-map has been generated by making α_3 vary between -2 and 2, and q vary between 0 and 4, and computing the corresponding values of n by solving Equations (8.2), (8.4), and (8.5). The figure highlights two regions of interest: the region including the IF combinations, corresponding to the area where q is zero (visible at the bottom of the plot); and the region of low noise, corresponding to the dark blue area in the colour-map.

In the first region (IF), the minimum noise amplification factor is equal to 2.47 and it is realized with α_3 approximately equal to -1.17. This value is only slightly smaller than the noise amplification factor in the L1-L5 IF combination (2.48), and it explains why adopting this minimum-noise, triple-frequency IF combination did not have a significant impact on the float PPP solution in Deo and El-Mowafy (2016), and in Elsobeiey (2014). In the second region (low noise), the noise in the GPS L1-L2-L5 pseudorange combination can be as little as 0.56 times the one in the L1 pseudorange, and the corresponding ionosphere amplification factor is 1.51.

Table 8.1 *Assumed ratios between the standard deviation of the errors in the GPS and Galileo pseudoranges with respect to the one on L1/E1.*

	L2	**L5/E5a/E5b**	**E5**	**E6**
n_i	1.3	0.8	0.4	1.0

Similarly, **Figure 8.2**, **Figure 8.3**, **Figure 8.4**, and **Figure 8.5** show the noise amplification factors for the Galileo triple-frequency combinations E1-E5a-E5b, E1-E5a-E6, E1-E5b-E6, and E1-E5-E6, respectively. Also, in these plots it is possible to identify an IF region, and a low noise region.

The minimum noise amplification factor in the IF region is realized by the E1-E5-E6 Galileo frequencies. This is equal to 2.34, only 5.65% smaller than the noise in the E1-E5a IF combination. The E1-E5-E6 frequencies also provides the combination with the minimum noise within the low noise region. This pseudorange combination, having a noise amplification factor of 0.35, is only slightly less noisy than the Galileo AltBOC modulated signal, and its impact in the PPP solution is expected to be only marginal with respect to using the pseudorange on E5.

The low noise regions of the surfaces in the space q-α_3-n describe GPS and Galileo pseudorange combinations characterized by a very large mitigation of the residual pseudorange errors, including multipath. Adopting this kind of combinations may be particularly useful in severe multipath environments, such as urban areas. Unfortunately, these triple-frequency pseudorange combinations are still affected by the ionospheric delay, which can be further amplified by a factor of 1.51 for the GPS L1-L2-L5 combination and by 1.63 for the Galileo E1-E5-E6 combination, or by 1.75 for the E5 pseudorange, with respect to the delay affecting measurements on L1 frequency. Major part of this research project will be dedicated to understanding how to exploit these pseudoranges, which have low noise, but are still affected by the ionospheric delay, to improve the PPP solutions.

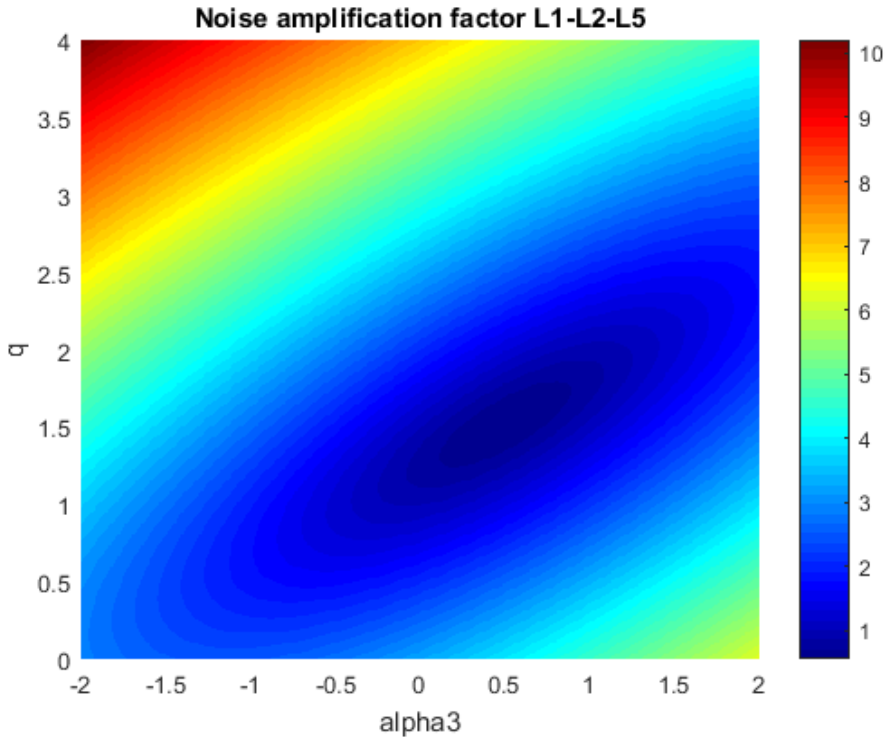


Figure 8.1 *Colour-map of the geometry-preserving surface in the space* q-α_3-*n for the GPS L1-L2-L5 pseudorange combinations.*

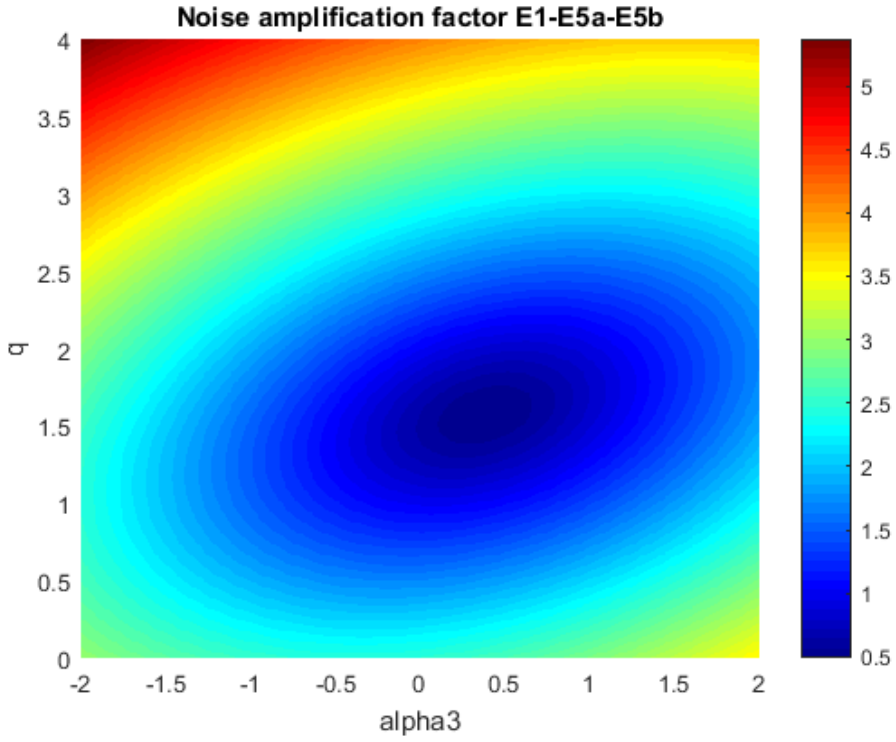


Figure 8.2 *Colour-map of the geometry-preserving surface in the space q-α3-n for the Galileo E1-E5a-E5b pseudorange combinations.*

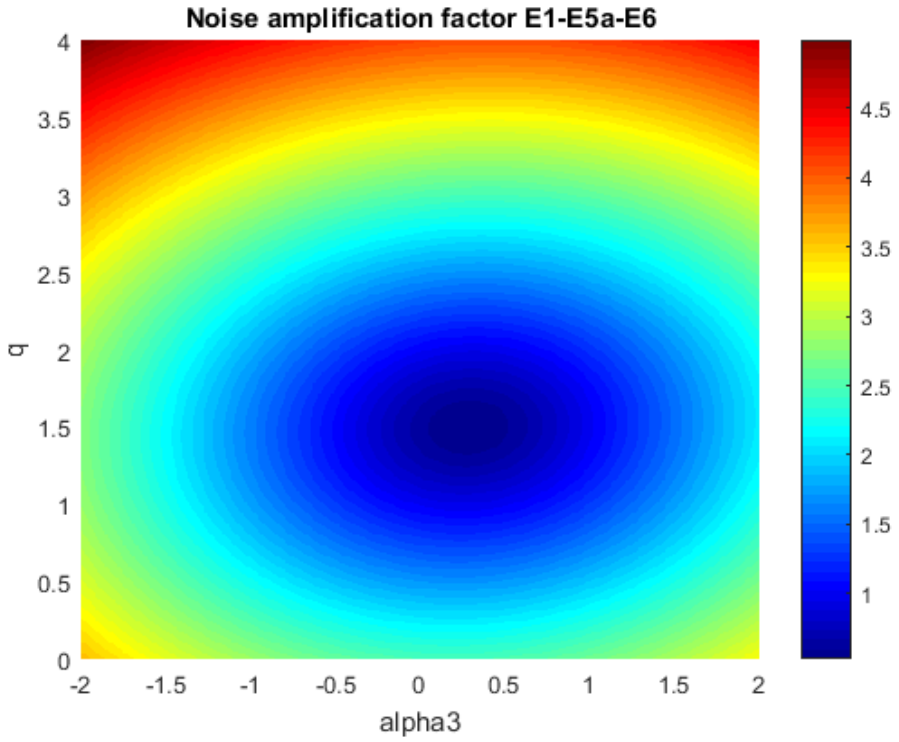


Figure 8.3 *Colour-map of the geometry-preserving surface in the space q-α3-n for the Galileo E1-E5a-E6 pseudorange combinations.*

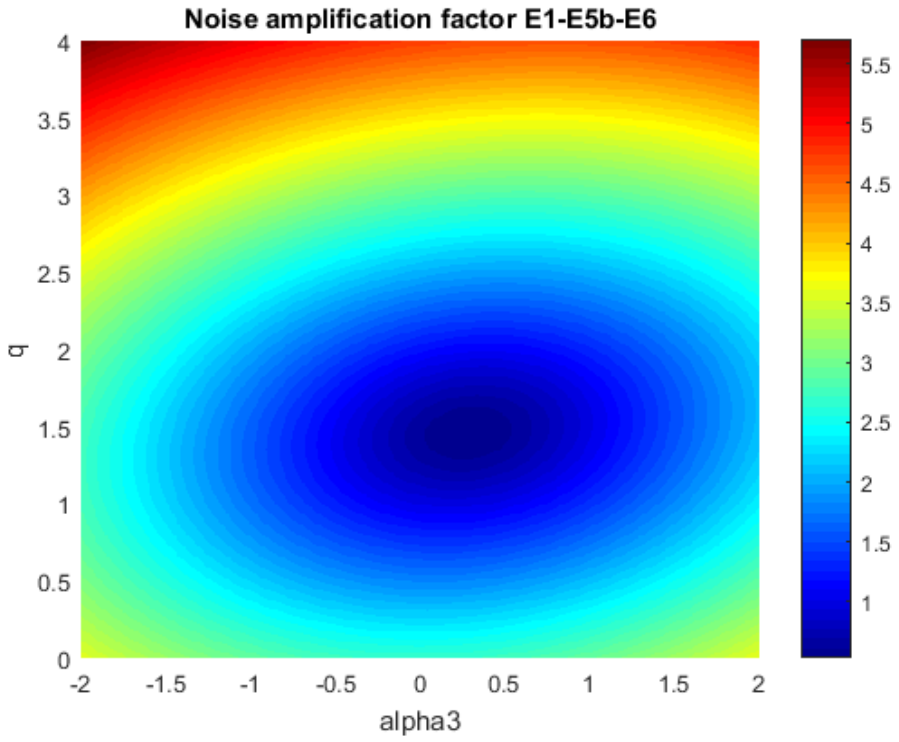


Figure 8.4 *Colour-map of the geometry-preserving surface in the space q-α3-n for the Galileo E1-E5b-E6 pseudorange combinations.*

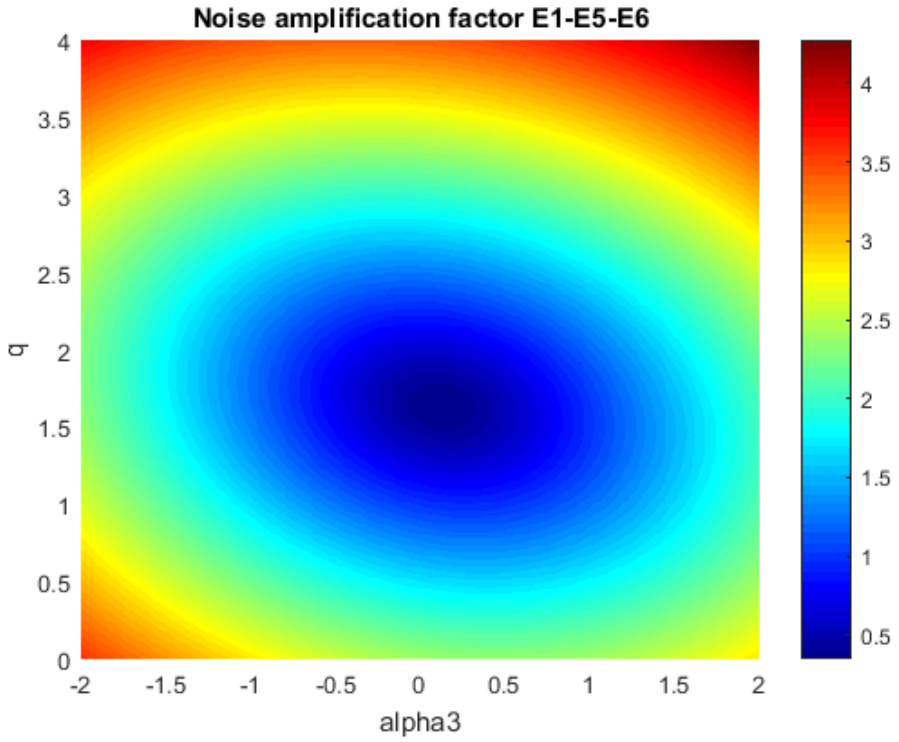


Figure 8.5 *Colour-map of the geometry-preserving surface in the space q-α3-n for the Galileo E1-E5-E6 pseudorange combinations.*

8.1.1.2 Smoothed ionosphere correction

Traditionally in PPP, the IF combinations between two-frequency pseudorange and carrier phase measurements are adopted. While on one hand the IF combinations mitigate for 99.9% of the ionospheric delay, on the other side they greatly increase the noise in the observables. This represents a big problem for PPP, since the larger pseudorange noise can be translated into longer convergence time (Abou-Galala et al., 2017). Equations (3.18) describes the IF combination between two-frequency pseudoranges. This formulation is equivalent to correcting the pseudorange $P_{r,1}^{s}$ with the ionospheric delay $I_r^{s,P}$ computed from the geometry-free combination between $P_{r,1}^{s}$ and $P_{r,2}^{s}$.

$$P_{r,IF}^{s} = P_{r,1}^{s} - I_r^{s,P} \tag{8.6}$$

$$I_r^{s,P} = \frac{P_{r,1}^{s} - P_{r,2}^{s}}{1 - \frac{f_1^2}{f_2^2}} \tag{8.7}$$

Alternatively, in this research a new type of IF combination is proposed. The ionosphere correction (8.7), here, is smoothed through a Hatch filter (Hatch, 1982) before being applied to the pseudorange (Paul D. Groves, 2013).

The Hatch filter is a special combination that adopts jointly the pseudorange and time-differenced carrier phase measurements and allows pseudoranges with reduced noise level to be obtained. Even though the single-channel pseudorange smoothing does not achieve the same quality as algorithms in which the phase ambiguities are rigorously estimated, for certain applications the Hatch filter represents an attractive alternative due to its computational simplicity.

The derivation of the Hatch filter applied to the pseudorange computed ionosphere is as follows

$$\tilde{I}_r^s(t_k) = \begin{cases} I_r^{s,P}(t_k) & ,k=1 \\ \frac{1}{k} I_r^{s,P}(t_k) + \left(1-\frac{1}{k}\right)\left[\tilde{I}_r^s(t_{k-1}) + \left(I_r^{s,L}(t_k) - I_r^{s,L}(t_{k-1})\right)\right] & ,k<N \\ \frac{1}{N} I_r^{s,P}(t_k) + \left(1-\frac{1}{N}\right)\left[\tilde{I}_r^s(t_{k-1}) + \left(I_r^{s,L}(t_k) - I_r^{s,L}(t_{k-1})\right)\right] & ,k\geq N \end{cases} \quad (8.8)$$

$$I_r^{s,L} = -\frac{L_{r,1}^s - L_{r,2}^s}{1-\frac{f_1^2}{f_2^2}} \quad (8.9)$$

The smoothed ionosphere correction $\tilde{I}_r^s(t_k)$ computed at epoch t_k can be expressed as in (8.8), where $I_r^{s,P}$ and $I_r^{s,L}$ are the ionosphere delays computed from the two-frequency pseudorange and carrier phase measurements, respectively, and *N* is the size of the selected smoothing window.

Usually, the performance of a Hatch filter greatly depends on the size of *N*. On one hand choosing a larger smoothing window leads to greater smoothing efficiency, whilst on the other hand too large values for *N* enable the, so called, code-carrier divergence. Because of the opposite sign of the ionospheric delay in the code and carrier observations, the smoothed pseudorange may diverge considerably from the original pseudorange if the ionosphere varies

significantly during the smoothing interval. Thus, when designing the Hatch filter, care must be taken when choosing a value for *N*: it has to be large enough to successfully smooth the pseudorange, but not too large to prevent significant errors due to code-carrier divergence. When two-frequency GNSS measurements are available, the effects of the ionosphere can be eliminated. One option is to totally remove the ionosphere by forming the IF combinations for pseudorange and carrier phase measurements. This approach is often called ionosphere-free Hatch filter. The results are free from the ionosphere, but the noise is largely amplified. A second option removes the code-carrier divergence without amplifying the noise. This approach consists in correcting the ionospheric delay in the carrier phase in such a way that its sign matches the one affecting the code pseudorange. This method is referred in literature as divergence-free Hatch filter (McGraw, 2009).

The time-series of the errors in the pseudorange smoothed by different configurations of the Hatch filter is shown in **Figure 8.6**. The blue plot, which represents a single-frequency Hatch filter with a smoothing window of 300 seconds, clearly illustrates the problem of the code-carrier divergence. The same smoothing widow is used in a divergence-free Hatch filter whose error is displayed in the red plot. The effect of the code-carrier divergence is eliminated with this configuration.

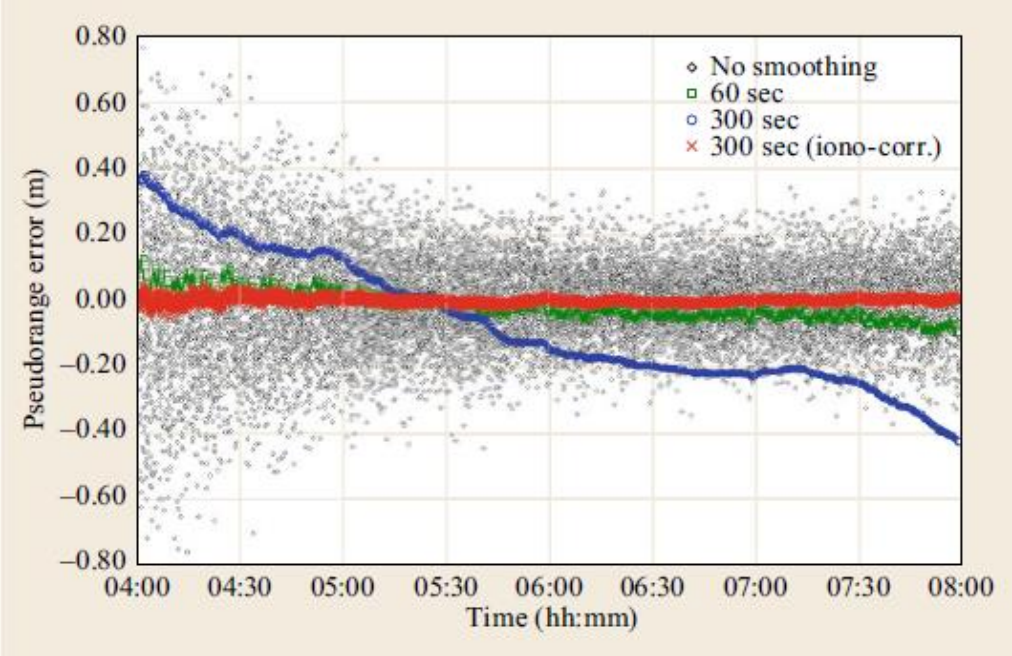


Figure 8.6 *Results for Hatch filters with different smoothing windows based on simulated data. The plot shows the errors in the raw pseudorange (black diamonds), the errors in the pseudorange smoothed by a single-frequency Hatch filter with N equal to 60 seconds (green squares) and 300 seconds (blue circles), and the errors in in the pseudorange smoothed by a divergence-free Hatch filter with N equal to 300 seconds (red crosses). Image from* Teunissen and Montenbruck (2017).

Similarly, the Hatch filter proposed in this section removes the effect of the divergence, since the opposite sign of the ionospheric term of the pseudoranges and carrier phases is taken into account. Therefore, a large smoothing window, even as large as the whole observation period, can be selected, resulting in excellent smoothing properties with no divergence. As an example, **Figure 8.7** shows the ionospheric delay affecting the GNSS signals transmitted by the GPS PRN 8 and recorded by the IGS station KITG, in Uzbekistan, on the 6th September 2017. The blue dots represent the ionospheric delay computed from the C1 and P2 pseudoranges using Equation (8.7), while the time-series of the delay computed from C1 and C5 is plotted as yellow dots. An offset of roughly 2 m is visible between the two delays. It is caused by the receiver and satellite DCBs. **Figure 8.7** also plots the smoothed ionospheric delays (the red line is relative to C1-P2, while the purple line is relative to C1-C5) obtained from Equation (8.8), in which a smoothing window of infinite width was adopted. No sign of code-carrier divergence is visible in the two plots, even though, on that day the Sun emitted two significant solar flares, the most intensive one peaking at 12:02 UTC, which made the ionosphere particularly active. According to Yasyukevich et al. (2018), the enhancement in the ionospheric activity

concerned mainly Europe, Africa and the western part of Asia (where KITG is located).

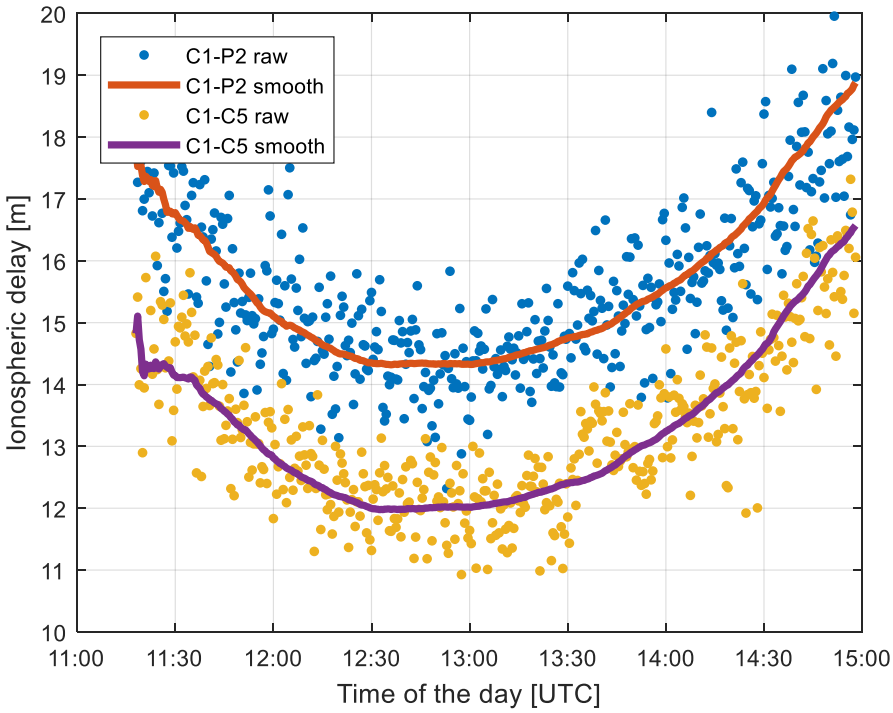


Figure 8.7 *Ionosphere delay computed from C1-P2 combination (raw blue dots, smoothed orange line), and C1-C5 combination (raw yellow dots, smoothed purple line).*

This smoothed ionosphere correction can be applied to the low noise pseudorange combinations to remove the effect of the ionosphere. In this way, once the Hatch filter has converged, ideally we have IF pseudoranges with much lower noise than the traditional ones. Indeed, assuming negligible noise in the converged smoothed ionosphere and considering the GPS low noise combination between triple-frequency pseudoranges discussed in the previous section, this configuration guarantees IF combinations with 82.5% less noise than the L1-L2 IF pseudorange combination, and with 77.4% less than the L1-L5 IF pseudorange combination. Similarly, by applying the smoothed ionosphere correction to the pseudorange on Galileo E5, it is possible to have an IF pseudorange with a noise level 83.9% smaller than the one on the E1-E5a IF pseudorange combination. Therefore, adopting these low noise IF pseudoranges in PPP can possibly be beneficial to the solution in the case of re-convergence. Since the (re-)convergence time of PPP also depends on the quality of the pseudorange measurements, much quicker re-convergence to centimetre levels of accuracy can be guaranteed by this approach.

8.1.1.3 Ionosphere prediction

In Equation (8.8), the raw ionosphere computed from dual-frequency pseudorange measurements is smoothed thanks to time differenced ionospheric delays from dual-carrier observations. Under the assumption that no cycle slips occur, the constant carrier phase ambiguity terms are cancelled out in the time difference. On the contrary, if a cycle slip destroys the continuity of the observations, the Hatch filter usually needs to be reinitialized from the raw pseudoranges. However, the proposed algorithm can exploit the long correlation time in the ionosphere to predict the delay computed from the dual-frequency carrier phases for a few epochs, thus preserving the original value of the ambiguity even in case of cycle slips. For this reason, in the case of cycle slips this configuration of the Hatch filter which is aimed at smoothing the ionosphere observable doesn't need to be restarted from the raw values.

Geng (2010) assessed the two different methods to predict the ionospheric delays proposed in Dai et al. (2003), namely a linear fitting model and a constant bias model, for the purpose of speeding up the re-convergence time of the PPP solution. In the first case, the ionosphere delay can be predicted using a linear fitting model where the delays computed from previous carrier phase measurements within a sliding time window are used to extrapolate the future ionospheric delay. In the second case, the ionospheric delay is assumed to be a constant bias over the prediction time. Geng (2010) proved that the prediction error depends on both the elevation angle of the transmitting satellite, the time latency of the observation, and the size of the time window that is used in the linear fitting model. In particular, the RMS of the prediction errors increase when the time latency is prolonged or when the elevation angle of the transmitting satellite is low. On the other hand, when using the linear fitting model, enlarging the time window width can slow down the divergence of the error with the prediction time. It was also shown that the constant bias model outperforms the linear fitting model with very short time windows. Eventually, Geng (2010) adopted the linear fitting model with a time window of 120 seconds for elevation angles above 30° and 240 seconds for satellites below 30°.

These ionosphere prediction models have been tested using the high-rate observation data recorded by the IGS station DAEJ, in South Korea, on the 25th July 2017. This station is the only one in the CDDIS repository that provides

RINEX observation files with a data rate of 1 Hz. The RMS of the prediction errors made by the constant bias model for different observation time latencies ranging from 1 second to 10 minutes was compared to the one made by the linear fitting model. Various widths of time window used to extrapolate the ionospheric delays were considered, from 1 minute to 5 minutes. Following Geng (2010), the results were divided into two groups with elevation angles above and below 30°. They are shown in **Figure 8.8** and **Figure 8.9**, respectively.

As also shown in Geng (2010), the RMS of the prediction errors generally increases with the time latency. For large prediction times (larger than 536 seconds), these results confirmed the general rule that increasing the width of the time window reduces the divergence of the prediction error. On the other hand, for prediction intervals shorter than 375 seconds, the linear fitting model with time windows of 120 seconds outperforms the other models. Contrary to what was shown in Geng (2010), the constant bias model performs better than the linear fitting model for long prediction intervals (larger than 252 seconds) and worse for short time latencies. In any case, the RMS of the errors is well below 10 cm for a prediction period of 10 minutes.

When the transmitting satellites are at low elevations, the prediction errors are much larger than those obtained with satellites at higher elevations. After 10 minutes, all the considered models have a prediction error above 13.5 cm. As in the previous case, when the linear fitting model is employed, increasing the width of the time window leads to better performance only if the time latency is quite large (larger than 371 seconds), while for short prediction intervals using a time window of 2 minutes provides the smallest prediction errors. For time latencies shorter than 23 seconds, the constant bias model has the same performance as the linear fitting model with a 2 minutes-long window, while for larger prediction times the errors are much higher. This result is in contrast to what found in **Figure 8.8**, but it matches the conclusions in Geng (2010).

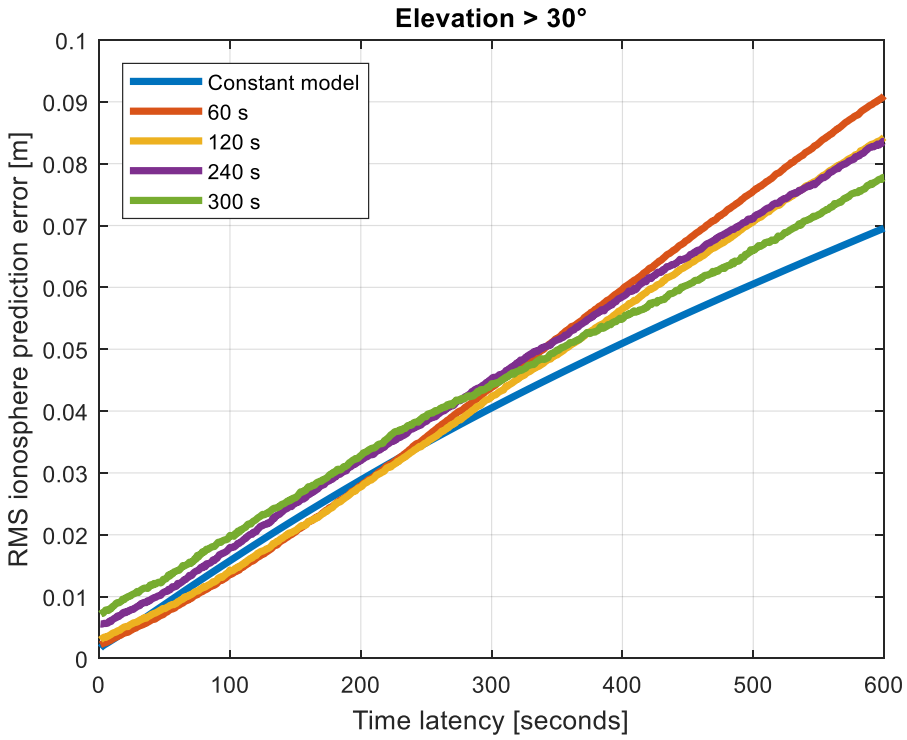


Figure 8.8 *RMS of the errors obtained when predicting the ionosphere using the constant bias model (blue), the linear fitting model with a time window large 60 seconds (red), 120 seconds (yellow), 240 seconds (purple), and 300 seconds (green). Elevation angles above 30°.*

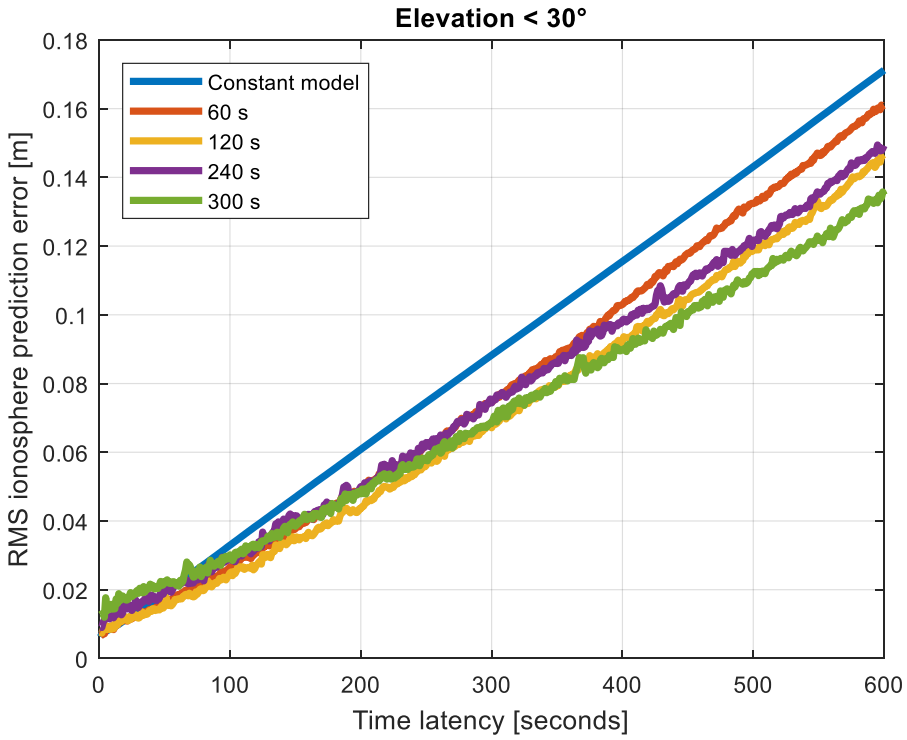


Figure 8.9 *RMS of the errors obtained when predicting the ionosphere using the constant bias model (blue), the linear fitting model with a time window large 60 seconds (red), 120 seconds (yellow), 240 seconds (purple), and 300 seconds (green). Elevation angles below 30°.*

From the previous analysis on the ionosphere prediction strategies based on the data recorded by the IGS station DAEJ, it is not clear whether the linear fitting model with a time window of 120 seconds adopted in Geng (2010) outperforms the constant bias model, especially with satellites at high elevation.

In order to further assess the best ionosphere prediction strategy to be used in this research, two GNSS kinematic data sets were analysed.

The first one was recorded by a GNSS receiver placed in a van driving around the city of Birmingham on the 22nd June 2016. Given the low number of satellites in view and the frequent tracking discontinuity due to the sub-urban environment, it was not possible to distinguish between the results based on satellites' elevation. **Figure 8.10** compares the ionosphere prediction errors for different time latencies made when using the constant bias model and the linear fitting model with a window of 120 seconds. From this plot it clearly emerged that, if the prediction interval is longer than 6 seconds, the linear fitting model outperforms the constant bias model. Indeed, the error made by predicting with the linear fitting model the ionospheric delay for 3 minutes is 2.4 cm, while it can be as large as 3.7 cm with the constant bias model.

On the other hand, one has to consider that, in order to predict the ionosphere with the linear model, at least 2 minutes of continuous observations from one satellite are needed. In urban environments, this requirements may be quite challenging to be achieved due to the presence of buildings that frequently obstruct the satellite visibility. Indeed, for this kinematic test, only 4.2% of all the continuous data arcs are longer than 120 seconds (see **Figure 8.11**). If the minimum number of epochs required to run the linear fitting model (in this case 120) is not available, the prediction has to start from the latest continous data arc which is long enough to extrapolate the ionospheric delay. For this reason, the actual prediction time may be much larger. The red plot in **Figure 8.11**, shows the RMS of the actual prediction intervals, when a given time window length is necessary to predict the ionospheric delay. The average prediction time is 21 minutes, if the linear fitting model with a time window of 120 seconds is employed. On the other hand, the RMS of the prediction time for the constant bias model is only 18.7 seconds. Since the prediction errors greatly diverge with the time latency, we might obtain a better prediction with the constant bias model than with the linear fitting model.

Similar conclusions can be drawn by analysing the observations recorded by a second van driving in the city of Nottingham on the 13th June 2017. From **Figure 8.12** we can observe that the prediction error made by the constant bias model drifts with the time latency much quicker than the error obtained with the linear fitting model. Indeed, by predicting the ionospheric delay with the constant bias model for 3 minutes we can have an error of about 5.8 cm, while it is only 2.1 cm with the linear fitting model. On the other hand, due to the lack of enough continuous measurements to create the linear fitting model, on average its actual prediction time is much longer than the one for the constant bias model. In this test, on average the data gaps are only 94 seconds, however we might need to predict the ionosphere for about 17 minutes due to the fact that only 13.9% of the data arcs are longer than 120 seconds (see **Figure 8.13**).

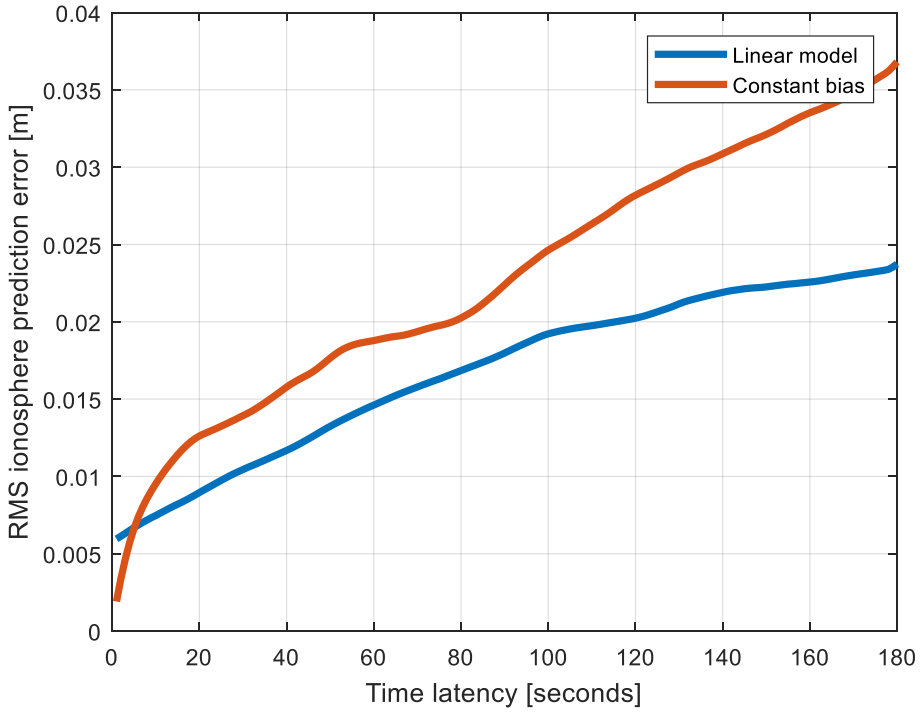


Figure 8.10 *RMS of the errors obtained when predicting the ionosphere using the constant bias model (blue), the linear fitting model with a time window large 120 seconds (red). Driving test around Birmingham.*

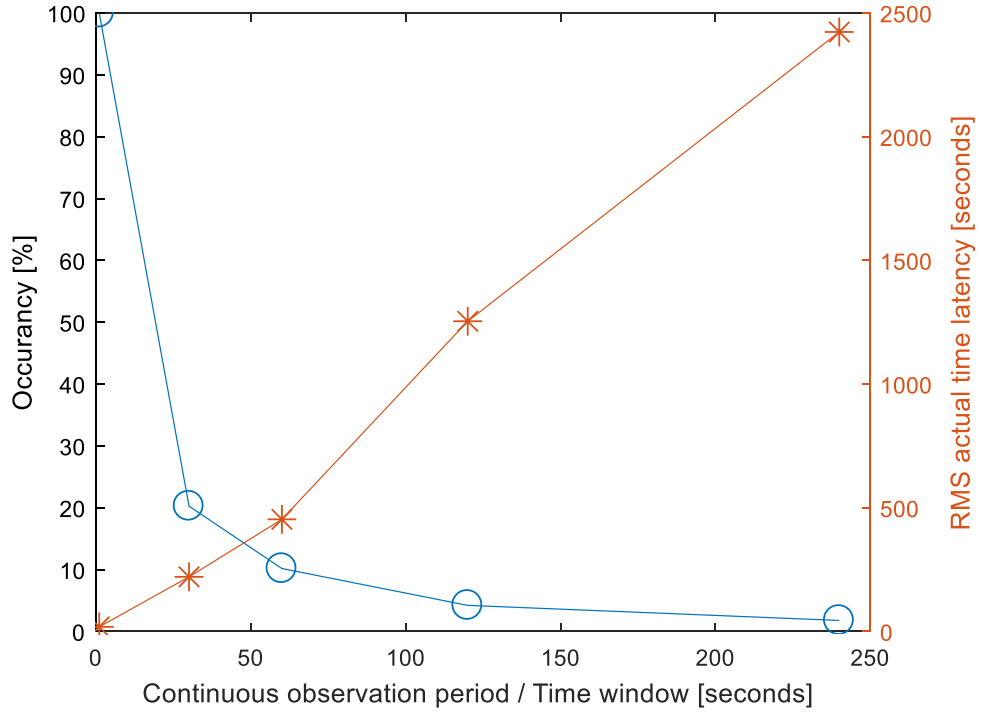


Figure 8.11 *Left plot (blue circle) is the percentage of continuous data arcs that are longer that the times on the x axis. Right plot (red star) is the RMS of the actual prediction time due to not having available the minimum number of observations required to run the linear fitting model. Driving test around Birmingham on the 22nd June 2017.*

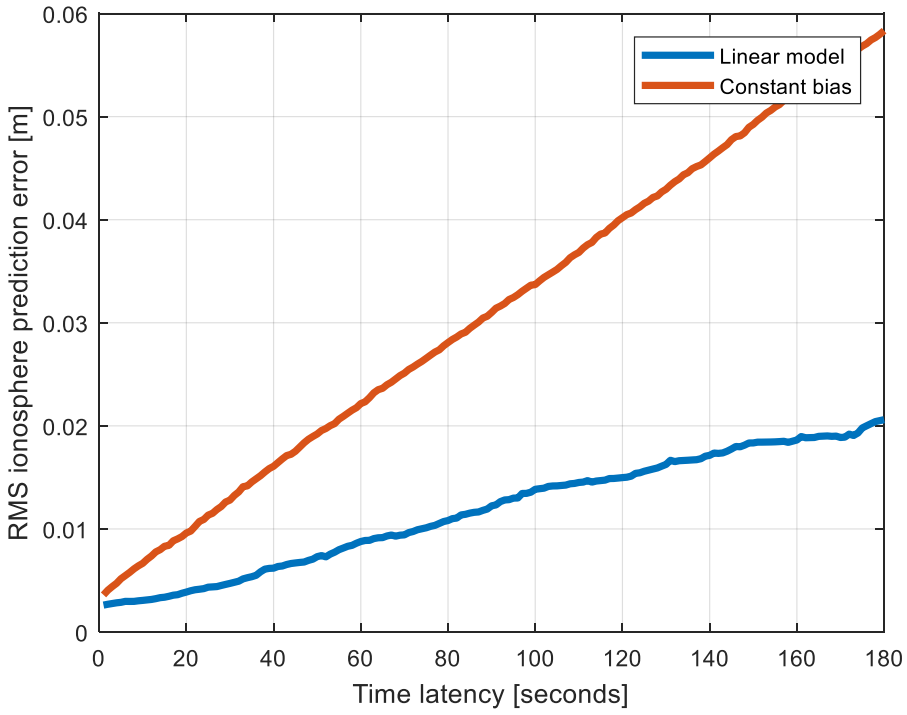


Figure 8.12 *RMS of the errors obtained when predicting the ionosphere using the constant bias model (blue), the linear fitting model with a time window large 120 seconds (red). Driving test in the city of Nottingham on the 13th June 2017.*

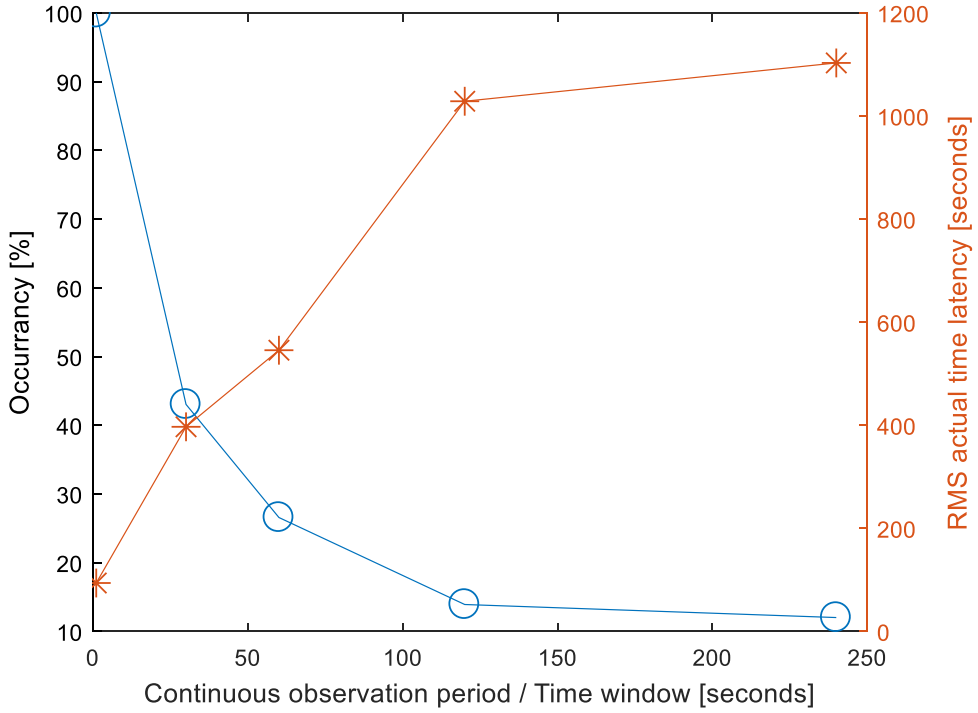


Figure 8.13 *Left plot (blue circle) is the percentage of continuous data arcs that are longer that the times on the x axis. Right plot (red star) is the RMS of the actual prediction time due to not having available the minimum number of observations required to run the linear fitting model. Driving test in the city of Nottingham on the 13th June 2017.*

From these results, we can conclude that although the linear fitting model provides the best prediction, in urban areas it might be difficult to continuously track a satellite for 120 seconds without having data gaps or cycle slips. For this reason, the constant bias model is generally adopted in this research, while the linear fitting model is used only when a data arc of at least 120 seconds is available.

Moreover, considering that, on average, the time for which the ionospheric delay needs to be predicted is only 94 seconds, the prediction errors are much smaller than the typical noise level in the pseudorange measurements. Hence, its contribution to the error in the IF pseudorange can be considered negligible.

8.1.1.4 Weighting method

The noise associated to the ionosphere corrected low-noise pseudorange combination depends on both the error in the pseudoranges and on the smoothed ionosphere correction. The latter is as large as metre-level before converging to centimetre-level. For this reason, a proper weighting method, that considers the varying noise on the ionosphere correction needs to be defined.

If the ionosphere corrected pseudorange combination, computed at epoch t_k, can be written as

$$P^s_{r,IF}(t_k) = \alpha_1 P^s_{r,1}(t_k) + \alpha_2 P^s_{r,2}(t_k) + \alpha_3 P^s_{r,3}(t_k) - q \cdot \tilde{I}^s_r(t_k) \qquad (8.10)$$

the variance of its error at epoch t_k, $\sigma^2_{P^s_{r,IF}}$, can be expressed as in Equation (8.11), if we assume that the noise on $P^s_{r,i}$ is white and that there is no correlation between the errors in the pseudoranges on different frequencies.

$$\begin{aligned}\sigma^2_{P^s_{r,IF}}(t_k) = {} & \alpha_1^2\sigma^2_{P^s_{r,1}} + \alpha_2^2\sigma^2_{P^s_{r,2}} + \alpha_3^2\sigma^2_{P^s_{r,3}} + q^2\sigma^2_{\tilde{I}^s_r}(t_k) - \\ & -2\alpha_1 q\sigma_{P^s_{r,1},\tilde{I}^s_r}(t_k) - 2\alpha_2 q\sigma_{P^s_{r,2},\tilde{I}^s_r}(t_k) - 2\alpha_3 q\sigma_{P^s_{r,3},\tilde{I}^s_r}(t_k)\end{aligned} \qquad (8.11)$$

In (8.11) $\sigma_{P^s_{r,i}}$ is the standard deviation of the error affecting the pseudorange measurements on frequency f_i ($P^s_{r,i}$), $\sigma_{\tilde{I}^s_r}(t_k)$ is the standard deviation of the error in the smoothed ionosphere correction at epoch t_k ($\tilde{I}^s_r$), and $\sigma_{P^s_{r,i},\tilde{I}^s_r}$ is the covariance between the errors in $P^s_{r,i}$ and in $\tilde{I}^s_r$.

Assuming an infinite smoothing window *N*, the variance of the error in the smoothed ionosphere at epoch t_k can be written as in the following Equation (8.12), where $\sigma^2_{I^{s,P}_r}$ is the variance of the error in the ionosphere observable computed from the pseudoranges, while $\sigma^2_{\bar{I}^s_r}$ is the variance of the ionosphere predicted using the time differenced carrier phase measurements. It can be computed from Equation (8.14), in which $\sigma^2_{I^{s,L}_r}$ is the variance of the error in the ionosphere observable computed from the carrier phases.

$$\sigma^2_{\tilde{I}^s_r}(t_k) = \frac{1}{k^2}\sigma^2_{I^{s,P}_r} + \left(1 - \frac{1}{k}\right)^2 \sigma^2_{\bar{I}^s_r}(t_k) \qquad (8.12)$$

$$\sigma^2_{I^{s,P}_r} = \frac{\sigma^2_{P^s_{r,1}} + \sigma^2_{P^s_{r,2}}}{\left(1 - \frac{f_1^2}{f_2^2}\right)^2} \qquad (8.13)$$

$$\sigma^2_{\tilde{I}^s_r}(t_k) = \sigma^2_{\tilde{I}^s_r}(t_{k-1}) + \frac{2}{k-1}\sigma^2_{I^{s,L}_r} \tag{8.14}$$

$$\sigma^2_{I^{s,L}_r} = \frac{\sigma^2_{L^s_{r,1}} + \sigma^2_{L^s_{r,2}}}{\left(1 - \frac{f_1^2}{f_2^2}\right)^2} \tag{8.15}$$

The covariance $\sigma_{P^s_{r,i},\tilde{I}^s_r}$ between the errors in $P^s_{r,i}$ and in $\tilde{I}^s_r$, computed at epoch t_k, are as in (8.16).

$$\left.\begin{aligned} \sigma_{P^s_{r,1},\tilde{I}^s_r} &= \frac{1}{1-\frac{f_1^2}{f_2^2}}\sigma^2_{P^s_{r,1}} \\ \sigma_{P^s_{r,2},\tilde{I}^s_r} &= -\frac{1}{1-\frac{f_1^2}{f_2^2}}\sigma^2_{P^s_{r,2}} \\ \sigma_{P^s_{r,3},\tilde{I}^s_r} &= 0 \end{aligned}\right\}, k = 1$$

$$\left.\begin{aligned} \sigma_{P^s_{r,1},\tilde{I}^s_r} &= \frac{1}{1-\frac{f_1^2}{f_2^2}}\frac{\sigma^2_{P^s_{r,1}}}{k} \\ \sigma_{P^s_{r,2},\tilde{I}^s_r} &= -\frac{1}{1-\frac{f_1^2}{f_2^2}}\frac{\sigma^2_{P^s_{r,2}}}{k} \\ \sigma_{P^s_{r,3},\tilde{I}^s_r} &= 0 \end{aligned}\right\}, k > 1 \tag{8.16}$$

Figure 8.14 shows how well this weighting method can describe the variation of the error in smoothed ionosphere with the time. The ionosphere observable, computed from simulated pseudoranges affected by multipath with a correlation time constant of 2 seconds, was smoothed with the Hatch filter. The red plot, which describes the error in the smoothed ionosphere, is perfectly included in the two yellow plots, which represent the 95% confidence level computed from Equation (8.12) and the pseudorange weights in **Table 7.7**.

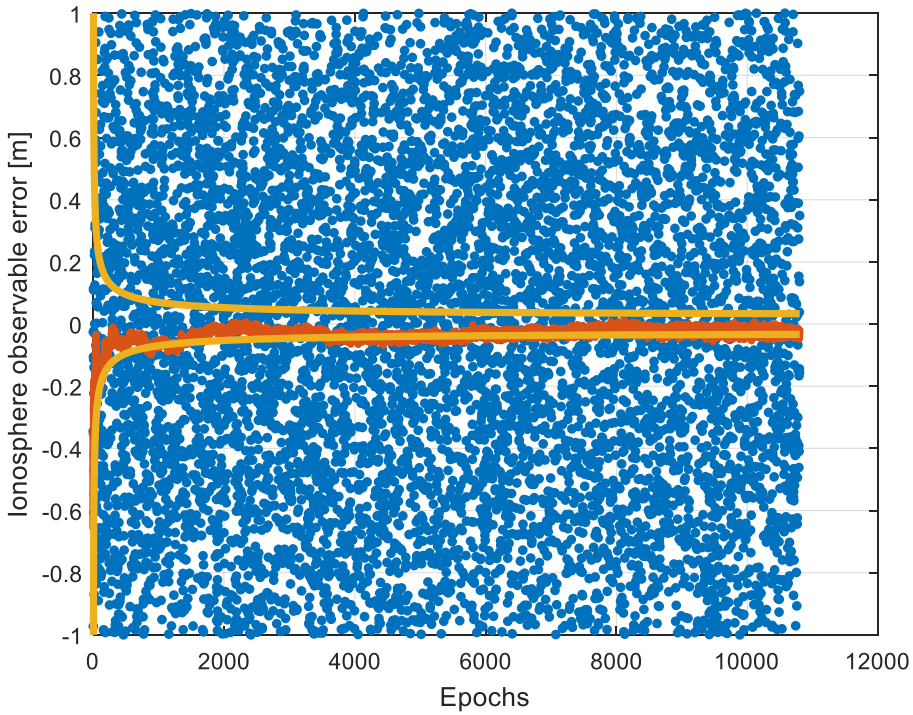


Figure 8.14 *Error in the ionospheric delay observable. Blue dots shows the time-series of the error in the ionosphere computed from the raw pseudoranges, the red line is the error in the smoothed ionosphere, while the yellow lines are the 95% confidence level (2σ) achieved by the proposed weighting method. Simulated data with a multipath time constant of 2 seconds.*

8.1.1.5 Results on quick re-convergence in open sky conditions

The algorithm based on the smoothed ionosphere correction described in this section was tested using the GPS/Galileo Simulink tool. Firstly, a simulation scenario in which a GPS+Galileo receiver was placed in an open sky environment located in the IGS station SEY2 was set. The assumed multipath level is described in Section 6.2.4. The GNSS measurements were recorded for three hours with an observation rate of 1 Hz. The GPS low-noise pseudorange combination and the pseudorange on Galileo E5 frequency were corrected by the smoothed ionosphere and processed, together with the L1-L5 and E1-E5 IF carrier phase combinations, with the POINT software in kinematic PPP mode. The values that populate the covariance matrices required to tune the Kalman filter can be found in **Table 8.2** and in **Table 8.3**. In order to test the effect of the proposed method on the PPP re-convergence, the positioning filter was forced to restart after 90 minutes.

Table 8.2 *Standard deviations of the initial error in the state vector and of the process noise used to tune the Kalman filter.*

State vector elements	Initial error	Process noise
Position components	2.0 m	1000.0 m/√s
Receiver clock offset	1000.0 m	10.0 m/√s
Residual wet ZTD	0.1 m	$3.0 \cdot 10^{-3}$ m/√s
Ambiguities	1000.0 cycles	0.0 cycles/√s

Table 8.3 *Expected standard deviation of the error in GPS and Galileo pseudoranges that was assumed when designing the Kalman filter. Units of meters.*

L1	L2	L5	E1	E5a	E5b	E5	E6
1.0	1.3	0.8	1.0	0.8	0.8	0.4	1.0

Figure 8.15 compares the error in the horizontal PPP solutions computed from GPS IF combinations and from the low-noise pseudorange combination corrected by the smoothed ionosphere combination, after the filter was forced to restart at minute 90. In the left subplot is the RMS of the horizontal error, while the 95th percentile is shown in the right subplot. We can see how the new configuration enables PPP re-convergence in a few tens of seconds. Indeed, the RMS error of the horizontal solution computed from the smoothed ionosphere corrected pseudoranges re-converges below 10 cm in 40 seconds, while the 95th percentile error re-converges in 3 minutes and 39 seconds. On the other hand, users have to wait for almost 6 minutes before the RMS error of the horizontal PPP solution based on IF combinations is again below 10 cm, and more than 14 and half minutes for the 95th percentile error to re-converge.

The RMS and 95th percentile of the horizontal positioning error in the Galileo solutions are plotted in **Figure 8.16**. The very small error in the E5 pseudorange let the PPP solution to re-converge on average in only 8 seconds and 95% of the time in only 3 minutes. For comparison, the 95% of the PPP solutions based on the Galileo E1-E5 IF combination take almost 10 minutes longer to re-converge below 10 cm.

When applied to two-constellation GNSS, the new algorithm allows 95% of the PPP solutions to re-convergence in less than a minute. As it is shown in the left subplot of **Figure 8.17**, the 95th percentile of the horizontal error is below 10 cm 43 seconds after the PPP filter was forced to restart.

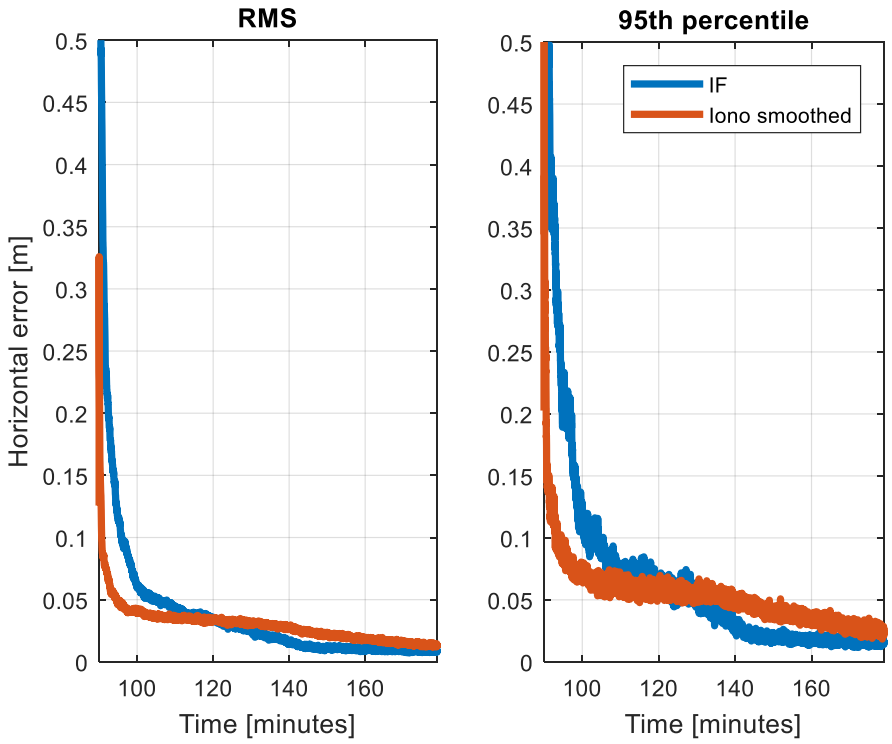


Figure 8.15 *Comparison between the horizontal error achieved using the GPS L1-L5 IF combination (blue) and the one obtained by using the low-noise pseudorange combination corrected by the smoothed ionosphere (red). The multipath correlation time is set to 2 seconds. Only the last one and a half hour is plotted.*

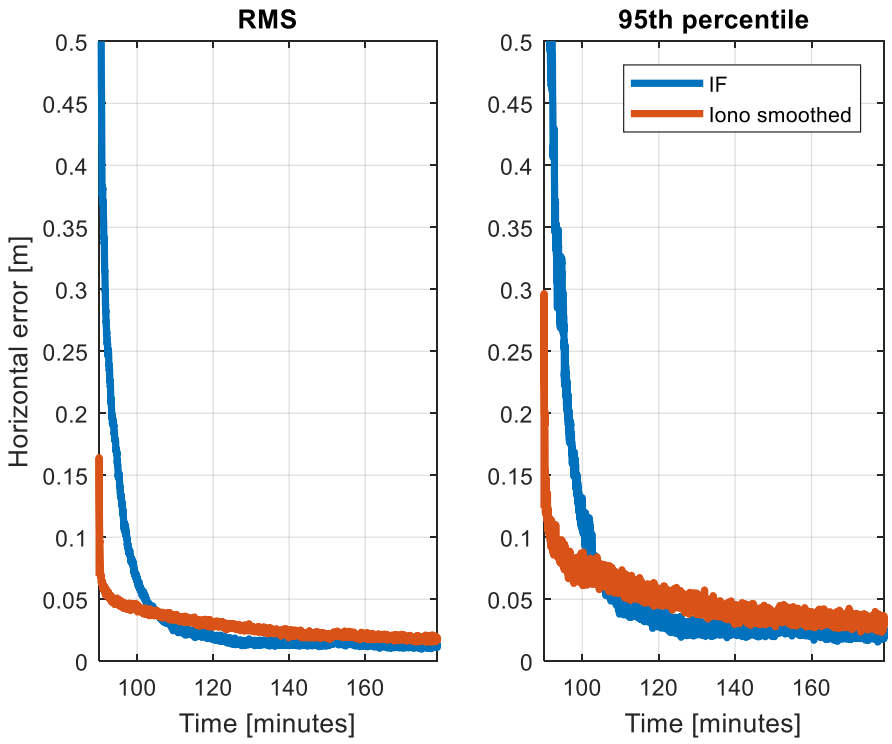


Figure 8.16 *Comparison between the horizontal error achieved using the Galileo E1-E5 IF combination (blue) and the one obtained by using the E5 pseudorange corrected by the smoothed ionosphere (red). The multipath correlation time is set to 2 seconds. Only the last one and a half hour is plotted.*

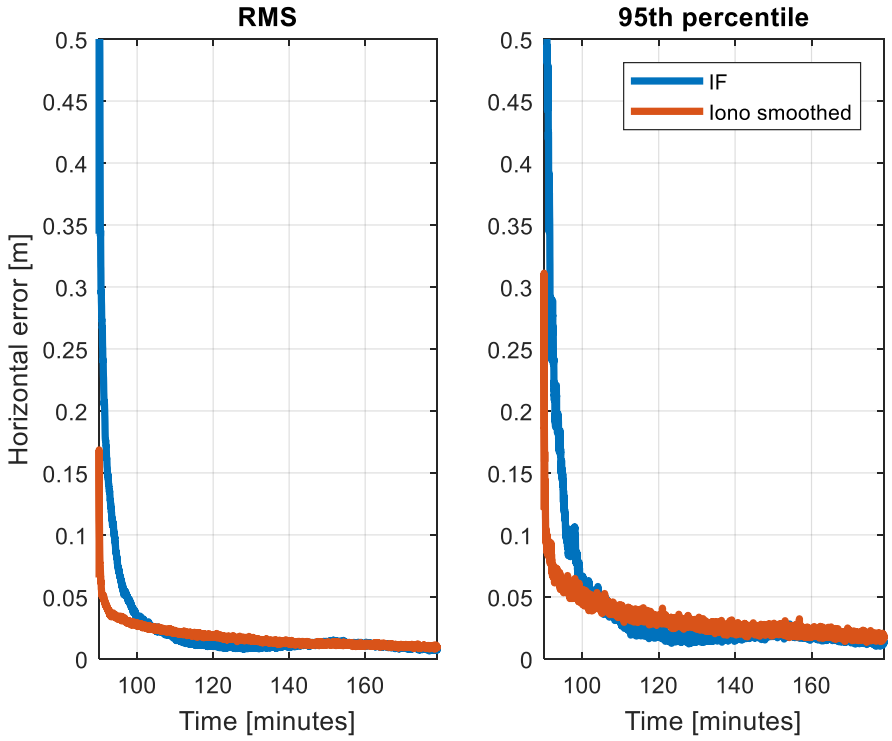


Figure 8.17 *Comparison between the horizontal error achieved using the GPS+Galileo IF combinations (blue) and the one obtained by using the low-noise pseudoranges corrected by the smoothed ionosphere (red). The multipath correlation time is set to 2 seconds. Only the last one and a half hour is plotted.*

Sensitivity of the method to different multipath correlation time constants

It is thoroughly recognized that the standard configuration of the Hatch filter doesn't perfectly smooth the multipath from the GNSS pseudoranges due to its high temporal correlation. For this reason, the proposed method configured to quickly recover centimetres-level PPP solutions might not perform well in presence of multipath errors with large correlation time constants.

In order to test the effect of different multipath correlation time constants on the proposed method, a new simulation scenario was set in which all the GNSS measurements were assumed to be affected by multipath with the same correlation time constant, from 2 to 60 seconds. Multipath correlation times within this range are typical for kinematic tests in urban environments (Khanafseh et al., 2018). The simulated measurements are then processed with POINT in kinematic PPP mode. After 90 minutes the positioning filter was forced to restart to simulate the re-convergence.

For each correlation time constant, the time the RMS and the 95th percentile of the horizontal float solution takes to re-converge below 10 cm, for the GPS, Galileo, and GPS+Galileo IF and ionosphere smoothed cases are reported in

Figure 8.18 and in **Figure 8.19**, respectively. When the GNSS measurements' error is poorly time correlated, the proposed method allows for much quicker re-convergence than the traditional PPP configuration based on two-frequency IF pseudoranges. For example, with a multipath correlation time constant equal to 5 seconds, the average re-convergence time (below 10 cm) for a GPS only PPP horizontal solution is 2 minutes and 45 seconds, more than 3 times less than PPP solution computed from the L1-L5 IF pseudorange combination, which takes about 9 minutes to re-converge to centimetres-level of accuracy. Similarly, the very low noise and excellent multipath mitigation properties of the Galileo E5 AltBOC pseudorange let the horizontal solution re-converge in about 4 minutes if corrected by the soothed ionosphere, while re-convergence may take more than 9 minutes when the pseudoranges are linearly combined in the E1-E5 IF combination.

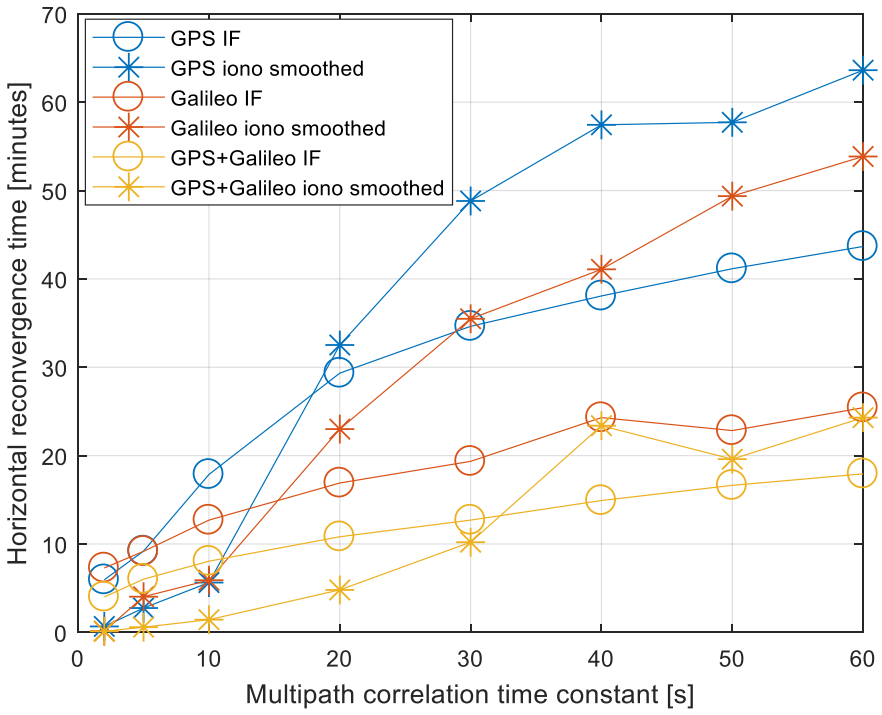


Figure 8.18 *Sensitivity of the convergece time (RMS) to different multipath correlation time for GPS (blue), Galileo (red), and GPS+Galileo (yellow) cases. Comparison between the IF pseudoranges (circle) and the smoothed ionosphere corrected low-noise pseudoranges (star).*

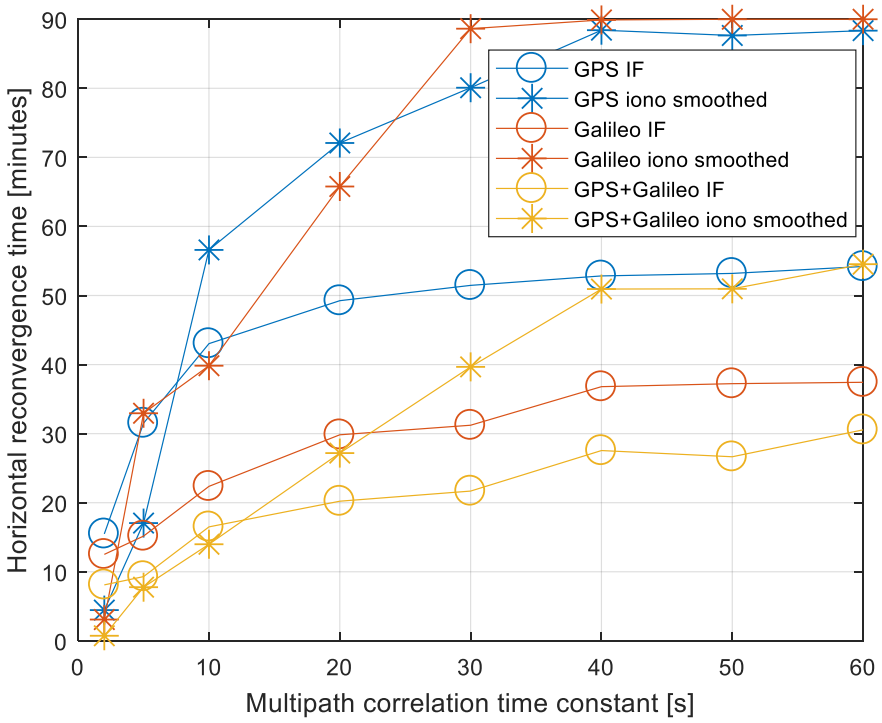


Figure 8.19 *Sensitivity of the convergece time (95th percentile) to different multipath correlation time constants for GPS (blue), Galileo (red), and GPS+Galileo (yellow) cases. Comparison between the IF pseudoranges (circle) and the smoothed ionosphere corrected low-noise pseudoranges (star).*

On the other hand, when the multipath correlation time equals 60 seconds, even though the ionosphere corrected pseudoranges have much less noise than the IF pseudorange combinations, the horizontal PPP solution computed with the new configuration takes longer than the traditional one to re-converge. For instance, the re-convergence time for average GPS horizontal solution is more than one hour for the ionosphere corrected low-noise pseudorange and less than 45 minutes for the L1-L5 IF combination. Users adopting the ionosphere corrected Galileo E5 pseudorange have to wait for almost 30 minutes more before re-convergence with respect to the E1-E5 IF case, while by considering the GPS+Galileo a degradation of 35% in the re-convergence of the horizontal PPP solution was registered.

Of course, assuming the multipath correlation time for all the simulated measurements to be equal to 60 seconds is a very conservative assumption. Indeed, it was proved in Khanafseh et al. (2018) that for 99% of the time the correlation time constant lies in the range between 2 and 60 seconds, for kinematic applications in urban areas.

For this reason, the ionosphere corrected low-noise pseudorange combinations were also tested in a scenario where the multipath correlation time constant was assumed to be normally distributed with a standard deviation of 10 seconds and a mean of 35 seconds. The results are presented in **Figure 8.20**, **Figure 8.21**, and **Figure 8.22**, for the GPS, Galileo, and GPS+Galileo cases. In each figure, the left subplot shows the RMS of the horizontal errors over the 50 simulations from minute 90, when the PPP filter was forced to restart, until the end of the simulation. In the right subplot is the 95^{th} percentile of the horizontal error.

Figure 8.20 compares the re-convergence patterns for the GPS L1-L5 IF pseudorange combination (blue) and the one based on the triple-frequency low-noise pseudorange combination corrected by the smoothed ionosphere combination (red). The RMS of the horizontal error for the IF case re-converges below 10 cm in almost 25 minutes, while it takes more than 55 minutes for the ionosphere smoothed case. The results for Galileo are shown in **Figure 8.21**. The solution based on the IF combinations takes on average 20 minutes to re-converge to a centimetre-level positioning accuracy, on the other hand the solution based on the E5 pseudorange corrected by the smoothed ionosphere combination requires 6 minutes more for re-convergence. **Figure 8.22** plots the error in the GPS+Galileo horizontal solutions. Although the RMS error of both solutions take about 12 minutes to re-converge, using the smoothed ionosphere corrected solution enlarges the horizontal re-convergence time of the 95^{th} percentile error by a factor of 2.66 with respect to using the IF combinations (51 minutes against 19.2 minutes).

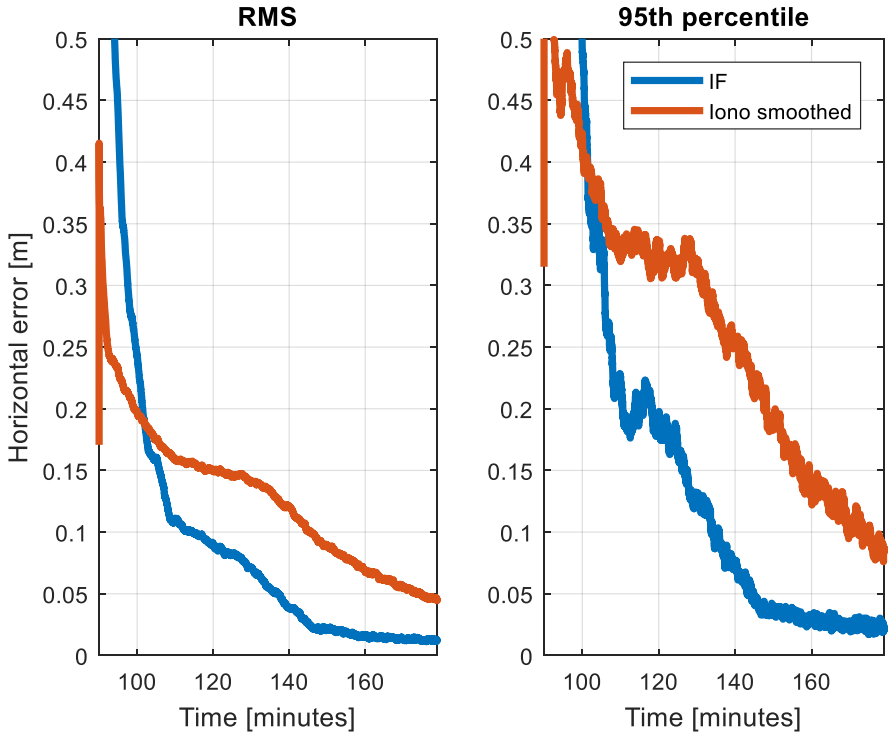


Figure 8.20 *Comparison between the horizontal error achieved using the GPS L1-L5 IF combination (blue) and the one obtained by using the low-noise pseudorange combination corrected by the smoothed ionosphere (red). The multipath correlation time is randomly generated. Only the last one and a half hour is plotted.*

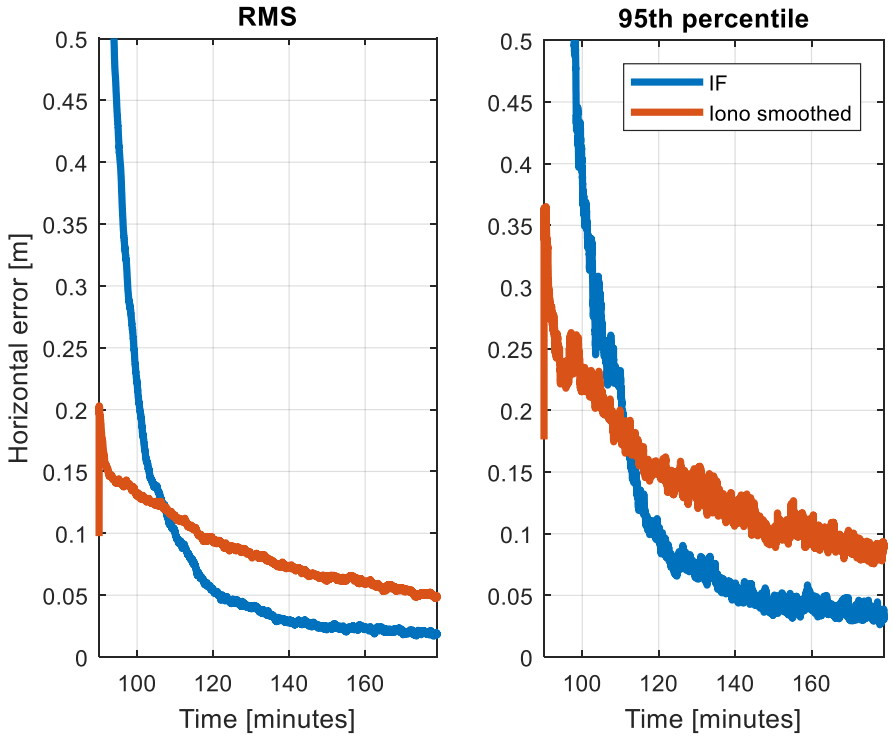


Figure 8.21 *Comparison between the horizontal error achieved using the Galileo E1-E5 IF combination (blue) and the one obtained by using the E5 pseudorange corrected by the smoothed ionosphere (red). The multipath correlation time is randomly generated. Only the last one and a half hour is plotted.*

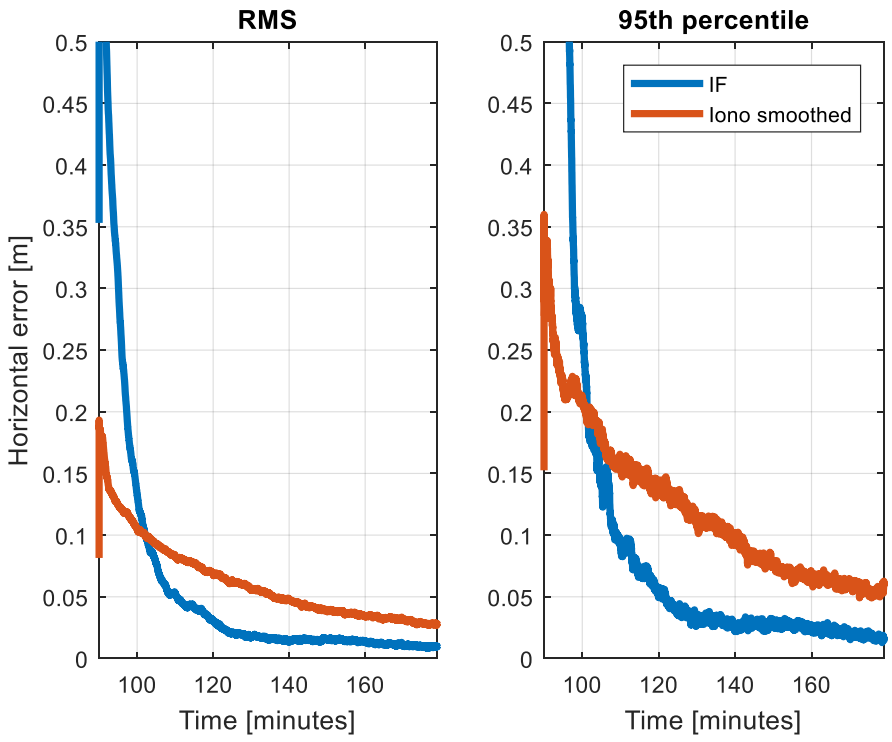


Figure 8.22 *Comparison between the horizontal error achieved using the GPS+Galileo IF combinations (blue) and the one obtained by using the low-noise pseudoranges corrected by the smoothed ionosphere (red). The multipath correlation time is randomly generated. Only the last one and a half hour is plotted.*

The reason why having multipath in the pseudoranges with larger correlation time constant led to poorer performance of the proposed method can be addressed to a wrong tuning of the Kalman filter. The filter expects to deal with more accurate pseudoranges than the actual ones. Indeed, the weighting method that was used to account for the varying quality of the ionosphere corrected pseudoranges assumes that the errors in the GNSS observables are white. In actuality, some components of the noise in the pseudorange and carrier phase measurements, for example the multipath, are strongly time correlated. For this reason, even though this weighting method correctly considers the time varying error in the ionosphere corrected low-noise pseudorange combinations, it still lead to an overoptimistic weighting, if the correlation time constant of the multipath is large. As an example, **Figure 8.23** compares the error in the smoothed ionospheric correction (red plot) with the 95% confidence bound (yellow plot) computed following Equation (8.16) when the GNSS measurements are affected by multipath with correlation time of 60 seconds. The error in the smoothed ionospheric error is often much larger than the expected one. As a consequence, the proposed weighting method has a negative

impact on the positioning solution. Indeed, excessively small values for the pseudorange error produces biased state estimates due to pseudorange noise having too great influence on them. Consequently, the Kalman filter takes longer to realign the positioning solution to its true value (Paul D Groves, 2013).

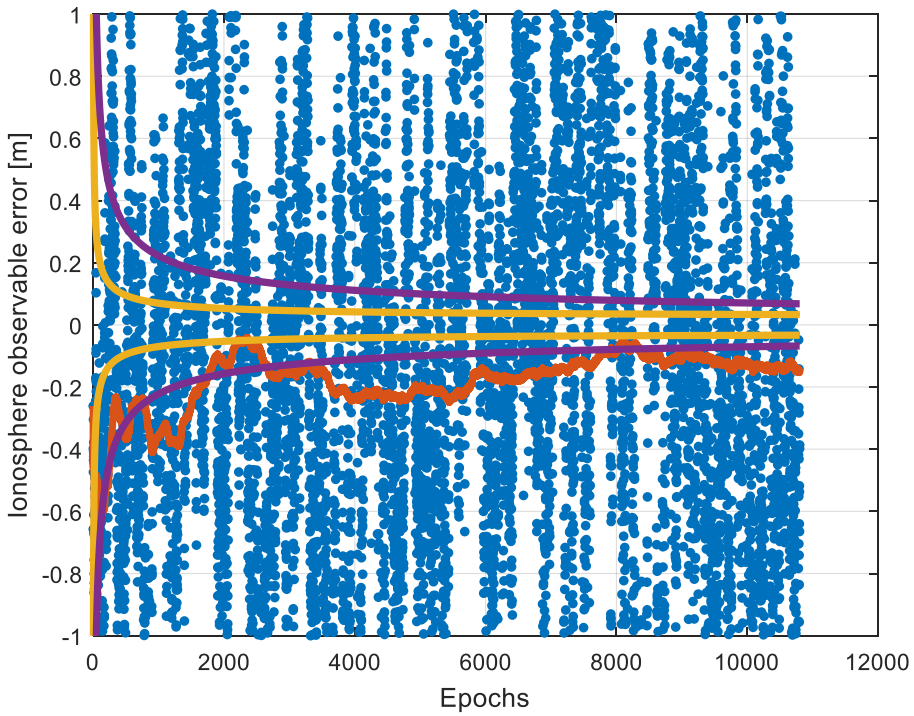


Figure 8.23 *Error in the ionospheric delay observable. Blue dots shows the time-series of the error in the ionosphere computed from the raw pseudoranges, while the red line is the error in the smoothed ionosphere. The 95% confidence level (2σ) achieved by the proposed weighting method (yellow line) and by the modified version (purple line) are also plotted . Simulated data with a multipath time constant of 60 seconds.*

It follows that there is a need to adjust the weighting method with a term that also considers the existing temporal correlation in the GNSS measurements' errors. Assuming the errors in the pseudoranges and carrier phases to behave as a first order Gauss-Markov process with time constant τ, the improved formula for the expected standard deviation of the error in the smoothed ionospheric delay is

$$\sigma^2_{\tilde{I}_r^s}(t_k) = \frac{1}{k^2}\sigma^2_{I_r^{s,P}} + \left(1-\frac{1}{k}\right)^2 \sigma^2_{\tilde{I}_r^s}(t_k) + 2\cdot\left[\frac{1}{k}\left(1-\frac{1}{k}\right)\frac{1}{k-1}e^{\frac{-\Delta t}{\tau}}\sigma^2_{I_r^{s,P}} - \left(1-\frac{1}{k}\right)^2\frac{1}{k-1}e^{\frac{-\Delta t}{\tau}}\sigma^2_{I_r^{s,L}}\right] \tag{8.17}$$

On top of that, it is also advisable to assume more conservative values for the measurements error.

The modified weighting method is plotted in purple in **Figure 8.23**, where the pseudorange noise is assumed to be two times larger than the values shown in **Table 7.7**. The 95% confidence bound computed with the modified weighting method offers a looser constraint on the pseudorange noise than the original one. As a consequence, we expect to have quicker re-convergence even in case of highly correlated multipath.

The effect of the modified weighting method on the PPP re-convergence can be seen in **Figure 8.24**, **Figure 8.25**, and **Figure 8.26**, for the GPS, Galileo, and GPS+Galileo cases. Unlike in the previous plots, the horizontal solutions based on low-noise pseudoranges corrected by the smoothed ionosphere combination take much shorter than the ones based on the IF pseudoranges even with large multipath correlation time constants. For the GPS case, 83.5% reduction in the re-convergence time (RMS error) is visible with the ionosphere smoothed configuration, while for the Galileo and GPS+Galileo cases the horizontal RMS error drops to centimetre-level in a few tens of seconds.

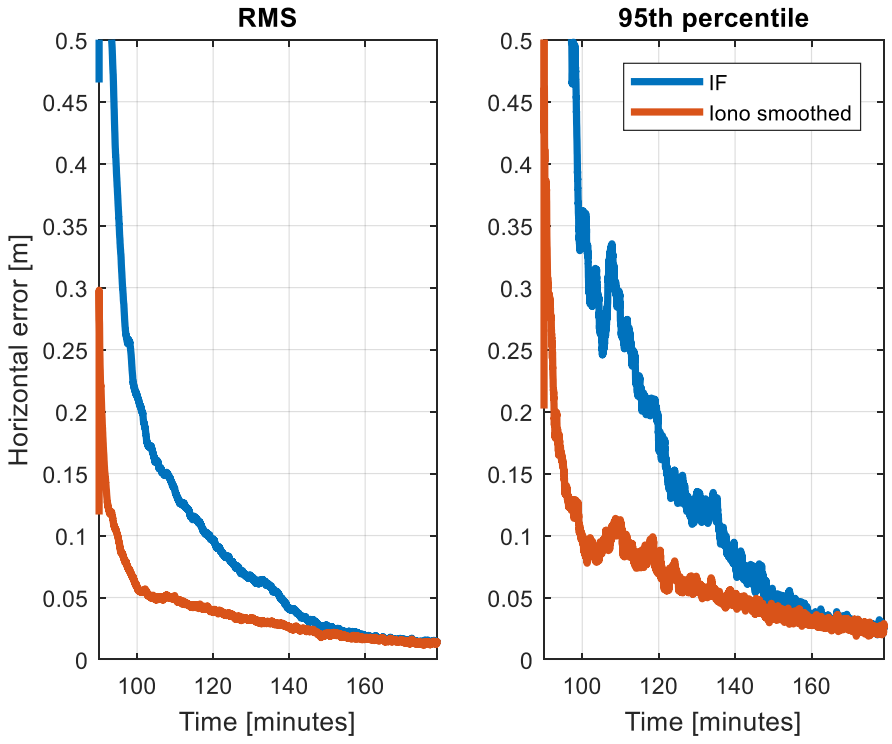


Figure 8.24 *Comparison between the horizontal re-convergence for the GPS L1-L5 IF case (blue) and for the smoothed ionosphere corrected low-noise pseudorange (red) with the modified weighting methd. The multipath correlation time is randomly generated.*

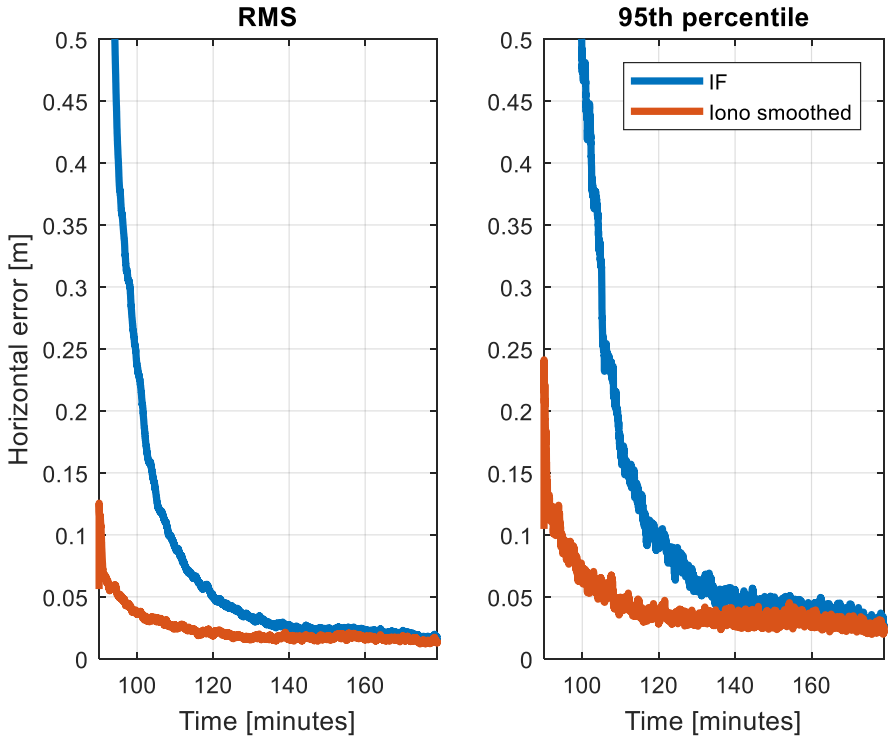


Figure 8.25 *Comparison between the horizontal re-convergence for the Galileo E1-E5 IF case (blue) and for the E5 pseudorange corrected by the smoothed ionosphere (red) with the modified weighting methd. The multipath correlation time is randomly generated.*

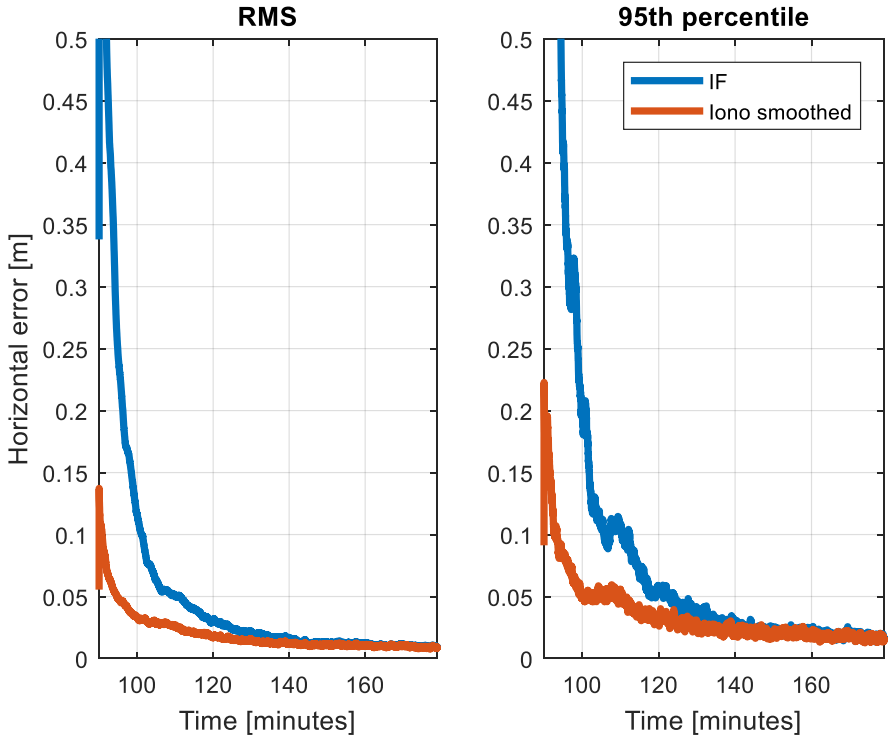


Figure 8.26 *Comparison between the horizontal re-convergence for the GPS+Galileo IF combinations (blue) and for the low-noise pseudoranges corrected by the smoothed ionosphere (red) with the modified weighting methd. The multipath correlation time is randomly generated*

8.1.1.6 Results on quick re-convergence in urban environments

The impact of the GPS and Galileo low-noise pseudoranges corrected by the smoothed ionosphere combination in the PPP re-convergence has also been analysed in the kinematic test scenario in which a pedestrian was simulated to be walking around the neighbourhood of the UCL campus in London. Further details regarding the scenario are given in Chapter 7. In this scenario, frequent data gaps, up to 12 minutes long, forced the PPP filter to restart. Hence, the developed algorithm can benefit from the ionosphere prediction strategy proposed in Dai et al. (2003), and analysed previously in this chapter, to obtain faster re-convergence than the traditional PPP solution based on the IF combination.

Unlike the test in Paragraph 7.3, realistic values for the multipath correlation time constant were adopted. It was assumed to be randomly generated with a mean of 35 seconds and a standard deviation of 10 seconds. In this way the correlation time lies within the 5-65 seconds range for 99.9% of the time (Khanafseh et al., 2018).

GPS and Galileo measurements were processed in kinematic PPP mode through POINT. The errors in the horizontal PPP solutions for the kinematic part of the simulation scenario, i.e. after minute 30 when the pedestrian starts moving, are presented in **Figure 8.27**. The left subplot compares the RMS errors for the IF (blue) and smoothed ionosphere corrected (red) pseudoranges, while in the right subplot the 95^{th} percentile of the horizontal errors are plotted. At the very beginning of the kinematic test, when many satellites are in view and the HDOP is very small, even smaller than 1, both horizontal solutions have a precision far better than 20 cm. At minute 33.23, the number of visible satellites drops below 6, and the HDOP becomes as large as 30 (see **Figure 7.12** in Chapter 7). From this point onwards, the first re-convergence pattern is visible in **Figure 8.27**. The horizontal solution based on the IF combination, starting from an error of 0.84 m (RMS), slowly converges towards higher accuracy levels. Unfortunately, because of the very slow re-convergence time of the PPP solution, combined with frequent positioning filter restarts due to buildings masking the satellite visibility, it is not possible to converge below 20 cm. On the other hand, by employing the algorithm proposed in this section a converged solution in a few tens of seconds is achieved. Indeed, after the positioning filter

had to restart, because of the low number of satellites in view, the RMS of the horizontal error re-converges to the 20 cm threshold in just 54 seconds. Similarly, after the second peak in the positioning error, that is visible in **Figure 8.27** at minute 38.43, the PPP solution re-converges in only 52 seconds.

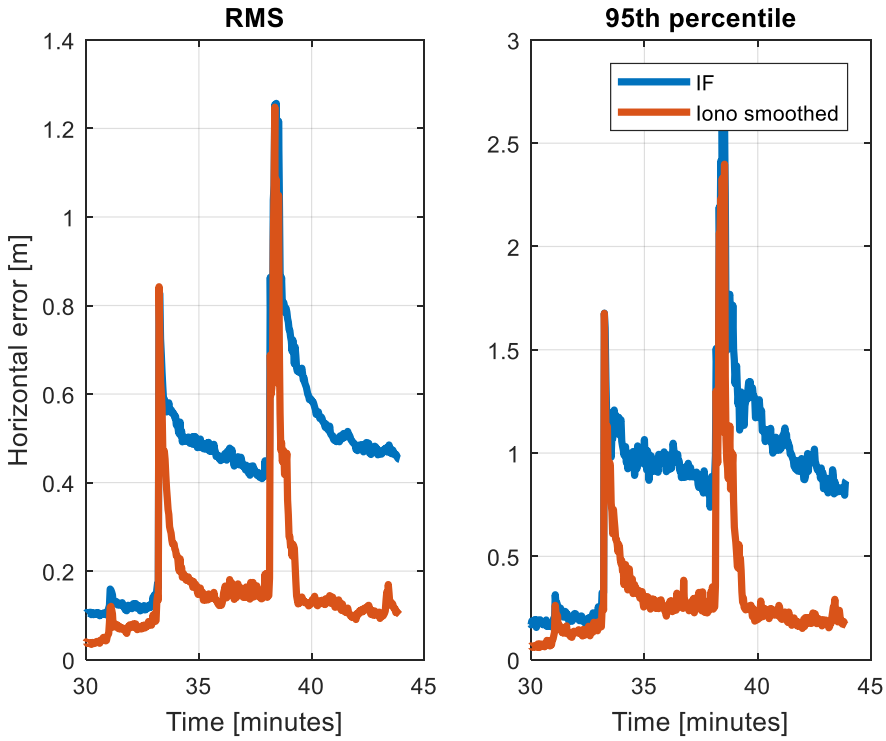


Figure 8.27 *Comparison between the horizontal error achieved using the traditional GPS+Galileo IF pseudorange combinations (blue) and the one obtained by using the low-noise pseudoranges corrected by the smoothed ionosphere (red). Kinematic test.*

As it was shown in the previous chapter (although the analysis was based on a more than optimistic assumption regarding the multipath time constant), the traditional PPP algorithm is perfectly able to fulfil the requirements of many land-based applications in cities requiring meters or sub-meters level of positioning accuracy. Unfortunately, due to its slow convergence time and the presence of urban infrastructure, that may obstruct satellite visibility and force the Kalman filter to reinitialize, PPP cannot guarantee the where-in-lane accuracy level needed in applications such as collision avoidance, intelligent speed assistance, lane control, or restraint deployment (Teunissen and Montenbruck, 2017). On the other hand, by correcting the low-noise pseudorange combinations with the smoothed ionosphere combination, and by employing appropriate ionosphere prediction strategies in PPP, decimetre or

centimetre level accuracy can be achieved after a very short re-convergence time of less than one minute.

It must be pointed out that the results shown in this section are strictly dependent on the ionospheric model that was used to simulate the error in the GNSS measurements. It was aimed to characterize the behaviour of the average ionosphere at medium latitudes. In order to fully evaluate the performance of the method on a global scale, especially in those area characterized by active ionosphere activity and scintillation (along the equator or in the northern regions), more analysis based on simulated as well as real data are necessary.

8.2 Quick convergence by amplifying the narrow-lane wavelength

Although it has been shown that triple-frequency IF combinations offer very little improvements to the float PPP solutions (Deo and El-Mowafy, 2016; Elsobeiey, 2014), many studies have confirmed that using the signals on the additional frequency can improve the time to first ambiguity fix. An example of these research efforts is the TCAR method, an instantaneous ambiguity resolution method which was originally proposed for relative positioning over short baselines (Forsell et al., 1997; Jung et al., 2000; Vollath et al., 1999; Werner and Winkel, 2003). The combinations presented in Geng and Bock (2013) demonstrated that fixed PPP solutions could be obtained within a few minutes. Unfortunately, this method performs well only in multipath-free environments. Better results can be achieved considering geometry preserving combinations and improved ambiguity resolution methods, such as integer bootstrapping or the LAMBDA method. For instance, Henkel and Gunther (2008) found an optimal triple-frequency ionosphere-free code-carrier combination for Galileo signals that provides an ambiguity fixed solution, via integer bootstrapping, in about 5 seconds. However, in this study, the effect of multipath on pseudorange measurements was not considered.

In this section, new triple-carrier IF combinations aimed to reduce the convergence time of the float PPP solution will be analysed.

8.2.1 Triple-carrier ionosphere free combinations that minimise the noise in the narrow lane ambiguity

A linear combination L_r^s between GNSS carrier phase measurements on three frequencies f_1, f_2, and f_3 recorded at time *t* by the receiver *r* and transmitted by the satellite *s* can be written as

$$\begin{aligned} L_r^s(t) &= \alpha_1 L_{r,1}^s(t) + \alpha_2 L_{r,2}^s(t) + \alpha_3 L_{r,3}^s(t) \\ &= (\alpha_1 + \alpha_2 + \alpha_3) \cdot \rho_r^s(t) + \\ &- \left(\alpha_1 + \alpha_2 \frac{f_1^2}{f_2^2} + \alpha_3 \frac{f_1^2}{f_3^2} \right) \cdot I_{r,1}^s(t) \\ &- \alpha_1 \lambda_1 N_{r,1}^s - \alpha_2 \lambda_2 N_{r,2}^s - \alpha_3 \lambda_3 N_{r,3}^s + \varepsilon_r^s(t) \end{aligned} \tag{8.18}$$

For simplicity, in Equation (8.18) the non-dispersive term ρ_r^s includes the geometric range, the receiver's and satellite's clock offsets, and the tropospheric delay. For the same reason, the fractional part of the ambiguity term, due to receiver and satellite hardware delays, is omitted from the equation. The ionospheric delay affecting signals on frequency f_1 ($I_{r,1}^s$) is amplified by the term

$$q = \left(\alpha_1 + \alpha_2 \frac{f_1^2}{f_2^2} + \alpha_3 \frac{f_1^2}{f_3^2} \right) \tag{8.19}$$

While the noise in the combination ε_r^s has a standard deviation

$$\begin{aligned} \sigma_{\varepsilon_r^s} &= \sqrt{\alpha_1^2 \sigma_{\varepsilon_{r,1}^s}^2 + \alpha_2^2 \sigma_{\varepsilon_{r,2}^s}^2 + \alpha_3^2 \sigma_{\varepsilon_{r,3}^s}^2} \\ &= \sigma_{\varepsilon_{r,1}^s} \sqrt{\alpha_1^2 + \alpha_2^2 + \alpha_3^2} \end{aligned} \tag{8.20}$$

$$n = \sqrt{\alpha_1^2 + \alpha_2^2 + \alpha_3^2} \tag{8.21}$$

which is *n* times larger than the standard deviation of the error in the carrier phase on frequency f_1 ($L_{r,1}^s$). In Equations (8.20) and (8.21), the carrier phase measurements on different frequencies were assumed to have the same noise level.

In order to preserve the non-dispersive term ρ_r^s in the combination, the following condition must be satisfied

$$\alpha_1 + \alpha_2 + \alpha_3 = 1 \tag{8.22}$$

Moreover, the ionosphere amplification factor *q* needs to be nullified to have an IF combination.

$$q = \left(\alpha_1 + \alpha_2 \frac{f_1^2}{f_2^2} + \alpha_3 \frac{f_1^2}{f_3^2} \right) = 0 \tag{8.23}$$

Equations (8.22) and (8.23) describe a system of two linear equations with three unknowns α_1, α_2, and α_3. Using the third frequency gives the solution space one degree of freedom that can be exploited to impose one more constraint to the combination, for example reducing the noise in the combination. On the other hand, Deo and El-Mowafy (2016) already proved that triple-frequency combinations with minimum noise don't bring large improvements to the PPP convergence time with respect to the dual-frequency case. For this reason this type of constraint will not be considered here.

In this research project, the effect of triple-frequency combinations that optimize the noise of the NL ambiguity observable on the PPP convergence time will be tested. It can be demonstrated that for a given pseudorange noise level (with variance $\sigma_{e_r^s}^2$), there exists a triple-carrier combination that reduces the error in the NL ambiguity observable. By rewriting the ambiguity terms in Equation (8.18) as a combination between the EWL ($N_{r,ew}^s$), WL ($N_{r,w}^s$), and NL ($N_{r,n}^s$) ambiguities

$$\begin{aligned} \alpha_1\lambda_1 N_{r,1}^s + \alpha_2\lambda_2 N_{r,2}^s + \alpha_3\lambda_3 N_{r,3}^s = \alpha_3\lambda_3 N_{r,ew}^s + \left(\alpha_2\lambda_2 + \alpha_3\lambda_3\right) N_{r,w}^s \\ + \left(\alpha_1\lambda_1 + \alpha_2\lambda_2 + \alpha_3\lambda_3\right) N_{r,n}^s \end{aligned} \tag{8.24}$$

$$\bar{\lambda}_n = \alpha_1\lambda_1 + \alpha_2\lambda_2 + \alpha_3\lambda_3 \tag{8.25}$$

the variance $\sigma_{N_{r,n}^s}^2$ of the error in the NL ambiguity observable is

$$\sigma^2_{N^s_{r,n}} = \frac{\sigma^2_{e^s_r} + \sigma^2_{\varepsilon^s_r}}{\left(\alpha_1\lambda_1 + \alpha_2\lambda_2 + \alpha_3\lambda_3\right)^2} \tag{8.26}$$

Figure 8.28 shows the error in the NL ambiguity observable as a function of the amplified NL wavelength $\bar{\lambda}_n$ for the GPS triple-frequency IF combination. Here, the error in the L1-L5 IF pseudorange combination was assumed to be equal to 2.48, which corresponds to the errors in the GPS code pseudoranges reported in **Table 8.7**, and the carrier phase measurements were assumed to have a precision of 1 cm. It can be seen from **Figure 8.28** that the error in the NL ambiguity observable is greatly reduced as the NL wavelength is amplified until the noise reaches its minimum at a NL wavelength of 0.66 m. After this point the error in the NL ambiguity observable slowly increases. As a general rule, the amplified NL wavelength that guarantees the minimum error in the NL ambiguity observable is always larger than the traditional NL wavelength.

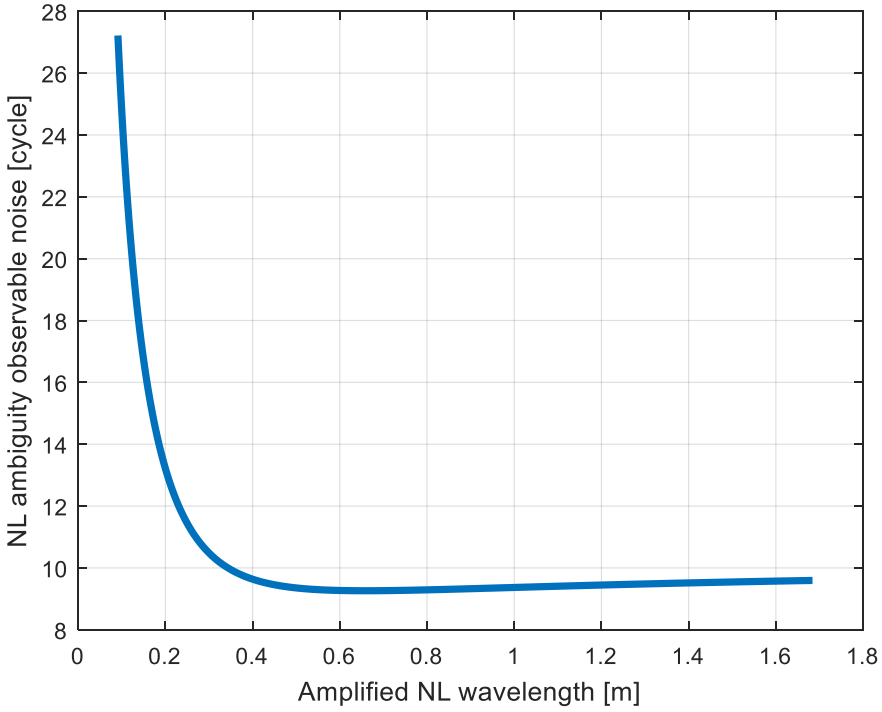


Figure 8.28 *Noise in the NL ambiguity observable as a function of the amplified NL wavelength. GPS L1-L2-L5 IF combinations.*

The coefficients α_1, α_2, and α_3 that correspond to the minimum error level of the NL ambiguity observable can be analytically computed by solving Equations (8.22), (8.23), and (8.27).

$$\frac{\partial \sigma^2_{N^s_{r,n}}}{\partial \alpha_3} = 0 \tag{8.27}$$

From (8.22) and (8.23) we can write

$$\begin{aligned} \alpha_1 &= -\frac{q_2}{1-q_2} + \frac{q_2 - q_3}{1-q_2}\alpha_3 = A + B\alpha_3 \\ \alpha_2 &= \frac{1}{1-q_2} - \frac{1-q_3}{1-q_2}\alpha_3 = C + D\alpha_3 \end{aligned} \tag{8.28}$$

Replacing (8.28) in (8.26)

$$\sigma^2_{N^s_{r,n}} = \frac{\sigma^2_{e^s_r} + \sigma^2_{\varepsilon^s_r}}{\left[\left(A\lambda_1 + C\lambda_2\right) + \left(B\lambda_1 + D\lambda_2 + \lambda_3\right)\cdot\alpha_3\right]^2} = \frac{\sigma^2_{e^s_r} + \sigma^2_{\varepsilon^s_r}}{\left[E + F\cdot\alpha_3\right]^2} \tag{8.29}$$

where

$$\sigma^2_{\varepsilon^s_r} = \sigma^2_{\varepsilon^s_{r,1}}\left[\left(A + B\alpha_3\right)^2 + \left(C + D\alpha_3\right)^2 + \alpha_3^2\right] \tag{8.30}$$

The solution of Equations (8.22), (8.23), and (8.27), by taking into account (8.28), (8.29), and (8.30), is

$$\begin{cases} \alpha_1 = A + B\alpha_3 \\ \alpha_2 = C + D\alpha_3 \\ \alpha_3 = -\dfrac{\sigma^2_{\varepsilon^s_{r,1}}\cdot\left[D\left(AB + CD\right) - F\left(A^2 + D^2\right)\right] - \sigma^2_{e^s_r}\cdot F}{\sigma^2_{\varepsilon^s_{r,1}}\cdot\left[E\left(B^2 + D^2\right) - F\left(AB + CD\right)\right]} \end{cases} \tag{8.31}$$

which is a function of the variances of the errors in the IF pseudorange combination $\sigma^2_{e^s_r}$ and in the single carrier phase $\sigma^2_{\varepsilon^s_{r,1}}$.

These triple-carrier IF combinations with larger NL wavelength enhance the observability of the NL ambiguities, hence one would expect some improvement in the convergence time of the float PPP solution. Unfortunately, using these combinations alone are not very effective since they are characterized by a large noise level. **Figure 8.29** compares the noise in the NL ambiguity observable and the noise in the corresponding triple-carrier IF combination for different amplified NL wavelengths. The IF combination that provides the best observability of the NL ambiguity has a noise 557.4 times larger than the error in the single carrier phase measurement. Assuming, for severe multipath environments, a carrier phase with an accuracy of 1 cm, the proposed IF combination has a noise level of 5.57 m. For this reason, the triple-carrier combination that minimises the error in the NL observable will be coupled with the traditional dual-frequency IF combination. In this way, while the first combination speeds up the convergence time in PPP, the second one is useful to keep the final accuracy to the centimetre-level.

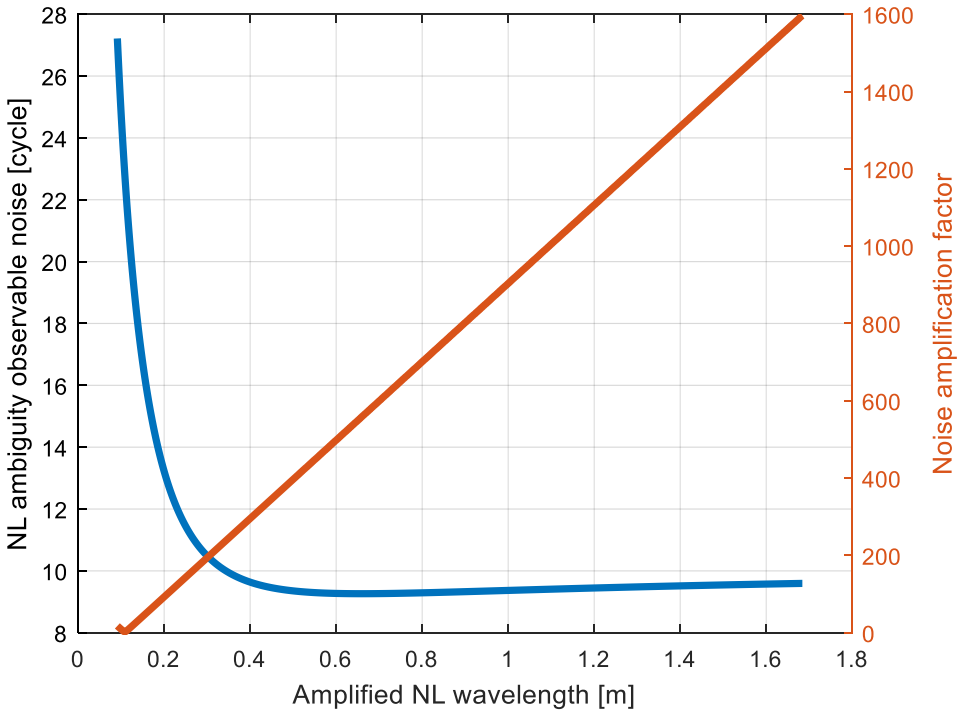


Figure 8.29 *Noise in the NL ambiguity observable (blue plot with y axis on the left) and amplification factor of the corresponding triple-carrier IF combination (red plot with y axis on the right) as a function of the amplified NL wavelength. GPS L1-L2-L5 IF combinations.*

In order to make this algorithm work, it is necessary that the two IF combinations are affected by the same ambiguity value. For this reason, the

EWL and WL ambiguities have to be fixed, and the FCBs must be corrected for. Corrections for the FCBs can be computed in a network solution and disseminated together with the precise products. The EWL and WL ambiguities, can be quickly fixed by using the TCAR method as in Equations (3.35) and (3.36).

8.2.1.1 Results on quick convergence in open sky conditions

To test the impact of the new triple-carrier IF combination on the float PPP solution, a simulation scenario where a receiver was assumed to be placed in a multipath-rich site with good satellite availability conditions was set. The multipath was simulated as a first order Gauss-Markov process with a correlation time equal to 5 seconds. The reference position corresponds to the IGS station SEY2. The GNSS measurements were recorded for two hours with an observation rate of 1 Hz. The GPS L1-L5 IF and Galileo E1-E5 IF pseudorange were processed, together with the L1-L5 IF and E1-E5 IF carrier phase combinations, with the POINT software in kinematic PPP mode. The solutions were then compared with the one achieved by also including the triple-carrier IF combinations discussed in this section.

Figure 8.30, **Figure 8.31**, and **Figure 8.32** compare the horizontal errors achieved by using the traditional two-frequency PPP model and the new method based on triple-carrier IF combinations that optimise the observability of the NL ambiguity. Three cases are considered: the GPS only solutions are plotted in **Figure 8.30**, the Galileo only solutions are in **Figure 8.31**, while the GPS+Galileo case is plotted in **Figure 8.32**. In each figure, the RMS (left) and the 95^{th} percentile (right) of the horizontal errors at each epoch are shown. From these figures it is possible to observe that at the moment the WL ambiguity is fixed, the horizontal errors achieved with the triple-carrier IF combinations with larger NL wavelengths drop. Indeed, on average, for the GPS only PPP solution the convergence below 10 cm is reduced from 425 seconds for the traditional two-frequency IF combination to 238 seconds for the new triple-carrier IF combination (see **Figure 8.30**). Even better improvements are observed in the Galileo case (**Figure 8.31**). The RMS of the error in the horizontal PPP solution computed from two-frequency IF pseudorange and carrier phase combinations reaches the 10 cm level after 8.22 minutes against the 3.18 minutes that are

required when the triple-carrier IF combination that enhance the observability of the NL wavelength is also used. Similarly, the convergence time of the GPS+Galileo float solution with the triple-carrier combinations proposed is reduced by 47% with respect to the two-frequency case (from 4.97 to 2.62 minutes).

Table 8.4 summarizes the horizontal convergence times obtained by processing in kinematic PPP mode two- and triple-frequency GPS, Galileo, and GPS+Galileo measurements with POINT. Up to 70% of improvement can be observed in the convergence time of the 95th percentile horizontal error (Galileo only). It is worth noticing that although the convergence time of the solution computed from the L1-L5 IF combinations is shorter than the one for E1-E5 IF, when the triple-carrier IF combinations are also employed, the Galileo only PPP float solution converges quicker than the GPS one. Indeed, for GPS the 95th percentile of the horizontal error takes 9 minutes to reach the 10 cm level, while it only takes 5.87 minutes for Galileo.

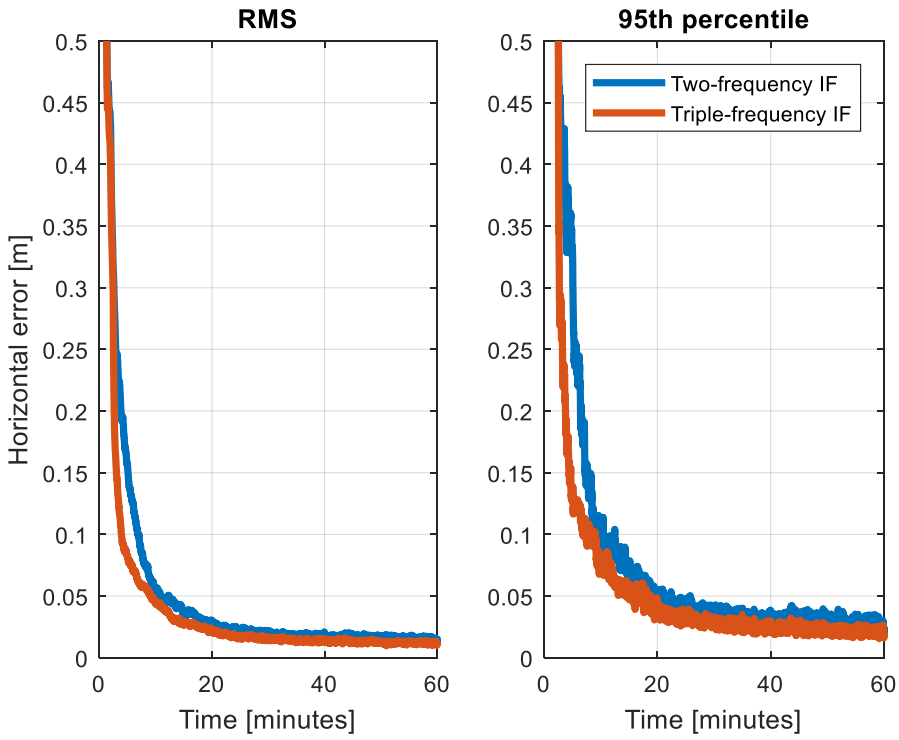


Figure 8.30 *Comparison between the horizontal error achieved using the traditional GPS L1-L5 IF combination (blue) and the one obtained by using also the triple-carrier IF combination that minimize the noise in the NL ambiguity observable (red). The multipath correlation time is equal to 5 seconds.*

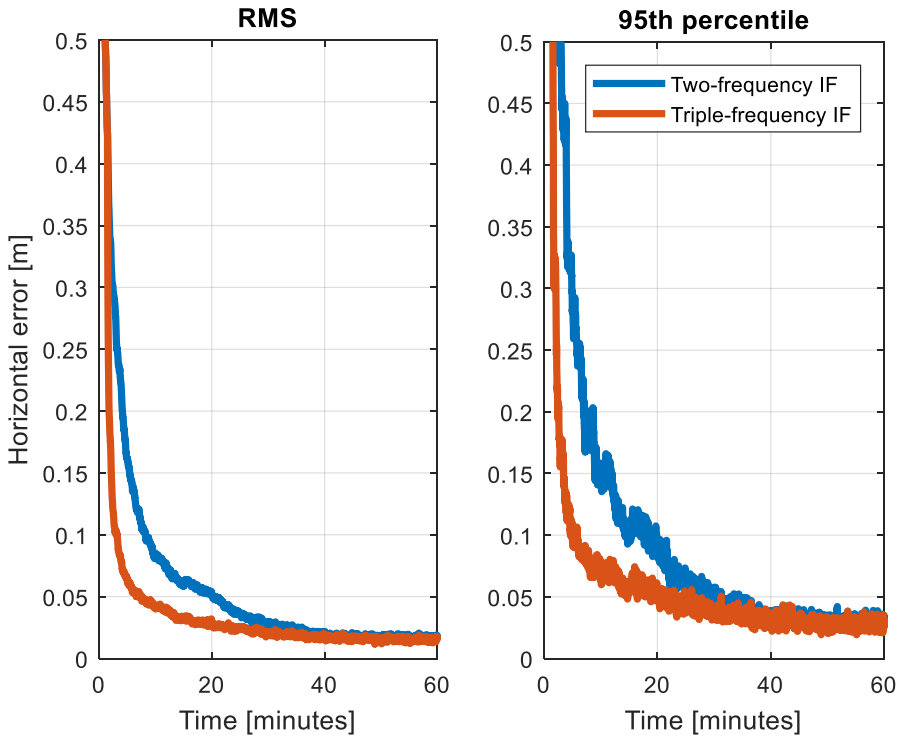


Figure 8.31 *Comparison between the horizontal error achieved using the Galileo E1-E5 IF combination (blue) and the one obtained by using also the triple-carrier IF combination that minimize the noise in the NL ambiguity observable (red). The multipath correlation time is equal to 5 seconds.*

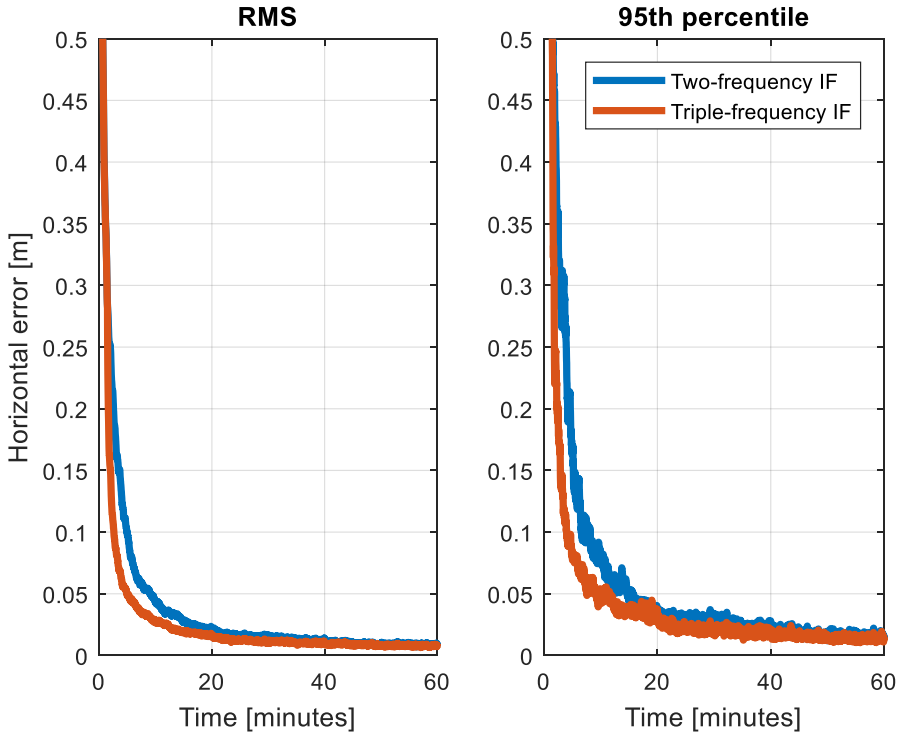


Figure 8.32 *Comparison between the horizontal error achieved using the GPS and Galileo IF combinations (blue) and the one obtained by using also the triple-carrier IF combinations that minimise the noise in the NL ambiguity observable (red). The multipath correlation time is equal to 5 seconds.*

Table 8.4 *Comparison between the horizontal convergence times obtained from using only the two-frequency IF combinations and also the triple-carrier IF combination that minimiz the error in the NL ambiguity observable. RMS and 95th percentile over 50 simulations. Station SEY2. The multipath correlation time is set to 5 seconds. Values in units of minutes. In bracket is the relative difference.*

	GPS		**Galileo**		**GPS + Galileo**	
	RMS	95%	RMS	95%	RMS	95%
Two-frequency IF	7.08	12.50	8.22	19.87	4.97	8.12
Triple-frequency IF	3.97 (-43.9%)	9.00 (-28.0%)	3.18 (-61.3%)	5.87 (-69.1%)	2.62 (-47.3%)	4.02 (-50.5%)

In all cases, after the convergence pattern the two PPP solutions reach the same precision level.

Sensitivity of the method to different multipath correlation time constants

The results presented in the previous section show that the triple-carrier IF combination that minimizes the error in the NL ambiguity observable starts being effective only after the EWL and WL ambiguities have been fixed using Equations (3.35) and (3.36). At the same time, in the next paragraph, it will be shown that the time required to fix the WL ambiguities greatly depends on the correlation time constant that was assumed to model the multipath error. The larger is the constant, the smaller is the correct-fix rate of the WL ambiguity resolution.

For this reason, the effect of different multipath correlation time constants on the proposed method is analysed in this section. To do so, a new simulation scenario was set in which all the GNSS measurements were assumed to be affected by multipath with the same correlation time constant, from 2 to 60 seconds. Multipath correlation times within this range are typical for kinematic tests in urban environments (Khanafseh et al., 2018). The simulated measurements are then processed with POINT in kinematic PPP mode.

For each correlation time constant, the time the RMS and the 95th percentile of the horizontal float solution takes to converge below 10 cm, for the GPS, Galileo, and GPS+Galileo two- and triple-frequency IF cases are reported in **Figure 8.33** and in **Figure 8.34**, respectively. Generally, the convergence time of the horizontal solution increases with the multipath correlation time constant. Even though the solution achieved by including the triple-carrier IF combinations in the observation vector are still characterized by quicker

convergence than the solution computed from the traditional two-frequency IF combinations, the difference in the performance is narrower for larger values of the multipath correlation time. For example, the convergence times for the RMS of the two Galileo solutions, when the multipath correlation time was set to 2 seconds, were 6.15 minutes and 1.85 minutes (70% less), respectively for the traditional E1-E5 IF combinations and for the triple-carrier IF combination. On the other hand, when the multipath correlation time constant was increased to 60 seconds, the improvement brought by the use of the new combination was as small as 4.7% (25.12 against 26.35 minutes). Similarly, for GPS an improvement of 69.7% was recorded for a multipath correlation time of 2 seconds, while it was only 19.5% with a correlation time of 60 seconds.

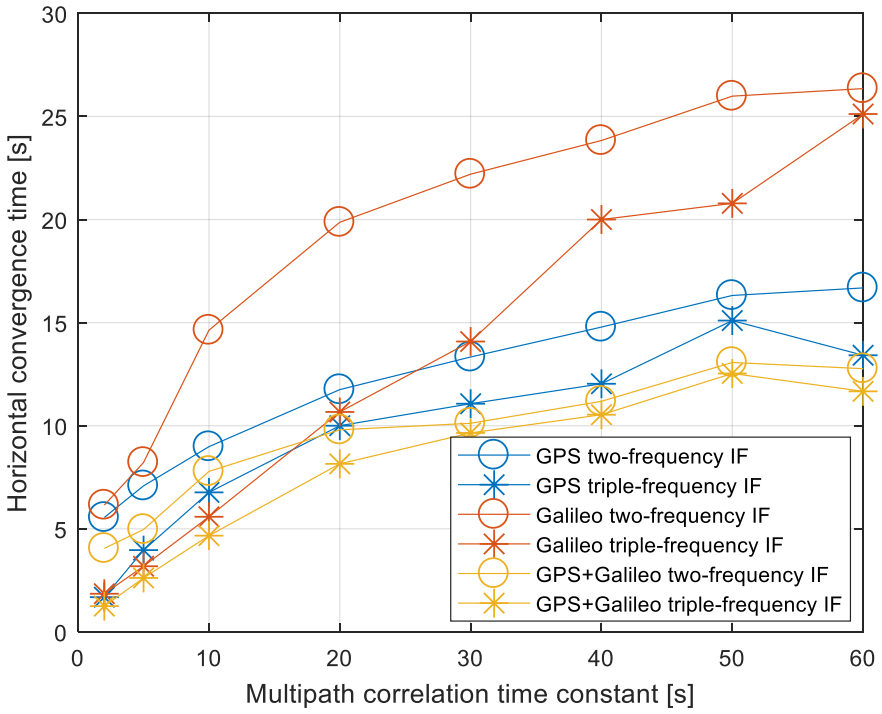


Figure 8.33 *Sensitivity of the horizontal convergence time (RMS) to different multipath correlation time for GPS (blue), Galileo (red), and GPS+Galileo (yellow) cases. Comparison between the two-frequency IF combinations (circle) and the triple-carrier IF combinations (star).*

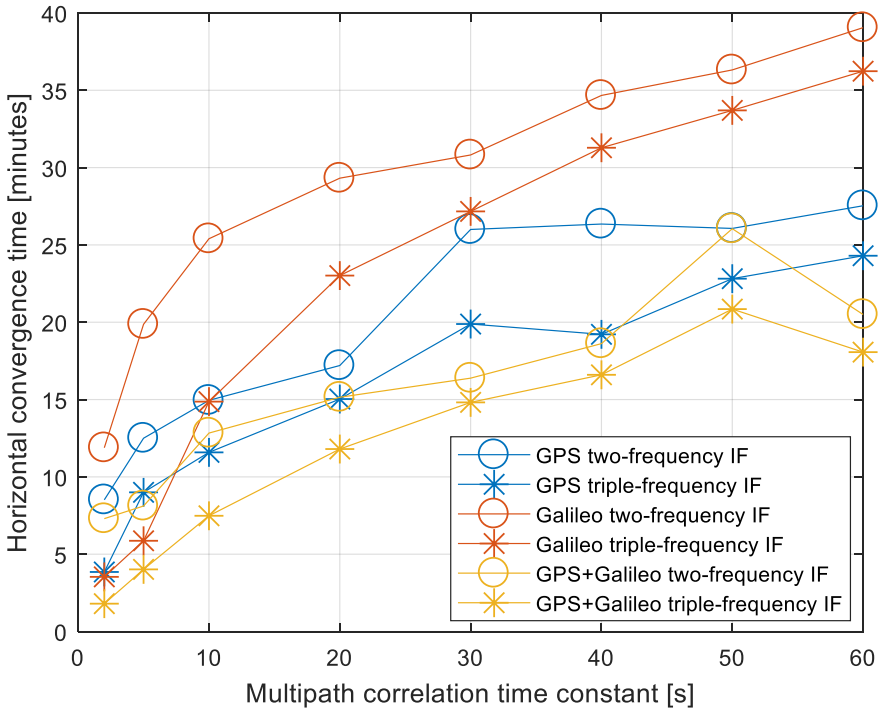


Figure 8.34 *Sensitivity of the horizontal convergence (95th percentile) time to different multipath correlation time for GPS (blue), Galileo (red), and GPS+Galileo (yellow) cases. Comparison between the traditional two-frequency IF combinations (circle) and the new triple-carrier IF combinations (star).*

As previously stated, assuming 60 seconds for the multipath correlation time for all the simulated measurements is a very conservative assumption since it was proved in Khanafseh et al. (2018) that for 99% of the time it lies in the range between 2 and 60 seconds, for kinematic applications in urban areas. For this reason, the new triple-carrier IF combination was also tested in a scenario where the multipath correlation time constant was assumed to be normally distributed with a standard deviation of 10 seconds and a mean of 35 seconds. The results for GPS, Galileo, and GPS+Galileo are plotted in **Figure 8.35**, **Figure 8.36**, and **Figure 8.37**, respectively. These plots confirmed once again that, although a significant improvement is observed, having a highly coloured noise in the pseudorange and carrier phase measurements limits the benefit of the proposed combinations. Indeed, the convergence time of the RMS horizontal solution computed from GPS measurements goes from 14.42 minutes to 13.53 minutes (6.2% of improvement), for Galileo it is reduced from 19.33 minutes to 12.77 minutes (33.9% better), and improves from 11.27 minutes to 10.17 (9.8% of reduction) when GPS+Galileo data are processed with POINT.

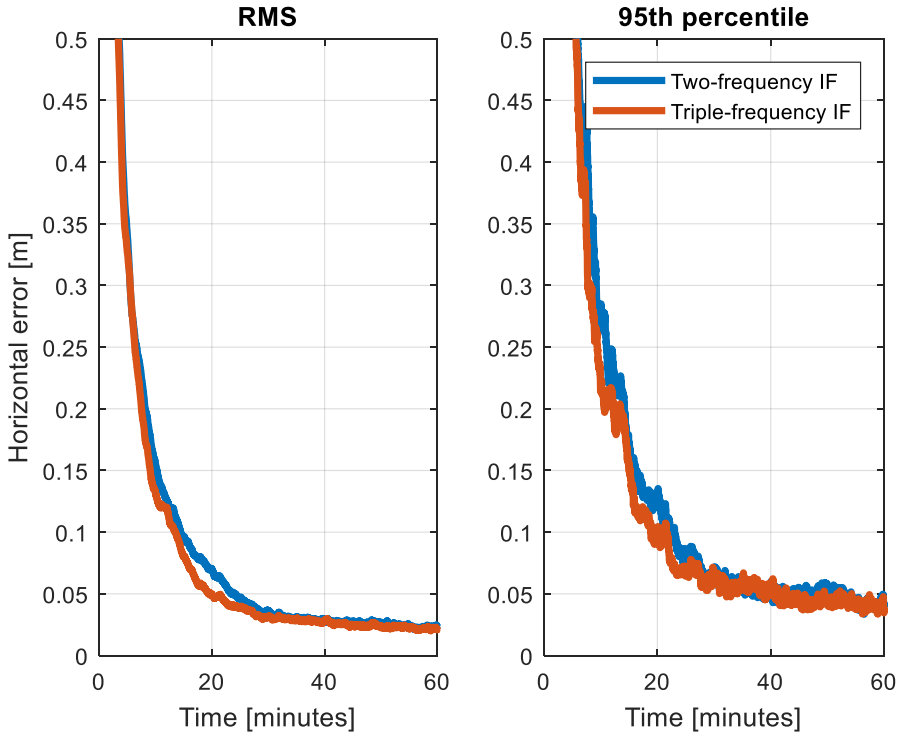


Figure 8.35 *Comparison between the horizontal error achieved using the GPS L1-L5 IF combination (blue) and the one obtained by using also the triple-carrier IF combination that minimises the noise in the NL ambiguity observable (red). The multipath correlation time is randomly generated.*

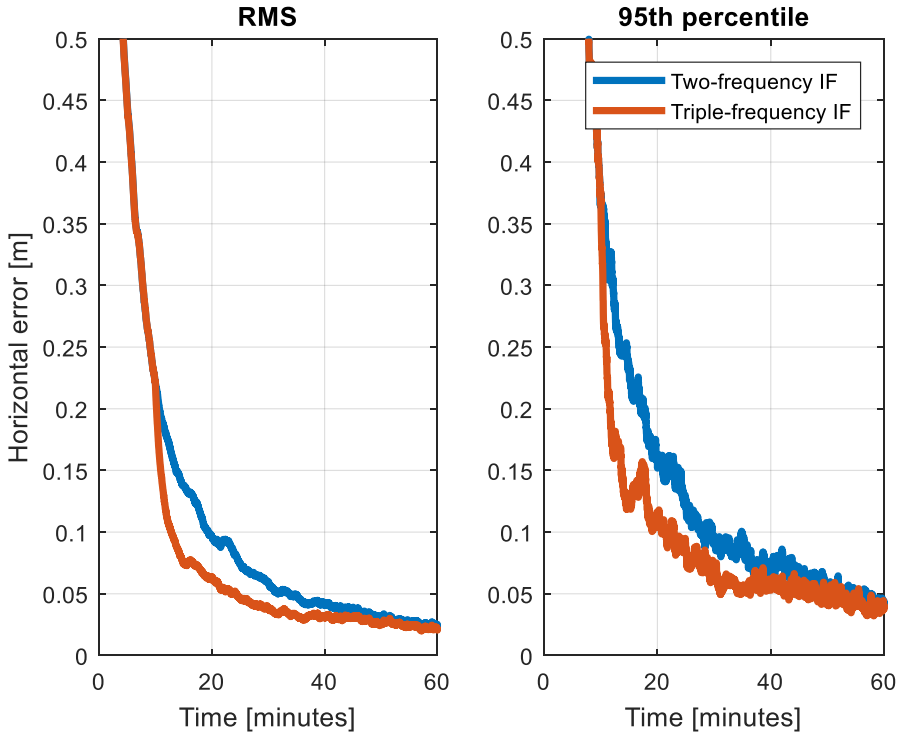


Figure 8.36 *Comparison between the horizontal error achieved using the Galileo E1-E5 IF combination (blue) and the one obtained by using also the triple-carrier IF combination that minimises the noise in the NL ambiguity observable (red). The multipath correlation time is randomly generated.*

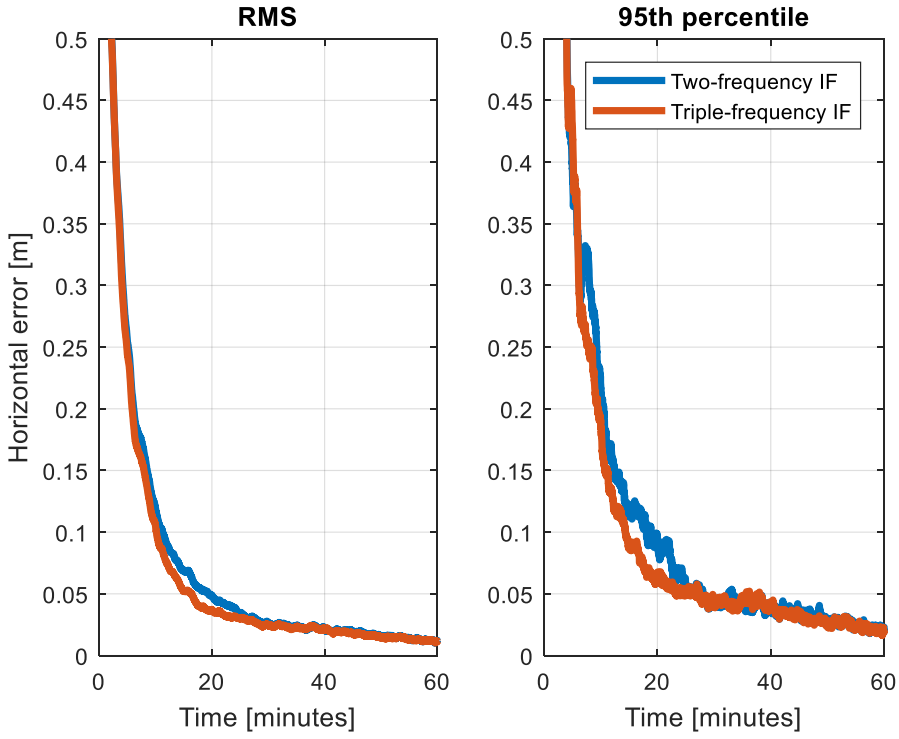


Figure 8.37 *Comparison between the horizontal error achieved using the GPS and Galileo two-frequency IF combinations (blue) and the one obtained by using also the triple-carrier IF combinations that minimise the noise in the NL ambiguity observable (red). The multipath correlation time is randomly generated.*

This behaviour can be explained by the fact that the new triple-carrier combination that minimises the error in the NL ambiguity observable affects the PPP solution only after the WL ambiguity has been fixed. In the next section, it will be shown that, with larger multipath correlation time constants, longer observation periods are required before the WL ambiguity can be reliably fixed. For example, with random correlation times, the WL ambiguity can be fixed following Equation (3.36) in 9 minutes for Galileo and in 14 minutes for GPS. By the time the WL ambiguities are fixed, the PPP solution is already almost converged below 10 cm. Hence, the main contribution to the estimation of the NL ambiguity is provided by its prediction rather than a further observable. This also explains why we still observe a significant improvement in the Galileo only solution. Since the Galileo WL ambiguities are the fastest to be fixed, and, at the same time, the float solution is the slowest to converge, the new triple-carrier combination has still a dominant effect in the estimation of the NL ambiguity. In the other two cases (GPS and GPS+Galileo), the horizontal solution has converged even before the WL ambiguity could be fixed. Hence, the observed

improvement is only due to having an extra observable and not to the properties of this observable.

Finding a way to better exploit the new triple-carrier IF combinations that have been proposed in this section was the main driver to research into more efficient geometry-free combinations aimed to fix the WL ambiguities. The results of these efforts are presented in the next paragraph. It will be shown that, by using the smoothed ionosphere combination to correct the ionosphere in low-noise pseudorange combinations, the time required to fix the WL ambiguity, when the GNSS measurements are affected by multipath with random correlation time constants, could be significantly reduced from 14 minutes to 7 minutes for GPS and from 9 minutes to about 3 minutes for Galileo.

As a result, the triple-carrier IF combinations that minimize the noise in the NL ambiguity start being effective earlier, hence the PPP solutions converge to sub-decimetre level of precision even faster. **Figure 8.38** compares the error in the horizontal component computed by processing the L1-L5 IF combination and by also employing the new triple-carrier IF combination. The average horizontal error goes below 10 cm in 13 minutes for the first case and in 9.7 minutes for the second configuration. Powered by a very quick WL ambiguity fix, the Galileo PPP solution experiences the biggest improvement when using the triple-carrier IF combination that enhance the observability of the NL ambiguity and the new WL fixing method. In this case, as shown in **Figure 8.39**, the average horizontal error converges in 8.6 minutes, 58% quicker than the solution computed from the E1-E5 IF pseudorange and carrier phase combinations. Even though two-constellation PPP already benefit the convergence time of the float PPP solution, it can be further improved by adopting the new configuration developed in this research. From **Figure 8.40** we can observe that the two-frequency two-constellation PPP solution takes on average 10.3 minutes to converge to centimetres accuracies, however the triple-carrier IF Galileo combination first, and GPS combination later, reduce the horizontal convergence time to 6.6 minutes.

The horizontal convergence times obtained by processing in kinematic PPP mode two- and triple-frequency GPS, Galileo, and GPS+Galileo measurements with POINT are also summarized in **Table 8.5**.

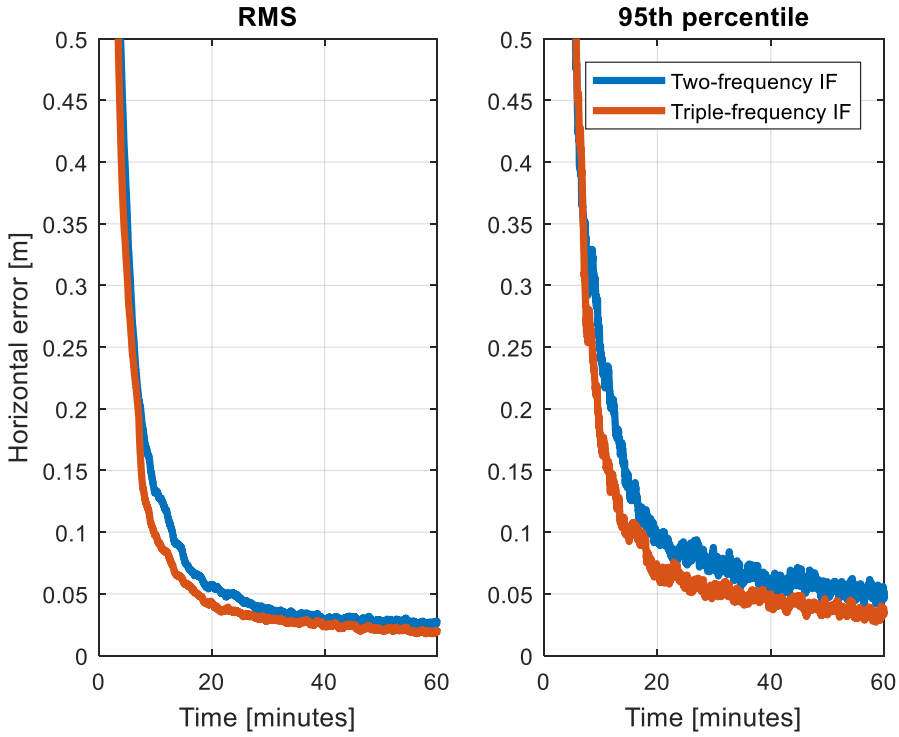


Figure 8.38 *Comparison between the horizontal error achieved using the GPS L1-L5 IF combination (blue) and the one obtained by using also the triple-carrier IF combination that minimises the noise in the NL ambiguity observable (red) when the WL ambiguity is fixed with the new method.*

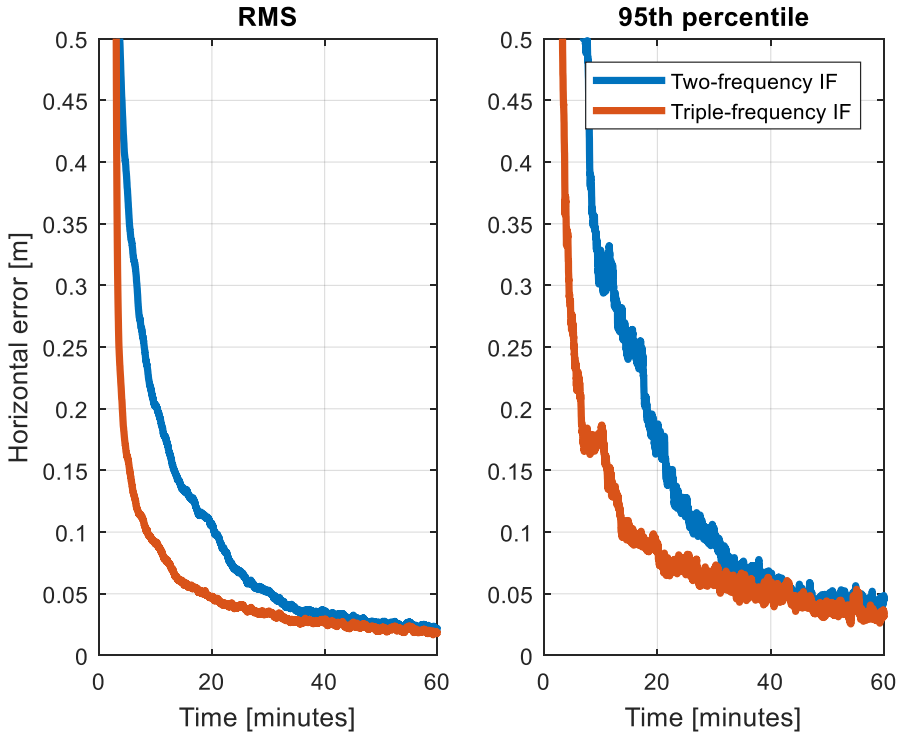


Figure 8.39 *Comparison between the horizontal error achieved using the Galileo E1-E5 IF combination (blue) and the one obtained by using also the triple-carrier IF combination that minimises the noise in the NL ambiguity observable (red) when the WL ambiguity is fixed with the new method.*

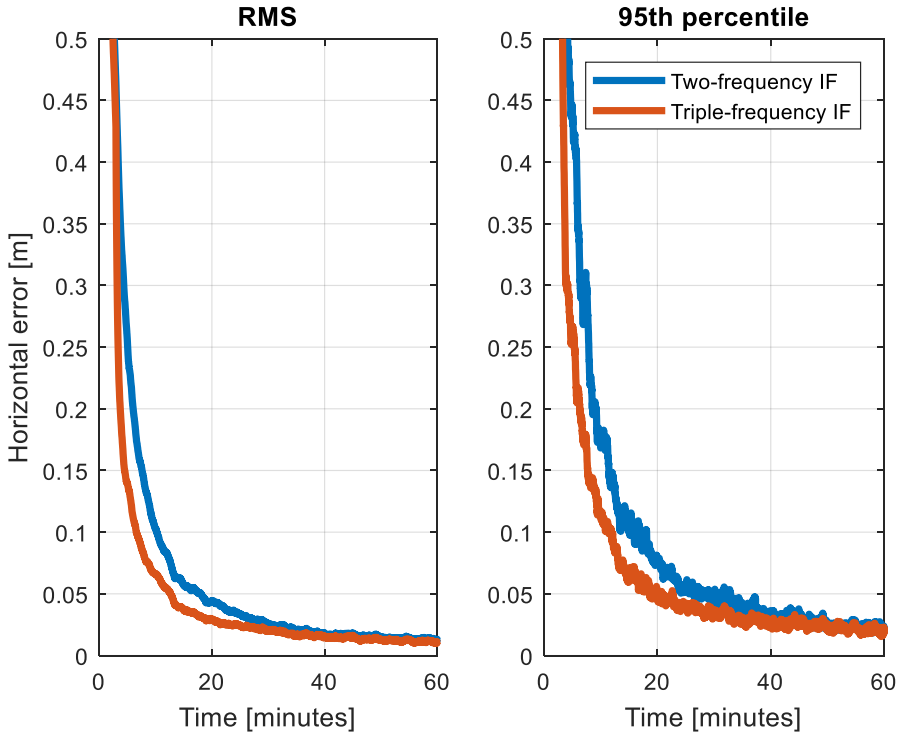


Figure 8.40 *Horizontal error achieved using the GPS and Galileo two-frequency IF combinations (blue) and the one obtained by using also the triple-carrier IF combinations that minimise the noise in the NL ambiguity observable (red) when the WL ambiguity is fixed with the new method.*

Table 8.5 *Comparison between the horizontal convergence times obtained from using only the two-frequency IF combinations and also the triple-carrier IF combination that minimiz the error in the NL ambiguity observable when the WL ambiguity is fixed with the new method presented in Section 8.3. RMS and 95th percentile over 50 simulations. The multipath correlation time is randomly generated. Values in units of minutes. In bracket is the relative difference.*

	GPS		**Galileo**		**GPS + Galileo**	
	RMS	95%	RMS	95%	RMS	95%
Two-frequency IF	13.00	21.23	20.43	29.98	10.27	18.10
Triple-frequency IF	9.73 (-25.2%)	16.77 (-21.0%)	8.58 (-58.0%)	17.15 (-42.8%)	6.62 (-35.5%)	11.85 (-34.5%)

8.3 Triple Carrier Ambiguity Resolution (TCAR) with smoothed ionosphere correction

In Section 3.3.3 the TCAR algorithm for PPP proposed in Geng and Bock (2013) was quickly described. This method subsequently fixes the ambiguity in the EWL, WL, and NL carrier combination by exploiting the gap-bridging concept. In the first step, the EWL ambiguity $N^{s}_{r,em}$ is fixed using the

Melbourne-Wubbena combination $L^s_{r,em}$ (Melbourne, 1985; Wubbena, 1985) between L2 and L5.

$$\begin{aligned} L^s_{r,em} &= \frac{f_2 P^s_{r,2} + f_5 P^s_{r,5}}{f_2 + f_5} - \frac{f_2 L^s_{r,2} - f_5 L^s_{r,5}}{f_2 - f_5} \\ &= \lambda_{ew}\left(N^s_{r,em} + d^s_{r,em}\right) \end{aligned} \tag{8.32}$$

In Equation (8.32), $d^s_{r,em}$ represents the receiver and satellite instrumental delays within the combination. They can be mitigated using the FCB corrections estimated within a network solution. The EWL wavelength λ_{ew} is so large (about 5.86 m) that makes the instantaneous AR success rate over 99.9%.

Once the EWL ambiguity is fixed, the WL ambiguity can be solved in the second step. The IF combinations between the pseudoranges on frequencies L1 and L2 ($P^s_{r,IF}$), and between the WL and the unambiguous EWL carrier phase combinations ($L^s_{r,x}$) are used for this purpose.

$$\begin{aligned} P^s_{r,IF} &= \frac{f_1^2}{f_1^2 - f_2^2} P^s_{r,1} - \frac{f_2^2}{f_1^2 - f_2^2} P^s_{r,2} \\ L^s_{r,x} &= \frac{f_1}{f_1 - f_5} L^s_{r,w} - \frac{f_5}{f_1 - f_5}\left(L^s_{r,ew} + \lambda_{ew}\bar{N}^s_{r,ew}\right) \\ &= g^s_r - \lambda_w \frac{f_1}{f_1 - f_5}\left(N^s_{r,w} + d^s_{r,x}\right) + \varepsilon^s_{r,x} \end{aligned} \tag{8.33}$$

In Equation (8.33), $d^s_{r,x}$ denotes the hardware biases in $L^s_{r,x}$ that have to be corrected to obtain an integer ambiguity. According to M. Ge et al. (2008), the accuracy of the estimated WL FCBs is as small as 0.05 cycles.

Even though the noisy $P^s_{r,IF}$ is used as base pseudorange and the noise on $L^s_{r,x}$ is roughly 110 times larger than the carrier phase error, the WL wavelength is amplified to 3.40 m, which is large enough to reliably fix the WL ambiguity to its nearest integer value in a few epochs. After a few tens of seconds, the WL ambiguity can be reliably fixed to its integer value $\bar{N}^s_{r,w}$ (Geng and Bock, 2013) and $L^s_{r,x}$ becomes unambiguous. This ambiguity fixed IF combination is also

known as AFIF and it can be used as base pseudorange to fix the NL ambiguity $N^s_{r,n}$ in the IF combination $L^s_{r,IF}$ between carrier phase measurements on L1 and L2. NL FCBs are required to remove the hardware biases $d^s_{r,n}$.

$$\begin{aligned} L^s_{r,IF} &= \frac{f_1^2}{f_1^2 - f_2^2} L^s_{r,1} - \frac{f_2^2}{f_1^2 - f_2^2} L^s_{r,2} + \frac{f_2^2}{f_1^2 - f_2^2} \lambda_2 \bar{N}^s_{r,w} \\ &= g^s_r - \lambda_n \left(N^s_{r,n} + d^s_{r,n} \right) + \varepsilon^s_{r,IF} \end{aligned} \tag{8.34}$$

Although $\varepsilon^s_{r,x}$ is at a few decimetres level, the AFIF combination represents a better option than $P^s_{r,IF}$ as base pseudorange to fix $N^s_{r,n}$. Unfortunately, the NL wavelength is so small (10.7 cm) that it still requires more than one minute to achieve an AR success rate over 99.9% (Geng and Bock, 2013).

Although Geng and Bock (2013) claims that a few tens of seconds are required to fix the WL ambiguity using (8.33), in reality the correct-fix rate of the WL ambiguity resolution depends on different factors, such as the quality of the measurements and the multipath correlation time constant. Indeed, one would expect longer times to achieve an ambiguity resolution correct-fix rate over 99.9% if the errors in the measurements adopted as base pseudorange to fix the WL ambiguity are large or highly time correlated.

For example, **Figure 8.41** compares the correct-fix rate of ambiguity resolution when the simulated measurements are recorded in a benign environment and when the receiver is located in a multipath-rich site. In order to simulate the multipath for a given measurement, the correlation time constant was obtained from a generator of normally distributed variables with mean equal to 35 seconds and standard deviation equal to 10 seconds. Observations spanning over four hours were divided into short sessions of t seconds, and WL ambiguity resolution was carried out at the last epoch of each session. The correct-fix rate is computed as the ratio between the numbers of t-second sessions with correct ambiguity resolution and the number of all t-seconds epochs. The same approach was used in Geng and Bock (2013) to prove the benefit of TCAR over dual-frequency ambiguity resolution. In absence of multipath, the WL ambiguity for GPS can be fixed in only 2 seconds, while users have to wait for as long as 14 minutes when the GPS pseudoranges and carrier phase

measurements are affected by multipath. Similarly, the ambiguity in Galileo carrier phase WL combinations can be instantaneously fixed for a multipath-free site, but in 9 minutes if the measurements have poor quality.

Also, the time required to have the WL ambiguity fixed greatly increases with the multipath correlation time constants. As shown in **Figure 8.42**, for a multipath correlation time of 10 seconds, the GPS and Galileo WL ambiguities can be fixed in 4.5 minutes and 3.5 minutes, respectively, but with a correlation time of 60 seconds users have to wait for more than 20 minutes to fix the WL ambiguities following the method presented in Geng and Bock (2013).

In a similar manner, the NL ambiguity fix success-rate also depends on the quality of the measurements. As it is shown in **Figure 8.43**, in the case when there is no multipath affecting the carrier phase measurements, the GPS and Galileo NL ambiguities can be fixed, respectively, in 45 and 17 seconds, while in a multipath-rich site (with random correlation time constants) not even after 6 hours could a correct-fix rate of 99.9% be obtained.

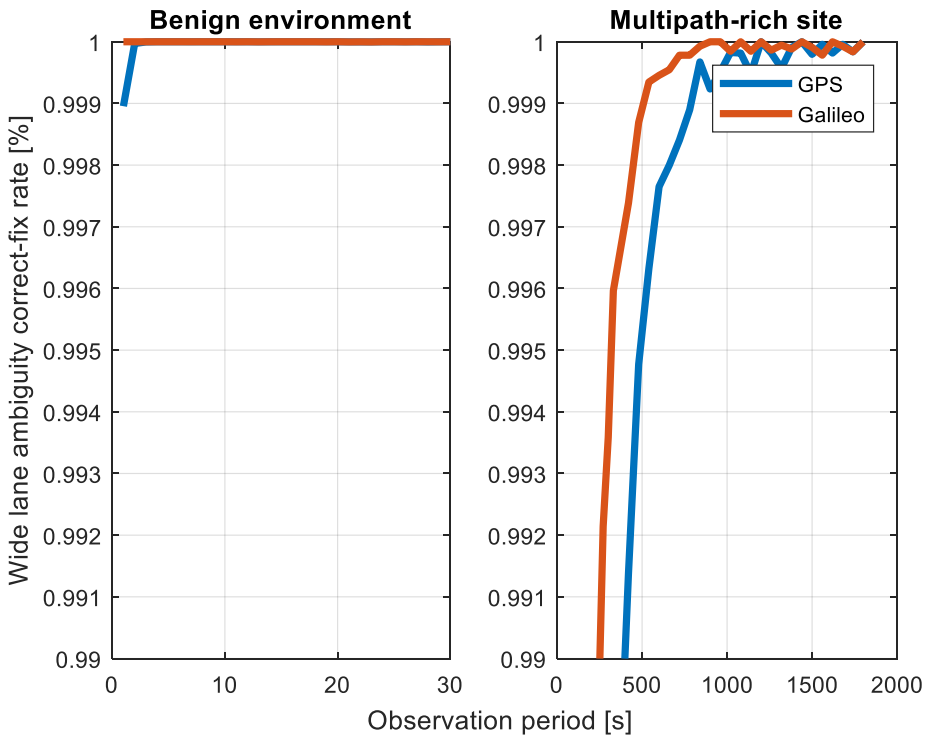


Figure 8.41 *WL ambiguity correct-fix rate for GPS L1-L2-L5 (blue) and Galileo E1-E5-E6 (red) combinations for a benign environment (left) and multipath-rich site (right).*

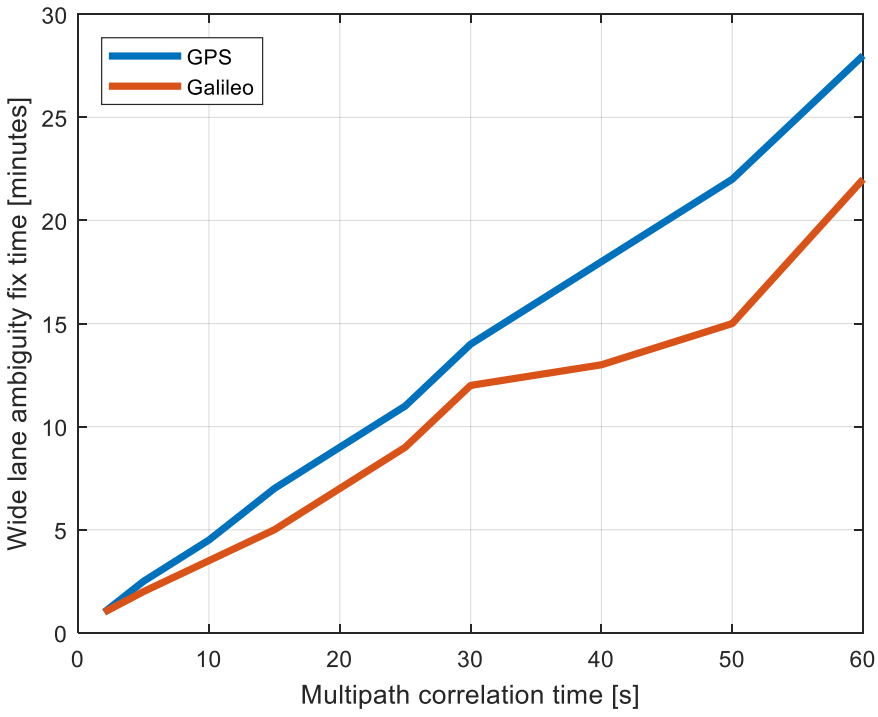


Figure 8.42 *Sensitivity of the WL ambiguity fix time to the multipath correlation time constant.*

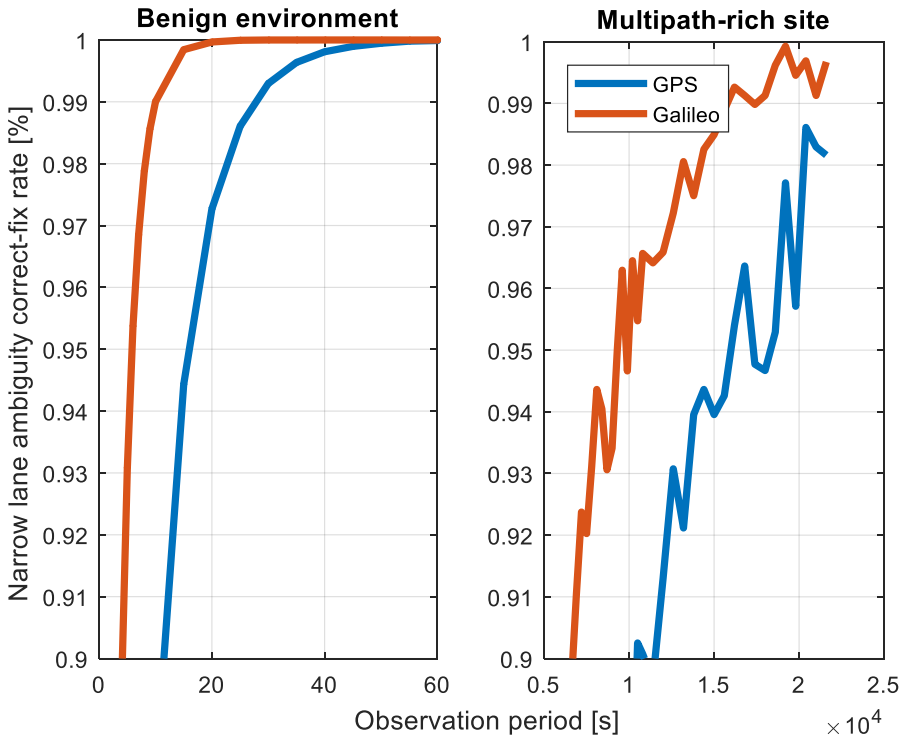


Figure 8.43 *NL ambiguity correctness rate for GPS L1-L2-L5 (blue) and Galileo E1-E5-E6 (red) combinations for a benign environment (left) and multipath-rich site (right). The NL ambiguity has been computed using the AFIF combination.*

These results confirm that, even though the ambiguity resolution success-rate is far better than the dual-frequency case, ambiguity resolution methods based on geometry-free combinations, such as TCAR methods, don't perform well in presence of multipath (Forsell et al., 1997; Jung et al., 2000; Vollath et al., 1999; Werner and Winkel, 2003). However, in open areas far away from reflective surfaces, TCAR represents a simple, yet effective, tool for quickly obtaining a fixed PPP solution.

In this research a different approach to fix the WL and NL ambiguities is presented. Instead of using the traditional IF combination, the low-noise pseudorange combination corrected by the smoothed ionosphere correction, introduced in Section 8.1.1 and described by Equation (8.10), is employed as base pseudorange to fix the WL ambiguity in the second step.

By assuming that a GNSS receiver is located in a benign open environment far from reflective surfaces that may cause multipath, it can be expected to have a noise level in the GPS and Galileo pseudorange as those reported in **Table 8.6**.

Table 8.6 *Expected standard deviation of the error in GPS and Galileo pseudoranges for benign environments. Values in unites of meters.*

L1	L2	L5	E1	E5a	E5b	E5	E6
0.4	0.7	0.3	0.3	0.2	0.2	0.1	0.3

With these values, as reported in **Table 8.7**, the combination between triple-frequency GPS pseudoranges that minimises the noise has an error with a standard deviation of 0.23 m (excluding the effect of the ionosphere).

Table 8.7 *GPS and Galileo low-noise pseudorange combinations: coefficients, ionosphere amplification factor, and noise in unit of meters. Benign environment.*

Combinations	α_1	α_2	α_3	q	Noise
L1 – L2 – L5	0.32	0.11	0.57	1.52	0.23
E1 – E5a – E5b	0.18	0.41	0.41	1.61	0.13
E1 – E5a – E6	0.24	0.53	0.24	1.54	0.15
E1 – E5b – E6	0.24	0.53	0.24	1.49	0.15
E1 – E5 – E6	0.09	0.82	0.09	1.66	0.09

Unfortunately, the smoothed ionosphere correction introduces a further error, which, coming from a Hatch filter, is highly time correlated and, therefore, over the short period, it can be treated as a bias. Like TCAR methods applied to differential GNSS, in case this bias is much smaller than the amplified WL wavelength (that is 3.4 meters for the GPS combination), the effect of the residual ionospheric error becomes negligible, and an (almost) instantaneous WL ambiguity fix may be enabled. **Table 8.8** summarizes the noise in the WL ambiguity observable computed from the low noise pseudorange combinations and the float AFIF combinations. When multipath doesn't affect the GNSS measurements, in theory, the WL ambiguity can be fixed instantaneously, since the noise in the ambiguity observable (0.07 cycles for GPS measurements) is much smaller than the threshold of 0.162 cycles (corresponding to a probability of successful ambiguity fix of 99.9%). However, this noise level does not include the residual error due to the smoothed ionosphere. On the other hand, the amplified WL wavelength (3.40 m for GPS combinations) is so large that it can easily absorb this further bias. Within the Galileo combinations, the best performance can be obtained when using the low noise pseudorange combinations involving E5. No difference was notable between the noise in the

WL ambiguity observable computed from the AFIF combination involving E1, E6, and any of the carrier phases in the E5 frequency band (E5a, E5b, or E5).

Table 8.8 *Noise in the WL ambiguity observable in unites of cycle for different pseudorange and carrier phase combinations. Begign environment.*

Pseudorange combinations	Carrier phase combinations	Amplified wavelength	Noise
L1 – L2 – L5	L1 – L2 – L5	3.40 m	0.07
E1 – E5a – E5b	E1 – E5a – E5b	3.21 m	0.07
	E1 – E5a – E6	3.99 m	0.04
	E1 – E5b – E6	4.32 m	0.04
	E1 – E5 – E6	4.15 m	0.04
E1 – E5a – E6	E1 – E5a – E5b	3.21 m	0.07
	E1 – E5a – E6	3.99 m	0.04
	E1 – E5b – E6	4.32 m	0.04
	E1 – E5 – E6	4.15 m	0.04
E1 – E5b – E6	E1 – E5a – E5b	3.21 m	0.07
	E1 – E5a – E6	3.99 m	0.04
	E1 – E5b – E6	4.32 m	0.04
	E1 – E5 – E6	4.15 m	0.04
E1 – E5 – E6	E1 – E5a – E5b	3.21 m	0.06
	E1 – E5a – E6	3.99 m	0.03
	E1 – E5b – E6	4.32 m	0.03
	E1 – E5 – E6	4.15 m	0.03

Similarly, by assuming that the receiver is placed in a severe multipath environment, it can be expected to have pseudoranges with higher errors as in **Table 8.9**.

To test the performance of the proposed combinations against the algorithm described in Geng and Bock (2013), the correct-fix rate of the WL ambiguity is analysed based on simulated data. Since the left subplot in **Figure 8.41** showed that the WL fixing method presented in Geng and Bock (2013) already guarantees instantaneous WL ambiguity fix in the case when the receiver is placed in a benign environment, the proposed method is tested only when multipath affects the pseudoranges and carrier phase measurements. The multipath is simulated as a Gauss-Markov process with a time constant that is typical of kinematic scenarios. It was assumed to be for 99% of the time within the range between 5 and 65 seconds (Khanafseh et al., 2018). Beside the

pseudorange combinations with minimum noise included in **Table 8.10**, other interesting combinations, characterised by slightly larger noise levels but lower ionosphere amplification factors, will be considered. For each ionosphere amplification factor between 0.7 and 1.5, the pseudorange combination with lowest noise will be tested. Although these combinations are noisier than the optimal one, they have a smaller ionosphere amplification factor that can be beneficial to absorb the residual error in the smoothed ionosphere correction.

Table 8.9 *Expected standard deviation of the error in GPS and Galileo pseudoranges for severe multipath environments. Values in unites of meters.*

L1	L2	L5	E1	E5a	E5b	E5	E6
1.0	1.3	0.8	1.0	0.8	0.8	0.4	1.0

Table 8.10 *GPS and Galileo low-noise pseudorange combinations: coefficients, ionosphere amplification factor, and noise in unit of meters. Severe multipath environments.*

Combinations	α_1	α_2	α_3	q	Noise
L1 – L2 – L5	0.32	0.19	0.50	1.51	0.56
E1 – E5a – E5b	0.24	0.38	0.38	1.57	0.49
E1 – E5a – E6	0.28	0.44	0.28	1.49	0.53
E1 – E5b – E6	0.28	0.44	0.28	1.45	0.53
E1 – E5 – E6	0.12	0.76	0.12	1.63	0.35

Table 8.11 shows the noise in the WL ambiguity observable computed from the low noise pseudorange combinations and the float AFIF combinations. In the case that the receiver is located in a multipath-rich site, the WL ambiguity cannot be instantaneously fixed even by neglecting the residual error due to the smoothed ionosphere, since the noise in the ambiguity observable (0.36 cycles for GPS measurements) is slightly larger than the threshold required to achieve a probability of successful ambiguity fix of 99.9%. In general, the Galileo combinations provide lower noise than the GPS one, apart from those between E1, E5a, and E5b. As in the previous case, the best performance can be obtained when using the low noise pseudorange combinations involving the Galileo E5. The lowest noise is recorded when the carrier phase measurements on E1, E5a, and E6 are combined. If on the one hand the E1-E5-E6 triple-carrier combination provides a WL ambiguity observable with only 0.02 cycles more noise than the E1-E5a-E6 combination, on the other hand it has an amplified

WL wavelength 16 cm larger. This larger wavelength can be useful for absorbing the residual bias due to the effect of the ionosphere. For this reason, the combinations between the Galileo measurements on E1, E5, and E6 will be considered.

To test the performance of the proposed combinations against the algorithm described in Geng and Bock (2013), the correct-fix rate of the WL ambiguity is analysed based on simulated data. Since the left subplot in **Figure 8.41** showed that the WL fixing method presented in Geng and Bock (2013) already guarantees instantaneous WL ambiguity fix in the case when the receiver is placed in a benign environment, the proposed method is tested only when multipath affects the pseudoranges and carrier phase measurements. The multipath is simulated as a Gauss-Markov process with a time constant that is typical of kinematic scenarios. It was assumed to be for 99% of the time within the range between 5 and 65 seconds (Khanafseh et al., 2018). Beside the pseudorange combinations with minimum noise included in **Table 8.10**, other interesting combinations, characterised by slightly larger noise levels but lower ionosphere amplification factors, will be considered. For each ionosphere amplification factor between 0.7 and 1.5, the pseudorange combination with lowest noise will be tested. Although these combinations are noisier than the optimal one, they have a smaller ionosphere amplification factor that can be beneficial to absorb the residual error in the smoothed ionosphere correction.

Figure 8.44 shows the WL ambiguity correct-fix rate for the new low-noise GPS pseudorange combinations corrected by the smoothed ionosphere correction and the traditional L1-L5 IF combinations. The combination that first guarantees a correct-fix rate of 99.9% is the one corresponding to an ionosphere amplification factor of 0.9. An observation period of only 7 minutes is required to reliably fix the WL ambiguity, against the 14 minutes needed with the L1-L5 IF combination and the 9 minutes with the lowest-noise pseudorange combination. For the Galileo system, WL ambiguity can be fixed in only 3 minutes using a triple-frequency pseudorange combination with an ionosphere amplification factor of 1.1 (see **Figure 8.45**), which is 30 seconds quicker than the combination with the lowest noise.

Table 8.11 *Noise in the WL ambiguity observable in unites of cycle for different pseudorange and carrier phase combinations. Severe multipath environment.*

Pseudorange combinations	Carrier phase combinations	Amplified wavelength	Noise
L1 – L2 – L5	L1 – L2 – L5	3.40 m	0.36
E1 – E5a – E5b	E1 – E5a – E5b	3.21 m	0.56
	E1 – E5a – E6	3.99 m	0.21
	E1 – E5b – E6	4.32 m	0.25
	E1 – E5 – E6	4.15 m	0.22
E1 – E5a – E6	E1 – E5a – E5b	3.21 m	0.56
	E1 – E5a – E6	3.99 m	0.21
	E1 – E5b – E6	4.32 m	0.26
	E1 – E5 – E6	4.15 m	0.23
E1 – E5b – E6	E1 – E5a – E5b	3.21 m	0.56
	E1 – E5a – E6	3.99 m	0.21
	E1 – E5b – E6	4.32 m	0.26
	E1 – E5 – E6	4.15 m	0.23
E1 – E5 – E6	E1 – E5a – E5b	3.21 m	0.55
	E1 – E5a – E6	3.99 m	0.19
	E1 – E5b – E6	4.32 m	0.24
	E1 – E5 – E6	4.15 m	0.21

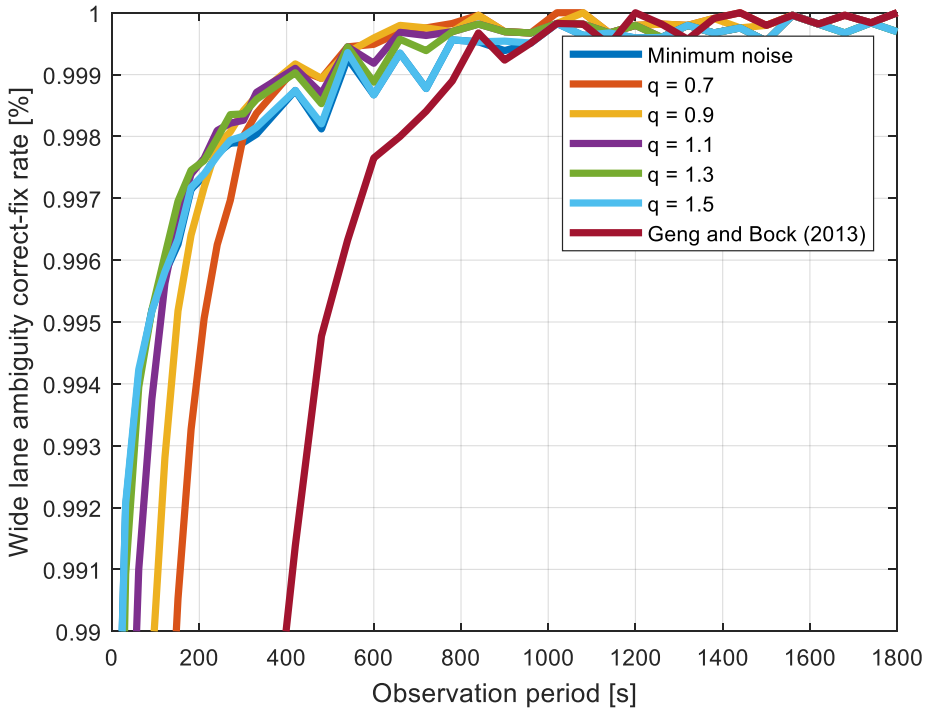


Figure 8.44 *Correct-fix rate of the wide lane ambiguity resolution for the new method and the one proposed in Geng and Bock (2013) for GPS L1-L2-L5 combinations. For the new method, low-noise combinations with different ionosphere amplification factors (q) are considered. Severe multipath case.*

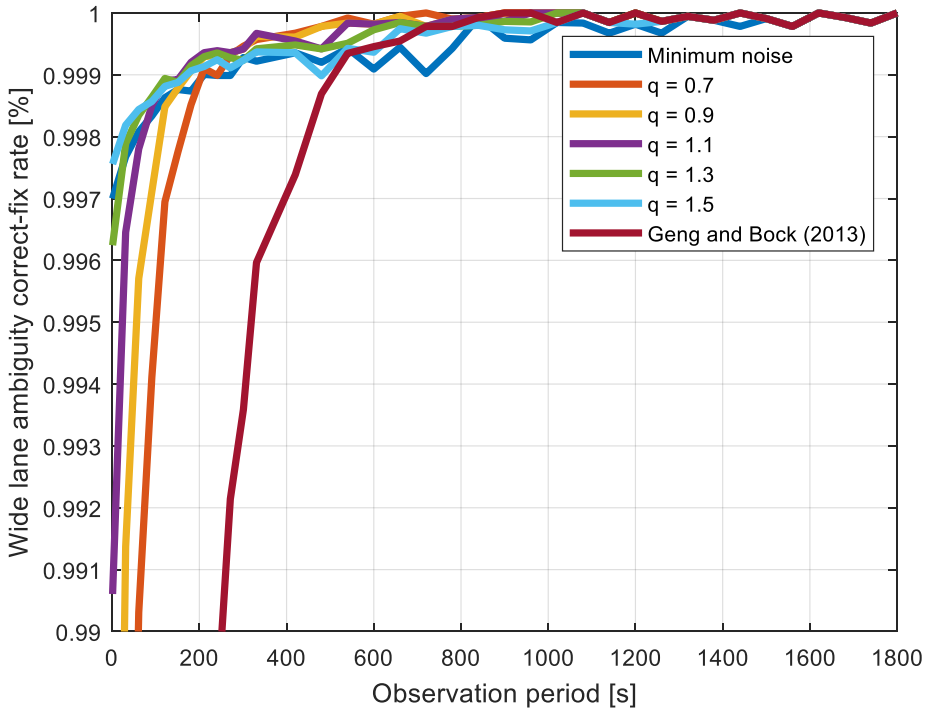


Figure 8.45 *Correct-fix rate of the wide lane ambiguity resolution for the new method and the one proposed in Geng and Bock (2013) for Galileo E1-E5-E6 combinations. For the new method, low-noise combinations with different ionosphere amplification factors (q) are considered. Severe multipath case.*

In the third step, the NL ambiguity can be fixed using the low-noise code pseudorange combinations, corrected by the smoothed ionosphere correction, described in Equation (8.10) as base pseudorange, and an IF combination between the fixed EWL and WL ($\overline{L}^s_{r,ew}$ and $\overline{L}^s_{r,w}$ respectively), and the ambiguous NL ($L^s_{r,n}$) carrier phase measurements:

$$\begin{aligned} L^s_r &= \beta_1 \overline{L}^s_{r,ew} + \beta_2 \overline{L}^s_{r,w} + \beta_3 L^s_{r,n} \\ &= g^s_r - \beta_3 \lambda_n (N^s_{r,n} + d^s_{r,n}) + \varepsilon^s_r \end{aligned} \tag{8.35}$$

In Equation (8.35), the coefficients β_1, β_2, and β_3 are used to form a geometry-preserving and ionosphere-free combination between $\overline{L}^s_{r,ew}$, $\overline{L}^s_{r,w}$, and $L^s_{r,n}$. The coefficient β_3 can be selected to amplify λ_n and, consequently, to reduce the error when estimating $N^s_{r,n}$. On the other hand, in order to further reduce the error in the ionosphere corrected low-noise pseudorange combination, the Hatch

filter can be applied to the ionosphere observable computed from a combination between $\bar{L}^s_{r,ew}$ and $\bar{L}^s_{r,w}$.

$$\tilde{I}^s_r(t_k) = \frac{1}{k} I^{s,w}_r(t_k) + \left(1 - \frac{1}{k}\right)\left(\tilde{I}^s_r(t_{k-1}) + I^{s,L}_r(t_k) - I^{s,L}_r(t_{k-1})\right) \quad (8.36)$$

$$I^{s,w}_r(t_k) = \frac{\bar{L}^s_{r,w}(t_k) - \bar{L}^s_{r,ew}(t_k)}{q_w - q_{ew}} \quad (8.37)$$

In Equation (8.38) the combination of observable used to fix the NL ambiguity with the new TCAR method is shown.

$$N^s_{r,n}(t_k) = \frac{P^s_{r,IF}(t_k) - L^s_r(t_k)}{\beta_3 \lambda_n} - d^s_{r,n} \quad (8.38)$$

The advantages of this configuration are clear: on one hand the noise on $P^s_{r,IF}$ is not so much larger than $\bar{L}^s_{r,x}$, on the other hand the NL wavelength is amplified by β_3. As in case of TCAR for double differenced observations, if the residual error due to the ionosphere correction is much smaller than the amplified wavelength, its effect in the ambiguity fixing is negligible.

Figure 8.46 shows the noise on the NL ambiguity observable in units of cycles as a function of the amplified NL wavelength ($\beta_3 \lambda_n$) for the two cases when the receiver is assumed to be placed in multipath-free (left subplot) and in multipath-rich (right subplot) environments.

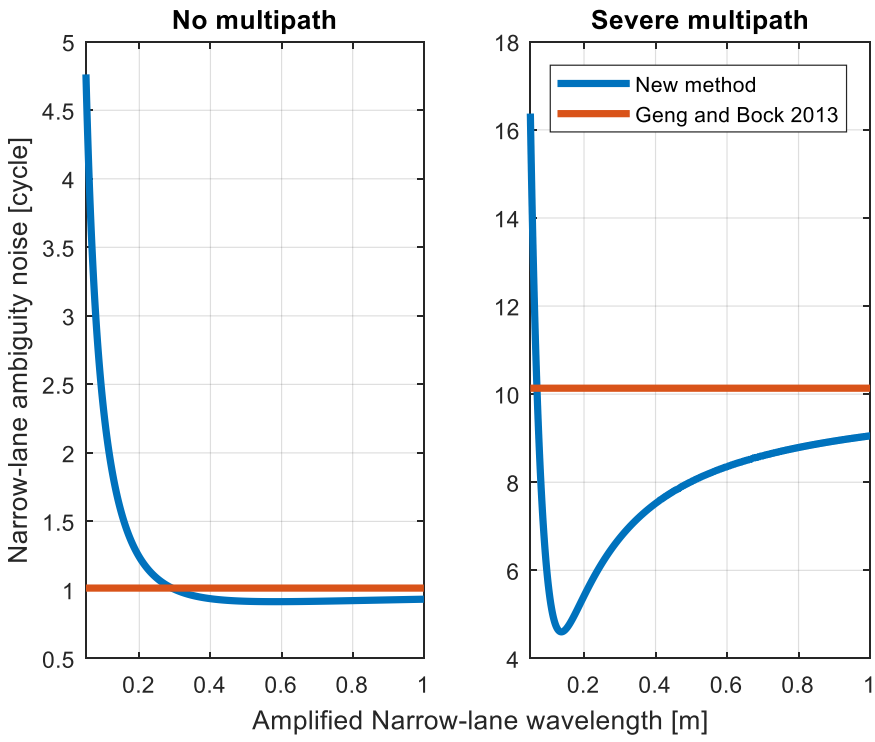


Figure 8.46 *Noise on the NL ambiguity observable achieved with the new method (blue) as a function of the NL wavelength amplified by the factor β_3. For comparison, the noise level obtained with the TCAR method proposed in Geng and Bock (2013) is also shown (red). GPS L1-L2-L5 signals are considered.*

In the first scenario, the minimum noise can be found for a wavelength of about 0.59 m, while, in the second case, the minimum noise corresponds to an amplified wavelength of 0.14 m. For comparison, the NL ambiguity observable noise obtained using the AFIF combination is also plotted. This noise level is always higher than the minimum achievable with the approach presented in this paper. At its minimum, the noise in the NL ambiguity computed with the new method is 10% smaller than the noise achievable with the AFIF in benign environments and 55% in severe multipath environments. Also, increasing the wavelength from the optimal one doesn't lead to a larger NL ambiguity noise than the one achievable with the AFIF. Indeed, if the noise corresponding to a NL wavelength of 1 m and the AFIF one are compared, there is an improvement of 8% for the multipath-free case, and 11% for the multipath-rich case. Although the improvement is much smaller, in particular for multipath-rich sites, on the other hand, having a larger NL wavelength is beneficial for the ambiguity resolution as it reduces the impact of the residual bias due to the smoothed ionosphere correction.

The NL ambiguity correct-fix rates for different low-noise pseudorange combinations corrected by the smoothed ionosphere correction and for different values of the amplified NL wavelength have been compared with the NL ambiguity success-rate for the AFIF combination introduced in Geng and Bock (2013). Only the multipath-free case was tested since it was already shown that TCAR doesn't perform well in presence of multipath. For GPS frequencies, the combinations that provide the highest NL ambiguity correct-fix rate are the minimum-noise pseudorange combination and the triple-carrier IF combination with amplified NL wavelength of 0.5 m. On the other hand, because of its very large ionosphere amplification factor of about 1.6, the Galileo minimum-noise pseudorange combination is not the one providing the best NL correct-fix rate. Indeed, for Galileo E1, E5, and E6 frequencies, the highest ambiguity fix success-rate is guaranteed by the low-noise pseudorange combination with q equal to 1.5 associated with triple-carrier IF combination characterized by an amplified NL wavelength of 0.5 m.

As shown in **Figure 8.47**, the method proposed in this thesis effectively improves the NL ambiguity fix success-rate. While the AFIF combination allows for a GPS PPP fixed solution after 60 second and a Galileo PPP fixed solution after 25 seconds, the new combinations provides a NL ambiguity correct-fix rate of 99.9% in about 30 seconds for GPS and in about 15 seconds for Galileo.

Although ambiguity resolution methods based on geometry-free combinations perform well only in absence of multipath, and therefore cannot be used in urban environments, they are an incredibly effective asset for quickly obtaining PPP fixed solutions in open areas. On the other hand, the combinations that have been proposed to improve the NL ambiguity correct-fix rate are the basis of the method described in Section 8.2 for speeding the convergence time of the PPP float solution.

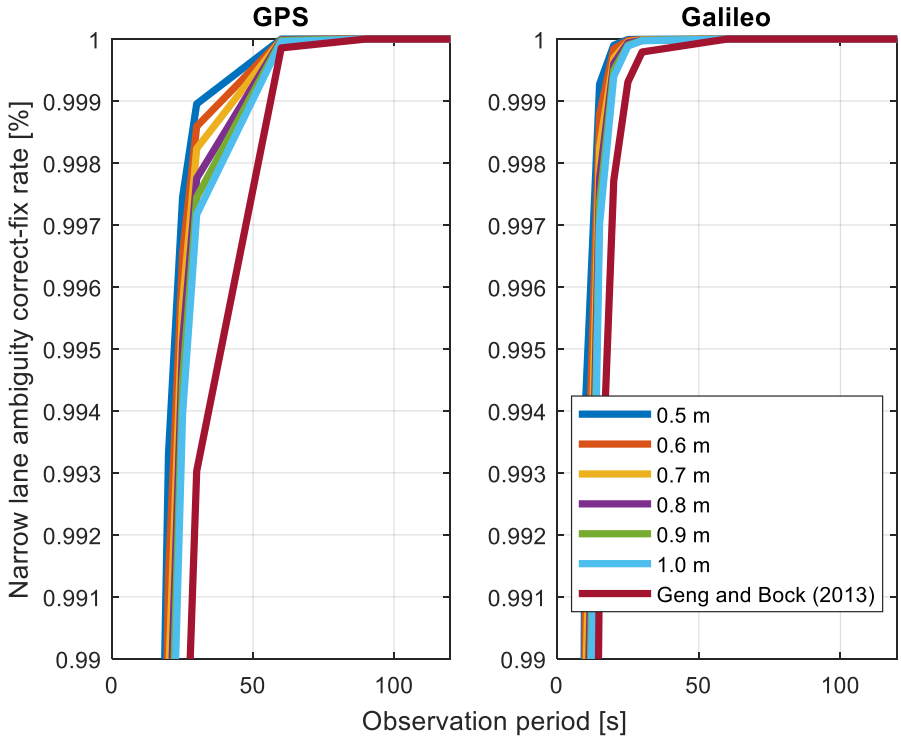


Figure 8.47 *Correct-fix rate of the narrow lane ambiguity resolution for the new method and the method proposed in Geng and Bock (2013) for GPS L1-L2-L5 (left subplot) and Galileo E1-E5-E6 (right subplot) combinations. For the new method, triple-carrier IF combinations with different amplified narrow lane wavelengths are considered. Benign environment.*

8.4 Chapter summary

In the last decade PPP has become an attractive solution for many applications seeking for high accuracy, such as earthquake and tsunami monitoring, or precision agriculture, in remote areas that, for logistics or economic reasons, cannot be served by nearby reference stations. Indeed, PPP enables decimetre-level (kinematic) or centimetre-level (static) accuracy everywhere on the globe. Unfortunately, the poor signal visibility and continuity associated to urban environments together with the slow (re-)convergence time of PPP, usually make it unsuitable for land navigation in cities. Within this chapter innovative methods to reduce the (re-)convergence time of float PPP solutions exploiting multi-frequency GPS and Galileo measurements have been proposed. These methods can be divided into two groups: the first set attempts to reduce the PPP (re-)convergence time by reducing the noise in the IF pseudorange combination, while the second set tries to increase the size of the wavelength in the NL carrier phase combination. By employing these combinations, the observability of the

ambiguity is improved and, consequently, the convergence time of the float PPP solution can be shortened.

In the first method, a research into triple-frequency pseudorange combinations that minimise the noise level was performed. It was observed that the error in GPS and Galileo IF combinations with low-noise is not much lower that the error in traditional two-frequency IF combinations. Hence, the use of triple-frequency IF combinations, instead of the dual-frequency IF, doesn't benefit the PPP solution. On the other hand, there exist triple-frequency pseudorange combinations that greatly damp the noise by up to 90% (E1-E5-E6) with respect to the corresponding IF combination (E1-E6 IF). Unfortunately, these combinations don't mitigate the effect of the ionosphere, but it is further amplified by up to 63% (E1-E5-E6) with respect to the ionospheric delay affecting GNSS measurements on L1 frequency. In an effort to exploit these low-noise pseudorange combinations in PPP, the concept of smoothed ionosphere correction is introduced. The ionosphere observable, computed from two-frequency geometry-free pseudorange combinations, is filtered through a Hatch filter before being applied to the low-noise pseudoranges. With this configuration, once the Hatch filter has converged, the corrected pseudoranges are characterized by very little noise and no ionospheric delay and can be very useful in case of data gaps or cycle slips that force the PPP filter to restart. Indeed, by exploiting the temporal correlation in the ionospheric delay, the Hatch filter doesn't need to be reinitialised from the raw values, meaning that the ionosphere corrected pseudorange still has a small noise. As a consequence, quick re-convergence in PPP can be reduced from about 19 minutes to roughly 5 minutes, for GPS in open sky conditions, and from about 18 minutes to a few tens of seconds, for Galileo, with no need to estimate the ionospheric delay in the Kalman filter as suggested in many publications (Geng et al., 2010a; Li, 2012; Zhang et al., 2013). In order to account for the varying error in the ionosphere correction, a proper weighting method has been defined.

The second method proposes to reduce the first convergence in PPP by adopting triple-carrier IF combinations that reduce the noise in the NL ambiguity observable. When coupled with the traditional two-frequency IF pseudorange and carrier phase combinations, and after the EWL and WL ambiguities have been fixed, the error in the horizontal solution drops to a few centimetres up to

more than two times faster (from almost 21 minutes to less than 9 minutes for the Galileo case) than the float PPP solution based on two-frequency IF combinations.

Finally, a new TCAR approach, based on low-noise pseudorange combinations corrected by the smoothed ionosphere and on triple-carrier IF combinations with large wavelengths, was introduced. This approach is aimed to further improve the ambiguity fix success-rate with respect to the method presented in Geng and Bock (2013). Although ambiguity resolution methods based on geometry-free combinations perform well only in absence of multipath, and therefore cannot be used in urban environments, they are an incredibly effective asset for quickly obtaining PPP fixed solutions in open areas.

Chapter 9

Conclusions

In the past years the interest in Precise Point Positioning has considerably grown due to its high computational efficiency, no need for any synchronous measurements from local reference stations and homogeneous positioning quality on a global scale. On the other hand, its long convergence time, of the order of several tens of minutes, has limited the adoption of PPP to precise positioning in open environments. In fact, although PPP is currently a standard for atmospheric studies (Douša, 2009; Zhang et al., 2012), earthquake and tsunami monitoring (Shi et al., 2010), and precision agriculture (Mondal and Tewari, 2007), it is rarely used for vehicle navigation in urban areas for three main reasons (Ohshima et al., 2015). The first reason is related to the accuracy. For the "where-in-lane applications" (see Section 7.3 and Teunissen and Montenbruck (2017)) drivers must know vehicles location well within the lane, which often translates to an accuracy of 10 cm or better, if we want to safely overtake other vehicles. Ideally, we would like to have such a high accuracy level from the beginning of the driving, when, for example, users move their car from the garage with precise manoeuvres. With the current PPP status, this is just impossible, as users should wait for several tens of minutes before starting their journey. Similarly, re-convergence also represents a big issue to navigate vehicles in an environment where there are many objects blocking satellites signals, and, therefore, causing frequent reinitializations. From the user's perspective, it is, indeed, unfeasible to rely on a system that can stop providing high positioning accuracy anytime. Hence, PPP in urban area can be an option only when centimetre-level accuracy is guaranteed at all times, for example, through advanced PPP algorithms based on multi-constellation multi-frequency GNSS augmented by inertial sensors.

As mentioned in Chapter 1, the overall aim of this research was to study the benefit of using Galileo signals, beside the modernized GPS system, on the PPP solutions in both open environments and urban areas. To pursue this aim the following objectives were identified:

- Contribute to the POINT software by completing the implementation of the Galileo capability

- Investigate the impact of the current state Galileo system, in combination with GPS, on the PPP solution, in comparison with the single constellation case, in terms of accuracy and convergence time.
- Develop a GPS/Galileo simulator in Simulink for multi-frequency GNSS observations and precise PPP products.
- Compare different GPS and Galileo ionosphere-free combinations and investigate those providing the most accurate PPP solution and the quickest convergence time.
- Compare the GPS, Galileo, and GPS+Galileo PPP solution in terms of final accuracy and convergence time.
- Analyse the satellite availability and geometry conditions offered by the GPS+Galileo system in urban environments.
- Analyse the PPP solutions based on GPS+Galileo measurements in urban environments.
- Investigate alternative multi-frequency ionosphere-free combinations that speed up the PPP (re-)convergence time.
- Clarify what is the best way to predict the ionospheric delay estimates in urban environments.
- Provide an efficient visualization method for studying the characteristics of triple-frequency combinations.

For each objective, the conclusions of the analysis performed in this PhD research project are discussed in the next sections.

9.1 Galileo capability in POINT

Galileo observables can now be processed in both single-constellation and multi-constellation PPP mode using the POINT software. Despite the low number of Galileo satellites in view and the poor quality of the MGEX products, centimetre-level positioning solutions have been successfully computed.

9.2 Effect of the current state Galileo constellation and MGEX products on PPP

In recognition of the evolving GNSS landscape, in 2012 the IGS has set up the MGEX to explore and promote the use of new navigation signals and constellations. Currently, six ACs are providing multi-GNSS products for MGEX on a routine basis. CODE is recognized to provide the best products

within all the ACs contributing to MGEX, therefore they have been used in this research.

The quality of CODE multi-constellation data processing was assessed against its traditional GPS only processing. For this purpose, the PPP solutions computed using CODE's products for MGEX and IGS were compared. The results from 2016 showed noticeable differences in the positioning performance, particularly in the convergence time. Indeed, using the COM products, the 3D convergence time increased from about 40 minutes to about 79 minutes. The gap between the convergence time in the PPP solutions based on COM and COD products was significantly reduced when CODE changed the data-rate of the COM clock products to 30 seconds. The results from 2018 showed that the 3D convergence times of the COD and COM solutions differ by only 2.6% (roughly 61 minutes for COD and 63 minutes for COM). However, small differences in the positioning errors, of the order of a couple of millimetres or less, were still apparent. This can be interpreted as a sign of mismodelling in the multi-constellation data processing that affect the quality of the MGEX products.

The GPS only PPP solutions were also compared to the GPS+Galileo PPP solutions. Even though a better performance of the two-constellation PPP was expected, the low number of Galileo satellites in view, the poor quality of the precise orbits and clocks, and the lack of accurate antenna corrections for Galileo made the GPS+Galileo PPP solution worse than the GPS only solution. For example, the RMS 3D error for station LMMF in 2018 increased from 1.16 cm, for a GPS only solution, to 7.27 cm, for a Galileo only solution. At the same time the RMS 3D convergence time passed from about 40 minutes to approximately 128 minutes. On the other hand, for station KERG, using Galileo together with GPS improved the PPP 3D accuracy from 3.17 cm to 1.87 cm, and the 3D convergence time from about 68 minutes to less than 50 minutes.

A Galileo only PPP solution was also computed using the data recorded at SEYG, when 5 Galileo satellites were simultaneously visible, but for this data-set centimetre-level positioning could be achieved. However, despite the fact that the Galileo pseudoranges are less noisy than the GPS ones (Richardson et al., 2016), the final accuracy of the GPS PPP solution is 0.15 cm, 1.10 cm, and 1.45 cm respectively in the north, east, and up directions, while for Galileo these

are 3.12 cm, 2.00 cm, and 4.54 cm. Similarly, the convergence times in the north, east, and up directions increase from 1.5, 22, and 8 minutes, for GPS, to 13.5, 151, and 70 minutes, for Galileo. This was attributed to the limitations mentioned previously.

From this analysis it is possible to conclude that the Galileo system and its PPP products are still not mature enough for a clear evaluation of the potential impact of Galileo signals in single and multi-constellation PPP. Despite having 14 Galileo satellites usable for positioning (June 2018), the results presented in this section still do not match the expected outcome from GPS+Galileo PPP as was forecast by previous studies based on simulated data. Moreover, given the technical limitations due to the current status of the next-generation GNSS constellations, it is decided to evaluate the future fully operational performance of Galileo and GPS+Galileo PPP, in comparison with GPS PPP, through the use of simulated data. At the moment (February 2019), the GPS only processing has to be considered that it is still the preferred data processing standard in PPP, at least until more satellites and more accurate products are made available for Galileo.

9.3 Simulation of the precise orbits and clocks

The performance of GPS+Galileo PPP were analysed through a Simulink tool that is able to simulate multi-frequency GPS and Galileo observables. In PPP, however, precise products are necessary in order to achieve high precision. The difference between the IGS real-time products and the final products provided by ESA showed a systematic and periodic behaviour. For this reason, the methods adopted in previous studies based on simulated data, where the error in the PPP products were either neglected or modelled using random numbers generator have to be considered unrealistic. In this research the error in the precise orbits and clocks were modelled as a sum of two sinusoids. The first one has a period equal to the orbital period of the GNSS constellation, and the second one has a period equal to the Earth rotation period. It is therefore recommended that this model should be included in all future PPP studies based on simulated data.

9.4 Best GPS and Galileo two-frequency combinations for PPP

In this study, a comparison aimed to identify the two-frequency IF combinations that guarantee the best PPP performance was performed. For GPS, the PPP solutions obtained by processing the L1-L2 IF and L1-L5 IF combinations showed similar accuracy levels, however a big difference in the convergence time was observed. In open sky conditions, with no nearby reflective surfaces, the time the horizontal solution computed from the L1-L5 IF combination takes to go below a 10 cm threshold was reduced by a factor of two, from 8 to 4 minutes, with respect to the L1-L2 IF solution. This result was expected considering that the pseudoranges on L5 have been simulated with lower noise and multipath than L2. It is well known that the quality of the pseudoranges have a significant impact on the PPP convergence.

For the same reason, high expectations were placed on the Galileo E5 pseudorange. Thanks to its very large bandwidth of 51 MHz, the AltBOC modulation provides pseudoranges with low noise and multipath characteristics. Surprisingly, no significant difference was observed between the PPP solutions achieved adopting E1-E5 IF and E1-E5a IF. The reason for this unexpected behaviour was attributed to the IF combination with E1.

It can be concluded that, when all the GPS satellites will be able to broadcast the L5 signal, it is advisable to adopt the L1-L5 IF combinations in any GPS two-frequency IF data processing. For Galileo, using E1-E5a IF combination not only guarantees less noisy pseudoranges, but this combination is also compatible with the clock corrections provided by the MGEX ACs, as well as included into the broadcast navigation message. As a consequence, it removes the need to apply the DCBs correction, as would have to be done if other IF combinations, such as E1-E5 IF, were adopted.

9.5 Comparison between GPS, Galileo, and GPS+Galileo PPP

In Chapter 7, the best GPS and Galileo IF combinations have been used to assess the performance of single and multi-constellation PPP. Two static scenarios in open sky conditions have been set in which the antenna was first placed in a benign multipath environment and then in a multipath-rich site. In the first case, the Galileo PPP results showed a much faster convergence time than the GPS PPP solutions. Indeed, the time required to have the RMS horizontal error

smaller than 10 cm was reduced from 4 minutes to 2.5 minutes. This outcome was attributed to the lower level of noise that was assumed (in the simulations) for the pseudorange measurements. On the other hand, when both the GPS and Galileo measurements were affected by similar level of multipath, the convergence of the GPS PPP solution was much quicker than the corresponding solution for Galileo (horizontal convergence times were 20 and 33.5 minutes for GPS and Galileo, respectively). As there were only small differences in the pseudorange noise level, the PPP convergence time, in this case, was mainly dictated by the speed of change in the user-to-satellite geometry. Since the GPS constellation is at lower altitude than the Galileo one, and the GPS satellites move therefore faster along their orbital paths, the change in the LOS for GPS is quicker than for Galileo. As a consequence, with similar pseudorange noise levels, the PPP convergence time for Galileo is slower than the corresponding convergence time for GPS. In both open sky scenarios, although the final accuracy was also improved, it is mainly the convergence time that benefits from multi-constellation PPP. Indeed the convergence time can be significantly reduced, by more than a factor of 2 (from 10.5 to 5 minutes for the vertical component) with respect to GPS alone in multipath-free environments.

Based on the results presented in this thesis, it is advisable to adopt the multi-constellation PPP model to partially reduce the convergence time of the PPP solution. Unfortunately, it is still impossible to obtain centimetre-level positioning accuracy in a few minutes or, even better, a few seconds.

9.6 Satellite availability and geometry conditions in urban areas

GPS and Galileo satellite visibility has been studied in a simulated urban area corresponding to the neighbourhood of the UCL campus in London. Accurate building boundaries with azimuth resolution of only 1° were adopted when designing this scenario. Satellite availability and geometry conditions have been analysed at five different sites around the simulated area, for a 24 hour period. These sites include two junctions, one wide street (three lanes plus footpath in both sides) surrounded by short buildings (four-five floors tall), one narrow street (one lane plus parking slots and footpath in both sides) surrounded by short buildings, and one narrow street surrounded by tall buildings (six-seven floors). It was noted that satellite availability and geometry conditions were at

their best at the two junctions, with at least 6 satellites in view and HDOP better than 5 for more than 97% of the time. The conditions of restricted satellite visibility along the two streets surrounded by short buildings makes GPS+Galileo based navigation quite challenging; HDOP values better than 5 were available for less than 86% of the time, while values better than 2 for less than 44% of the epochs. When completely surrounded by tall buildings, it is almost impossible to have the minimum number of satellites to compute the GPS+Galileo PPP solution. It can be concluded that the presence of tall buildings compromises the satellite availability and, therefore, the possibility of computing GNSS based positioning solutions in urban environments. On the other hand, it was shown that GNSS may work in certain areas where the streets are wide, or the surrounding buildings are shorter than six floors. In traditional European cities, in proximity of the historical centres, it is common to find narrow roads and relatively short buildings packed together. These streets are usually good candidates for GNSS based positioning. On the other hand, it is not uncommon for drivers and pedestrians to find, even in these areas, slightly taller buildings that completely obstruct the transmitting GNSS satellites. Similar, or even worse, conditions may occur in the business districts of European cities or in modern American or Asian metropolis, where skyscrapers are very popular. An example is Canary Wharf in London. In this kind of area, it is very difficult to compute user's position with a GNSS receiver. Things could be slightly improved by also considering GLONASS and Beidou measurements.

9.7 GPS+Galileo PPP in a kinematic urban scenario

Simulated GPS+Galileo observations, recorded by a pedestrian walking around the UCL campus, were processed in kinematic PPP mode. It was noticed that, although the satellite availability and geometry conditions throughout the kinematic test were generally good (the HDOP was well below 5 for most of the time), the convergence time of the GPS+Galileo PPP solution is still too slow to guarantee a re-converged solution, after the Kalman filter had to restart (due to interruptions in the measurements). Indeed, during this test, on only two occasions did the minimum number of satellites drop below 6, and yet the GPS+Galileo PPP solution never managed to re-converge below 20 cm of

accuracy, even when a very optimistic value for the multipath correlation time was assumed. From this short example, it was demonstrated what the main limitation for PPP in urban areas is: the discontinuity of the signals due to urban infrastructures. Nonetheless, GPS+Galileo PPP easily enables sub-meter level horizontal accuracy. Hence, land based applications such as in-car navigation, fleet management, urban traffic control, emergency calls, dynamic route guidance, selective vehicle priority, road pricing, stolen vehicle recovery, or trip information can already benefit from GPS+Galileo PPP. Other applications in which better knowledge of the position is necessary, for example collision avoidance, intelligent speed assistance, lane control, or restraint deployment cannot rely on the traditional PPP solution based on GPS and Galileo IF measurements. To fulfil the needs of these type of user requirements, more refined positioning algorithms are required.

9.8 Quick (re-)convergence PPP enabled by multi-frequency IF combinations

The convergence time in PPP is intimately related to the estimation of the carrier phase ambiguities. It is only when the float ambiguity estimates have reached a steady constant value that the PPP solution is fully converged.

One of the factors that impact on the convergence time is the large noise of the pseudoranges. The use of the IF combination is a limiting factor for PPP as it greatly amplifies the pseudorange noise. Indeed, today most successful techniques to reduce the PPP convergence time exploit un-combined observations in which the ionosphere is corrected using VTEC maps and the residual delay is estimated as a Kalman filter state. The temporal and spatial correlations in the slant ionospheric delay can be used to tightly constrain the estimation of the ambiguity in the Kalman filter and, consequently, achieve fast convergence. However, these configurations perform the best only if the user is located in proximity of the reference receivers used to estimate the ionosphere corrections. This means that the main property that differentiates PPP from RTK, i.e. high accuracy globally, is lost. On the other hand, by using the low-noise pseudorange combinations corrected by the smoothed ionosphere combination it is possible to obtain re-convergence to a centimetre-level of accuracy after only a few tens of seconds, without relying on external

ionosphere information and without the need to increase the size of the state vector by including the additional ionospheric states. This architecture fully exploits the potential of the Galileo E5 pseudorange. Unfortunately this method only benefits the re-convergence time and not the time for first convergence. Indeed, the smoothed ionosphere combination has to converge to decimetre-level of accuracy in order to be effective. The results showed that this method is a simple, yet extremely useful, tool to improve the PPP solution in urban environments.

The first convergence below 10 cm of error can be obtained in almost 6 minutes (on average) if triple-carrier IF combinations that optimize the noise in the NL ambiguity observable are used beside the traditional two-frequency IF combinations. This algorithm becomes effective only after the EWL and WL ambiguity are fixed. For this reason, methods to quickly fix these types of ambiguities are necessary.

9.9 Prediction of the ionosphere estimate in urban environments

The method proposed in this thesis to reduce the reconvergence time of the PPP solution depends on the way the ionospheric delay is predicted in case of data-gaps caused by the urban environment. The two methods proposed in Dai et al. (2003) and, later, assessed in Geng (2010) for quick PPP reconvergence in open sky conditions, namely a linear fitting model and a constant bias model, were considered. Although the linear fitting model overall offers better accuracy, it must be noticed that, in urban environments, is very difficult to have continuous ionosphere observations for the time required to build the linear fitting model. Indeed, for the kinematic test in Birmingham for example, only 4.2% of all the continuous data arcs are longer than 120 seconds. If the minimum number of epochs required to run the linear fitting model (2 minutes) is not available, the prediction has to start from the latest continous data arc which is long enough to extrapolate the ionospheric delay. For this reason, the actual prediction time may be much larger, on average 21 minutes (for the test in Birmingham). On the other hand, the average prediction time for the constant bias model is only 18.7 seconds, leading to a better prediction with the constant bias model than with the linear fitting model.

9.10 Use of the q-α_3-n plot for studying triple-frequency GNSS measurements combinations

In Section 8.1.1.1, the q-α_3-n plot was used to analyze the noise in different triple-frequency pseudorange combinations. It proved to be a simple, yet effective, visualization tool for studying the characteristics of the pseudorange combinations and to evaluate the best one to be used in the algorithms proposed throughout this thesis.

9.11 Conclusions summary

The foremost contributions of this thesis to the knowledge can be summarised as follows:

- Based on the analysis performed in this thesis, the error in the precise real-time PPP products (with respect to the final PPP products) cannot be considered as white noise. A better and more realistic way to simulate the precise PPP products is to model their error as the sum of two sinusoids with periods equal to the orbital period of the constellation and to the Earth rotation period.
- L1-L5 IF is the two-frequency GPS combination that provides the quickest convergence of the PPP solutions below 10 cm of error.
- E1-E5a IF is the two-frequency Galileo combination that provides the quickest convergence of the PPP solutions below 10 cm of error.
- Despite its low noise, the Galileo E5 pseudorange does not benefit the PPP solution, if combined in the E1-E5 IF combination.
- Galileo PPP solution offers quicker convergence than the GPS PPP solution if the receiver is located in multipath-free environments.
- GPS+Galileo PPP solution offers quicker convergence than both the GPS only and Galileo only PPP solutions.
- GPS+Galileo based navigation is in theory possible in most urban areas, however high accuracy through PPP is still limited by the long (re-) convergence time. On the other hand, sub-meter level of accuracy can be easily achieved.
- Quick re-convergence in PPP can be achieved in a few tens of seconds without relying on external ionospheric information and without increasing the size of the state vector.

- Although it was shown that triple-frequency, low-noise IF combinations do not have any significant benefit on the PPP solution, rapid convergence in approximately 6 minutes can be enabled by employing triple-carrier IF combinations that minimize the noise in the NL ambiguity observable.

9.12 Recommendations for future work

This research has been conducted with certain restrictions, some of which could be addressed in the future.

- The availability of accurate building boundaries was only limited to the area of the UCL campus. On the other hand, the methods proposed could be tested in a wider range of urban scenarios, if they are properly simulated.
- Because of the technical limitations discussed in this thesis, this research was exclusively based on simulated data. When these limiting factors will be resolved, the results presented in this thesis could be validated through replication using real data.
- This study only focused on the benefits led by the Galileo constellation, in combination with the GPS system, to the PPP solutions. It would be worth assessing the PPP solutions based on the combined use of the four GNSS systems.
- Ambiguity resolution for PPP was not fully considered: only TCAR method approaches were analysed in this thesis. It would be important to assess the impact of the proposed combinations on geometry-based ambiguity resolutions algorithms, such as LAMBDA or integer bootstrapping.

References

Abou-Galala, M., Rabah, M., Kaloop, M., Zidan, Z.M., 2017. Assessment of the accuracy and convergence period of Precise Point Positioning. Alexandria Eng. J. 57, 1721–1726.

Adjrad, M., Groves, P.D., 2016. Intelligent Urban Positioning using Shadow Matching and GNSS Ranging Aided by 3D Mapping, in: 29th International Technical Meeting of The Satellite Division of the Institute of Navigation (ION GNSS+ 2016). pp. 534–553.

Afifi, A., El-Rabbany, A., 2015. Performance Analysis of Several GPS/Galileo Precise Point Positioning Models. Sensors (Basel) 15, 14701–14726.

Afifi, A., El-Rabbany, A., 2014. Enhanced model for precise point positioning with single and dual frequency GPS/Galileo observables. ISPRS - Int. Arch. Photogramm. Remote Sens. Spat. Inf. Sci. XL–2, 173–177.

Alizadeh, M.M., Wijaya, D.D., Hobiger, T., Weber, R., Schuh, H., 2013. Ionospheric Effects on Microwave Signals, in: Atmospheric Effects in Space Geodesy. pp. 35–71.

Allan, D.W., 1966. Statistics of Atomic Frequency Standards. Proc. IEEE 54, 221–230.

Aminov, Y., 2012. FBD - Find the Best Distribution tool.

Angrisano, A., Gaglione, S., Gioia, C., Borio, D., Fortuny-Guasch, J., 2013. Testing the Test Satellites: the Galileo IOV Measurement Accuracy, in: International Conference on Localization and GNSS (ICL-GNSS). pp. 1–6.

Arnold, D., Meindl, M., Beutler, G., Dach, R., Schaer, S., Lutz, S., Prange, L., Sośnica, K., Mervart, L., Jäggi, A., 2015. CODE's new solar radiation pressure model for GNSS orbit determination. J. Geod. 89, 775–791.

Ashby, N., 2003. Relativity in the Global Positioning System. Living Rev. Relativ. 6.

Banville, S., Collins, P., Zhang, W., Langley, R.B., 2014. Global and regional ionospheric corrections for faster PPP convergence. Navig. J. Inst. Navig. 61, 115–124.

Bar-Sever, Y.E., Kroger, P.M., Borjesson, J.A., 1998. Estimating horizontal gradients of tropospheric path delay with a single GPS receiver. J.

Geophys. Res. Solid Earth 103, 5019–5035.

Basile, F., Moore, T., Hill, C., 2019. Analysis on the Potential Performance of GPS and Galileo Precise Point Positioning using Simulated Real-Time Products. J. Navig. 72, 19–33.

Basile, F., Moore, T., Hill, C., 2017. Analysis on the Potential Performance of GPS and Galileo Precise Point Positioning using simulated Real-Time products, in: International Navigation Conference (INC).

Basile, F., Moore, T., Hill, C., McGraw, G., 2018a. Performance Analysis of Triple Carrier Ambiguity Resolution in Precise Point Positioning with Smoothed Ionosphere Corrections, in: 31st International Technical Meeting of The Satellite Division of the Institute of Navigation (ION GNSS+ 2018). pp. 3868–3880.

Basile, F., Moore, T., Hill, C., McGraw, G., Johnson, A., 2018b. Multi-Frequency Precise Point Positioning using GPS and Galileo Data with Smoothed Ionospheric Corrections, in: IEEE/ION PLANS. pp. 1388–1398.

Basile, F., Moore, T., Hill, C., McGraw, G., Johnson, A., 2018c. Two are better than one: Multi-Frequency Precise Point Positioning Using GPS and Galileo. GPS World 29, 27–37.

Bassiri, S., Hajj, G., 1993. Higher-order ionospheric effects on the global positioning system observables and means of modeling them. Manuscripta Geod. 18, 280–289.

Bertiger, W., Desai, S.D., Haines, B., Harvey, N., Moore, A.W., Owen, S., Weiss, J.P., 2010. Single receiver phase ambiguity resolution with GPS data. J. Geod. 84, 327–337.

Black, H.D., Eisner, A., 1984. Correcting satellite Doppler data for tropospheric effects. J. Geophys. Res. 89, 2616.

Boehm, J., Heinkelmann, R., Schuh, H., 2007. Short Note: A global model of pressure and temperature for geodetic applications. J. Geod. 81, 679–683.

Boehm, J, Niell, A., Tregoning, P., Schuh, H., 2006. Global Mapping Function (GMF): A new empirical mapping function based on numerical weather model data. Geophys. Res. Lett. 33.

Boehm, Johannes, Werl, B., Schuh, H., 2006. Troposphere mapping functions for GPS and very long baseline interferometry from European Centre for

Medium-Range Weather Forecasts operational analysis data. J. Geophys. Res. Solid Earth 111.

Cai, C., Luo, X., Liu, Z., Xiao, Q., 2014. Galileo Signal and Positioning Performance Analysis Based on Four IOV Satellites. J. Navig. 67, 810–824.

Chatre, E., Verhoef, P., 2018. Galileo Programme Status Update, in: Proceedings of the 31st International Technical Meeting of the Satellite Division of The Institute of Navigation (ION GNSS+ 2018). pp. 733–767.

Chen, K., Gao, Y., 2005. Real-Time Precise Point Positioning Using Single Frequency Data. Proc. 18th Int. Tech. Meet. Satell. Div. Inst. Navig. (ION GNSS 2005) 32, 312–315.

Circiu, M.-S., Meurer, M., Felux, M., Gerbeth, D., Thölert, S., Vergara, M., Enneking, C., Sgammini, M., Pullen, S., Antreich, F., 2017. Evaluation of GPS L5 and Galileo E1 and E5a Performance for Future Multifrequency and Multiconstellation GBAS. Navigation 64, 149–163.

Cocard, M., Bourgon, S., Kamali, O., Collins, P., 2008. A systematic investigation of optimal carrier-phase combinations for modernized triple-frequency GPS. J. Geod. 82, 555–564.

Collins, P., 2008. Isolating and Estimating Undifferenced GPS Integer Ambiguities, in: National Technical Meeting of The Institute of Navigation. pp. 720–732.

Commission of the European Communities, 1998. Communication from the Commission to the Council and the European Parliament - Towards a Trans-European Positioning and Navigation Network: including A European Strategy for Global Navigation Satellite Systems (GNSS).

Commission of the European Communities, 1994. Communication from the Commission - Satellite Navigation Services: a European Approach.

Dai, L., 2000. Dual-Frequency GPS/GLONASS Real-Time Ambiguity Resolution for Medium-Range Kinematic Positioning, in: 13th International Technical Meeting of the Satellite Division of The Institute of Navigation (ION GPS). pp. 1071–1080.

Dai, L., Eslinger, D., Sharpe, T., 2007. Innovative Algorithms to Improve Long Range RTK Reliability and Availability, in: National Technical Meeting of The Institute of Navigation. pp. 860–872.

Dai, L., Wang, J., Rizos, C., Han, S., 2003. Predicting atmospheric biases for real-time ambiguity resolution in GPS/GLONASS reference station networks. J. Geod. 76, 617–628.

De Jonge, P., Tiberius, C., 1996. The LAMBDA method for integer ambiguity estimation: Implementation aspects.

Deo, M., El-Mowafy, A., 2016. Triple-frequency GNSS models for PPP with float ambiguity estimation: performance comparison using GPS. Surv. Rev. 50, 249–261.

Dilssner, F., Schonemann, E., Springer, T., Flohrer, C., Enderle, W., 2017. Galileo Declassified: IOV Spacecraft Metadata and Its Impact on Precise Orbit Determination, in: EGU General Assembly. p. 14378.

Dong, D.-N., Bock, Y., 1989. Global Positioning System Network analysis with phase ambiguity resolution applied to crustal deformation studies in California. J. Geophys. Res. Solid Earth 94, 3949–3966.

Douša, J., 2009. The impact of errors in predicted GPS orbits on zenith troposphere delay estimation. GPS Solut. 14, 229–239.

Elsobeiey, M., 2014. Precise Point Positioning using Triple-Frequency GPS Measurements. J. Navig. 68, 480–492.

Erto, P., 2008. Probabilita' e statistica per le scienze e l'ingegneria.

ESA, 2015. Salvage in Space: Recovering Galileo 5 and 6.

European GNSS Agency, 2018. Constellation Information.

European GNSS Agency, 2017a. GNSS Market Report, Issue 5.

European GNSS Agency, 2017b. Galileo Satellite Metadata.

European GNSS Agency, 2016a. Notice Advisory for Galileo Users (NAGU) 2016029.

European GNSS Agency, 2016b. Notice Advisory for Galileo Users (NAGU) 2016030.

European Union, 2016a. Galileo Initial Services - Open Service - Service Definition Document.

European Union, 2016b. European GNSS (Galileo) Open Service - Ionosphere Correction Algorithms for Galileo Single Frequency Users.

European Union, 2015. European GNSS (Galileo) Open Service Signal In Space Interface Control Document.

Falcone, M., Navarro-Reyes, D., Hahn, J., Otten, M., Piriz, R., Pearlman, M.,

2006. Satellite Laser-Ranging Campaigns: GIOVE's track. GPS World 17, 34–37.

Feng, S., Ochieng, W., 2006. User Level Autonomous Integrity Monitoring for Seamless Positioning in All Conditions and Environments. Eur. Navig. Conf.

Feng, S., Ochieng, W., Moore, T., Hill, C., Hide, C., 2008. Carrier phase-based integrity monitoring for high-accuracy positioning. GPS Solut. 13, 13–22.

Feng, Y., 2005. Future GNSS Performance-Predictions Using GPS With a virtual Galileo Constellation. GPS World 16, 46–52.

Forsell, B., Martin-Neira, M., Harris, R.A., 1997. Carrier phase ambiguity resolution in GNSS-2, in: 10th International Technical Meeting of the Satellite Division of The Institute of Navigation (ION GPS 1997). pp. 1727–1736.

Garcia, A.M., Piriz, R., Samper, M.D.L., 2010. Multisystem Real Time Precise-Point-Positioning, today with GPS+GLONASS in the near future also with QZSS, Galileo, Compass, IRNSS. Int. Symp. GPS/GNSS.

Ge, M, Gendt, G., Rothacher, M., Shi, C., Liu, J., 2008. Resolution of GPS carrier-phase ambiguities in Precise Point Positioning (PPP) with daily observations. J. Geod. 82, 389–399.

Ge, M., Gendt, G., Rothacher, M., Shi, C., Liu, J., 2008. Resolution of GPS carrier-phase ambiguities in Precise Point Positioning (PPP) with daily observations. J. Geod. 82, 389–399.

Geng, J., 2010. Rapid Integer Ambiguity Resolution in GPS Precise Point Positioning.

Geng, J., Bock, Y., 2013. Triple-frequency GPS precise point positioning with rapid ambiguity resolution. J. Geod. 87, 449–460.

Geng, J., Meng, X., Dodson, A.H., Ge, M., Teferle, F.N., 2010a. Rapid re-convergences to ambiguity-fixed solutions in precise point positioning. J. Geod. 84, 705–714.

Geng, J., Meng, X., Dodson, A.H., Teferle, F.N., 2010b. Integer ambiguity resolution in precise point positioning: method comparison. J. Geod. 84, 569–581.

Geng, J., Teferle, F.N., Shi, C., Meng, X., Dodson, A.H., Liu, J., 2009a. Ambiguity resolution in precise point positioning with hourly data. GPS

Solut. 13, 263–270.

Geng, J., Teferle, F.N., Shi, C., Meng, X., Dodson, A.H., Liu, J., 2009b. Ambiguity resolution in precise point positioning with hourly data. GPS Solut. 13, 263–270.

Gibbons, G., 2009. The Golden Age of GNSS. Insid. GNSS 4, 10.

Gioia, C., Borio, D., Angrisano, A., Gaglione, S., Fortuny-Guasch, J., 2014. A Galileo IOV assessment: measurement and position domain. GPS Solut. 19, 187–199.

Global Positioning Systems Directorate - Systems Engineering & Integration, 2014. Interface Specification IS-GPS-200 - Navstar GPS Space Segment/Navigation User Interfaces.

Global Positioning Systems Wing (GPSW) - Systems Engineering & Integration, 2010. Interface Specification IS-GPS-705 - Navstar GPS Space Segment / User Segment L5 Interfaces.

Grejner-Brzezinska, D.A., Arslan, N., Wielgosz, P., Hong, C.-K., 2009. Network Calibration for Unfavorable Reference-Rover Geometry in Network-Based RTK: Ohio CORS Case Study. J. Surv. Eng. 135, 90–100.

Griffiths, J., Ray, J.R., 2009. On the precision and accuracy of IGS orbits. J. Geod. 83, 277–287.

Groves, Paul D., 2013. Principles of GNSS, Inertial, and Multisensor Integrated Navigation Systems.

Groves, Paul D, 2013. Principles of GNSS, Inertial, and Multisensor Integrated Navigation Systems, 2nd ed. Artech House.

Guo, F., Li, X., Zhang, X., Wang, J., 2016. Assessment of precise orbit and clock products for Galileo, BeiDou, and QZSS from IGS Multi-GNSS Experiment (MGEX). GPS Solut. 21, 279–290.

Guo, J., Xu, X., Zhao, Q., Liu, J., 2016. Precise orbit determination for quad-constellation satellites at Wuhan University: strategy, result validation, and comparison. J. Geod. 90, 143–159.

Gurtner, W., Estey, L., 2018. RINEX: the Receiver Independent Exchange Format Version 2.11.

Hadas, T., Bosy, J., 2015. IGS RTS precise orbits and clocks verification and quality degradation over time. GPS Solut. 19, 93–105.

Hatch, R., 1982. The synergism of GPS code and carrier measurements, in:

International Geodetic Symposium on Satellite Doppler Positioning. pp. 1213–1231.

Henkel, P., Gunther, C., 2008. Precise point positioning with multiple Galileo frequencies, in: ION PLANS. IEEE, pp. 592–599.

Héroux, P., Kouba, J., 2001. GPS precise point positioning using IGS orbit products. Phys. Chem. Earth, Part A Solid Earth Geod. 26, 573–578.

Hofmann-Wellenhof, B., Lichtenegger, H., Collins, J., 2001. Global Positioning System: Theory and Practice. Springer-Verlag Wien.

IGS, 2018a. Products [WWW Document]. URL http://www.igs.org/products

IGS, 2018b. Real-time Service - Contributors [WWW Document]. URL http://www.igs.org/rts/contributors

IGS, 2017. Current IGS Site Guidelines [WWW Document]. URL https://kb.igs.org/hc/en-us/articles/202011433-Current-IGS-Site-Guidelines

Istituto Nazionale di Geofisica e Vulcanologia (INGV), 2018. Ionosphere.

Jean, Y., Dach, R., 2014. International GNSS Service Technical Report.

Ji, S., Chen, W., Ding, X., Chen, Y., Zhao, C., Hu, C., 2010. Potential Benefits of GPS/GLONASS/GALILEO Integration in an Urban Canyon – Hong Kong. J. Navig. 63, 681–693.

Jokinen, A., Feng, S., Ochieng, W., Hide, C., Moore, T., Hill, C., 2012. Fixed ambiguity Precise Point Positioning (PPP) with FDE RAIM, in: ION PLANS. IEEE, pp. 643–658.

Jokinen, A., Feng, S., Schuster, W., Ochieng, W., Hide, C., Moore, T., Hill, C., 2013a. Integrity monitoring of fixed ambiguity Precise Point Positioning (PPP) solutions. Geo-spatial Inf. Sci. 16, 141–148.

Jokinen, A., Feng, S., Schuster, W., Ochieng, W., Yang, L., Hide, C., Moore, T., Hill, C., 2013b. Fixed Ambiguity Precise Point Positioning (PPP) Using Tropospheric Corrections Based on Numeric Weather Modeling (NWM), in: ION Pacific PNT Meeting. pp. 319–329.

Joosten, P., Tiberius, C., 2002. LAMBDA: FAQs. GPS Solut. 6, 109–114.

Juan, J.M., Hernandez-Pajares, M., Sanz, J., Ramos-Bosch, P., Aragon-Angel, A., Orus, R., Ochieng, W., Feng, S., Jofre, M., Coutinho, P., Samson, J., Tossaint, M., 2012. Enhanced Precise Point Positioning for GNSS Users. IEEE Trans. Geosci. Remote Sens. 50, 4213–4222.

Jung, J., Enge, P., Pervan, B., 2000. Optimization of Cascade Integer Resolution with Three Civil GPS Frequencies, in: 13th International Technical Meeting of the Satellite Division of The Institute of Navigation (ION GPS 2000). pp. 2191–2200.

Kaplan, E., Hegarty, C., 2005. Understanding GPS: Principles and Applications, 2nd ed. Artech House.

Kazmierski, K., Sośnica, K., Hadas, T., 2018. Quality assessment of multi-GNSS orbits and clocks for real-time precise point positioning. GPS Solut. 22, 11.

Khanafseh, S., Kujur, B., Joerger, M., Walter, T., Pullen, S., Blanch, J., Doherty, K., Norman, L., de Groot, L., Pervan, B., 2018. GNSS Multipath Error Modeling for Automotive Applications, in: 31st International Technical Meeting of The Satellite Division of the Institute of Navigation (ION GNSS+ 2018). pp. 1573–1589.

Klobuchar, J., 1987. Ionospheric Time-Delay Algorithm for Single-Frequency GPS Users. IEEE Trans. Aerosp. Electron. Syst. AES-23, 325–331.

Klobuchar, J.A., 1987. Ionospheric Time-Delay Algorithm for Single-Frequency GPS Users. IEEE Trans. Aerosp. Electron. Syst. AES-23, 325–331.

Kouba, J., 2008. A simplified yaw-attitude model for eclipsing GPS satellites. GPS Solut. 13, 1–12.

Kouba, J., Héroux, P., 2001. Precise Point Positioning Using IGS Orbit and Clock Products. GPS Solut. 5, 12–28.

Laurichesse, D., Banville, S., 2018. Instantaneous Centimeter-Level Multi-Frequency Precise Point Positioning. GPS World 29, 42–47.

Laurichesse, Denis, Mercier, F., Berthias, J.-P., Broca, P., Cerri, L., 2009. Integer Ambiguity Resolution on Undifferenced GPS Phase Measurements and Its Application to PPP and Satellite Precise Orbit Determination. Navigation 56, 135–149.

Laurichesse, D., Mercier, F., Berthias, J.P., Broca, P., Cerri, L., 2009. Integer ambiguity resolution on undifferenced GPS phase measurements and its applications to PPP and satellite precise orbit determination. Navig. J. Inst. Navig. 56, 135–149.

Leandro, R., Santos, M., Langley, R., 2006. UNB neutral atmosphere models:

development and performance, in: National Technical Meeting of The Institute of Navigation. pp. 564–573.

Li, B., Shen, Y., Zhang, X., 2013. Three frequency GNSS navigation prospect demonstrated with semi-simulated data. Adv. Sp. Res. 51, 1175–1185.

Li, X., 2012. Improving Real-time PPP Ambiguity Resolution with Ionospheric Characteristic Consideration, in: Proceedings of the 25th International Technical Meeting of the Satellite Division of The Institute of Navigation (ION GNSS 2012). Nashville, United States, pp. 3027–3037.

Li, X., Ge, M., Zhang, H., Wickert, J., 2013. A method for improving uncalibrated phase delay estimation and ambiguity-fixing in real-time precise point positioning. J. Geod. 87, 405–416.

Li, X., Zhang, X., Ren, X., Fritsche, M., Wickert, J., Schuh, H., 2015. Precise positioning with current multi-constellation Global Navigation Satellite Systems: GPS, GLONASS, Galileo and BeiDou. Sci Rep 5, 8328.

Markrose, S., Alentorn, A., 2011. The Generalized Extreme Value Distribution, Implied Tail Index, and Option Pricing. J. Deriv. 18, 35–60.

McGraw, G., 2009. Generalized Divergence-Free Carrier Smoothing with Applications to Dual Frequency Differential GPS. Navigation 56, 115–122.

McGraw, G., Murphy, T., Brenner, M., Pullen, S., Van Dierendonck, A.J., 2000. Development of the LAAS Accuracy Models, in: International Technical Meeting of the Satellite Division of The Institute of Navigation. pp. 1212–1223.

Meindl, M., Dach, R., Jean, Y., 2011. International GNSS Service Technical Report.

Melbourne, W.G., 1985. The Case for Ranging in GPS-based Geodetic Systems, in: International Symposium on Precise Positioning with the Global Positioning System. pp. 373–386.

Mervart, L., Lukes, Z., Rocken, C., Iwabuchi, T., 2008. Precise Point Positioning with Ambiguity Resolution in Real-Time, in: 21st International Technical Meeting of the Satellite Division of The Institute of Navigation (ION GNSS 2008). pp. 397–405.

Miguez, J., Gisbert, J.V.P., Perez, R.O., Garcia-Molina, J.A., Serena, X., Gonzales, F., Granados, G.S., Crisci, M., 2016. Multi-GNSS PPP

Performance Assessment with Different Ranging Accuracies in Challenging Scenarios, in: International Technical Meeting of The Satellite Division of the Institute of Navigation. pp. 2069–2081.

Mohammed, J., Moore, T., Hill, C., Bingley, R.M., 2018. An assessment of the precise products on static precise point positioning using multi-constellation GNSS, in: IEEE/ION PLANS 2018. pp. 634–641.

Mohammed, J., Moore, T., Hill, C., Bingley, R.M., 2017. Alternative Strategy for Estimating Zenith Tropospheric Delay from Precise Point Positioning. Atmos. Meas. Tech. Discuss. 1–24.

Mohammed, J., Moore, T., Hill, C., Bingley, R.M., Hansen, D.N., 2016. An assessment of static precise point positioning using GPS only, GLONASS only, and GPS plus GLONASS. Measurement 88, 121–130.

Mondal, P., Tewari, V.K., 2007. Present Status of Precision Farming: A Review. Int. J. Agric. Res. 2, 1–10.

Montenbruck, O., 2003. Kinematic GPS positioning of LEO satellites using ionosphere-free single frequency measurements. Aerosp. Sci. Technol.

Montenbruck, O., Gill, E., 2000. Satellite Orbits. Springer Berlin Heidelberg, Berlin, Heidelberg.

Montenbruck, O., Gill, E., Kroes, R., 2005. Rapid orbit determination of LEO satellites using IGS clock and ephemeris products. GPS Solut. 9, 226–235.

Montenbruck, O., Rizos, C., Weber, R., Weber, G., Neilan, R.E., Hugentobler, U., 2013. Getting a Grip on Multi-GNSS: the International GNSS Service MGEX Campaign. GPS World 24, 44–49.

Montenbruck, O., Steigenberger, P. eter, Hauschild, A. ndré, 2018. Multi-GNSS signal-in-space range error assessment – Methodology and results. Adv. Sp. Res. 61, 3020–3038.

Montenbruck, Oliver, Steigenberger, P., Hauschild, A., 2015. Broadcast versus precise ephemerides: a multi-GNSS perspective. GPS Solut. 19, 321–333.

Montenbruck, O, Steigenberger, P., Hugentobler, U., 2015. Enhanced solar radiation pressure modeling for Galileo satellites. J. Geod. 89, 283–297.

Montenbruck, O., Steigenberger, P., Khachhikyan, R., Weber, G., Langley, R., Mervart, L., Hugentobler, U., 2014. IGS-MGEX: Preparing the Ground for Multi-Constellation GNSS Science. Insid. GNSS 9, 42–49.

Navigation Center, 2016. Notice Advisory to NAVSTAR Users (NANU)

2016022.

Niell, A.E., 1996. Global mapping functions for the atmosphere delay at radio wavelengths. J. Geophys. Res. Solid Earth 101, 3227–3246.

Nurmi, J., Lohan, E.S., Sand, S., Hurskainen, H., 2015. GALILEO Positioning Technology, The Journal of The Institute of Electrical Engineers of Japan, Signals and Communication Technology. Springer Netherlands, Dordrecht.

O'Keefe, K., 2001. Availability and Reliability Advantages of GPS/Galileo Integration, in: ION GPS. pp. 2096–2104.

O'Keefe, K., Petovello, M., Lachapelle, Gér., Cannon, M.E., 2006. Assessing Probability of Correct Ambiguity Resolution in the Presence of Time-Correlated Errors. Navigation 53, 269–282.

Ochieng, W.Y., Feng, S., Moore, T., Hill, C., Hide, C., 2008. User Level Integrity Monitoring and Quality Control for High Accuracy Positioning using GPS/INS Measurements. J. Glob. Position. Syst. 7, 104–114.

Ochieng, W.Y., Sauer, K., Cross, P.A., Sheridan, K.F., Iliffe, J., Lannelongue, S., Ammour, N., Petit, K., 2001. Potential Performance Levels of a Combined Galileo/GPS Navigation System. J. Navig. 54, 185–197.

Ohshima, Y., Soga, H., Kawai, S., Kato, I., Taguchi, N., Mutoh, K., Yoshikawa, K., Osawa, T., Taniyama, A., Sakamoto, A., Sawamura, T., Tanaka, Y., Yoshimi, O., Hiroshi, S., Shigeki, K., Ichiro, K., Nobuyuki, T., Katsuhiko, M., Kazuhiro, Y., Tomoya, O., Aki, T., Aki, S., Toshikazu, S., Yuuki, T., 2015. Application of Precise Point Positioning (PPP) and Precise Real-Time Ephemeris to Achieve "where-in-lane" Positioning Accuracy for Vehicles, in: ION 2015 Pacific PNT Meeting. pp. 583–590.

Pan, L., Cai, C., Santerre, R., Zhang, X., 2016. Performance evaluation of single-frequency point positioning with GPS, GLONASS, BeiDou and Galileo. Surv. Rev. 49, 197–205.

Pascual-Sánchez, J.-F., 2007. Introducing relativity in global navigation satellite systems. Ann. Phys. 16, 258–273.

Penna, N., Dodson, A., Chen, W., 2001. Assessment of EGNOS Tropospheric Correction Model. J. Navig. 54, 37–55.

Petit, G., Luzum, B., 2010. IERS Conventions (2010), IERS Technical Note No. 36.

Petrie, E.J., Hernández-Pajares, M., Spalla, P., Moore, P., King, M.A., 2011. A Review of Higher Order Ionospheric Refraction Effects on Dual Frequency GPS. Surv. Geophys. 32, 197–253.

Prange, L., Dach, R., Lutz, S., Schaer, S., Jäggi, A., 2013. The CODE MGEX Orbit and Clock Solution. Int. Assoc. Geod. Sci. Assem.

Prange, L., Orliac, E., Dach, R., Arnold, D., Beutler, G., Schaer, S., Jäggi, A., 2016. CODE's five-system orbit and clock solution—the challenges of multi-GNSS data analysis. J. Geod. 91, 345–360.

Ray, J.R., Gurtner, W., 2018. RINEX Extensions to Handle Clock Information.

Richardson, T., Hill, C., Moore, T., 2016. Analysis of Multi-Constellation GNSS Signal Quality, in: International Technical Meeting of The Institute of Navigation. pp. 631–638.

Rizos, C., 2007. Alternatives to current GPS-RTK services and some implications for CORS infrastructure and operations. GPS Solut. 11, 151–158.

Rizos, C., Higgins, M., Hewitson, S., 2005. New GNSS developments and their impact on survey service providers and users. Spat. Sci. Conf.

Rizos, C., Montenbruck, O., Weber, R., Weber, G., Neilan, R.E., Hugentobler, U., 2013. The IGS MGEX Experiment as a Milestone for a Comprehensive Multi-GNSS Service, in: ION Pacific PNT Meeting. pp. 289–295.

Rockwell Collins, 1997. Results of Cycle Slip and Parity Error Rate Quantification for GPS-4000.

Romay Merino, M.M., Garcia, A.M., Medel, C.H., 2004. GSTB-V1: The First Step Towards the Development of Galileo Navigation Algorithms. IGS Work.

Saastamoinen, J., 1972. Contributions to the theory of atmospheric refraction. Bull. géodésique 105, 279–298.

Schmid, R., Steigenberger, P., Gendt, G., Ge, M., Rothacher, M., 2007. Generation of a consistent absolute phase-center correction model for GPS receiver and satellite antennas. J. Geod. 81, 781–798.

Shaer, S., Gurtner, W., Feltens, J., 1998. IONEX: The IONosphere Map EXchange Format Version 1, in: IGS AC Workshop.

Shen, X., Gao, Y., 2006. Analyzing the Impacts of Galileo and Modernized GPS on Precise Point Positioning, in: National Meeting of the Institute of

Navigation. pp. 837–846.

Shi, C., Lou, Y., Zhang, H., Zhao, Q., Geng, J., Wang, R., Fang, R., Liu, J., 2010. Seismic deformation of the Mw 8.0 Wenchuan earthquake from high-rate GPS observations. Adv. Sp. Res. 46, 228–235.

Simsky, A., Mertens, D., Sleewaegen, J.-M., Hollreiser, M., Crisci, M., 2008. Experimental Results for the Multipath Performance of Galileo Signals Transmitted by GIOVE-A Satellite. Int. J. Navig. Obs. 2008, 1–13.

Sośnica, K., Prange, L., Kaźmierski, K., Bury, G., Drożdżewski, M., Zajdel, R., Hadas, T., 2017. Validation of Galileo orbits using SLR with a focus on satellites launched into incorrect orbital planes. J. Geod. 92, 131–148.

Spofford, P.R., Remondi, B.W., 2018. The National Geodetic Survey Standard GPS Format SP3.

Steigenberger, P., Hugentobler, U., Loyer, S., Perosanz, F., Prange, L., Dach, R., Uhlemann, M., Gendt, G., Montenbruck, O., 2015. Galileo orbit and clock quality of the IGS Multi-GNSS Experiment. Adv. Sp. Res. 55, 269–281.

Svehla, D., Rothacher, M., Cacciapuoti, L., 2016. Thermal Re-Radiation Acceleration in the GNSS Orbit Modelling Based on Galileo Clock Parameters. IGS Work.

Teunissen, P.J.G., 1998. Success probability of integer GPS ambiguity rounding and bootstrapping. J. Geod. 72, 606–612.

Teunissen, P.J.G., 1995. The least-squares ambiguity decorrelation adjustment: a method for fast GPS integer ambiguity estimation. J. Geod. 70, 65–82.

Teunissen, P.J.G., Montenbruck, O., 2017. Springer Handbook of Global Navigation Satellite Systems. Springer International Publishing, Cham.

Teunissen, P.J.G., Odijk, D., Zhang, B., 2010. PPP-RTK: Results of CORS network-based PPP with integer ambiguity resolution. J. Aeronaut. Astronaut. Aviat. 42, 223–230.

Uhlemann, M., Gendt, G., Ramatschi, M., Deng, Z., 2013. GFZ Global Multi-GNSS Network and Data Processing Results, in: International Association of Geodesy Scientific Assembly. Springer International Publishing, pp. 673–679.

Viandier, N., Rabaoui, A., Marais, J., Duflos, E., 2009. Enhancement of Galileo and multi-constellation accuracy by modeling pseudorange noises. Int.

Conf. Intell. Transp. Syst. Telecommun.

Villiger, A., Dach, R., 2017. International GNSS Service Technical Report.

Villiger, A., Dach, R., 2016. International GNSS Service Technical Report.

Vollath, U., Birnbach, S., Landau, L., Fraile-OrdoÑEz, J.M., MartÍ-Neira, M., 1999. Analysis of Three-Carrier Ambiguity Resolution Technique for Precise Relative Positioning in GNSS-2. Navigation 46, 13–23.

Wang, J., Keller, W., Sharifi, M., 2006. Comparison Of Availability Of Galileo, Gps And A Combined Galileo/Gps Navigation Systems. Artif. Satell. 41, 3–15.

Wang, L., Groves, P.D., Ziebart, M.K., 2012. Multi-Constellation GNSS Performance Evaluation for Urban Canyons Using Large Virtual Reality City Models. J. Navig. 65, 459–476.

Wang, L., Li, Z., Ge, M., Neitzel, F., Wang, Z., Yuan, H., 2018. Validation and Assessment of Multi-GNSS Real-Time Precise Point Positioning in Simulated Kinematic Mode Using IGS Real-Time Service. Remote Sens. 10, 337.

Wang, M., Gao, Y., 2006. GPS Un-Differenced Ambiguity Resolution and Validation, in: 19th International Technical Meeting of the Satellite Division of The Institute of Navigation (ION GNSS 2006). pp. 292–300.

Werner, W., Winkel, J., 2003. TCAR and MCAR Options with Galileo and GPS, in: 16th International Technical Meeting of the Satellite Division of The Institute of Navigation (ION GPS/GNSS 2003). pp. 790–800.

Wu, J.T., Wu, S.C., Hajj, G.A., Bertiger, W.I., 1993. Effects of antenna orientation on GPS carrier phase. Manuscripta Geod. 18, 91–98.

Wubbena, G., 1985. Software Developments for Geodetic Positioning with GPS using TI-4100 Code and Carrier Measurements, in: International Symposium on Precise Positioning with the Global Positioning System. pp. 403–412.

Wubbena, G., Schmitz, M., Menge, F., Seeber, G., Volksen, C., 1997. A New Approach for Field Calibration of Absolute Antenna Phase Center Variations. Navig. J. Inst. Navig. 44, 247–256.

Yang, L., Hill, C., Moore, T., 2013. Numerical weather modeling-based slant tropospheric delay estimation and its enhancement by GNSS data. Geo-spatial Inf. Sci. 16, 186–200.

Yasyukevich, Y., Astafyeva, E., Padokhin, A., Ivanova, V., Syrovatskii, S., Podlesnyi, A., 2018. The 6 September 2017 X-Class Solar Flares and Their Impacts on the Ionosphere, GNSS, and HF Radio Wave Propagation. Sp. Weather 16, 1013–1027.

Yunck, T.P., 1993. Coping with the Atmosphere and Ionosphere in Precise Satellite and Ground Positioning, in: Environmental Effects on Spacecraft Positioning and Trajectories. pp. 1–16.

Zhang, B., Ou, J., Yuan, Y., Li, Z., 2012. Extraction of line-of-sight ionospheric observables from GPS data using precise point positioning. Sci. China Earth Sci. 55, 1919–1928.

Zhang, H., Gao, Z., Ge, M., Niu, X., Huang, L., Tu, R., Li, X., 2013. On the Convergence of Ionospheric Constrained Precise Point Positioning (IC-PPP) Based on Undifferential Uncombined Raw GNSS Observations. Sensors 13, 15708–15725.

Zhang, Y., Gao, Y., 2006. Influence Analysis of Tropospheric Model and Mapping Function on Precise Tropospheric Delay Estimation Using PPP, in: 19th International Technical Meeting of the Satellite Division of The Institute of Navigation (ION GNSS 2006). pp. 1884–1890.

Zumberge, J.F., Gendt, G., 2001. The demise of selective availability and implications for the international GPS service. Phys. Chem. Earth, Part A Solid Earth Geod. 26, 637–644.

Zumberge, J.F., Heflin, M.B., Jefferson, D.C., Watkins, M.M., Webb, F.H., 1997. Precise point positioning for the efficient and robust analysis of GPS data from large networks. J. Geophys. Res. Solid Earth 102, 5005–5017.